UNIVERSITY
*of*
GLASGOW

# Novel Structures and Fabrication Techniques for the Observation of Solitons in AlGaAs.

Submitted to the faculty of Engineering of the University of Glasgow for the degree of Doctor of Philosophy.

By
Craig James Hamilton.

Department of Electronics
& Electrical Engineering.
University of Glasgow.
Glasgow.
Scotland.
G12 8QQ.

December 1995.

© Craig James Hamilton.

ProQuest Number: 11007916

All rights reserved

INFORMATION TO ALL USERS
The quality of this reproduction is dependent upon the quality of the copy submitted.

In the unlikely event that the author did not send a complete manuscript
and there are missing pages, these will be noted. Also, if material had to be removed,
a note will indicate the deletion.

ProQuest 11007916

Published by ProQuest LLC (2018). Copyright of the Dissertation is held by the Author.

All rights reserved.
This work is protected against unauthorized copying under Title 17, United States Code
Microform Edition © ProQuest LLC.

ProQuest LLC.
789 East Eisenhower Parkway
P.O. Box 1346
Ann Arbor, MI 48106 – 1346

Thesis
10562
Copy 1

GLASGOW
UNIVERSITY

# Acknowledgements.

To spend over twenty years at school and say that I have enjoyed every last minute would be nothing but a lie. I have however, enjoyed some very good times at the university studying for this thesis, and it must be said that without the continual help and support of many people this work would never have been completed.

Without doubt the support, guidance and friendship I have received from my supervisor Stewart Aitchison, has played a major part in the path my work has taken. I would therefore like to thank him for the freedom he gave me to follow my nose, also for naming his children after me and not beating me up for destroying his house.

When things have looked grim, support from friends has helped to keep things in perspective. I would like to thank some new friends; Jim, John, Mike, Callum, Philip, Gary, Judith, Patsy, Chris and Andy for being an ear to bend when it was needed. Some old friends more than deserve a mention; Paul, Mikey, Kev, Davy and Belhaven Export for keeping my feet firmly on the ground when my head was in the clouds.

I am extremely grateful to Professor Laybourn for the use of the departmental facilities. Also I must thank John Marsh, Richard De la Rue and Charlie Ironside for their advice and encouragement. Support from the technical staff has been unfailing especially Jim "bald eagle" Young who deposited enough silica to double glaze my house, Jim Gray for fixing everything I broke, Dougie Irons and his team for building the everything which I broke and everyone else who went out of their way to make things a lot easier for me.

Without the help of F. Lederer and the Peschel Brothers in Jena the ARROW work would not of been half as interesting. I must also thank Brian Smith and Frasier Clark at the University of Paisley for their help on the ARROWs, and lets's hope we manage to publish another paper from the Bull Inn school of photonics research. The university also deserves a big thank you for funding my study. I would especially like to thank J. D. Gray as the scholarship was paid from her fund.

Last but not least I must thank all of my family who have continued to give me their unfaltering support (not at least financial) for as long as I can remember. I would also like to thank my other family in Bridge of Weir, most especially my little sunnybeam; Kirsten, for all of her love and understanding especially when I had my spud head on. Finally I must thank my parents; Rosie and Jim, for giving me the opportunity, love and support I have needed to follow my studies.

**Thanks!**

***Mum and Dad.***

# Abstract.

Novel structures and fabrication techniques applicable to the study of both spatial and temporal solitons in AlGaAs are investigated.

A new and novel technique for suppressing the intermixing of GaAs/AlGaAs MQWs has been demonstrated. The technique relies on a hydrogen plasma discharge to produce a $Ga_2O_3$ layer from the native oxides on the GaAs surface and suppress vacancy formation. This method for suppressing intermixing has been shown to be free from damage, highly reproducible, can be made area selective using a patterned silica mask, does not introduce impurities and can be used to fabricate relatively long, low loss GaAs/AlGaAs MQW waveguides.

This technique was subsequently used to produce samples with approximately 40 nm shift in the band edge, which lead to a corresponding change in the nonresonant optical nonlinearity of in excess of 60 %. This potentially opens the way for the production of many novel nonlinear optics devices which previously had no possible fabrication means.

Also it has been experimentally shown that by using properly designed AlGaAs ARROW waveguides, the natural normal dispersion of the semiconductor can be overcome and waveguide modes can be made anomalous. This fact has been used to demonstrate solitonic compression of 1.51 μm femtosecond pulses propagating in the guides, and the results are observed to correlate well with the theoretically predicted values.

# Publications.

## Journal Publications.

C. J. Hamilton, S. E. Hicks, B. Vögelle, J. H. Marsh and J. S. Aitchison, *"Suppression of bandgap shifts in GaAs/AlGaAs MWQ's using hydrogen plasma processing."*, Electron. Lett. Vol. 31 (16), (1995), pp. 1393.

B. Smith, D.F. Clark and C. Hamilton, *"Characterisation of planar Antiresonant reflecting optical wave-guide structures on silicon by an Abbe refractometer."*, Opt. Lett. **20**, 20, pp. 2048, 1995.

C. J. Hamilton, G. T. Kennedy, W. Sibbett, W. Biehlig, U. Peschel, T. Peschel, F. Lederer and J. S. Aitchison, *"Observations of Bright Solitary Pulses in Semiconductors near Half-the-Band-Gap.."*, Submitted to Phys. Rev. Lett. 1995.

C. J. Hamilton, G. T. Kennedy, W. Sibbett and J. S. Aitchison, *"Localised Kerr Type Nonlinearities in GaAs/AlGaAs Multiple Quantum Well structures at 1.55 μm."*, Submitted to Appl. Phys. Lett. 1995.

## Conference Publications.

C. J. Hamilton, G. T. Kennedy, W. Sibbett and J. S. Aitchison., *"Nonlinear Properties of Disordered GaAs/AlGaAs MQW structures at 1.55 μm."*, ECIO, Delft, Netherlands, 1995.

C. J. Hamilton, G. T. Kennedy, W. Sibbett, W. Biehlig, U. Peschel, T. Peschel, F. Lederer and J. S. Aitchison., *"Experimental Observations of Bright Temporal Solitons in AlGaAs Arrow Waveguides."*, Q. E. 12, O. R. C. Southhampton, England. 1995.

C. J. Hamilton, G. T. Kennedy, W. Sibbett, W. Biehlig, U. Peschel, T. Peschel, F. Lederer and J. S. Aitchison., *"First experimental observations of solitary pulse propagation in semiconductors below half-theband-gap."* PD32, O. S. A., Nonlinear Guided Waves And Their Applications, Dana Point, February 1995.

# Contents.

# Chapter 1.

# Introduction.

In the early days of electronic communication, the telegraph and telephone revolutionised the way we communicate with one another. It has since become clear that the ability to exchange information without direct contact, is one of the greatest ever technological advances. Francis Bacon (1561-1626) said "Knowledge is power", and it is obvious that for everyone to benefit from knowledge, it should be as widely available as possible. Indeed it is no accident that at the present moment, that the internet has arguably become one of the decade's most topical subjects.

Therefore, to attain the benefits of available information, it is essential to provide an infrastructure where data flows fast and free. However, this thirst for knowledge has resulted in a situation where the desire for greater data carrying capacity (Bandwidth), appears to be escalating upon an almost daily basis[1]. This increase in information services, has led directly to today's electronic networks becoming inadequate. Therefore

faster, simpler, and more cost effective methods of communication are continually researched.

Electronic data communications systems limit network[2], channels to less than 5 Gb $s^{-1}$, and hence, interest has been stimulated in the extensive bandwidth[3], and low loss propagation[4] available from optical communications[5]. Such optical transmission techniques have been shown to propagate data rates in excess of 5 Gb $s^{-1}$ over more than 14 000 Km[6], and as yet the full capacity (TeraHertz)[7] of fibre transmission systems has still to be realised. To fully achieve the transmission potential offered by optical networks two distinct points must be addressed:

- **Data routing and processing must occur in an all optical format.**
- **It must be possible to transmit data over long haulage distances.**

Fast data routing and processing will only be possible if an all optical switch is realised. This device requirement has spawned a whole field within the study of nonlinear optical research[8]. At present most long haul communications are performed either by satellites or hardwire undersea links. The latter is of most relevance here, since in general it is the most commonly used, and data is typically transferred using the current generation of hybrid electronic and optical fibre communication systems (figure 1.1.).

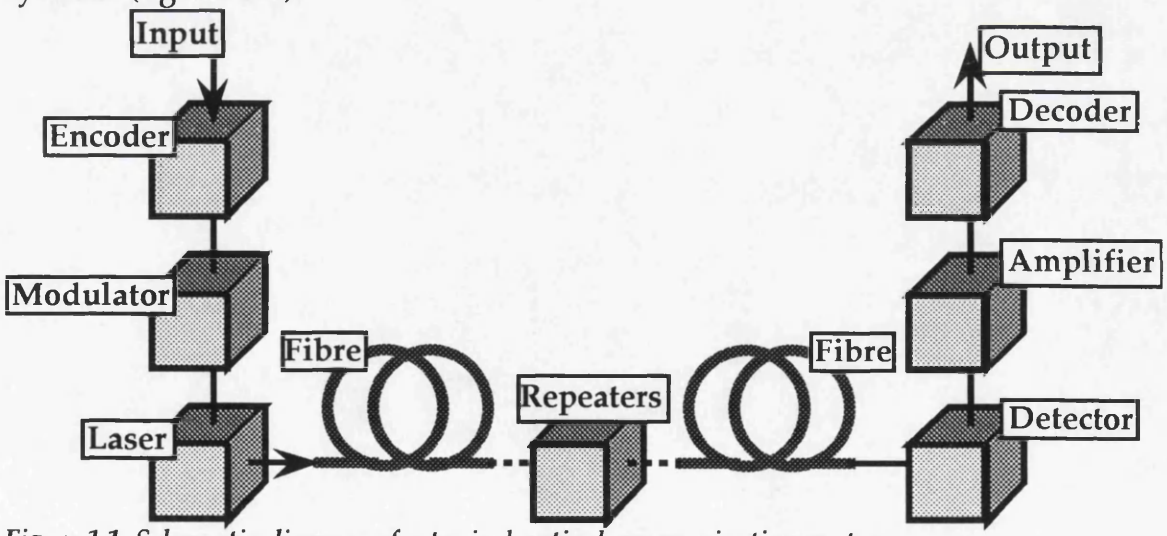


*Figure 1.1. Schematic diagram of a typical optical communication system.*

Generally these systems use 1.55 μm lasers, because they coincide with the lowest loss silica fibre window[9]. The optical fibres are typically dispersion shifted[10] or dispersion flattened, so that they can propagate

pulses in this low loss regime with minimum distortion, however pulses will experience some loss, and therefore signals will have to be periodically amplified.

At present this is performed by electronic repeaters spaced by approximately 100 km[11], and hence repeaters have two disadvantages, they impose severe speed limitations, and significantly increase the cost of data transfer systems. It has been for these reasons that soliton based optical systems have been investigated. Solitons can provide distortion free data communication over long distances at extremely high data rates, and also have the great advantage that periodic amplification can be performed without using electronics.

The following sections give a general introduction to nonlinear optics, ultrashort pulse generation and propagation, as this will enable a basic understanding of the role solitons can play in future communication systems.

### 1.1. Nonlinear Optics.

Nonlinear optics is the study of the interaction of intense light, with materials. Effects can manifest themselves in many different ways, such as:

- **Raman scattering[12].**
- **Second harmonic generation[13].**
- **Frequency mixing[14].**
- **Intensity dependent refractive index[15].**

This thesis is predominately concerned with the last of these effects, when it occurs on an effectively instantaneous time scale. In this case it is referred to as the **Kerr Effect**. The Kerr effect was first observed by the Reverend John Kerr at the University of Glasgow in 1875. Kerr initially observed the effect in glass using a specially developed cell, which is still retained at the university and is shown in figure 1.2..

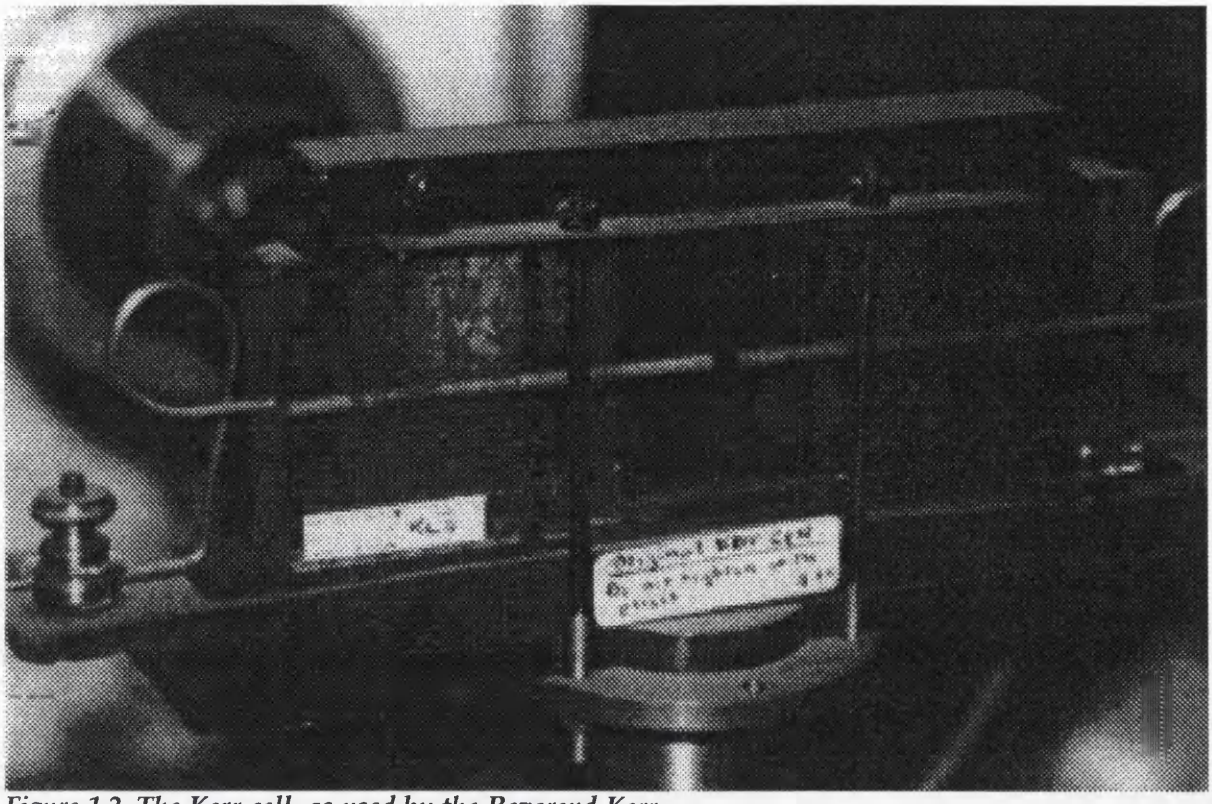

*Figure 1.2. The Kerr cell, as used by the Reverend Kerr.*

After the invention of the laser the light intensities required ($\approx 2.5$ kW cm$^{-2}$) to observe optical nonlinearities became readily available, and subsequently the field of nonlinear optics exploded. Many materials have been examined for their suitability e.g. glasses[16], and polymers[17]. However, where $\chi^{(3)}$ is concerned semiconductors and optical fibres have attracted the most interest. In optical fibres the magnitude of $\chi^{(3)}$ is relatively small but their ultra low loss allows propagation over long distances makes them a very suitable experimental system. With semiconductors the value of $\chi^{(3)}$ is much larger, and they also posses a mature fabrication base which makes them extremely attractive for nonlinear studies. Where communication systems are concerned the interest in Kerr nonlinearities exists, because in general it is the mechanism that makes all optical switching and soliton propagation possible.

Nonlinear optical switching is concerned with the use, of the intensity dependent refractive index to fabricate all-optical switches. This intensity dependence makes it possible for the device output to be dependent upon the input, which is by definition a switch. All optical switching has been proposed in a number of different forms:

- **Nonlinear directional coupler[18] (NLDC).**
- **Asymmetric Mach-Zehnder Interferometers[19] (AMZI).**
- **Spatial soliton based couplers[20].**

And physical devices have been produced in various formats:

- **NLDC in AlGaAs MQW Strain induced waveguides[21].**
- **AMZI in AlGaAs waveguides[22].**
- **Optical fibre nonlinear loop mirror[23].**
- **Optical bistable devices[24].**
- **X-Junction in AlGaAs waveguides[25].**

Optical solitons have been proposed as the data transfer "bit" in the next generation data communication systems, as they will be able to exploit the linear and nonlinear properties of conventional optical fibre. However, the future of optical soliton communications is not certain, as many problems still have to be addressed. These problems are predominately concerned with timing uncertainties associated with jitter[26] and soliton interactions[27]. These are being dealt with solutions such as sliding filters[28] and indeed solitons have demonstrated data transmission in optical communication[29] systems up to 80 Gb $s^{-1}$.

## 1.2. Nonlinear Optical Theory.

When light propagates through a dielectric medium the valence band electrons of the material oscillate in a manner, that is related to the amplitude and frequency of the propagating electric field. This reaction of the electric dipoles to the light is termed the polarisation (P), and is expressed in units of dipole moments per unit volume. At low intensities the polarisation follows the amplitude and frequency of the light and can be expressed as:

$$P = \varepsilon_o \chi^{(1)} E \qquad \textbf{1.1.}$$

Where $\varepsilon_o$ is the permittivity of a vacuum, $\chi^{(1)}$ is the linear susceptibility of the material, and E is the applied electric field. The susceptibility is related to the linear refractive index through:

$$n = \sqrt{\mathrm{Re}\left(1+\chi^{(1)}\right)} \qquad \textbf{1.2.}$$

However, at high light intensities the response becomes nonlinear, and can be expressed in the more general form:

$$P = \varepsilon_o\left(\chi^{(1)}E + \chi^{(2)}EE + \chi^{(3)}EEE + \ldots\right) \qquad \textbf{1.3.}$$

Where $\chi^{(j)}$ is $j^{th}$ order susceptibility which is tensor of rank j+1. The second term of the polarisation (i. e. the $\varepsilon_o\chi^{(2)}E^2$ term) represents a second order nonlinearity, and gives rise to such effects as second harmonic generation, optical rectification and optical parametric generation. It should be noted that this polarisation term contains an $E^2$ component, which means that it can only exist in materials that do not posses inversion symmetry (section 1.2.1.). The third order term in the series is non-zero for all materials, and is responsible for many effects which include self phase modulation, four wave mixing, and self focusing. If terms above $\chi^{(3)}$ are ignored the refractive index becomes intensity dependent, and can be expressed by the relation:

$$n = n_o + n_2 I \qquad \textbf{1.4.}$$

Where $n_o$ is the linear refractive index, I is the light intensity and $n_2$ is the nonlinear refractive index, which is defined as:

$$n_2 = \frac{12\pi^2}{n_o c}\chi^{(3)} \qquad \textbf{1.5.}$$

This nonlinear refractive index is termed the Kerr coefficient and is around $1 \times 10^{-13}\,cm^2\,W^{-1}$ in AlGaAs. In the following sections some nonlinear optical processes are discussed.

### 1.2.1. Second Harmonic Generation .

In equation 1.3. it is apparent from the $\varepsilon_o\chi^{(2)}E^2$ term that the polarisation possess a squared relation with the electric field. In general the electric field of propagating light has a harmonic

form (i. e. cos ωt), and squaring it will lead to the generation of a signal at 2 ω, this is known as second harmonic generation (SHG). One of the most important things to note about SHG, is that it cannot be performed in crystals that posses inversion symmetry, and it needs a crystal arrangement such as gallium arsenide which has a zinc-blende structure (figure 1.3.).

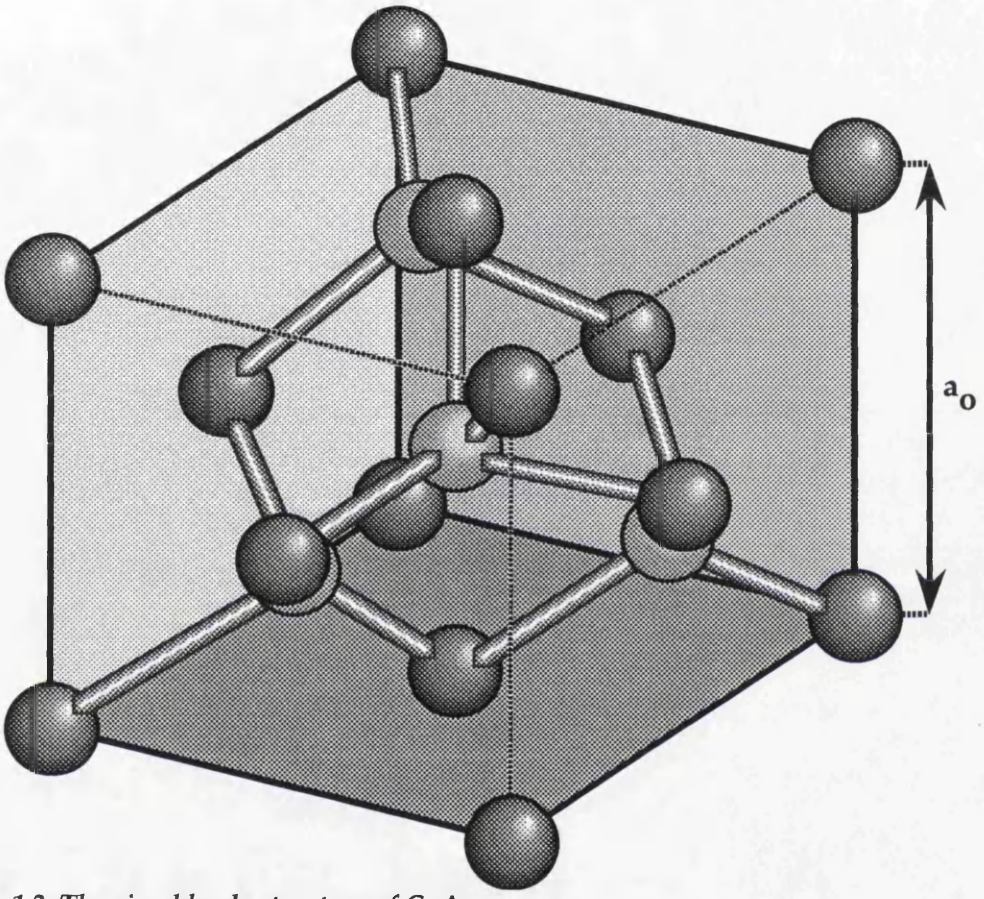


*Figure 1.3. The zinc-blende structure of GaAs.*

In figure 1.3. $a_o$ is the lattice constant (GaAs ≈ 5.65Å).

If an electric field is applied to a symmetrical molecule, a polarisation is induced in the same direction as the applied field. If the field direction is now reversed the polarisation is also reversed, and because the crystal is centrosymmetric the magnitude of the polarisation must be the same in both directions (i. e. P(E) = -P(-E)). From equation 1.3. it is clear that the only way for this to hold true is if $\chi^{(2)}$ is zero.

One of the major problems associated with SHG is phase matching, which is concerned with matching the propagation

constants of the fundamental and signal frequencies ($\omega$ and $2\omega$ for SHG). Phase matching is required since the fundamental and SHG waves posses different propagation constants. As the fundamental propagates through the material any signal generated at $2\omega$, will have a different propagation constant and will then walk in and out of phase with the fundamental. Phase matching is typically achieved by setting the propagation constant of the two waves to be the same. For example using a birefringent material. Generally the refractive index is tuned by either angle or temperature, to achieve a match between the two propagation constants of the two waves.

### 1.2.2. Self Focusing.

Typically a laser beam has a gaussian intensity profile. This means that in a medium possessing a positive nonlinearity, a beam will experience a higher refractive index at the centre, compared to the wings. Therefore, the centre of the beam will be slowed down compared with the edges, and consequently the wavefronts will become concave and effectively focus. As the wave focuses, the intensity becomes higher and as a result the wavefront will continue to focus further. This process will continue until either a critical threshold value is met, and the material is damaged[30], or the process is altered by some higher order effect. Conversely, if a negative Kerr coefficient is encountered, the opposite is true and the beam will effectively defocus.

### 1.2.3. Self Phase Modulation.

Self Phase Modulation (SPM) arises due the nonlinear refractive index, reacting with the time varying intensity of the propagating optical pulse. Since the intensity across a typical optical pulse is not uniform there will be a phase shift incurred across the pulse which is equal to:

$$\phi_{nl} = \frac{2\pi n_2}{\lambda} \text{I} \text{L} \qquad \textbf{1.6.}$$

Where L is the propagation length, I is the light intensity, $n_2$ is the nonlinear refractive index and $\lambda$ is the wavelength. This effect is discussed in more depth in section 3.5.1..

### 1.2.4. Multi-Photon Absorption.

When incident photons have energies that are less than the bandgap, the optical absorption is extremely low. If the light is very intense, then a phenomenon known as Two Photon Absorption (TPA) can become important and limit the throughput of a device. TPA occurs when the total energy of two incident photons are greater than, or equal to, the bandgap, and the photons are absorbed by way of a virtual state (figure 1.4.). The two photons need not posses the same energy as one another, but they must both arrive within a time period governed by the uncertainty principle.

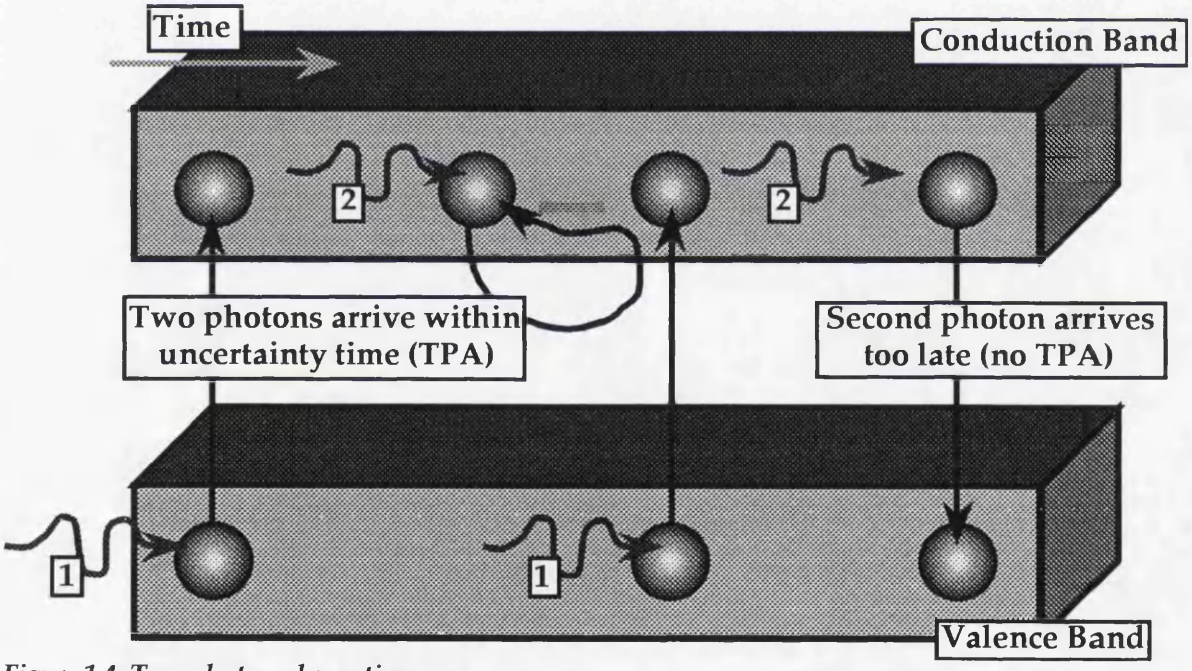


*Figure 1.4. Two photon absorption.*

TPA is highly useful in some areas of spectroscopy[31], especially for measuring conduction and valence band offsets. This is because TPA is not governed by the same selection rules as linear absorption, and to measure these offsets, the energy difference between successive quantised energy levels must be known.

## 1.3. Solitons.

Solitonic behaviour was first observed by Scottish shipbuilder John Scott Russell in August 1834. While he was horse riding on the banks of the Union canal (between Glasgow and Edinburgh), Russell observed a surface water wave which propagated for a few miles without changing shape. He named this "singular and beautiful phenomenon" the **wave of translation**, and then proceeded to characterise the phenomenon by a series of experiments using a water tank[32]. Interest in the phenomenon then waned, until sixty years later when Korteweg and de Vries published the now well known KdV equation[33], which described the motion of water waves in a shallow channel.

In systems that can be described by nonlinear Schrödinger equation, solitons arise from the balancing of a linear dispersion term, with a nonlinear phase modulation term. Solitons are extremely robust and can survive strong perturbations within a system and indeed they can be represented as particle like objects[34]. Some examples of systems where solitonic behaviour can exist are:

- **Oscillating soliton stars, which are solutions to general relativity equations[35].**
- **Trains of solitons have been photographed propagating in the wake of the Tsunami wave by satellites[36].**
- **Plasma solitons in space[37].**

Temporal optical solitons were first predicted by Hasegawa and Tappert[38] in 1973, and in 1980 Mollenauer[39] experimentally verified their predictions by propagating a bright optical soliton. At first temporal solitons were thought to be too complicated, and power hungry to be any practical use in communication systems. The invention of Erbium Doped Fibre Amplifiers (EDFAs) has lead to a resurgence of interest, and long distance soliton transmission systems are beginning to receive serious consideration. EDFAs have rekindled interest in soliton systems, due to the possibility of periodic signal amplification without the speed, and cost restrictions of electronic repeaters.

Spatial solitons arise from the balancing of diffraction and induced self focusing of an optical beam, these typically occur in materials possessing a positive nonlinear Kerr coefficient. Spatial optical solitons are completely analogous to temporal solitons and have been observed experimentally in various formats:

- **$CS_2$ liquid waveguides[40].**
- **Ion exchange glass waveguides[41].**
- **AlGaAs semiconductor waveguides[42].**

They have also been shown to exhibit particle like properties, in soliton interactions[43].

To physically understand how solitons arise it helps to consider figure 1.5. Three brothers are out for drive in their respective cars. As they live in the west of Scotland it is always raining and the ground has a spongy mattress like feel to it. The eldest brother being an accountant has a fast car, the middle brother has a regular steady job and therefore enjoys a reliable average type of car, however, the youngest brother who plumped for a job in engineering, has ended up driving an old slow banger. Being brothers they want to drive to their favourite pub for a relaxing lunch, but they keep getting split up due to their car's respective performances.

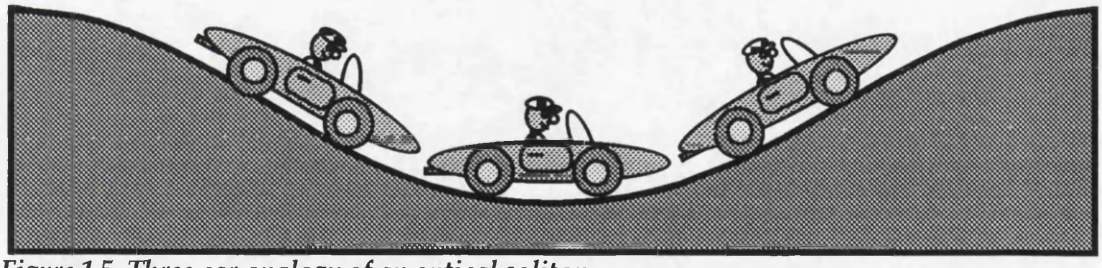

*Figure 1.5. Three car analogy of an optical soliton .*

Although the younger brother is by far the worse paid, being an optical engineer he is extremely sharp. Therefore, he proposes that they drive directly behind one another, with the oldest brother out in front followed by the middle brother, and he will bring up the rear in his old banger. Due to the land deformation the eldest brother uses his greater power to continually drive his car up hill, the middle brother drives his car on the flat and the youngest brother drives downhill all the way to a free lunch (because he is

extremely smart), using the deformation caused by the other two cars.

By imagining the brothers' cars are the spectral components of a pulse, it is possible to relate this analogy to temporal optical solitons, in the negative dispersion regime of typical optical fibres. The fast car corresponds to the blue frequencies, the slow car the red frequencies and the middle car is the average wavelength. In this regime the red spectral components see a higher refractive index than the blue ones and the spectral components will spread out as they propagate (section 1.6.1.). The land deformation is equivalent to the refractive index profile induced through the nonlinear Kerr effect, which effectively slows the blue frequencies and speeds up the red ones, and hence the pulse propagates without break up.

### 1.3.1. Temporal Optical Solitons.

It is possible to describe temporal solitons in mathematical terms. using the following partial differential equation:

$$i\frac{\partial A}{\partial z} = \beta_2 \frac{1}{2}\frac{\partial^2 A}{\partial T^2} + \gamma |A|^2 A \qquad 1.7.$$

This is known as the nonlinear Schrödinger equation, where A (z,T) is the amplitude of the pulse envelope, $\beta_2$ is the dispersion parameter and is a nonlinearity parameter $\gamma$ is defined by:

$$\gamma = \frac{n_2 \omega_o}{c A_{eff}} \qquad 1.8.$$

However it is easier to solve this equation when it is reduced to a standard form, therefore if the following factors are introduced:

$$U = \frac{A}{\sqrt{P_o}}, \xi = \frac{z}{L_d}, \tau = \frac{T}{T_o} \qquad 1.9.$$

Where $P_o$ is the peak power, $T_o$ is the width of the incident pulse and $L_d$ is the dispersion length (equation 1.37.), equation 1.7. can be represented by:

$$i\frac{\partial U}{\partial \xi} = sgn(\beta_2)\frac{1}{2}\frac{\partial^2 U}{\partial \tau^2} - \gamma|U|^2 U \qquad \textbf{1.10.}$$

The parameter N is defined as the square of the ratio of the nonlinear length $\left(L_N = \frac{1}{\gamma P_o}\right)$ to the dispersion length, if another parameter u is defined:

$$u = NU = A\sqrt{\frac{\gamma T_o^2}{|\beta_2|}} \qquad \textbf{1.11.}$$

This then gives the nonlinear Schrödinger equation in its standard form:

$$i\frac{\partial u}{\partial \xi} + \frac{1}{2}sgn(\beta_2)\frac{\partial^2 u}{\partial \tau^2} + |u|^2 u = 0 \qquad \textbf{1.12.}$$

The second term characterises linear dispersion, and the third term is related to the nonlinear propagation, and it is possible to use this equation to describe how solitons propagate. If the action of the dispersive term is considered first, by ignoring the nonlinear term and considering the basic form of the resulting equation:

$$\frac{\partial u}{\partial \xi} = \frac{i}{2}\frac{\partial^2 u}{\partial \tau^2} \qquad \textbf{1.13.}$$

This equation is easily dealt with in the frequency domain, by using Fourier transforms:

$$\frac{\partial \tilde{u}}{\partial \xi} = -\frac{i}{2}\omega^2 \tilde{u} \qquad \textbf{1.14.}$$

The general solution of this equation is:

$$\tilde{u}(\xi,\omega) = \tilde{u}(0,\omega)e^{-i\left(\frac{\omega^2 \xi}{2}\right)} \qquad \textbf{1.15.}$$

This solution shows that essentially the dispersive term only rearranges the phase of the frequency components. If the nonlinear term is considered alone, the general form is:

$$\frac{\partial u}{\partial \xi} = i|u|^2 u \qquad \textbf{1.16.}$$

Neglecting amplitude variations the solution of this equation in the time domain is:

$$u(\xi,\tau) = \tilde{u}(0,\tau)e^{-i|u|^2\xi} \qquad \textbf{1.17.}$$

It is obvious from this equation, that the nonlinear term modifies the phase in relation to the intensity of the pulse envelope, and hence adds new frequency components. However, it is not clear how time broadening due to the linear dispersive term, and spectral broadening due to the nonlinear term can cancel one another and result in soliton propagation. This can be explained by considering the first order effects of both terms. The nonlinear term generates a phase change:

$$d\phi(\tau) = |u(\tau)|^2 d\xi \qquad \textbf{1.18.}$$

It is well known that if a function f(ξ, τ) is real, the general equation:

$$\frac{\partial u}{\partial \xi} = if(\xi,\tau)u \qquad \textbf{1.19.}$$

simply generates a phase change (with respect to ξ):

$$d\phi(\tau) = f(0,\tau)d\xi \qquad \textbf{1.20.}$$

From studying equation 1.13. it is obvious that the linear dispersive term generates a phase change:

$$d\phi = \left(\frac{1}{2}\frac{\partial^2 u}{\partial \tau^2}\right)d\xi \qquad \textbf{1.21.}$$

If a sech pulse envelope (i. e. u = sech(τ)) is considered, it is seen that the nonlinear term generates a phase change:

$$d\phi_{NL} = \mathrm{sech}^2(\tau)d\xi \qquad \textbf{1.22.}$$

and the linear dispersive term:

$$d\phi_{disp} = \left[\tfrac{1}{2} - \mathrm{sech}^2(\tau)\right]d\xi \qquad \textbf{1.23.}$$

Clearly these phase shifts are the complements of each other and under certain conditions will cancel.

### 1.3.2. Spatial Optical Solitons.

Spatial solitons are unique solutions of the nonlinear Schrödinger equation, and can be described in a similar manner to temporal solitons. The only difference is that the time dependence is replaced by a spatial one (diffraction). Spatial solitons are essentially self trapped optical beams, and can be likened to an optical waveguide (figure 1.6.).

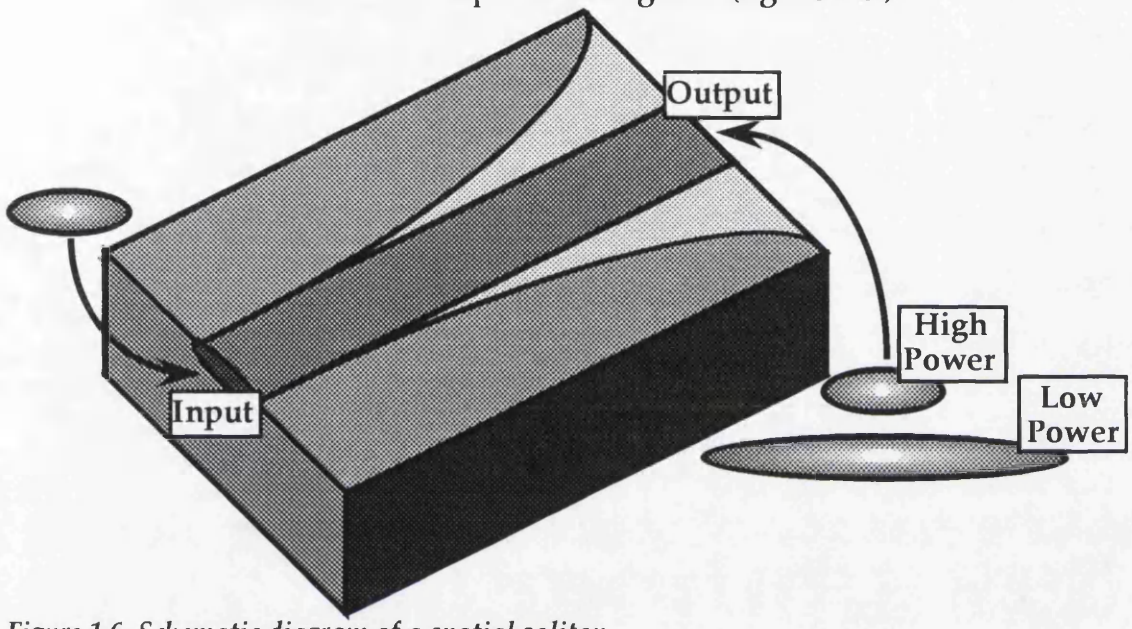


*Figure 1.6. Schematic diagram of a spatial soliton.*

Since spatial solitons can be described in an analogous fashion to their temporal counterparts, they too have a sech-like shape which can be described by:

$$E(x) = A\,\mathrm{sech}\left(\frac{x - x_o}{a_o}\right) \qquad \textbf{1.24.}$$

Where $a_o$ is a measure of the beam width. A spatial soliton will propagate at a power level:

$$P_s = \frac{2n_o w}{n_2 a_o k^2} \qquad \textbf{1.25.}$$

Where $n_o$ is the linear refractive index, $n_2$ is the nonlinear refractive index, k is the wavevector of the light and w is the transverse mode size. It should be noted that since w is typically much less than $a_o$ it has little effect. From studying equation 1.25. it is clear that at different power levels, solitons

of different widths will propagate. Indeed for launched power levels between $0.25 \times P_s$ and $2.25 \times P_s$, the beam will evolve into a soliton with a characteristic width.

It has been proposed to use spatial solitons for optical processing by making use of some of their unique properties. All optical switching using spatial solitons could make use of Snell's law at a nonlinear interface to produce a spatial scanner[44]. Or, it may be possible to use soliton emission from waveguides[45] to produce soliton couplers.

## 1.4. Generation of Ultrashort Optical Pulses.

There are two main types of mode locking used in the production of ultrashort optical pulse trains, these are active[46] and passive mode locking. Active mode locking operates by applying an external modulation, to either the amplitude (AM), or the phase (PM) of the light within the optical cavity. The purpose of this modulation is to generate new optical frequencies, which will have different longitudinal modes in the cavity. The length of the cavity can then be used to lock the modes, which posses an integer number of half cycles together, and hence produce optical pulses. Passive mode locking makes use of nonlinear optical element, which has a high loss at low intensities, however, the loss saturates at high intensities therefore reducing its effects. The maximum emission principle[47] states that a laser will operate in a state that maximises its output, and therefore under certain conditions the laser will tend to operate in a mode locked state, whereby it emits high power pulses. Some mode locking techniques which are applicable to this study are described in the following sections.

### 1.4.1. Frequency modulation (Active).

Mode locking by frequency modulation (section 4.2.2.) can be described adequately in both the frequency and time domains. It is usually accomplished by the introduction of a sinusolidally driven electro-optic material, at one end of a laser cavity. If the time domain is considered first, light which passes through the electro-optic material will experience a phase shift, and thus a frequency shift $\left(f = \frac{d\phi}{dt}\right)$. However, when the modulator drive

signal is zero the light will see no phase shift. If the length of the cavity is now "locked" to the frequency of the drive signal, the light at the "null point" will be successively amplified. Where as the rest of the light, will be pushed outside the gain bandwidth by successive passes through the modulator.

In the frequency domain it is possible to represent the modulated signal by:

$$E(t) = E_o \cos(\omega_o t + \gamma \cos \omega_m t) \qquad \textbf{1.26.}$$

Where $\gamma$ is the modulation index, $\omega_o$ is the central light frequency and $\omega_m$ is the modulation frequency. It is possible to mathematically represent equation 1.26. using Bessel functions:

$$E(t) = E_o \sum J_m(\gamma) \cos(\omega_o + m\omega_m) \qquad \textbf{1.27.}$$

Where $J_m$ is the Bessel function of first kind and rank m. From equation 1.27. it is quite obvious, that there are frequency components of $\omega_o \pm m\omega_m$ within the cavity. There is however a problem associated with FM mode locking, as it is apparent that there are two null points in a sinusoidal waveform (positive and negative going), which can lead to instabilities in the mode locking.

### 1.4.2. Synchronous pumping (Active).

Mode locking by synchronously pumping[48] (section 4.3.2.), is typically applied to either semiconductor lasers, or lasers which are pumped by another laser. In the latter case of the slave and pump laser, the pump laser is mode locked and the slave laser cavity is adjusted, so that its length is exactly the same, or an integer multiple of that of the pump laser. In this mode locking scheme pulses are shortened by a combination of gain modulation and gain saturation. By studying figure 1.7. the pulse shortening process can be easily followed.

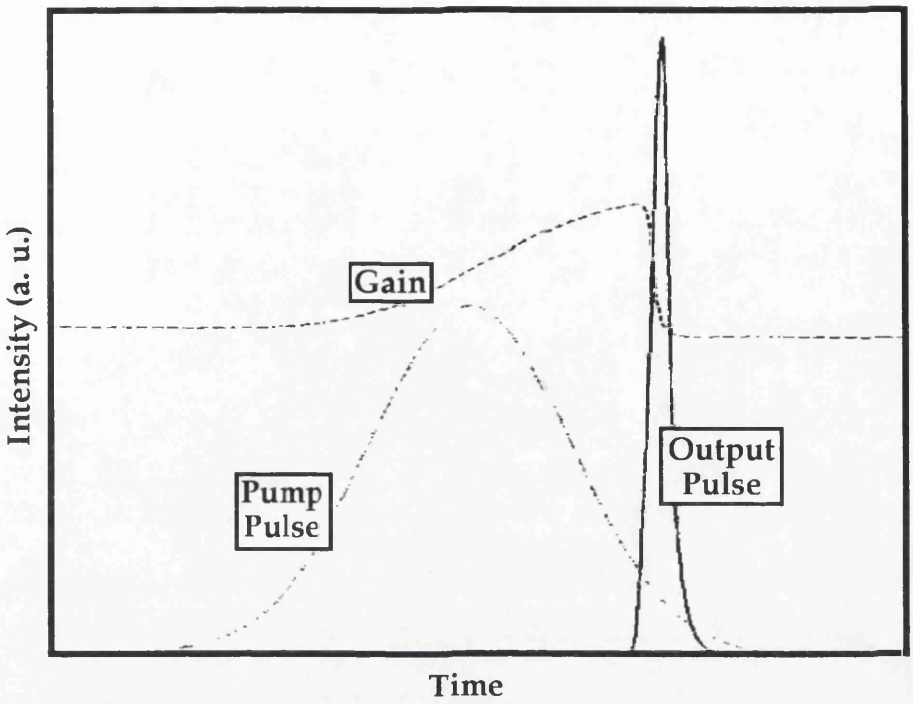


*Figure 1.7. The mode locking dynamics of synchronously pumped lasers.*

Initially the gain of the slave laser is zero, but after the arrival of the pump pulse the gain increases until it exceeds the optical loss within the cavity. When the slave laser pulse arrives it is amplified; this also depletes the gain, and as it falls the trailing edge of the pulse is not amplified, and thus the pulse becomes shorter. This process continues and the pulse is continually shortened and amplified, until some steady state condition is reached. To ensure proper mode locking both cavities must be matched in length, since if the slave cavity is too long any spontaneous emission may be amplified, and this will result in a broad and noisy pulse. If the cavity is too short the gain may have time to recover after the initial depletion, and a second pulse may be formed within the cavity. It should also be clear that since the processes that shape the front and back of the pulses are different, asymmetric pulse profiles may result. Also since the gain must be depleted to achieve pulse shortening, this technique is most suited to laser mediums that have large gain cross sections and short lifetimes.

### 1.4.3. Additive Pulse Mode Locking (Passive).

By employing nonlinear elements in the laser cavity ultrafast $\chi^{(3)}$ effects can be used to mode lock lasers. In Additive Pulse

Mode Locking[49] (APM), also know as coupled cavity mode locking the laser is built as an interferometer, with one arm containing the gain medium and the other a nonlinear element. By studying the Michelson configuration in figure 1.8. the operation of the mode locking scheme can be understood.

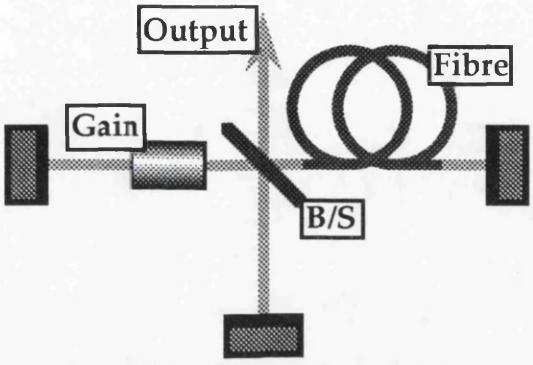


**Michelson Configuration**

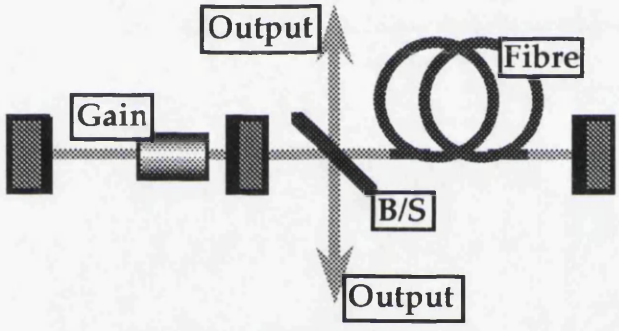


**Fabry-Pérot Configuration**

*Figure 1.8. Cavity configurations for Additive Pulse Mode locking.*

The usual end mirror of the cavity is replaced by a beam splitter which directs the light into the two arms of Michelson interferometer. One of these arms contains a highly reflective mirror, and the light is redirected back into the cavity. The other arm contains a nonlinear element, which is typically a piece of optical fibre. An optical pulse is split into two at the beam splitter and these continue through the cavity, both parts obtain a phase shift and then recombine at the beam splitter where an output is obtained. Through self-phase modulation in the fibre, a nonlinear phase shift is imparted on the part of the pulse within the nonlinear arm. The static phase difference between the nonlinear and linear arms is now set, so that when both pulse parts recombine they experience constructive interference in the centre, and destructive interference in the wings, which will lead to shorter pulses within the cavity.

## 1.5. Measurement of Ultrashort Optical Pulses.

Generally the method employed for the detection of optical pulses depends on the duration of the pulses involved. For most applications basic linear detection using a fast photodiodes and a fast oscilloscope are adequate. However, the bandwidth of oscilloscopes typically limits the application of these techniques to the order of a few nanoseconds (resolution $\approx 1$ ns). To directly measure the pulse width of shorter pulses it is usually a streak camera[50] that is employed, as it can provided a resolution of around 1 ps and even sub picosecond ($\approx 300$ fs) in state of the art lab research. For the measurement of femtosecond pulses the most widely used technique used is second harmonic autocorrelation, as this gives the best temporal resolution with the only disadvantage being the loss of some pulse shape information.

### 1.5.1. Second harmonic Autocorrelation.

For the detection of ultrashort pulses ($< 1$ ps) nonlinear autocorrelation techniques[51] are required. These techniques essentially change the measurement of ultrashort time scales, to that of small distances which are easily quantified. Typically autocorrelators operate by splitting an optical pulse into two components, and propagating these components along two optical paths of similar length. One of these paths however, possess a variable time delay, which will sweep one pulse through the other as they are combined in a SHG crystal (section 1.2.1.). Since the magnitude of SHG signal depends quadradically on the input intensity, a second order autocorrelation will be generated, as the two pulses pass through each other. The duration of the pulse can now be quite easily inferred from the autocorrelation, from measuring the delay introduced by the variable optical path.

There are four typical types of SHG autocorrelator, all of which are classified depending on the type of phase matching, and the geometry of the interfering beams. Autocorrelators can use either type I, (similarly polarised) or type II, (orthogonally polarised) phase matching to produce the SHG signal, and the input beams to the crystal can have a collinear or noncollinear

geometry. The collinear geometry means that both beams are collinear along the same path, through the SHG crystal and on into the Photo-Multiplier Tube (PMT). Therefore, either beam can independently generate a second harmonic signal, and therefore these type of autocorrelators posses an inherent background level. In a noncollinear geometry (figure 1.9.) the two beams cross each other at an angle inside the crystal, which then produces a second harmonic signal at an angle that bisects the input beams. This means that a background free autocorrelation can be obtained, by placing an aperture before the PMT which will filter out the fundamental beams.

The autocorrelator primarily used for this project was type I phase matched Michelson interferometer with noncollinear geometry, and is shown schematically in figure 1.9.

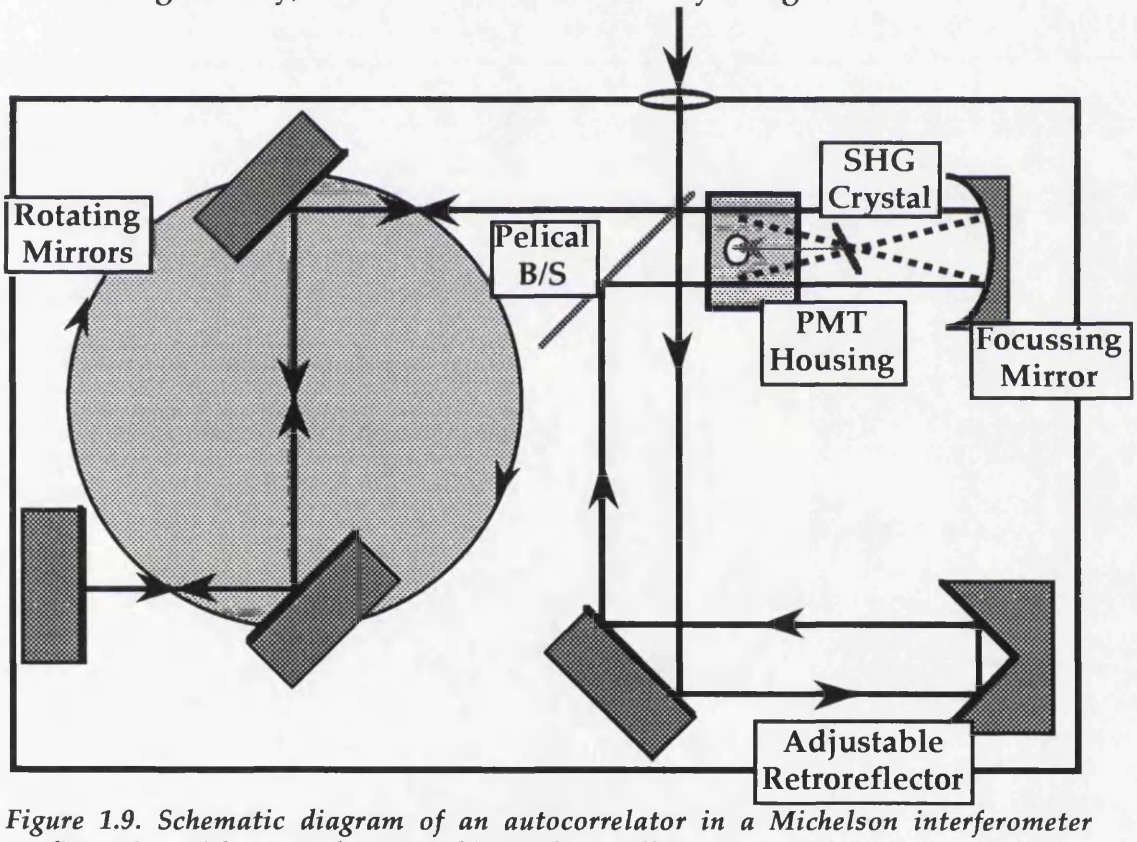


*Figure 1.9. Schematic diagram of an autocorrelator in a Michelson interferometer configuration with type I phase matching and noncollinear geometry.*

The linear delay is generated by a pair of parallel rotating mirrors, and it is known that for small angular changes the pulse delay about the zero is linear, and it can be described by:

$$T = \left(\frac{4\pi f D}{c}\right) t \qquad \textbf{1.28.}$$

Where T is the time delay, D is the distance between mirrors, f is the frequency of rotation and c is the speed of light. A repetitive linear delay is generated by rotation of the mirror assembly, which when used in the shown configuration, will provide a continuous display of the autocorrelation function, on an oscilloscope synchronised to the mirror rotation. The total autocorrelation scan range can be given by:

$$T_t = \sqrt{2}\frac{d}{c} \qquad \textbf{1.29.}$$

Where d is the diameter of the scanning mirror. In the configuration used the total scan length was ≈ 120 ps, with a resolution of less than 20 fs, and a nonlinearity factor across the scan of 7 % / 100 ps.

### 1.5.2. Fast PD.

To monitor optical pulses the most convenient method is to use direct linear detection by using a fast photodiode and a fast oscilloscope. Most commercially available fast photodiodes have a bandwidth of around 20 GHz, although bandwidths in excess of 100 GHz have been reported[52]. It is therefore the oscilloscopes that limit the resolution of the pulse width, and this is typically around 1-2 GHz. Although this detection method does not allow individual pulses to be resolved, it does permit for pulse trains to be monitored.

## 1.6. Propagation of Ultrashort Optical Pulses.

The propagation characteristics of optical pulses in dielectric waveguides have been extensively studied in a number of device formats, (e. g. Fibres[53] and integrated waveguides[54]), and various materials have been used for these studies (e. g. glass[55], lithium niobate[56] and semiconductors[57]). These studies have typically been concerned with, the dynamics of pulse propagation in relation to optical communications. In general when using single mode waveguides and neglecting the optical losses, the main effects pulses experience during propagation, are dispersion and various nonlinear effects. Dispersion gives rise to temporal modulation of the pulse width, which is due to group velocity dispersion

interacting with the initial pulse chirp. When pulses begin to posses significant peak powers nonlinear effects become important, and these can manifest themselves in different ways due to a number of processes. However, these process are characterised by changing the pulse spectrum, and some examples are spectra broadening due to SPM (section 1.2.3.), frequency shift due to Raman scattering etc.. The following section gives a basic introduction to linear pulse propagation, as it is essential for understanding the dynamics of ultrashort in optical waveguides.

### 1.6.1. Group Velocity dispersion.

When an optical wave interacts with a dielectric material the bound electrons respond in a fashion, that is dependent on the frequency of the propagating wave. In linear terms this is basically shown as frequency dependence of the refractive index, and can be described through Sellmier's equation:

$$n^2(\lambda) = 1 + \sum_{j=1}^{k}\left(\frac{B_j\lambda^2}{\lambda^2 - \lambda_j^2}\right) \qquad \textbf{1.30.}$$

Where n is the refractive index, $\lambda$ is the wavelength, $\lambda_j$ is the $j^{th}$ resonant wavelength of the material, and $B_j$ is the coefficient associated with the $j^{th}$ resonance. The sum extends over all resonances in the wavelength region of interest, and $B_j$ is usually found by curve fitting to experimental data.

Since ultrashort pulses contain a large bandwidth, the dispersion of the refractive index can have a significant effect on the temporal shape of a pulse. This is due to the fact that the various frequencies in the pulse will propagate at different speeds. Therefore, it is preferable to describe the pulse propagation by using the mode propagation constant ($\beta(\omega)$). The propagation constant is usually written as an expansion of the Taylor series:

$$\beta(\omega) = \beta_o(\omega_o) + \beta_1(\omega - \omega_o) + \frac{1}{2}\beta_2(\omega - \omega_o)^2 + \frac{1}{6}\beta_3(\omega - \omega_o)^3 + \ldots \qquad \textbf{1.31.}$$

Where $\omega_o$ is the central frequency of the pulse, and the dispersion terms are:

$$\beta_j = \left.\frac{d^j\beta}{d\omega^j}\right|_{\omega=\omega_o} \qquad \textbf{1.32.}$$

The physical understanding of the dispersion coefficients and their expression are as follows:

$$\beta_o = \frac{\omega_o}{\text{PhaseVelocity}} = \frac{2\pi n}{\lambda} \qquad \textbf{1.33.}$$

$$\beta_1 = \frac{1}{\text{GroupVelocity}} = \frac{1}{c}\left(n - \lambda\frac{dn}{d\lambda}\right) \qquad \textbf{1.34.}$$

$$\beta_2 = \text{GroupVelocityDispersion} = \frac{\lambda^3}{2\pi c^2}\frac{d^2n}{d\lambda^2} \qquad \textbf{1.35.}$$

$\beta_2$ is termed the Group Velocity Dispersion (GVD), and in general it is positive in the visible region, and turns negative in the near infrared. Obviously this means that there is some point where the GVD is zero, and this is referred to as the zero dispersion wavelength, which for typical fused silica fibres is around 1.30 μm. Using special fibre geometeries this wavelength can be shifted, to coincide with the low loss window at 1.55 μm, and is therefore extremely important in communication systems. At the zero dispersion point pulses can essentially propagate with no alteration to the pulse shape, or duration. The GVD can be defined by the parameter D, which is defined as the pulse spreading per unit wavelength, and can be characterised by:

$$D = -\frac{2\pi c}{\lambda^2}\beta_2 \qquad \textbf{1.36.}$$

Although perhaps a better physical parameter for characterising the GVD is the dispersion length, which is defined as the length over which a gaussian pulse increases its width by a factor of $\sqrt{2}$.

$$L_D = \frac{T_o^2}{|\beta_2|} \qquad \textbf{1.37.}$$

Where $T_0$ is the $\frac{1}{e}$ duration of the pulse, which is related to the more commonly used Full Width at Half Maximum (FWHM) duration by:

Gaussian Pulse.

$$T_{FWHM} = 1.665T_o \qquad 1.38.$$

Sech$^2$ Pulse.

$$T_{FWHM} = 1.763T_o \qquad 1.39.$$

## 1.7. Conclusions.

In conclusion the need for upgrading to faster data communications systems has been highlighted, and relevance of both temporal and spatial optical solitons in these systems has been discussed. Temporal solitons are being investigated, as the fundamental component that will increase data transmission to in excess of 100 Gb $s^{-1}$. Spatial solitons may hold the key to all optical processing in these future systems, because they have the potential to provide discrete optical switching in solitonic couplers. They also have potential in the realms of multi channel multiplexing, since soliton bouncing at nonlinear interfaces, could realise all optical scanners.

General nonlinear optics as well as specific examples such as self phase modulation, and self focusing have also been discussed, as they enable an understanding of the processes related to optical solitons. Finally the production, propagation and detection ultrashort pulses is also investigated, since these pulses are of fundamental importance in the study of nonlinear optics.

# References.


1 P. W. Smith, "On the role of photonic switching in future communications systems.",IEEE International Conference on Communications, June 1987.

2 M. N. Islam, "Ultrafast switching with nonlinear optics.", Physics Today, 34, May 1994.

3 J. K. Lucek, K. Smith and K. J. Blow, "Ultrafast all-optical information processing.", IEE Professional Group E13 Colloquium, "Ultra-short optical pulses.", 9, November, 1993.

4 F. P. Kapron, D. B. Keck and R. D. Maurer, "Radiation losses in glass optical waveguides.", Appl. Phys. Lett. 17, 423,1970.

5 C. Lin and D. Marcuse., "Dispersion in single mode fiber: The question of maximum transmission bandwidth.", Paper TUC5, 100C81, San Francisco (1981).

6 N. S. Bergano, J. Aspell, C. R. Davidson, P. R. Trischitta, B. M. Nyman and F. W. Kerfoot, "Bit error rate measurements of 14000KM 5 GBIT/S Fiber-amplifier transmission system using circulating loop.", Electron. Lett. 27, 1889, 1991.

7 C. N. Ironside., "Ultrafast all-optical switching.", Contempary Physics, 34, 1, 1993.

8 G. I. Stegeman and E. M. Wright, "All-optical waveguide switching.", Opt. and Quant. Electron. 22, 95, 1990.

9 T. Miya, Y. Terunuma, T. Hosaka and T. Miyashita, "Ultimate low-loss single-mode fiber at 1.55 μm.", Electron. Lett., 15, 106, 1979.

10 L. G. Cohen, C. Lin and W. G. French, "Tailoring zero chromatic dispersion into the 1.5-1.6 μm low-loss spectral region of single mode fibers.", Electron. Lett., 15, 334, 1979.

11 J. Gowar, "Optical communication systems.", Prentice Hall, 1993.

12 Y. H. Kao, M. N. Islam, J. M. Saylor, R. E. Slusher and W. S. Hodson, "Raman effect in AlGaAs Waveguides for subpicosecond pulses." J. Appl. Phys., 78, 2198, 1995.

13 M. V. Hobden, "Phase-matched second-harmonic generation in biaxial crystals.", J. Appl. Phys., 38, 4365, 1967.

14 D. C. Hutchings, "Applied nonlinear optics.", University of Glasgow course notes, 1995.

15 "Principles and applications of nonlinear optical materials.", Edited by R. W. Munn and C. N. Ironside, Blackie Academic & Professional, 1993.

16 K. C. Byron, "Kerr modulation of signals at 1.3 and 1.5 μm in polarisation-maintaining fibres pumped at 1.06 μm.", Electron. Lett. 23. 1324. 1987.

[17] G. F. Lipscombe, A. F. Garito and R. S. Narang, "Exceptionally large linear electro-optic effect in the organic solid MNA.", J. Chem. Phys. 75, 1509, 1981.

[18] S. M. Jensen., "The Nonlinear coherent coupler", IEEE J. Quant. Elec., Vol. QE **18**, 10, 1982.

[19] H. Kawaguchi., "Proposal for a new all optical waveguide functional device.", Opt. Lett., **10**, 8, 1985.

[20] D. R. Heatly, "Dynamics of solitons in nonlinear optical waveguides.", Ph. D. Thesis, University of Arizona, 1991.

[21] P. Li Kam Wa, J. H. Marsh, P. N. Robson, J. S. Roberts, N. J. Mason., "Nonlinear propagation in GaAs/AlGaAs MQW waveguides.", SPIE proc., Vol 578, 1985.

[22] K. Al-Hemyari, J. S. Aitchison, C. N. Ironside, G. T. Kennedy, R. S. Grant and W. Sibbett, "Ultrafast All-optical switching in a GaAlAs integrated interferometer in the 1.55μm spectral region", Electron. Lett. Vol. 28(12), 1992.

[23] K. J. Blow and K. Smith, "Nonlinear loop mirror devices and applications.", BT Technol. J., 11, **2**, 99, 1993.

[24] J. S. Aitchison, "Optical bistability in semiconductor waveguides.", Ph. D. Thesis, Heriot Watt University. 1987.

[25] J. S. Aitchison, A. Villeneuve, and G. I. Stegeman: "Ultrafast all-optical switching in an AlGaAs X-junction.", Opt. Lett. **18** p. 1153. 1993.

[26] J. P. Gordon and H. A. Haus, "Random-walk of coherently amplified solitons in optical fiber transmission.", Opt. Lett. 11, 665, 1986.

[27] J. P. Gordon, "Interaction forces among solitons in optical fibers.", Opt. Lett. 8, 596, 1983.

[28] L. F. Mollenauer, E. Lichtman, M. J. Neubelt and G. T. Harvey, "Demonstration, using sliding-frequency guiding filters, of error-free soliton transmission over more than 20 mm at 10 Gbit/s, single-channel, and over more than 13 mm at 20 Gbit/s in a 2-channel WDM", Electron. Lett. 29, 910, 1993.

[29] S. G. Evangelides, L. F. Mollenauer, J. P. Gordon and N. S. Bergano, "Polarization multiplexing with solitons.", J. Lightwave Technol. 10, 28, 1992.

[30] R. Kashyap and K. J. Blow, "Observation of catastrophic self-propelled self-focusing in optical fibres.", Electron. Lett. 24, 47, 1988.

[31] K. Tai, A. Mysyrowicz, R. J. Fischer, R. E. Slusher and A. Y. Cho, "Two-photon absorption spectroscopy in GaAs quantum wells.", Phys. Rev. Lett., 62, 1784, 1989.

[32] J. Scott-Russell, "Report on waves.", Proc. Roy. Soc. Edinburgh, 319, 1844.

[33] D. J. Korteweg and G. de Vires, Phil. Mag. 39, 422, 1895.

[34] J. V. Moloney, A. C. Newell and A. B. Aceves, "Spatial soliton optical switches: a soliton-based equivalent particle approach.", Opt. and Quant. Electron., 24, 1269, 1992.

[35] E. Siedel and W. M. Suen, "Oscillating solitons stars.", Phys. Rev. Lett. 66, 1659, 1991.

[36] D. K. Campbell, "Nonlinear science from paradigims to practicality.", Los Alamos Science special issue on Stanislam Ulam, 218, 1987.

[37] R. Z. Sagdeev and C. F. Kennel, "Collisionless shock waves.", Scientific American, 264, 106, 1991.

[38] A. Hasegawa and F. D. Tappert, "Transmission of stationary nonlinear optical pulses in dispersive fibers, 1. Anomalous dispersion.", Appl. Phys. Lett. 23, 142, 1973.

[39] L. F. Mollenauer, R. H. Stolen and J. P. Gordon, "Experimental observations of picosecond pulse narrowing and solitons in optical fibers.", Phys. Rev. Lett. 45, 1095, 1980.

[40] A. Barthelemy, S. Maneuf and C. Froehy, "Propagation soliton et auto-confinement de faisceaus laser par non linearité optique de Kerr.", Opt. Commun., 55, 201, 1985.

[41] J. S. Aitchison, A. M. Weiner, Y. Silberberg, M. K. Oliver, J. L. Jackel, D. E. Leaird, E. M. Vogel and P. W. E. Smith, "Observation of spatial solitons in a nonlinear glass waveguide.", Opt. Lett., 15, 471, 1990.

[42] J. S. Aitchison, K. Al-Hemyari, C. N. Ironside, R. S. Grant and W. Sibbett, "Observation of spatial solitons in AlGaAs waveguides.", Electron. Lett., 28, 1879, 1992.

[43] J. S. Aitchison, A. M. Weiner, Y. Silberberg, D. E. Leaird, M. K. Oliver, J. L. Jackel, and P. W. E. Smith, "Experimental observation of spatial soliton interactions.", Opt. Lett., 16, 15, 1991.

[44] A. B. Aceves, P. Varatharajah, A. C. Newell, E. M. Wright, G. I. Stegeman, D. R. Heatly, J. V. Moloney and H. Adachihara, "Particle aspects of collimated light channel propagation at nonlinear interfaces and in waveguides.", J. Opt. Soc. of Am. B, 7, 963, 1990.

[45] D. R. Heatly, E. M. Wright and G. I. Stegeman, "Soliton coupler.", Appl. Phys. Lett., 53, 172,1988.

[46] F. T. S. Yu and I. C. Khoo, "Principles of optical engineering.", John Wiley & Sons. 1990.

[47] H. Statz and C. L. Tang, "Phase locking of modes in lasers.", J. Appl. Phys. 36, 3923, 1965.

[48] L. F. Mollenauer, N. D. Vieira and L. Szeto., "Mode locking by synchronously pumping using a gain medium with microsecond decay times.", Opt. Lett. **7**, 9, 414, 1982.

[49] G. P. A. Malcolm, P. F. Curley and A. I. Ferguson., "Additive-pulse mode locking of a diode pumped Nd:YLF laser.", Optic. Lett. **15**, 22, 1990.

[50] A. Finch, G. Chen, W. E. Sleat and W. Sibbett, "Pulse asymmetry in the colliding-pulse mode-locked dye-laser.", J. Mod. Opt. 35, 345, 1988.

[51] R. L. Fork, C. H. Brito Cruz, P. C. Becker and C. V. Shank, "Compression of optical pulses to six femto seconds by using cubic phase compression.", Opt. Lett., 12, 483, 1987.

[52] D. G. Parker, P. G. Say, A. M. Hansom and W. Sibbett, "110 GHz high-efficiency photodiodes fabricated from indium tin oxide-GaAs.", Electron. Lett., 23, 527, 1987.

[53] R. V. Penty, I. H. White, and A. R. L. Travis, "Nonlinear, two-moded, single-fibre, interferometric switch.", Electron. Lett., 24, 1338, 1988.

[54] J. L. Jackel, E. M. Vogel and J. S. Aitchison, "Ion-exchange optical waveguides for all optical switching.", Appl. Opt., 29, 3126, 1990.

[55] J. G. Fujimoto, "Femtosecond techniques for the characterisation of nonlinear and linear waveguide devices and studies of all optical switching.", NATO ASI Series E, Vol 226., 1990.

[56] H. A. Haus and N. A. Whitaker, "All-optical logic in optical waveguides.", Phil. Trans. R. Soc London. A313, 311, 1984.

[57] E. Garmire, "Optical waveguides in single layers of $Ga_{1-x}Al_xAs$ grown on GaAs substrates.", Appl. Phys. Lett., 23, 403, 1973.

# Chapter 2.

# Optoelectronic Properties of AlGaAs.

In recent years AlGaAs has emerged as the material choice, for research in nonlinear optical guided wave devices. This is due to elimination of TPA by working below half the bandgap, and the high level of control that can be exercised over AlGaAs material parameters, through variation of the aluminium content. Indeed in recent years the refinement of semiconductor growth techniques has reached the point where structures can be controlled to monolayer precision (e. g. GaAs monolayer ≈ 5.65 Å). Techniques such as Molecular Beam Epitaxy (MBE)[1] and Metal Organic Chemical Vapour Deposition (MOCVD)[2], have opened the way for the study of many quantum effects[3], which have been very effectively exploited in the production of high efficiency semiconductor lasers[4].

Although the nonresonant nonlinear effect in AlGaAs is the major interest throughout this study, it has been shown that the Kerr effect is dependent on the fundamental bandgap of the compound (section 2.4.2). Hence, a review of the background of the linear and nonlinear optical

properties of AlGaAs is essential, as it enables an understanding of how the nonresonant nonlinearity can be manipulated. Therefore, in the following sections various properties of both bulk and quantum well AlGaAs are outlined, with an emphasis on the optical properties and their relevance to nonlinear optics.

## 2.1. Optical Properties of AlGaAs.

Of compound semiconductors, AlGaAs is the most highly researched as an optical material system. This research bias exists for a multitude of reasons:

- **The direct bandgap of III-V semiconductors.**
- **Good lattice match for all aluminium compositions.**
- **Precise control over both the bandgap and refractive index.**

AlGaAs has been shown to be the choice for the demonstration of various integrated all ultrafast optical nonlinear devices[5]. This is since it has a Kerr type nonlinearity that is almost 3 orders of magnitude larger than that of silica fibres, and it also possess an extremely mature fabrication base.

### 2.1.1. Absorption in Bulk AlGaAs.

In the spectral region of the fundamental absorption edge of semiconductors, incident photons can cause carrier transitions between energy bands. These transitions will only occur if the photons posses energies which are equal to or larger than, the energy difference between the highest nearly filled band and the lowest nearly empty band. When incident photons posses energies less than the band gap, absorption is extremely small and due mostly to band tail states close to the bandedge, and nonlinear process at greater detunings. As the photon energies are increased and the band edge is passed, the absorption can increase by factors in excess of $10^4$. For III-V semiconductors the band structure that best describes optical absorption is the Kane band model (figure 2.1.), and as it is also used in the calculation of the nonlinear refractive index of AlGaAs it will be beneficial to describe it here.

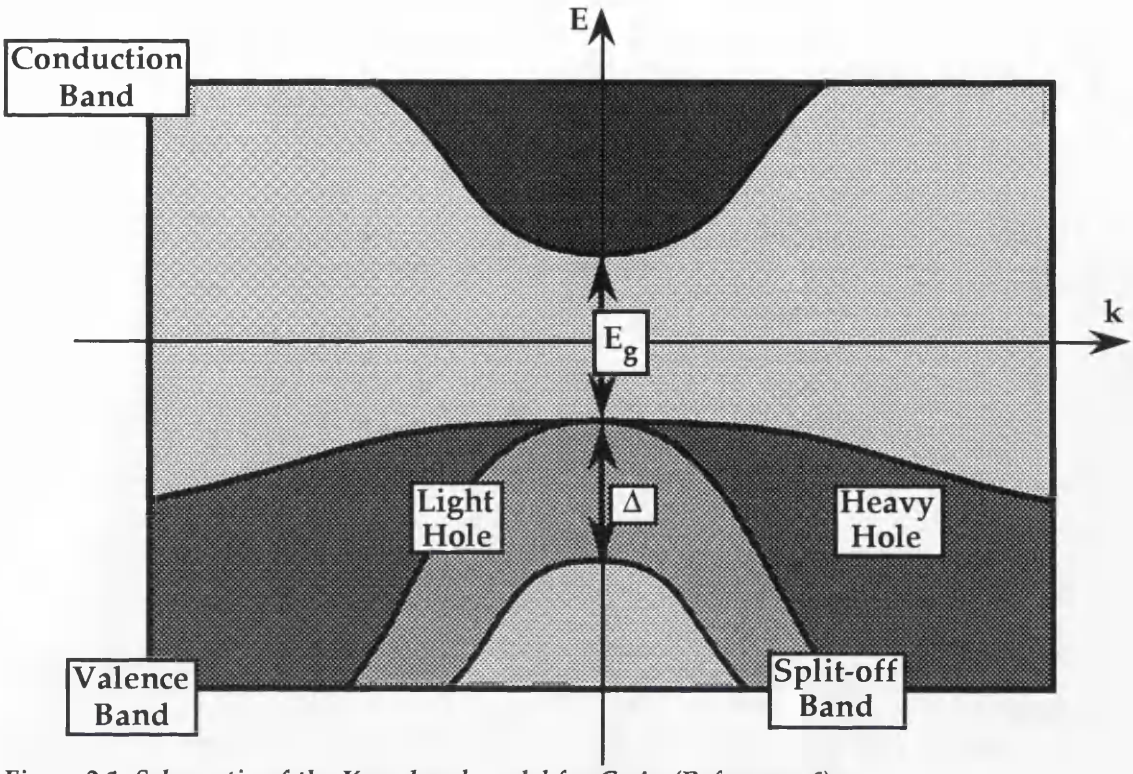


*Figure 2.1. Schematic of the Kane band model for GaAs (Reference 6).*

It is well known for nondegenerate material that the Fermi level lies between the conduction and valence bands. Fundamental optical absorption occurs between the heavy/light hole and the first electron level in the conduction band, as the photon energy increases transitions involving the split off band are incorporated. In general terms the dispersion relations for the various bands in a III-V compound, are given by (reference 6):

$$E_c = \frac{E_g}{2} + \frac{k^2\hbar^2}{2m} + \frac{E_g}{2}\bullet\sqrt{1+4\frac{k^2\hbar^2}{2m_c}\frac{f_1(E_c)}{E_g}} \qquad \textbf{2.1.}$$

$$E_{hh} = \frac{k^2\hbar^2}{2m} - \frac{k^2\hbar^2}{2m_{hh}}\bullet\left(1-\gamma'\frac{k_x^2k_y^2+k_y^2k_z^2+k_z^2k_x^2}{\frac{1}{3}k^4}\right) \qquad \textbf{2.2.}$$

$$E_{lh} = \frac{E_g}{2} + \frac{k^2\hbar^2}{2m} - \frac{E_g}{2}\bullet\sqrt{1+4\frac{k^2\hbar^2}{2m_c}\frac{2(E_g+\Delta)}{3E_g+2\Delta}\frac{f_2(E_{lh})}{E_g}} \qquad \textbf{2.3.}$$

$$E_{so} = -\frac{\Delta}{2} + \frac{k^2\hbar^2}{2m} - \frac{\Delta}{2}\bullet\sqrt{1+4\frac{k^2\hbar^2}{2m_c}\frac{E_g}{3E_g+2\Delta}\frac{f_3(E_{so})}{\Delta}} \qquad \textbf{2.4.}$$

Where $\gamma'$ is a measure of the warping of the energy surfaces of the $E_{hh}$ bands and $f_1$, $f_2$ and $f_3$ are slowly varying functions of energy of the form:

$$f_1 = \frac{\left(E_g + \Delta\right)}{\left(E_g + \frac{2}{3}\Delta\right)} \frac{\left(E_c + \frac{2}{3}\Delta\right)}{\left(E_c + \Delta\right)} \qquad 2.5.$$

$$f_2 = \frac{3}{2} \frac{\left(E_{lh} + \frac{2}{3}\Delta\right)}{\left(E_{lh} + \Delta\right)} \qquad 2.6.$$

$$f_3 = \frac{3\left(E_g + \Delta\right)}{\Delta} \frac{\left(E_{so} + \frac{2}{3}\Delta\right)}{\left(E_{so} - E_g\right)} \qquad 2.7.$$

Where m is the free electron mass, and $m_c$ is related to the effective electron mass by:

$$\frac{1}{m_e} = \frac{1}{m_c} + \frac{1}{m} \qquad 2.8.$$

If only small values for the wave vector are considered and ignoring warping, it is possible to reduce equations 2.1. to 2.4. to:

$$E_c \approx E_g + \frac{k^2\hbar^2}{2m}\left[1 + \frac{m}{m_c}\right] \qquad 2.9.$$

$$E_{hh} = -\frac{k^2\hbar^2}{2m}\left[\frac{m}{m_v} - 1\right] \qquad 2.10.$$

$$E_{lh} = -\frac{k^2\hbar^2}{2m}\left[\frac{m}{m_c}\frac{2\left(E_g + \Delta\right)}{3E_g + 2\Delta} - 1\right] \qquad 2.11.$$

$$E_{so} = -\Delta - \frac{k^2\hbar^2}{2m}\left[\frac{m}{m_c}\frac{E_g}{3E_g + 2\Delta} - 1\right] \qquad 2.12.$$

Where $m_v$ is related to the heavy hole mass by:

$$\frac{1}{m_{hh}} = \frac{1}{m_v} - \frac{1}{m} \qquad 2.13.$$

Moss and Hawkins[6] have used this theory to calculate the room temperature absorption of GaAs (figure 2.2.).

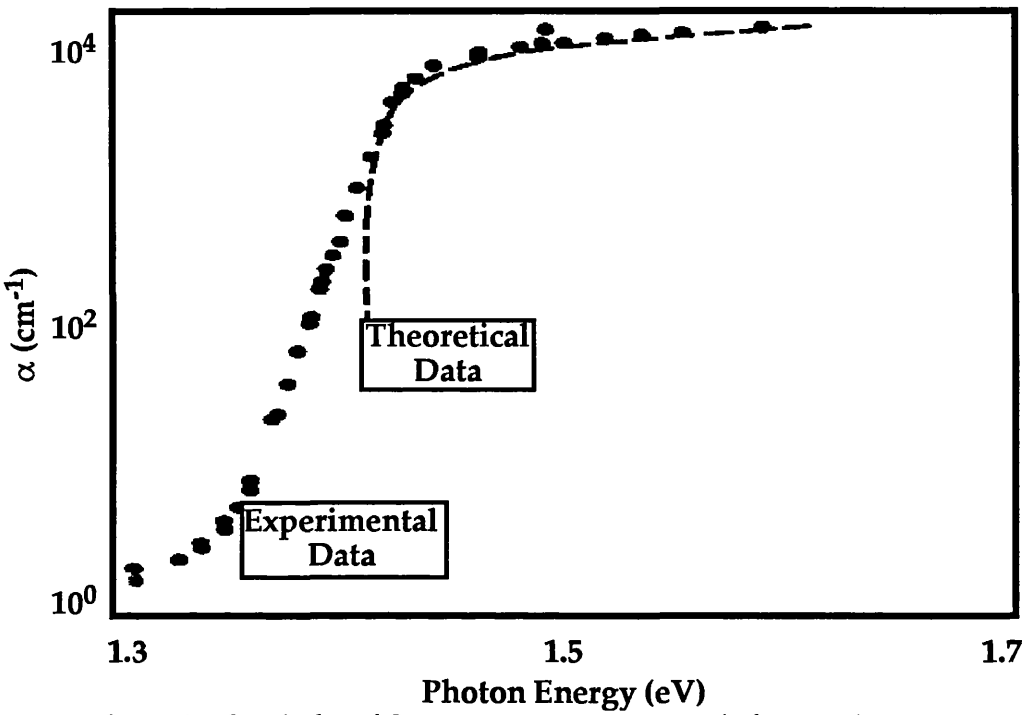


*Figure 2.2. Absorption band edge of GaAs at room temperature. (reference 6.)*

The parameters used for the calculation were, $E_g$ = 1.41 eV, $\Delta$ = 0.33 eV, $m_c$ = 0.072 m, and an average heavy hole mass of 0.68 m.

### 2.1.2. Excitons in Bulk AlGaAs.

Electrons in the conduction band and holes in the valence band are electrically charged particles which posses opposite charges. Therefore, it is possible for them to interact with one another, and be drawn together through Coulomb forces. This interband attraction causes the formation of bound states which are termed excitons. Excitons can be thought of as being hydrogen like systems, and they can therefore be described in a similar fashion. By first considering the Bohr radius ($a_{3D}$):

$$a_{3D} = \frac{\varepsilon_o \hbar^2}{m_r e^2} \qquad 2.14.$$

Where $\hbar$ is Plank's constant, e is the electron charge, $\varepsilon_0$ is the dielectric constant and $m_r$ is the reduced mass of the electron hole pair:

$$\frac{1}{m_r} = \frac{1}{m_e} + \frac{1}{m_h} \qquad \textbf{2.15.}$$

The binding energy of the exciton in the ground state can now be described as:

$$b_{3D} = -\frac{\mu_r}{m_o}\frac{1}{\varepsilon_o^2}R_y \qquad \textbf{2.16.}$$

Where $\mu_r$ is the reduced electron-hole mass. The energy in the ground level of the exciton is proportional to the Rydberg constant ($R_y$). In a similar fashion to the hydrogen atom, an infinite number of energy levels exist for the exciton, and the value for the $j^{th}$ level can be characterised by:

$$E_j^{3D} = E_g - \frac{b_{3D}}{j^2} \qquad \textbf{2.17.}$$

Where $E_g$ is the bandgap energy and j is an integer. For GaAs the binding energy of the ground state and the Bohr radius are 4.20 meV and 14 nm respectively[7]. At room temperatures the exciton effect in bulk GaAs is not well defined, due to the excitonic peak being significantly thermally broadened by scattering with LO phonons. However, providing low temperature measurements are carried out, the exciton effect can be seen as a sharp spike just below the bandgap in the absorption spectrum (figure 2.3).

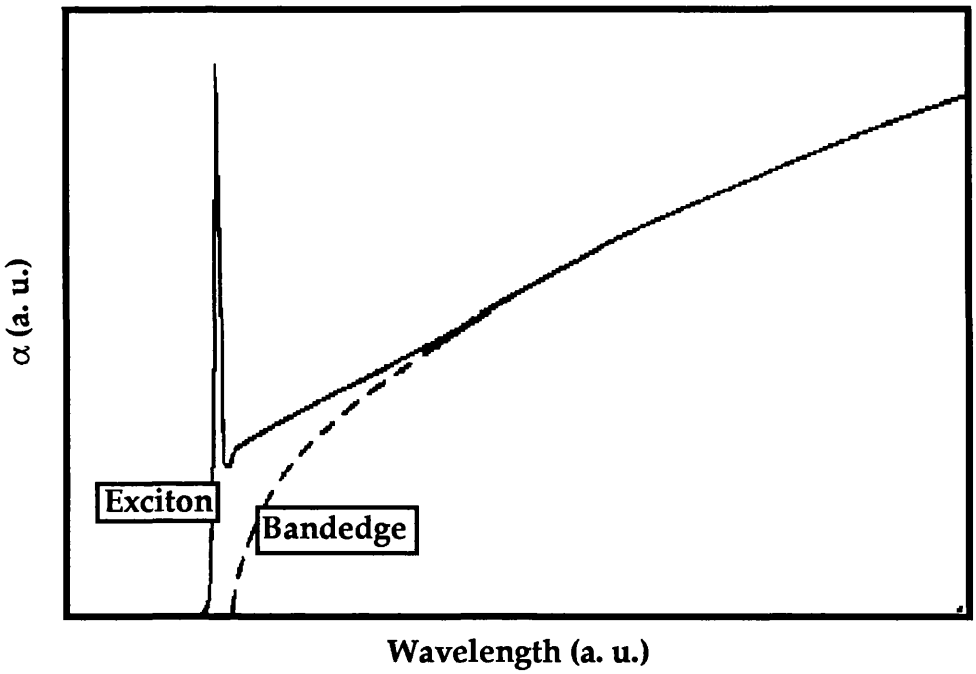


*Figure 2.3. The low temperature absorbance spectrum of GaAs, showing the exciton peak just below the bandedge. (reference 8.)*

## 2.2. AlGaAs Quantum Wells.

AlGaAs Quantum Wells (QW) consist of two relatively thick layers of AlGaAs (Barriers), sandwiching a thin layer of AlGaAs (Well) which has a lower Al content (i. e. narrower bandgap). The well width is chosen so that it is smaller than the mean free electron path ($\approx 30$ nm), and thick enough to provide the desired confinement. If care is taken to ensure that lattice constants are well matched, the band discontinuity at the junctions can be considered to be sharp enough for the well to be modelled by a finite square well (figure 2.4.). Quantum wells allow electrons and holes to move freely in the plane of the well, but constrain movement normal to the well.

### 2.2.1. Absorption in Quantum Wells.

It is possible to model the quantisation of AlGaAs quantum wells by using a finite potential well.

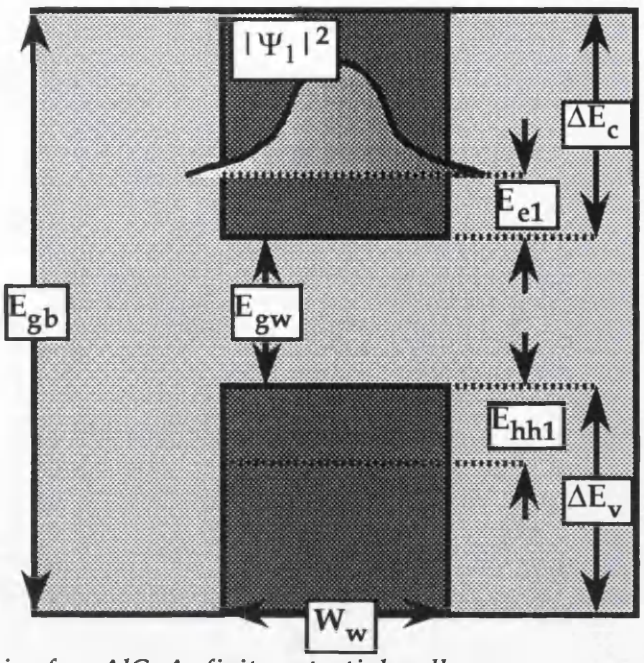


*Figure 2.4. Schematic of an AlGaAs finite potential well .*

Effectively the quantum well confines the motion of electrons and holes to the plane (x-y). If a section of this well is considered, the time independent Schrödinger equation can be used to describe the electron hole bound states:

$$E\psi(z) = -\frac{\hbar^2}{2m^*}\frac{\partial^2\psi(z)}{\partial z^2} + H\psi(z) \qquad \textbf{2.18.}$$

Where $m^*$ is the effective mass of the particle, $\hbar$ is Plank's constant and H is dependent upon position relative to the well, $H = 0$ in the well or $V_o$ (well potential height) otherwise. Since the effective mass of a particle depends on the composition of the material, there are different effective masses for both the barrier and the well $\left(m_b^* \text{ and } m_w^*\right)$. The solution to equation 2.18. has the form:

$$\psi(z) = Ae^{(k_b z)} \qquad z \le \frac{-W_w}{2} \qquad \textbf{2.19.}$$

$$\psi(z) = B\sin(k_w z) + C\cos(k_w z) \qquad \frac{-W_w}{2} \le z \le \frac{W_w}{2} \qquad \textbf{2.20.}$$

$$\psi(z) = De^{-(k_b z)} \qquad z \ge \frac{W_w}{2} \qquad \textbf{2.21.}$$

Where the $k_w$ and $k_b$ are defined as:

$$k_w = \sqrt{\frac{2m_w^{\bullet}E_n}{\hbar^2}} \qquad 2.22.$$

$$k_b = \sqrt{\frac{2m_b^{\bullet}(V_o - E_n)}{\hbar^2}} \qquad 2.23.$$

Where A, B, C and D are constants, which can be obtained by applying the boundary conditions such that $\psi(z)$, and the derivatives are equal at the walls. The solution of equation 2.18. is:

$$W_w\sqrt{\frac{2m_w^{\bullet}E_n}{\hbar^2}} - \tan^{-1}\sqrt{\frac{m_w^{\bullet}}{m_b^{\bullet}}\left(\frac{V_o - E_n}{E_n}\right)} - n\pi = 0 \qquad 2.24.$$

Where n is an integer defining the quantum number. Equation 2.24. can be solved numerically to calculate the $n^{th}$ eigenvalue $E_n$. Figure 2.5. shows a diagram of the three lowest levels of a quantum well.

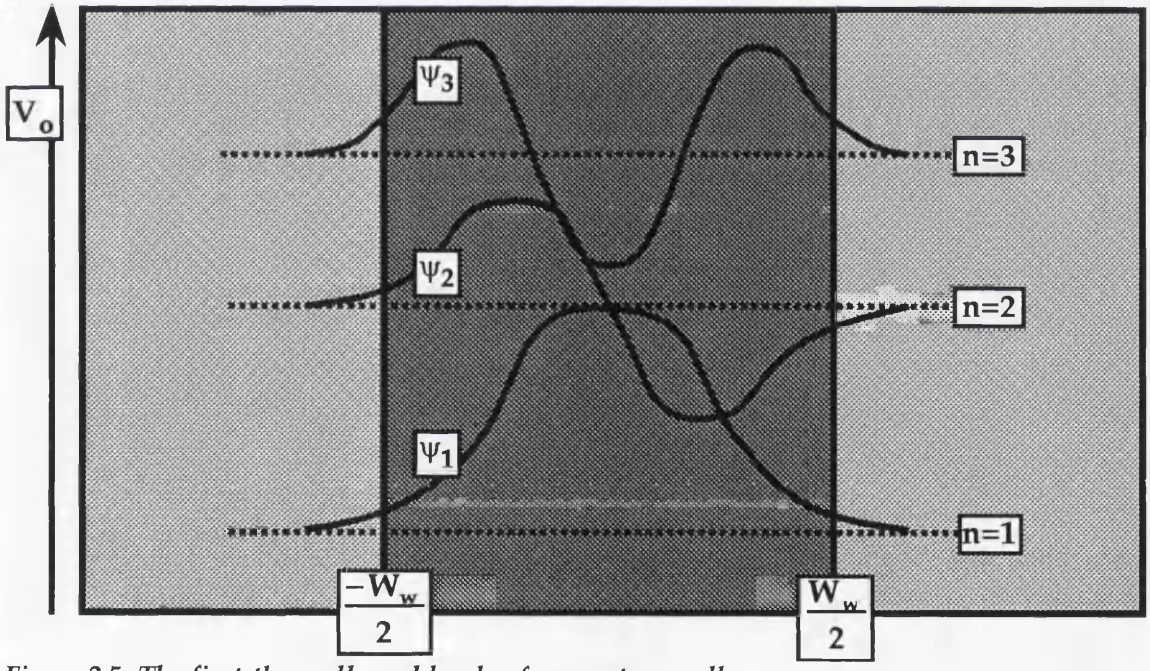


*Figure 2.5. The first three allowed levels of a quantum well.*

In a quantum well the three dimensional dispersion between the energy and wave vector can be described by:

$$E = E_n + \frac{h^2k_x^2}{2m^{\bullet}} + \frac{h^2k_y^2}{2m^{\bullet}} \qquad 2.25.$$

Where $E_n$ is the $n^{th}$ quantised energy level in the z-direction, which is the solution of equation 2.18., $k_x$ and $k_y$ are the De Broglie wave numbers in the plane of the well. It is clear from equation 2.25 that the allowed energy levels are dependent on the effective particle mass and the potential well height. This leads to different energy levels for both the valence and conduction bands, since the barrier heights and the effective masses are different. Furthermore, since the effective masses of the heavy hole and light hole subbands are different, the degenerencey at k = 0 of these bands is removed, and the two levels are split (figure 2.6.).

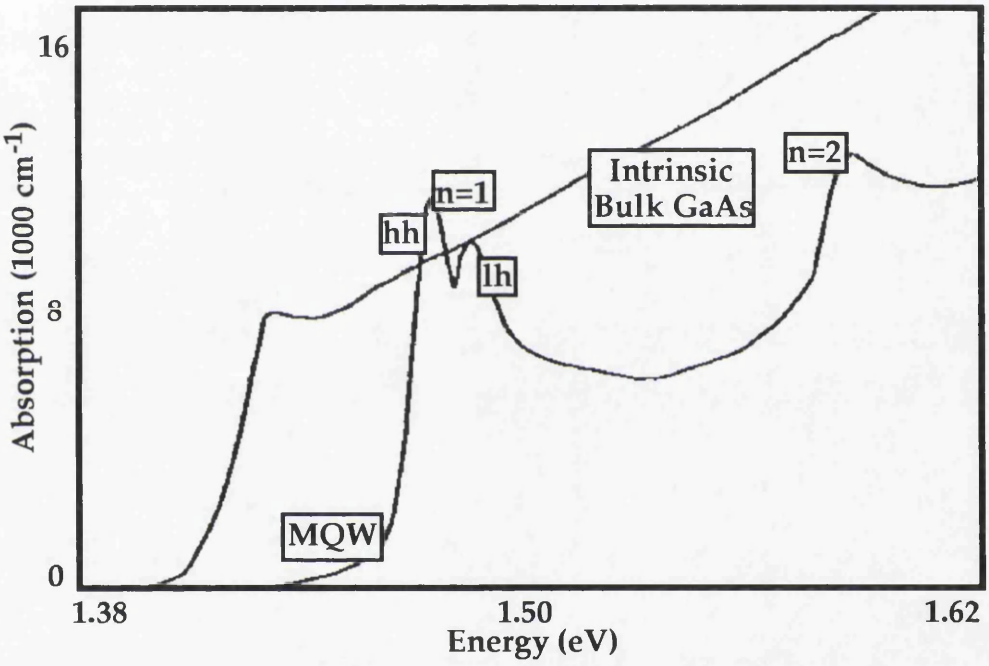


*Figure 2.6. Splitting of the heavy and light hole subbands. (reference 4.)*

In a quantum well carriers are only allowed to move in two dimensions, this leads to the density of states being very different to that of a bulk semiconductor. If a ring of states in 2 D phase space is considered:

$$g(E)dE = 2\frac{2\pi k dk}{\left(\frac{2\pi}{L}\right)^2} \qquad \textbf{2.26.}$$

Where g(E) is the density of states (i. e. number of carriers in the energy range E to dE), k is the radius and dk is the thickness. If a parabolic system is assumed:

$$k = \sqrt{\frac{2m^{\bullet}E}{\hbar^2}} \qquad 2.27.$$

and:

$$dk = \frac{1}{2}\sqrt{\frac{2m^{\bullet}}{\hbar^2 E}}dE \qquad 2.28.$$

Which then gives:

$$\frac{g(E)}{A} = \frac{m^{\bullet}}{\pi\hbar^2} \qquad 2.29.$$

Where A is the area that the states occupy. This result is valid for one band, but it is easily extended over all the bands by summation:

$$\rho(E) = \frac{m^{\bullet}}{\pi\hbar^2}\sum_n H(E - E_n) \qquad 2.30.$$

Where $\rho(E)$ is the density of states per unit area, and H is the Heavy side Function. If the density of states in the conduction band is mapped out (figure 2.7.), it is possible to see the step-like density of states which can be inferred from equation 2.30.. The picture in the valence band is similar, however, the energy levels are calculated from the top of the band.

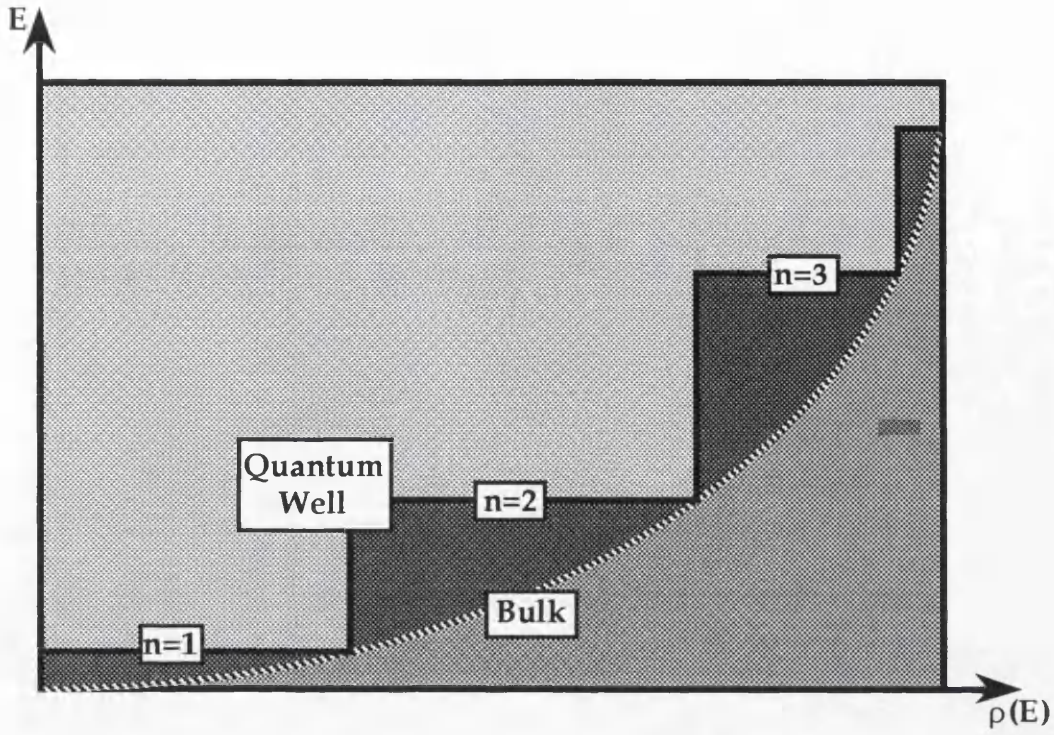


*Figure 2.7. Density of states for both a quantum well (solid line) and bulk material (dotted line).*

### 2.2.2. Excitons in AlGaAs Quantum Wells.

If an exciton is now placed in a potential well where the well width is less than the exciton orbit (≈ 14 nm), and the potential step is significantly large, the exciton behaviour is extremely different from the bulk. If the barrier is high enough to be reasonably approximated by an infinitely high barrier, the wavefunction must be zero in the barrier and also at the interface. This leads to an enhancement of the wavefunction localisation, which in turn increases the Coulomb interaction and hence the exciton binding energy becomes larger. This increase of the exciton binding energy is not extremely large, but it is of the order of a few meV, and therefore it does lead to some important practical considerations.

At room temperature the probability of the exciton being ionised can be derived from the Boltzman factor:

$$B = e^{-\frac{|b_{3D}|}{k_b T}} \qquad \textbf{2.31.}$$

Where T is temperature, and $k_b$ is Boltzman constant. Since $k_bT$ is approximately 25 meV at room temperature[8], it is unlikely that excitons will be observed in bulk GaAs. In quantum wells the binding energy of excitons is increased, and it follows that the probability of the exciton being ionised is reduced. The effect of excitons on the absorbance spectra can be seen in figure 2.8..

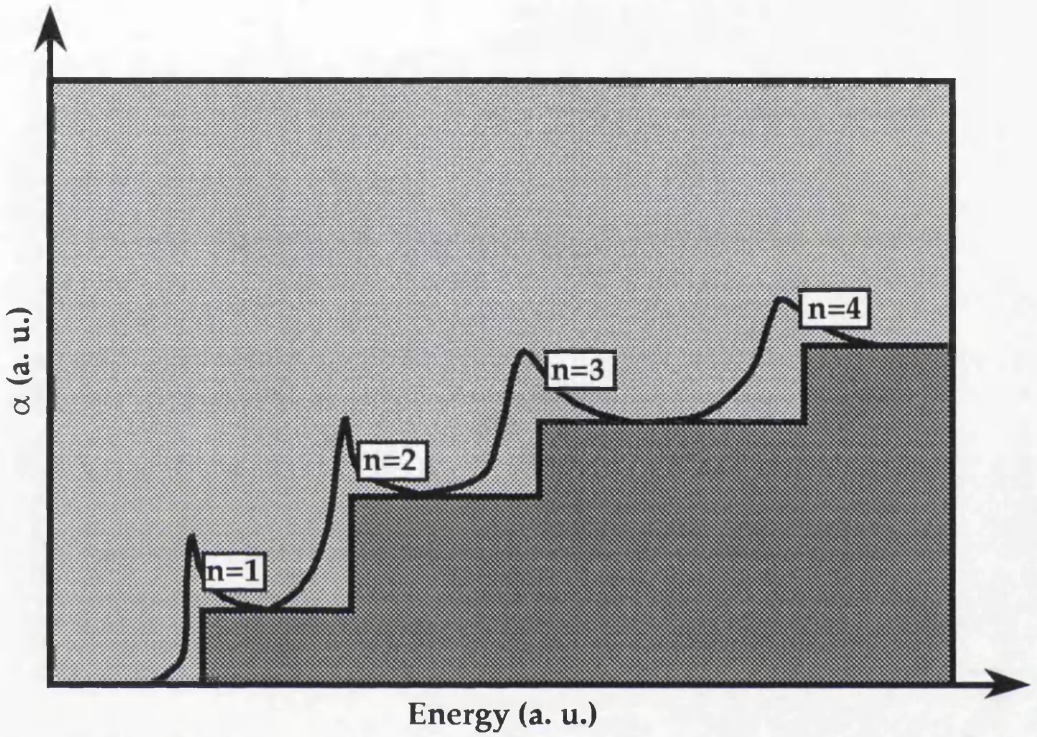


*Figure 2.8. The absorbance spectra for quantum well material, showing the effect of excitons at each well level.*

The excitons are seen as peaks just below the quantum well band to band transitions.

### 2.2.3. AlGaAs Quantum wells.

It is now possible using the results from the previous two sections, to explore the available energy transitions within an AlGaAs quantum well. The energy level transitions can now be calculated from the electron levels, light and heavy hole levels and the exciton energies. Figure 2.9. shows the calculated n = 1 transitions for an AlGaAs quantum well as a function of well width for a number of different well aluminium compositions, where the barriers are held at a constant 40 %.

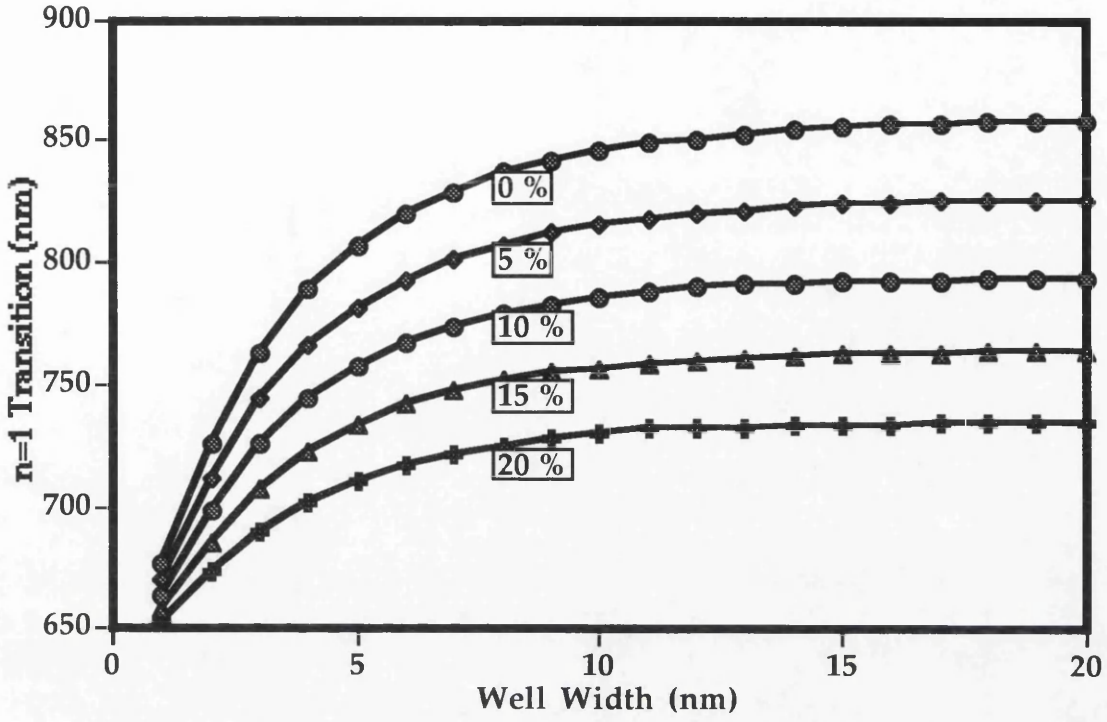


*Figure 2.9. Transitions in an AlGaAs quantum well, as a function of well width for a number of different well aluminium compositions (barriers are held at a constant 40 %).*

It is clear that as aluminium is added to the well the transition energy is increased as expected.

## 2.3. Refractive Index of AlGaAs.

The refractive index of a material is related to absorption through the Kramers-Krönig relations. These relations are the mathematical manner of stating causality. For the design of waveguiding devices we are concerned initially with only the linear refractive index. Various models[9] have been proposed for calculation of the refractive index of AlGaAs, however, from correlation with departmental studies[10], it was decided to use Adachi's model as it appeared to give the closest agreement with experimental data.

### 2.3.1. Refractive Index of Bulk AlGaAs.

When calculating the refractive index of III-V compounds below the bandedge the following model proposed by Adachi[11] is typically used. It has been shown to give good agreement with experimentally measured refractive indices of various III-V binaries[12] and quaternaries, and has been shown to provide reasonable results for AlGaAs. Assuming the AlGaAs

compound has a direct bandgap, the real part of the dielectric constant can be expressed as:

$$\varepsilon(\omega) = A_o\left\{f(\chi) + \frac{1}{2}\left[\frac{E_o}{E_o + \Delta_o}\right]^{\frac{3}{2}} f(\chi_{so})\right\} + B_o \qquad 2.32.$$

Where the following functions are defined:

$$f(\chi) = \chi^{-2}\left[2 - \sqrt{(1+\chi)} - \sqrt{(1-\chi)}\right] \qquad 2.33.$$

$$\chi = \frac{\hbar\omega}{E_o} \qquad 2.34.$$

$$\chi_{so} = \frac{\hbar\omega}{(E_o + \Delta_o)} \qquad 2.35.$$

Where $\hbar$ is Plank's constant and $\omega$ is the angular frequency. $E_o$ and $\Delta_o$ are critical point energies and are defined as[13]:

$$E_o(x) = 1.425 + 1.55x + 0.37x^2 \qquad 2.36.$$

$$\Delta_o(x) = 0.37 + 0.10x - 0.10x^2 \qquad 2.37.$$

The constants $A_o$ and $B_o$ are determined empirically by fitting to experimental data:

$$A_o(x) = 6.3 + 19.0x \qquad 2.38.$$

$$B_o(x) = 9.4 - 10.2x \qquad 2.39.$$

Finally it is well known for lossless materials, that the dielectric constant and refractive index are related through the relationship:

$$n(\omega) = \sqrt{\varepsilon_r(\omega)} \qquad 2.40.$$

It is therefore possible to calculate the spectral dependence of the refractive index of AlGaAs, for various levels of aluminium content. Figure 2.10. shows the spectral dependence of AlGaAs for 0, 10, 20, 30 and 40 % aluminium concentrations.

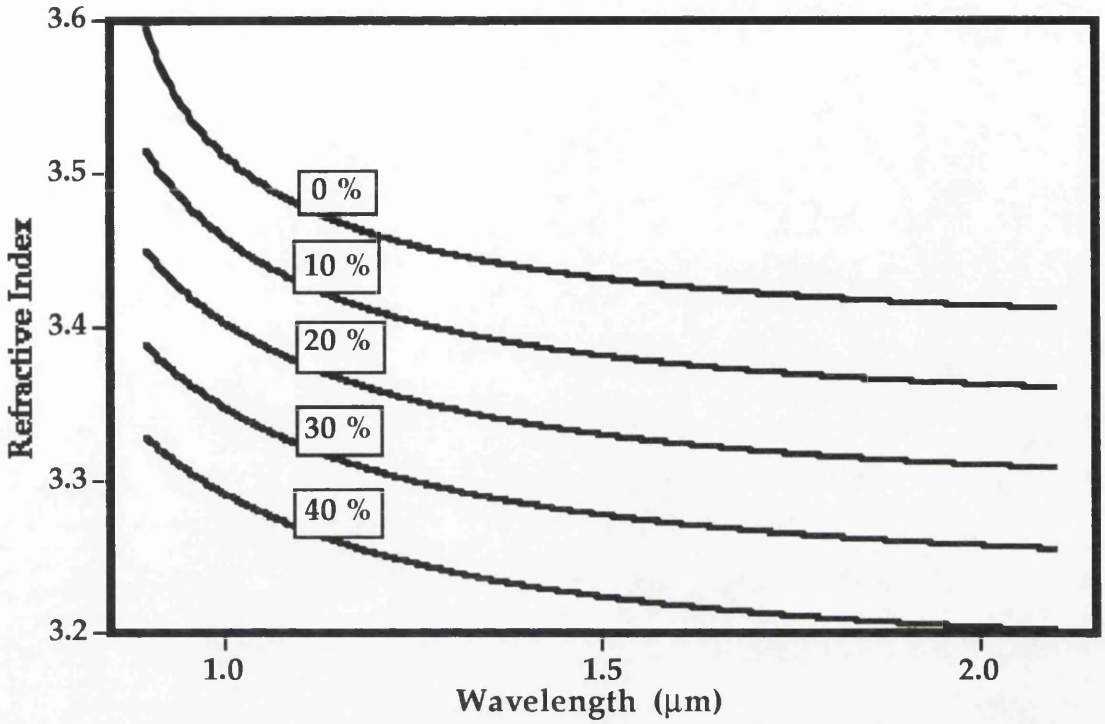


*Figure 2.10. Spectral dependence of the refractive index of AlGaAs for various aluminium concentrations.*

### 2.3.2. Refractive Index of AlGaAs Quantum Wells.

When excited below half bandgap the linear refractive index of AlGaAs MQW structures, has been shown to be related to that of the bulk compound, which contains the equivalent average aluminium[14]. In MQW material there also exists a polarisation dependence, and the value of refractive index must be deduced separately for the TE and TM modes, using weighted models for the separate modes:

**TE Mode**

$$n_{TE} = \sqrt{\frac{n_w^2 W_w + n_b^2 W_b}{W_w + W_b}} \qquad \textbf{2.41.}$$

**TM Mode**

$$n_{TM} = \sqrt{\frac{n_w^2 n_b^2 (W_w + W_b)}{n_b^2 W_w + n_w^2 W_b}} \qquad \textbf{2.42.}$$

These relationships are derived using because different boundary conditions exist, for the two orthogonal polarisations

of the light, and only the light hole contributes to absorption in the TE case.

## 2.4. Optical Nonlinearities in AlGaAs.

Generally optical nonlinearities in semiconductors fall into one of two categories:

- **Resonant nonlinearities.**
- **Nonresonant nonlinearities.**

Resonant nonlinearities are those which are concerned with the generation of carriers in the semiconductor. Essentially when photons possessing energies greater than the bandgap are absorbed, electrons move from the valence band into the conduction band. If the light is relatively intense large carrier densities can be generated, and this will alter the characteristics of the semiconductor, which then leads to nonlinear behaviour. Examples of resonant nonlinearities are band filling[15], plasma effects[16] and optothermal effects[17].

Although the light intensities needed for the observation of resonant nonlinearities is small compared with that required for nonresonant nonlinearities, they do have some drawbacks. Not least of these is the fact that they require the production of carriers, and therefore limit the throughput of the device due to the optical absorption. Another problem is that the generated carriers have a finite lifetime, which is normally in the region of at least nanoseconds, and can be as long as milliseconds. Therefore, unless some method such as sweeping the carriers out by an electric field is used, these type of nonlinearities are not fast enough for ultrafast nonlinear optical studies.

Nonresonant optical nonlinearities are in general much smaller than resonant ones, however, they are less wavelength sensitive. Their main advantage is that they are directly due to the incident optical field, and hence their effects are essentially instantaneous. The most commonly investigated process are nonlinear refraction (Kerr effect) and second harmonic generation, but effects such as

three wave mixing and parametric oscillation are also very important.

### 2.4.1. Two Photon Absorption.

Two Photon Absorption (TPA) is a process whereby photons with energies less than the semiconductor bandgap, can generate real carrier populations. TPA was predicted early on this century[18], but since the TPA coefficient is related to the intensity of the incident light, it was not experimentally verified until after the invention of the laser[19].

TPA occurs when a carrier from the valence band is excited into the conduction band via an intermediate state, by absorbing two photons whose individual energies are lower than the bandgap, but the combined energy is greater than it. This state can be anywhere within the semiconductor band structure, but momentum must also be conserved during the transition. Also since energy has not been conserved[20], the electron cannot exist in this intermediate state for a time greater than that governed by the uncertainty principle. It is known that the highest probability for a transition is when the energy difference between the two states is at its smallest[21]. When a second photon arrives within the uncertainty time the electron will reach its final excited state.

The TPA coefficient can be defined along with the linear absorption coefficient (section 3.3.), as the rate of change of the intensity of light propagating through the medium, this can be expressed by Beer's law:

$$\frac{dI}{dz} = -\alpha I - \beta I^2 \qquad \textbf{2.43.}$$

Where $\beta$ is the TPA coefficient, z is the propagation distance into the material, I is the light intensity and $\alpha$ is the linear absorption coefficient. Equation 2.43. can be solved for the intensity as a function of distance:

$$I(z) = \frac{I(0)\alpha e^{-\alpha z}}{\alpha + \beta I(0)\left(1 - e^{-\alpha z}\right)} \qquad \textbf{2.44.}$$

Equation 2.44. makes it clear that one of the easiest ways to determine $\beta$, is by measuring the sample transmission for various input intensities, where an input beam possessing photons with energies in the range $E_g/2 < \hbar\omega < E_g$ is used. In general $\beta$ can be represented for many semiconducting materials by[22]:

$$\beta(\omega) = K\frac{\sqrt{E_p}}{n^2 E_g^3} f\left(\frac{2\hbar\omega}{E_g}\right) \qquad 2.45.$$

Where K is a material independent constant, n is the refractive index, f is a function which depends on the band structure and $E_p$ is the Kane momentum energy which is nearly material independent, with a value around 21 eV for most semiconductors.

### 2.4.2. Kerr Type Nonlinearity.

Early attempts to theoretically model the nonresonant optical nonlinearity, relied on Kramers-Krönig transformations of nonlinear absorption effects, such as TPA, Raman transitions and the ac Stark effect. Using a simple two band model for a direct bandgap semiconductor, the nondegenerate nonlinear absorption was calculated, and then transformed using the Kramers-Krönig integral to define the nonlinear refraction as[23]:

$$\Delta n(\omega;\Omega) = \frac{c}{\pi} \wp \int_0^\infty \frac{\Delta\alpha(\omega';\Omega)}{\omega'^2 - \omega^2} d\omega' \qquad 2.46.$$

Where $\Delta n$ is the change in refractive index, $\Delta\alpha$ is the change in the absorption coefficient brought about by a perturbation at $\Omega$, and $\wp$ denotes the principal part of the integral, which essentially excludes the singularity at $\omega' = \omega$. This nonlinear Kramers-Krönig relation essentially means, that if the absorption coefficient changed under illumination by intense light, there will be a corresponding change in the nonlinear refraction, although it may occur at a different wavelength. The values given by this formula, were shown to be consistent with

known experimental data for various materials refractive index.

Recently this theory has been superseded by the use of a Kane band structure model, to determine the ultrafast nonlinear refraction ($n_2$) of semiconductors. The model uses the four-band structure as shown in figure 2.1., and has been shown to be accurate in providing values for the TPA coefficient in several zinc-blende semiconductors[24]. The values for $n_2$ are calculated directly, from the real part of the $\chi^{(3)}$ susceptibility term. This ensures that all the nonresonant semiconductor processes are included in the calculation, and that the dominant effects of TPA and the ac Stark shifts are treated consistently. If the nonlinear refractive index is defined as, the instantaneous change of the refractive index per unit irradiance level (i. e. $\frac{\Delta n}{I}$), and linearly polarised light is assumed, for an isotropic medium $n_2$ can be defined as:

$$n_2(\omega) = \frac{3}{4\varepsilon_o c n_o^2} \mathrm{Re}\chi^{(3)}_{xxxx}(-\omega,\omega,\omega) \qquad \textbf{2.47.}$$

Where $n_o$ is the linear refractive index at the frequency $\omega$. Using the density matrix treatment, in general the third order susceptibility can be described by:

$$\chi^{(3)}_{ijkl}(\omega_1,\omega_2,\omega_3) = \frac{e^4}{3!\hbar^3\varepsilon_o m_o^4}\frac{1}{(\omega_1+\omega_2+\omega_3)\omega_1\omega_2\omega_3} \times S_T \sum_{g,\alpha,\beta,\gamma} \frac{(\hat{e}_i^* \bullet p_{g\alpha})(\hat{e}_j^* \bullet p_{\alpha\beta})(\hat{e}_k^* \bullet p_{\beta\gamma})(\hat{e}_l^* \bullet p_{\gamma g})}{(\Omega_{\alpha g}-\omega_1-\omega_2-\omega_3)(\Omega_{\beta g}-\omega_2-\omega_3)(\Omega_{\gamma g}-\omega_3)} \qquad \textbf{2.48.}$$

Where $m_o$ is the free electron mass, $\hat{e}_i$ is the unit vector in the direction of the $i^{th}$ polarisation, $p_{\alpha\beta}$ is the matrix momentum element differences and $\hbar\Omega_{\beta\alpha}$ is the matrix energy element differences. $S_T$ denotes that the following expression is summed over all 24 permutations of the pairs (i, $(-\omega_1-\omega_2-\omega_3)$), (j, $\omega_1$), (k, $\omega_2$) and (l, $\omega_3$). This treatment leads to the realisation that the magnitude of the real part of $\chi_3$ is determined to be inversely proportional to $E_g^4$:

$$\chi^{(3)}_{xxxx} \propto \frac{\sqrt{E_p}}{E_p^4} f\left(\frac{\hbar\omega}{E_g}, \frac{\Delta}{E_g}\right) \qquad \textbf{2.49.}$$

This relationship is also reflected in the value of $n_2$, and recently this theory has been extended to more bands[25], which have indicated an anisotropic dependence for $n_2$, which has been experimentally verified[26]. Figure 2.11. shows $n_2$ dispersion data calculated for both of the discussed theories (Kramers-Krönig relations and the Kane band formulisation), and how they are related to experimental measured data[27]. The aluminium concentration in the compound is 18 %, and the arrow indicates the associated half band gap wavelength.

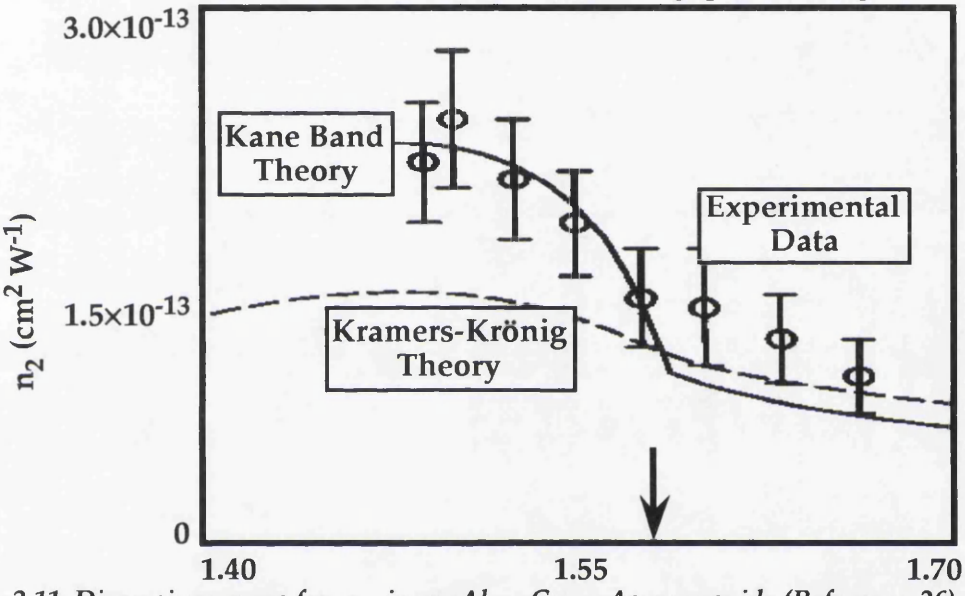


*Figure 2.11. Dispersion curves for $n_2$, in an $Al_{0.18}Ga_{0.82}As$ waveguide (Reference. 26).*

### 2.4.3. Figure of Merit.

When studying nonlinear optical effects it is important that linear and nonlinear absorption are not so strong, that they significantly reduce the optical intensity before the nonlinear effect has occurred. It is also important that the relaxation time of the material is as short as possible, so as to ensure nonlinearity recovery between optical pulses. Typically figures of merit are used in the context of nonlinear switching, however, since they allow different nonlinear optical materials to be compared, they are a good general guide on a materials suitability for nonlinear studies. Therefore, considering all the previously indicated requirements, a figure of merit can be defined:

$$M = \frac{\Delta n}{\alpha \tau} \qquad 2.50.$$

Where $\Delta n$ is the optically induced change in the refractive index, $\alpha$ is a measure of both the linear and nonlinear absorption coefficients, and $\tau$ characterises the recovery time. When considering the ultrafast nonresonant nonlinearity, the material recovery time is comparable to a cycle of light and is therefore not an issue. However, the absorption becomes dominated by the nonlinear terms, especially the TPA, hence the figure of merit can be shown to be a function of the photon energy to the bandgap energy[28]:

$$M = \frac{\hbar\omega}{E_g}\left(\frac{\left|G\left(\frac{\hbar\omega}{E_g}\right)\right|}{F\left(\frac{\hbar\omega}{E_g}\right)}\right) \qquad 2.51.$$

This is a dimensionless figure that is of most use in the discussion of all-optical switching, however, it still gives an idea of how well a material is suited to nonlinear studies and is plotted in figure 2.12. for $Al_{0.18}Ga_{0.82}As$.

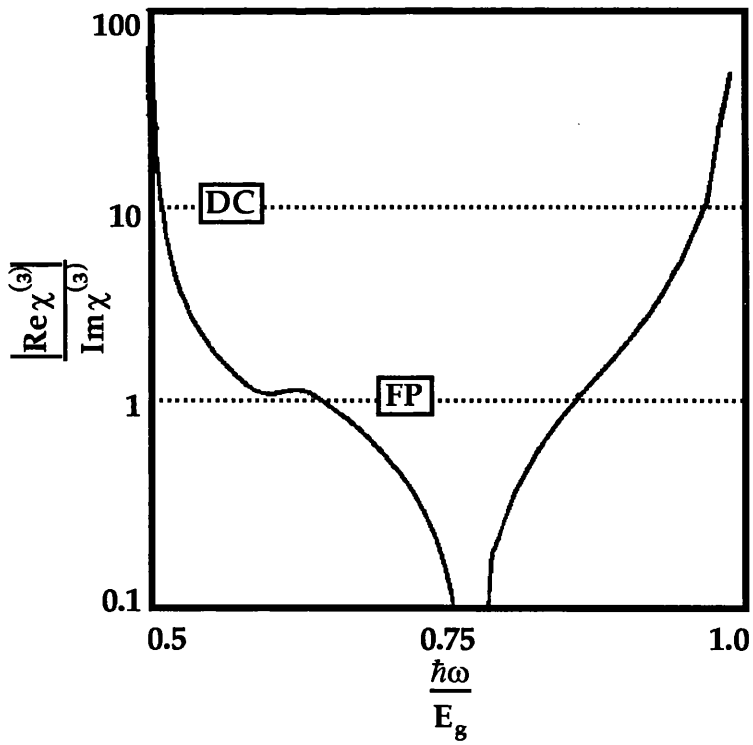


*Figure 2.12. Material dependent figure of merit (M) as a function of the ratio of photon energy to bandgap energy.*

The dashed lines in figure 2.12. are critical values which have to be exceeded for all-optical switching to take place in both a directional coupler (DC) and a Fabry-Pérot interferometer (FP). From figure 2.12. it is clear that when GaAs is operated above half of the band gap it is not suited to nonlinear optical studies. However below half-band this is not the case, the diagram shows that there is a dramatic enhancement in the figure of merit at this point, and this coupled along with the mature fabrication base makes it the best candidate for ultrafast nonlinear optical studies.

## 2.5. Conclusions.

In conclusion various properties of AlGaAs have been reviewed, with an emphasis on those which are particularly relevant to the study of nonlinear optics. The optical absorption properties of AlGaAs in both bulk and MQW formats have been discussed, with a discussion of how quantum wells can significantly change the optical properties of the material and introduce extra control over the material engineering. Refractive index models for both bulk and MQW structures have also been discussed, and a computer program has been written which can be used when modelling semiconductor optical waveguides.

The nonlinear optical processes of TPA and nonlinear refraction have also been discussed and a review of the mathematical models used for the calculation of the Kerr type nonlinearity have been discussed. Finally, the figures of merit that can be used for the comparison of various materials for all optical switching and nonlinear optical studies have been discussed and their importance into characterising these optical materials have shown that presently AlGaAs is the best material for researching nonlinear processes at the 1.5 μm.

# References.


1 B. Joyce, "Molecular beam epitaxy growth.", Low dimensional structures summer school, Nottingham, 1985.

2 P. J. Skevington, M. G. A. Halliwell, M. H. Lyons, S. J. Amin, M. A. Z. Rejman-Greene and G. J. Davis, "Growth of InP/InGaAs multiple quantum well structures by chemical beam epitaxy.", J. Cryst. Growth, 120, 328, 1992.

3 D. F. Welch, G. M. Wicks, D. W. Woodard and L. F. Eastman, "GaInAs-AlInAs heterostructures for optical devices grown by MBE.", J. Vacc. Sci. and Tech. **B**. 1, 202, 1983.

4 G. P. Agrawal and N. K. Dutta, "Long wavelength semiconductor lasers.", Van Nostrand Reinhold, 1986.

5 D. C. Hutchings, "Ultra-fast switching in semiconductor waveguides.", European summer school on photonics, Copenhagen, September, 1994.

6 T. S. Moss and T. D. F. Hawkins, Infrared Phys., 1, 111, 1962.

7 N. Peyghambarian and H. M. Gibbs, "Optical nonlinearity, bistability and signal processing in semiconductors.", J. Opt. Soc. Am. **B.**, **2**, 1215, 1985.

8 M. Jaros, "Physics and applications of semiconductor microstructures.", Oxford University Press. 1989.

9 M. A. Afromowitz, "Refractive index of $Ga_xAl_{1-x}As$.", Solid State. Commun., 15, 59, 1974.

10 S. I. Hansen, "The refractive index change of GaAs-AlGaAs MQWs due to IID using neutral impurities.", Ph. D. Thesis, University of Glasgow, 1992.

11 S. Adachi, "GaAs, AlAs, and $Al_xGa_{1-x}As$: Material parameters for use in research and device applications.", J. Appl. Phys. 58, **3**, R1, 1985.

12 S. Adachi, "Refractive-indexes of III-V compounds - key properties of InGaAsP relevant to device design.", J. Appl. Phys. 53, 5863, 1982.

13 M. Cardona, K. L. Shaklee and F. H. Pollak, Phys. Rev. 154, 696, 1967.

14 S. Ohke, T. Vmeda and Y. Cho, "Optical waveguides using GaAs-AlGaAs multiple quantum wells.", Optical Commun., 56, 235, 1985.

15 D. A. B. Millar, C.T. Seaton, M. E. Prise and S. D. Smith, "Band-gap-resonant nonlinear refraction in III-V semiconductors", Phys. Rev. Lett., Vol 47, 1981.

16 D. A. B. Millar, S. D. Smith and B. S. Wherrett, "The microscopic mechanism of third-order nonlinearity in InSb", Opt. Commun., Vol 35, 1980.

[17] H. Kawai, K. Kaneko and N. Watanabe, "Photoluminescence of GaAs/GaAlAs quantum wells grown by metal organic chemical vapour deposition", J. Appl. Phys., Vol. 56, 1984.

[18] M. Goppert-Mayer, "Über elementarakte mit zwei quantensprüngen.", Ann. Phys. 9, 273, 1931.

[19] W. Kaiser and C. G. B. Garrett, "Two-photon excitation in $CaF_2$:$Eu^{2+}$.", Phys. Rev. Lett. 7, 229, 1961.

[20] A. Miller, D. A. B. Miller and S. D. Smith, "Dynamic nonlinear optical processes in semiconductor.", Advances in Phys. 30, 697, 1981.

[21] H. N. Spector, "Two-photon absorption in semiconducting quantum-well structures.", Phys. Rev. B. 35, 5876, 1987.

[22] E. W. Van Stryland, H. Vanherzeele, M. A. Woodall, M. J. Soileau, A. L. Swirl, S. Guha and T. F. Boggess, "Two-photon absorption, nonlinear refraction, and optical limiting in semiconductors.", Opt. Eng., 24, 613, 1985.

[23] M. Shiek-Bahae, D. C. Hutchings, D. J. Hagan and E. W. Van Stryland, "Dispersion of bound electronic nonlinear refraction in solids.", IEEE J. Quantum Electron. 27, 1296, 1991.

[24] D. C. Hutchings and B. S. Wherrett, "Theory of the dispersion of ultrafast nonlinear refraction in zinc-blende semiconductors below the band edge.", Phys. Rev. **B.**, 50, 4622, 1994.

[25] D. C. Hutchings and B. S. Wherrett, "Theory of the Anisotropy of ultrafast nonlinear refraction in zinc-blende semiconductors.", Phys. Rev. **B.**, 52, 8150, 1995.

[26] D. C. Hutchings J. S. Aitchison, B. S. Wherrett, G. T. Kennedy and W. Sibbett, "Polarisation dependence of ultrafast nonlinear refraction in an AlGaAs waveguide at the half-band-gap.", Opt. Lett., 20, 991, 1995.

[27] A. Villenuve, C. C. Yang, G. I. Stegeman, C. H. Lin and H. H. Lin, "Nonlinear refractive index near half the band gap in AlGaAs.", Appl. Phys. Lett., 62, 2465, 1993.

[28] V. Mizrahi, K. W. DeLong, G. I. Stegeman, M. A. Saifi and M. J. Andrejeco, "2-photon absorption as a limitation to all-optical switching.", Opt. Lett., 14, 1140, 1989.

# Chapter 3.

# Fabrication & Characterisation of AlGaAs Waveguide Devices.

In the study of nonresonant nonlinear optics the magnitude of the nonlinearity is typically very small (e. g. AlGaAs $\approx 10^{-13}$ cm$^2$ W$^{-1}$), therefore to maximise its effectiveness high optical intensities must be maintained over long the interaction lengths. Single mode waveguides are therefore, extremely desirable, since they can maintain high optical intensities over comparatively long distances. Single mode waveguides also reduce the number of variables present within an experiment and hence, conclusions can be reached in a less ambiguous manner.

The fabrication of semiconductor waveguide devices is a very involved process, which entails many intricate stages: design, fabrication and characterisation. In this chapter, a review of the relevant waveguide theory, fabrication techniques and characterisation methods will be presented.

## 3.1. Design of AlGaAs Optical Waveguides.

The most common type of waveguide is that which provides confinement in two transverse directions and is used to guide light from point to point. However, the 1 D "slab"[1] waveguide is of interest in both the basic modelling and testing of general waveguide characteristics (e. g. confinement, single propagating mode, etc.). The slab waveguide provides a basic understanding of many 2 D structures (figure 3.1.) through the combination of both orthogonal planes using the **effective index method**[2].

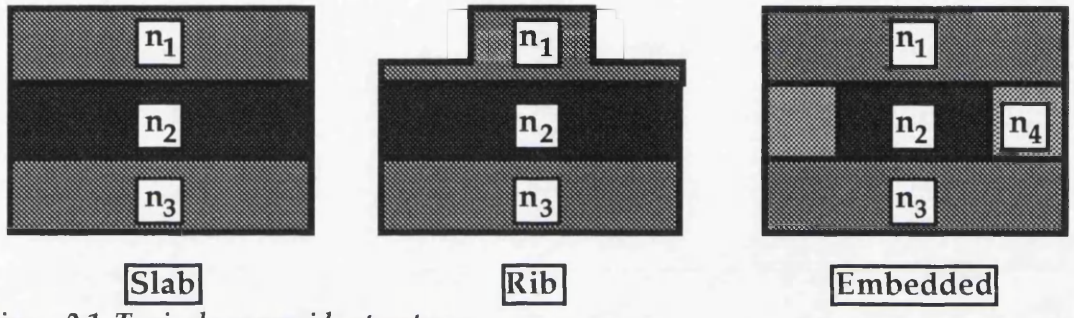


*Figure 3.1. Typical waveguide structures.*

The slab waveguide is also a necessity for observing spatial solitons (section 1.3.2.) as it provides confinement in one direction which guards against catastrophic self focusing, but leaves one dimension free for observing the self focusing phenomenon. Therefore, to gain an insight on the light confinement and propagation of waveguides some of the methods used for analysing both 1 D and 2 D optical waveguides are outlined in the following sections.

### 3.1.1. Slab Waveguide Theory.

The easiest optical waveguide to understand is the simple three layer dielectric slab waveguide. Figure 3.2. shows a schematic representation of a light ray propagating in a slab waveguide.

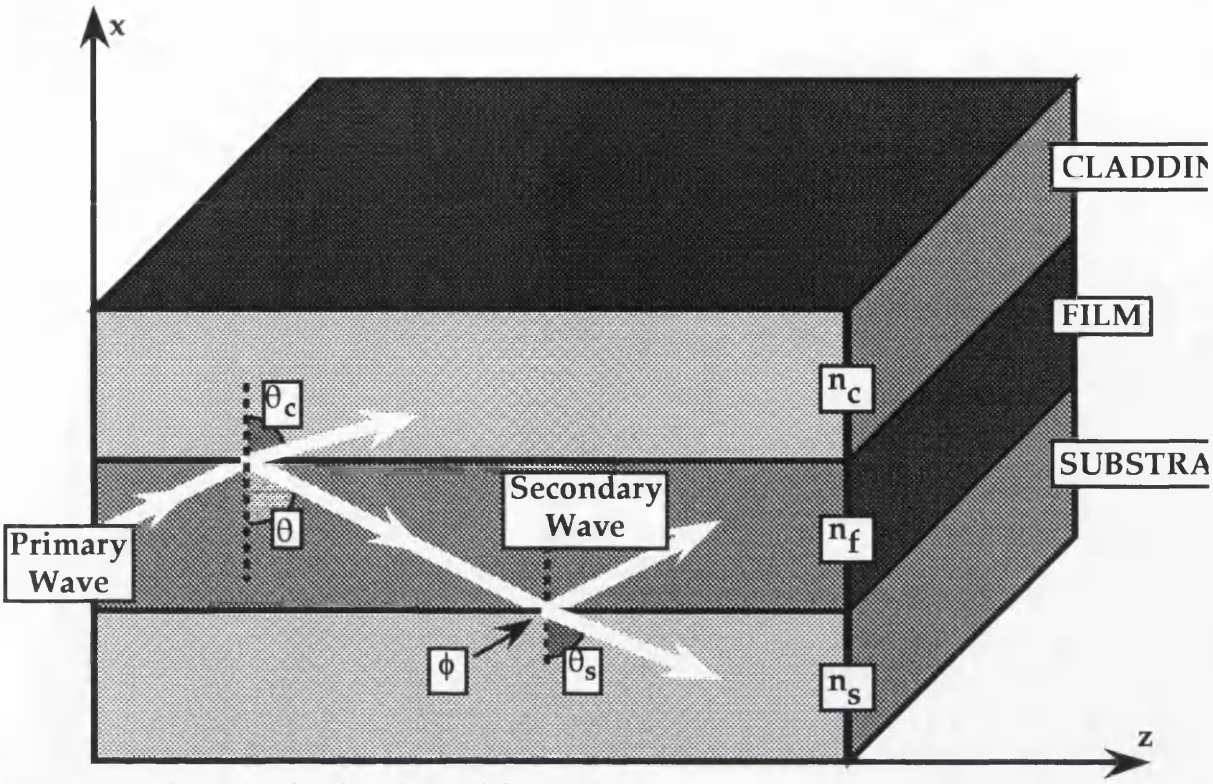


*Figure 3.2. Schematic of a three layer slab waveguide.*

Light propagates down a dielectric slab through the phenomenon of total internal reflection[3] . Total internal reflection occurs when light travelling in a relatively high index medium, strikes an interface with a lower index medium, at an angle which exceed the critical angle[4] (equation 3.1.).

$$\theta_{critical} = \sin^{-1}\left(\frac{n_2}{n_1}\right) \qquad 3.1.$$

Where $n_1$ is the refractive index of the medium the incident ray is travelling in, and $n_2$ is the refractive index of the medium beyond the interface. However, this is not the whole story, because in the slab light is bouncing back and forth between two interfaces, which effectively sets up an interference pattern. If these reflections interfere constructively (i. e. the primary and secondary waves are in phase with each other) across the waveguide core, the light will form a standing wave pattern and it will be able to propagate. This resonance condition in which the light propagates is called a waveguide mode[5]. This mode can be described very easily in mathematical

terms by applying some basic geometrical optical priciples to the waveguide structure.

In figure 3.2. ø is the phase shift[6] due to total internal reflection at the interface, $n_s$, $n_c$, $n_f$ are the refractive indices of the substrate, cladding and film respectively, **d** is the thickness of the waveguide and θ is the propagation angle (to the normal) of the light ray. If the situation where $n_s < n_c > n_f$ is considered, there is total internal reflection at both of the waveguide core boundaries, this leads to purely Fresnel reflection coefficients[7] and phase shifts, at the substrate/film and cladding/film boundaries ($\phi_s$ & $\phi_f$ respectively). Across the waveguide there will be a phase change which is related to the distance the light wave travels, this is easily accounted for by simple geometry:

$$\varphi = 2n_c\beta d\cos\theta \qquad 3.2.$$

where φ is the phase change across the guide and β is the wave number. As previously indicated for a guided mode to propagate, the reflections across the core must interfere constructively (i. e. the total phase shift across the guide must be multiple of 2π). This leads to the waveguide **characteristic equation.**

$$2n_c\beta d\cos\theta + \phi_s + \phi_f = 2p\pi \qquad 3.3.$$

Where **p** is an integer, and describes the order of propagating mode of the waveguide. After solving equation 3.3. it is possible to calculate effective index of the propagating modes.

$$n_p^{eff} = n_c\beta_p \qquad 3.4.$$

It is also possible to substitute for the Fresnel coefficients in 3.3., and describe the waveguide for both TE and TM guided modes (eigen value equations.).

<u>TE mode.</u>

$$n_c\beta d\cos\theta - \tan^{-1}\left[j\frac{n_f\cos\theta_f}{n_c\cos\theta}\right] - \tan^{-1}\left[j\frac{n_s\cos\theta_s}{n_c\cos\theta}\right] = p\pi \qquad 3.5.$$

TM mode.

$$n_c\beta d\cos\theta - \tan^{-1}\left[j\frac{n_c\cos\theta_f}{n_f\cos\theta}\right] - \tan^{-1}\left[j\frac{n_c\cos\theta_s}{n_s\cos\theta}\right] = p\pi \qquad 3.6.$$

Where $\theta_f$ and $\theta_s$ specify the angle of the propagating ray , in both the film and substrate respectively. In the case where the differences between the refractive indices of the substrate, film and cladding are small, equations 3.5. and 3.6. are almost equivalent, and it is therefore possible to use either equation to find the effective index of the guide, and this is termed the **scalar approximation.** This method is fine for obtaining a basic value for the propagation constant of the waveguide. Alternatively, a more rigorous solution can be found using Maxwell's equations[8], but this method can become messy for waveguides possessing more than four layers, and it is more appropriate to use the matrix method (section 6.3.), which can also be used to analyse slab waveguides with arbitrary geometry.

### 3.1.2. Effective Index Method.

The Effective Index Method (EIM) is an approximate method which converts a complicated two dimensional (i. e. rib) waveguide problem, into several easily solved one dimensional (i. e. slab) problems. It is best described through a diagram (figure 3.3.). The EIM divides the rib waveguide into three sections of slab waveguide, one under the rib and two on either side of the rib. The effective index and mode size for each section is then deduced using either ray optics, or electromagnetic analysis.

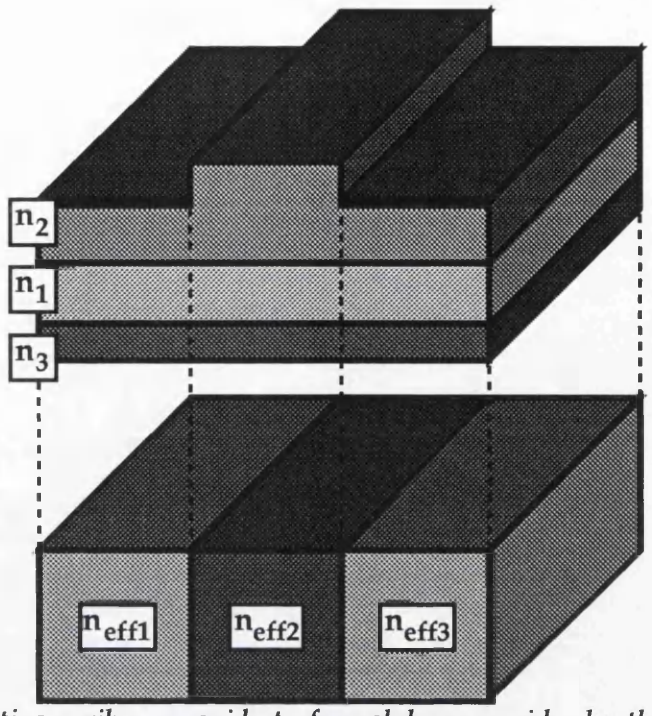


*Figure 3.3. Converting a rib waveguide to four slab waveguides by the effective index method.*

The next step is to combine the effective indices for each of these sections into a singular slab waveguide. This "sandwich" can then be analysed similarly to the previous slabs, but in the orthogonal plane (i. e. the opposite polarisation) due to the theoretical "turning" of the waveguide, during the conversion to a single slab. The core thickness and index of this new slab, is set by the width of the waveguide rib and the effective index calculated for the middle slab. The cladding index is approximated by infinite layers, of the effective index calculated for the etched outer regions. The effective index for the guide as a whole can then be calculated, and finally by combing the results for both dimensions we can determine the modal confinement of the rib waveguide.

The main limitation of the EIM is that the approximation begins to breakdown as the outer slab becomes cut off. However, the great advantage of the EIM is that it provides a quick, and reasonably accurate insight into the behaviour of a proposed waveguide design. Initial designs can therefore be evaluated quickly, and then refined to produce a reasonable design that can be strictly analysed by more accurate methods.

### 3.1.3. Finite Difference Method.

Finite difference methods[9] can be used to analyse the modal characteristics of waveguide structures. They are based on dividing the guide into a finite number of discreet points, by defining a mesh for the structure (figure 3.4.).

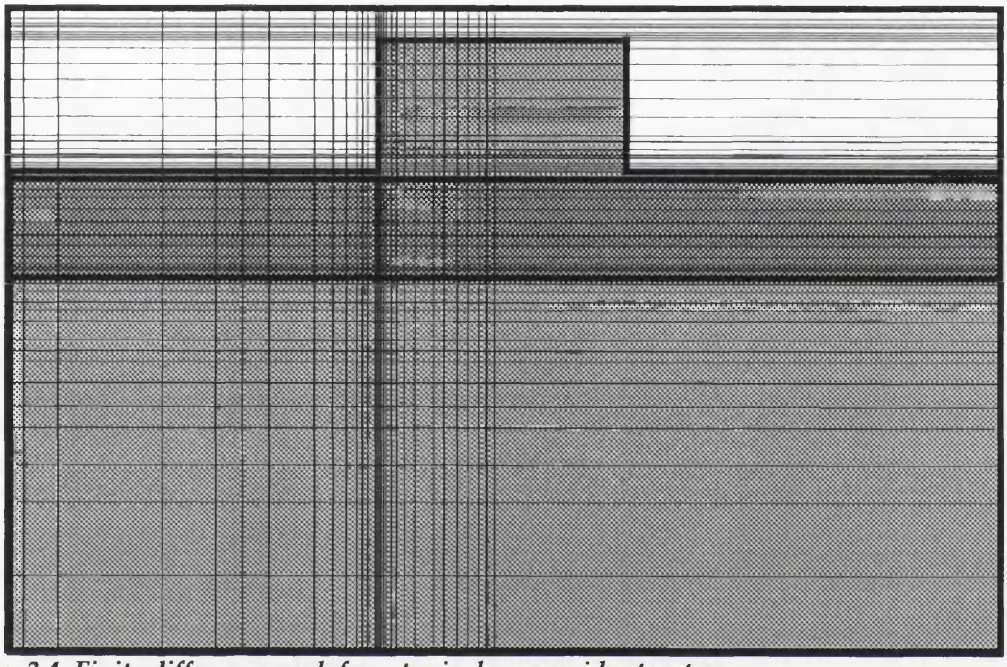

*Figure 3.4. Finite difference mesh for a typical waveguide structure*

It is clear that one side of the mesh contains many more points than the other, this is because symmetry can be used to map one side on to the other, and thus reduce calculation time by a factor of two. The nonuniform mesh also increases the efficiency of the calculation. Since the structure has been broken down into a collection of discrete points, the partial derivatives of electric field can now be represented by two simple equations:

<u>x-direction.</u>

$$\frac{\partial^2 E_x}{\partial x^2} = \frac{E(I+1,J) + E(I-1,J) - 2E(I,J)}{(\Delta x)^2} \qquad 3.7.$$

<u>y-direction.</u>

$$\frac{\partial^2 E_y}{\partial y^2} = \frac{E(1+J,I) + E(1-J,I) - 2E(I,J)}{(\Delta y)^2} \qquad 3.8.$$

Where $\Delta x$ and $\Delta y$ are distances between neighbouring points in the x and y directions respectively. If the TE modes are considered, when these two equations are substituted into the Helmholtz wave equation[10]:

$$\nabla^2_{x,y}E_y + k_o^2\left[n^2(x,y) - n^2_{eff}\right]E_y = 0 \qquad 3.9.$$

The field distribution can be described by:

$$E(I,J) = \frac{E(I+1,J) + E(I-1,J) - R^2\{E(1+J,I) + E(1-J,I)\}}{2(1+R^2) - k_o^2(\Delta x)^2\left\{N^2(I,J) - N^2_{eff}\right\}} \qquad 3.10.$$

Where $R = \frac{\Delta x}{\Delta y}$, N(I, J) is the refractive index at the point (I$\Delta$x, J$\Delta$y) and $N_{eff}$ is the effective index of the waveguide. An arbitrary field distribution is selected and then integrated using the Raleigh-Ritz procedure to provide the first estimate of the effective index, from the scalar variational expression.

$$F(E_y) = \beta_2 = \frac{\int\int_{-\infty}^{\infty}\left(\nabla^2 E_y + k^2(x,y)E_y\right)E_y dxdy}{\int\int_{-\infty}^{\infty} E_y E_y dxdy} \qquad 3.11.$$

This can then be used in conjunction with equation 3.10. to determine the electric field distribution. The process will then continue to refine the data by an iteration process, until the solution achieves some preset accuracy limit.

A finite difference program for analysing optical waveguides called FWave[11] (© MRS Taylor), was available within the department. FWave solves for both the refractive index and field distribution of waveguides, couplers and arbitrary defined structures, it also is configured to deal with nonlinear indices. Figure 3.5. shows a FWave solution for a typical waveguide. The contours represent the field at 10 % increments, with the final countour being the 1 % one.

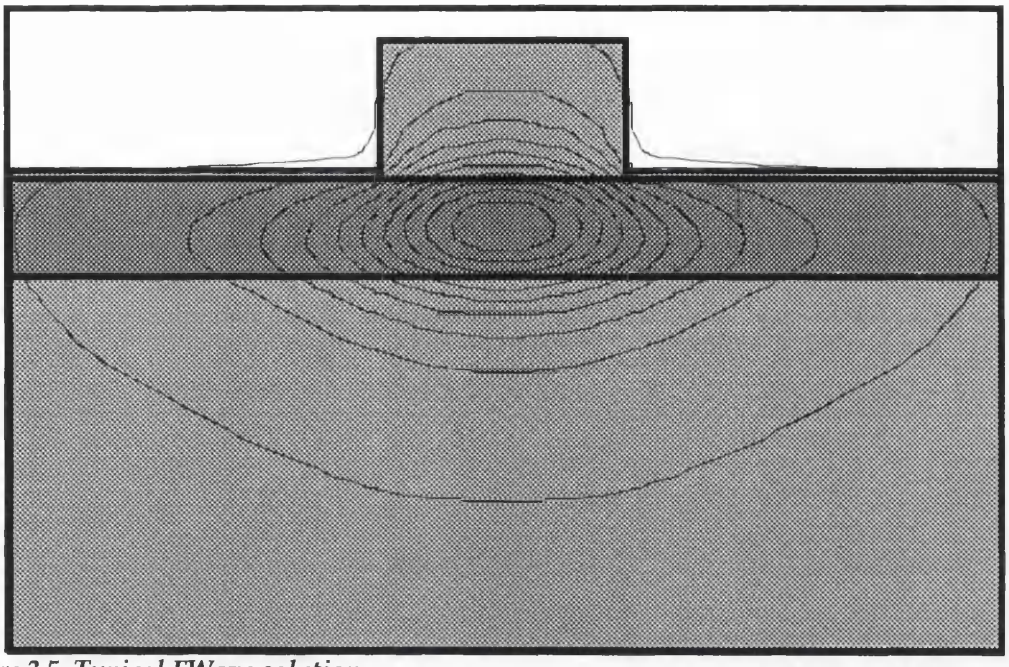

*Figure 3.5. Typical FWave solution.*

## 3.2. Fabrication of AlGaAs Waveguide Devices.

For the study of nonlinear optics in AlGaAs it is essential that devices fabricated have low optical losses [12], and a highly controlled structure. This ensures that it is possible to maintain the high optical intensities required to observe the desired nonlinear effects and that these effects can be modelled in a reasonable fashion. It therefore follows that all fabrication procedures must be carried out in a highly controlled environment, so as to ensure that these procedures are both effective and consistent. All waveguides used in this study were grown by Molecular Beam Epitaxy (MBE). Temperature, humidity, light conditions and dust contamination were all strictly controlled during device processing, by using class 100 clean cabinets within a class 1000 clean room. In the following sections the basic procedures for manufacturing nonresonant optical devices are outlined.

### 3.2.1. Preparation.

Samples are chemically cleaned in an ultrasonic bath, to ensure that all forms of contamination are removed from the surface. Samples to be cleaned were placed in beakers and subjected to

ultrasonic agitation for a few minutes. The process was repeated using the following chemicals.

- **Opticlear (removes grease).**
- **Acetone (removes opticlear).**
- **Methanol (removes organic contamination).**
- **RO (Reverse Osmosis) water (removes traces of solvents).**

The last stage of the chemical cleaning is followed by blowing the sample dry with filtered nitrogen followed by a bake at $\approx 45\ ^{o}C$ on a hotplate. This removes any final traces of moisture at the surface, since it may cause problems with the adhesion of the photoresist.

### 3.2.2. Photolithography.

The main photoresist used to coat samples was S140017. This photoresist, when spun at 4000 r. p. m., for 30 seconds, gives a relatively even film across the sample about 1 μm thick. On days of high humidity (> 50 %) prior to coating, the sample was treated with a priming agent to ensure that it was free of all residual water. After coating, the samples were softbaked at 90 $^{o}C$ for 30 minutes, this removes the solvents from the resist rendering it photosensitive. The parameters of the softbake are extremely important since they control the adhesion of the film, and also the degree of its photosensitivity and hence, the final pattern quality.

The resist is developed by exposure to ultraviolet light using a mask aligner which gives good alignment of mask and sample. The resist is exposed through a chrome mask to produce the pattern, the exposure time for S140017 is 3 to 4 seconds. To develop the exposed photoresist, the sample was immersed in a 1:1 solution of AZ developer and RO water for around 60 seconds. The samples were rinsed in RO water to remove the developed resist, and then finally dried with filtered dry nitrogen.

### 3.2.3. Reactive Ion Etching.

Reactive Ion Etching (RIE) which is also known as Dry etching[13], was the principal method employed to produce rib waveguides. Since optical waveguide devices are highly sensitive to etch depth and profile, tight control over these properties is required and the use of RIE can provide this. However, dry etching produces damage which contributes to the propagation losses of the device, therefore, the dry etch conditions must be optimised to ensure this damage is kept to a reasonable level.

Typically RIE systems are the parallel plate variety shown in figure 3.6.. The upper electrode is grounded and the lower electrode is driven by a r. f. generator. The sample is placed on the lower electrode and the process gas is fed into the plasma reactor, which is an evacuated chamber.

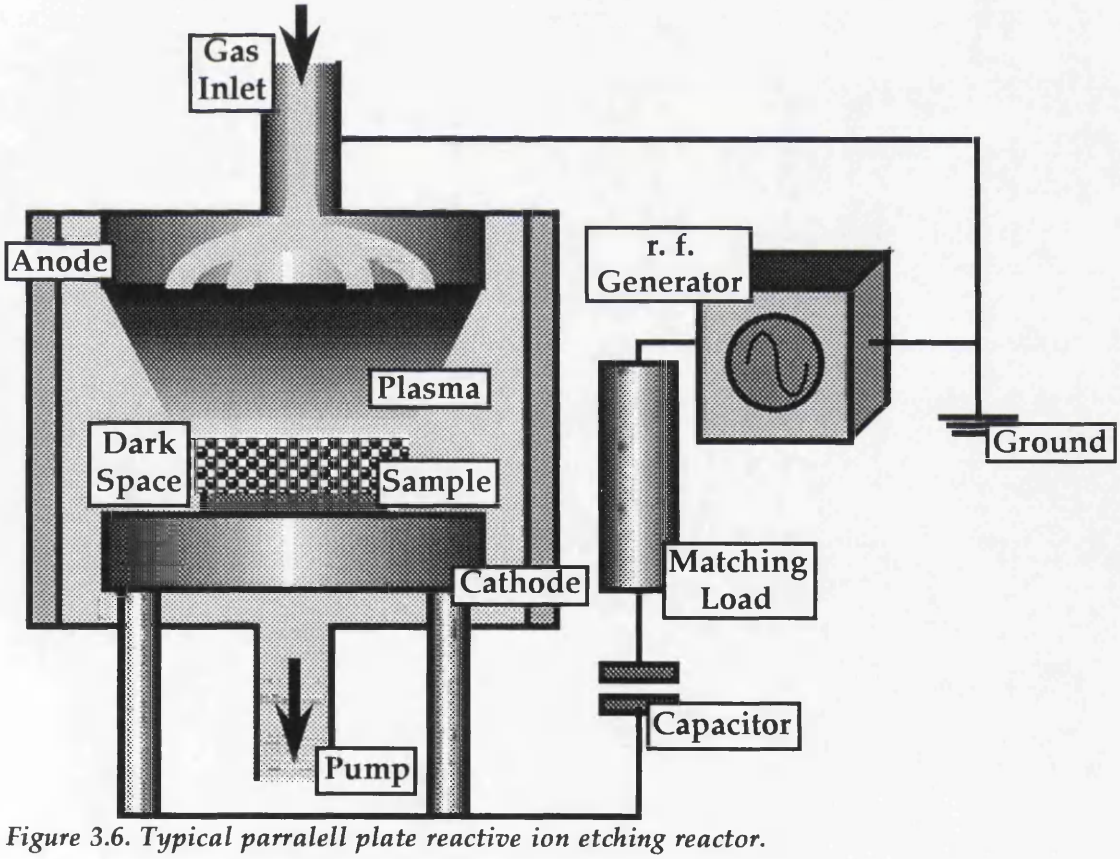


*Figure 3.6. Typical parralell plate reactive ion etching reactor.*

The r. f. power in the chamber ionises the gas, and the free electrons in the chamber follow the oscillations of the power supply. Considering the electric field at the cathode it is possible

to deduce how the plasma reacts to r. f. power supplied to the electrodes. On the positive half of the cycle the light and highly mobile electrons are attracted to this electrode, they are thus accelerated toward it which results in the accumulation of a large negative charge. On the negative half of the cycle the positive ions are attracted to the electrode, but since they are very heavy compared to the electrons, only a relitively small amount of them actually hit the electrode. Due to the charge accumlation a high electric field called the "dark space" is formed above the cathode, and it is here that ions are accelerated before striking the cathode. Since the etch pressures in plasma chambers are typically low (< 100 mTorr), the mean free path of the ions is large, and this results in the path being directed toward the cathode.

The AlGaAs sample was etched in a Oxford Plasmatechnology RIE 80 with $SiCl_4$ as the etch gas, and the following parameters were used to give a reasonable etch rate ($\approx 200$ nm $min^{-1}$) with good controllability.

- **Gas overpressure:** → **12 mTorr.**
- **Gas flow rate:** → **9 sccm.**
- **Table temperature:** → **40 °C.**
- **Plasma exposure time:** → **3 minutes.**
- **R. F. power:** → **100 W.**

### 3.3. Linear Optical Characterisation.

In nonlinear optics waveguides must posses low losses, so as to ensure that the intensity stays at a level, that will ensure the desired effects can be observed. The power transmitted ($P_t$) through a waveguide, may be related to the incident power ($P_o$) by the following relation:

$$P_t = P_o e^{-(\alpha L)} \qquad 3.12.$$

$\alpha$ is the linear attenuation coefficient and is measured in units of $cm^{-1}$, however in optical systems it is usual to express this parameter in units of $dB\,cm^{-1}$, through the relation:

$$\alpha_{dB} = -\frac{10}{L}\log\left(\frac{P_t}{P_o}\right) = 4.343\alpha \qquad 3.13.$$

There are various mechanisms which contribute to the loss in AlGaAs waveguides[14]. However, as the waveguides studied here are operated below half their bandgap, losses from direct interband transitions can be discounted. The major sources of linear optical loss in below bandgap AlGaAs waveguides are shown schematically below in figure 3.7..

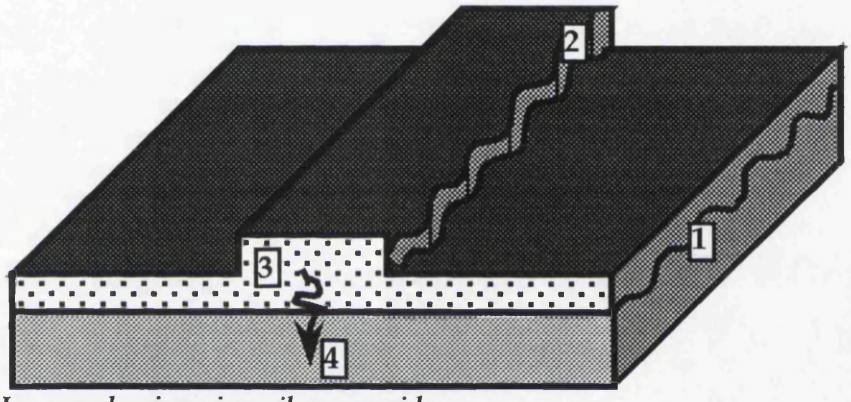


*Figure 3.7. Loss mechanisms in a rib waveguide.*

The loss mechanisims can be summerised as follows:

1. **Epitaxial layer interfaces[15].**
2. **Sidewall roughness[16].**
3. **Leakage into substrate[17].**
4. **Extrinsic carrier absorption.**

There are many ways to experimentally determine the optical losses of waveguides, these include the sequential cleaving method[18] and the optimum coupling method[19]. The most common way of determining the linear losses of semiconductor waveguides is the Fabry-Pérot method[20] and it was this method that was used in this study.

### 3.3.1. Fabry-Pérot Propagation Loss Measurements.

The Fabry-Pérot method of measuring linear losses uses the fact that the transmission of a Fabry-Pérot resonator, may be changed by altering the optical length of the resonator. It is therefore, possible to deduce the optical loss by measuring the resonance and anti-resonance transmission. It is known that the power transmitted by a Fabry-Pérot resonator is:

$$T(\phi) = \frac{(1-R)^2 e^{-\alpha L}}{(1-\Re)^2 + 4\Re \sin^2(\phi)} I_o \qquad 3.14.$$

Where $I_o$ is the effective input intensity, which includes the input and output coupling, $\alpha$ is the linear propagation loss coefficient, L is the waveguide length, R is the reflectivity, $\Re = R\left(e^{-\alpha L}\right)$, $\phi = 2\pi n_{eff}\frac{L}{\lambda}$ is the single-pass phase shift, $n_{eff}$ is the effective mode index. A coherent, monochromatic light source is assumed[21]. It is quite apparent that the transmission will be periodic due to the sine term in the denominator. The transmission feature contrast is given by:

$$K = \frac{T_{max} - T_{min}}{T_{max} + T_{min}} = \frac{2\Re}{1+\Re^2} \qquad 3.15.$$

By substituting for $\Re$ and rearranging:

$$\Re = Re^{-\alpha L} = \frac{1-\sqrt{1-K^2}}{K} \qquad 3.16.$$

Hence the attenuation coefficient can be expressed as[22]:

$$\alpha = -\frac{1}{L}\ln\left(\frac{1-\sqrt{1-K^2}}{RK}\right) \qquad 3.17.$$

If the polarisation of the light is assumed to be parallel to the incident plane and it is assumed that the waveguide is perpendicular to the end facets, which is true in typical AlGaAs structures, then the reflectivity can be expressed as[23]:

$$R = \frac{(n_{eff}-1)^2}{(n_{eff}+1)^2} \qquad 3.18.$$

Where $n_{eff}$ is the effective modal index. From equation 3.15. through to 3.18., it should be apparent that to accurately measure the linear loss we should determine the resonance and anti-resonance transmission at different waveguide lengths. This can be conducted in a nondestructive way, through changing the optical length, by temperature tuning of the waveguides. Figure 3.8. shows a typical Fabry-Pérot loss measurement.

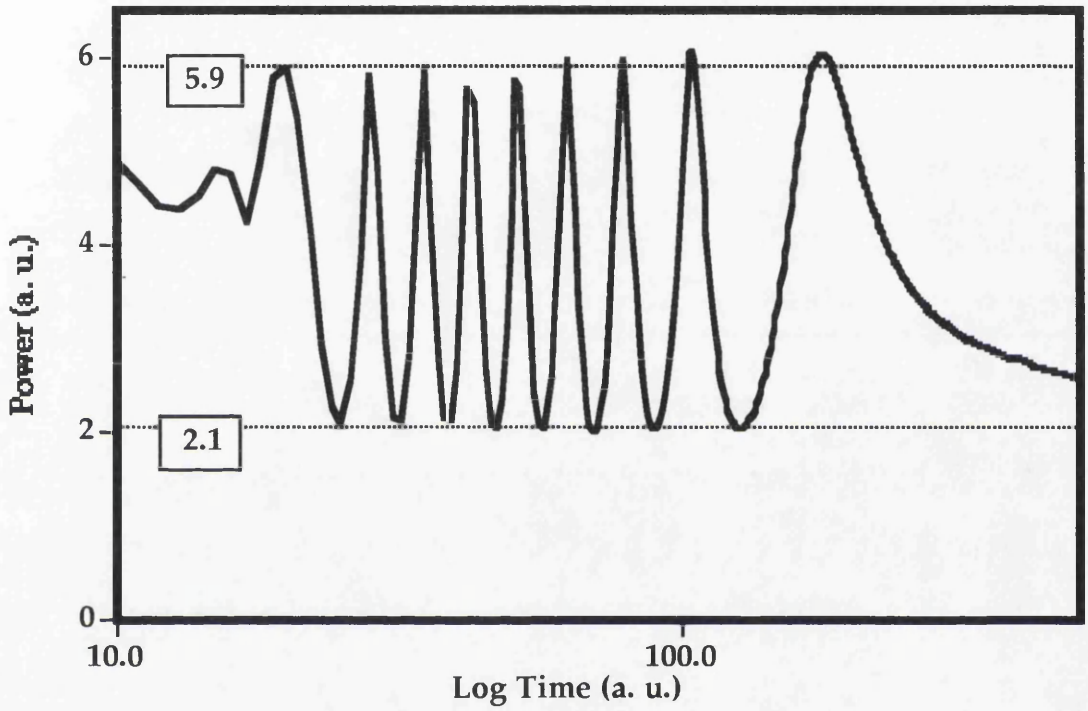


*Figure 3.8. Typical Fabry-Pérot loss measurement showing fringes on a log scale.*

In figure 3.8. $T_{max} = 5.9$ and $T_{min} = 2.1$ this gives a value for K of 0.475. The waveguide was 9.4 mm long and therefore $\alpha$ was calculated as 0.18 $cm^{-1}$ or 0.74 dB $cm^{-1}$. The above Fabry-Pérot measurement was recorded by cooling the waveguides, in the presence of a liquid nitrogen soaked "cotton bud", the bud was then removed and the fringes recorded as the sample returned to room temperature. Measuring the fringe pattern as the sample returned to room temperature produced a more stable set of fringes. The fringes are typically shown on a log time scale, so as to remove the logarithmic dependence of the temperature change in the waveguides.

### 3.3.2. Photoluminescence Spectroscopy.

Photoluminescence Spectroscopy[24] measurements provide a quick and easy method to characterise the bandgap of materials. When a semiconductor material is excited by photons possessing energy greater than the bandgap, some electrons will jump from the valence band to the conduction band and hot carriers will be formed. These carriers will emit phonons and relax down through the band until recombination occurs, and a photon is emitted at an energy equal to the bandgap.

To increase the accuracy of the photoluminescence technique, measurements were generally taken at liquid nitrogen (77 °K) temperatures, since this reduced thermal broadening of the photoluminescence peaks. Figure 3.9. details the experimental setup.

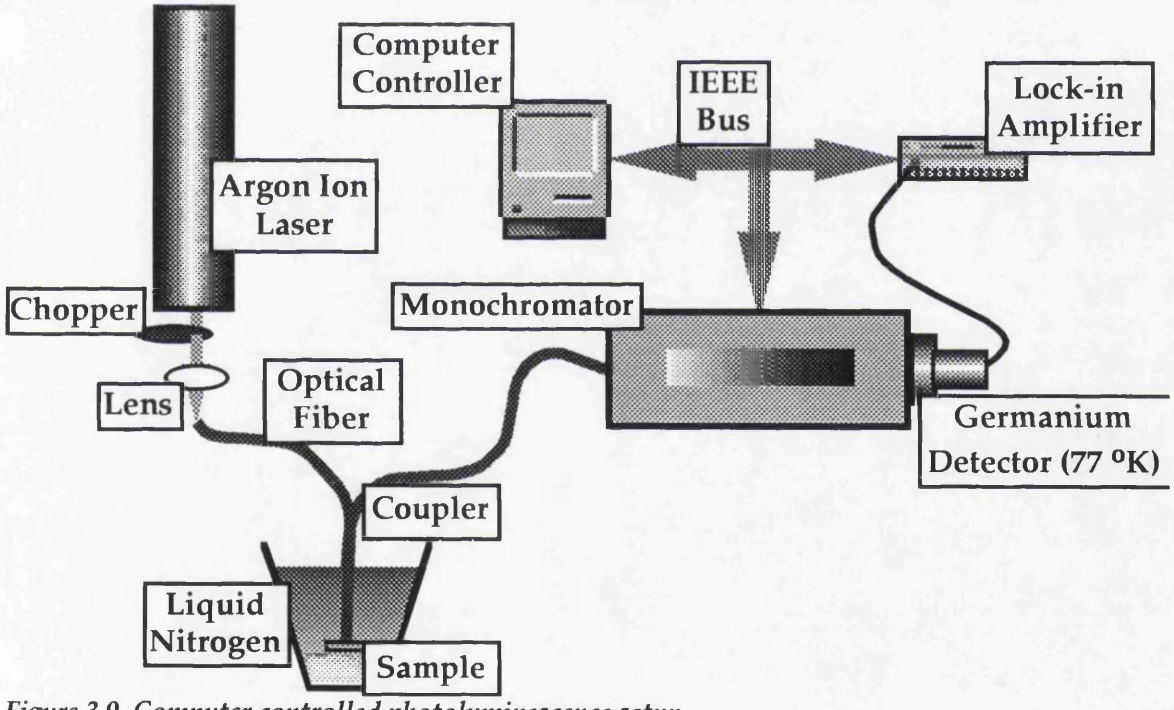


*Figure 3.9. Computer controlled photoluminescence setup.*

The 514.5 nm line from an argon ion laser was coupled into one arm of optical fiber coupler, the sample was placed on to the protective metal ferrule at the end of one arm using an extremely weak adhesive solution. The sample was then completely submerged in a polystyrene beaker containing liquid nitrogen, the other end of the fiber coupler (bar arm) is connected to the entrance of a monochromator.

Photoluminescence from the sample travels along the fiber, and is directed toward the monochromater by the directional coupler. The monochromater is stepped through the various wavelengths of interest, and at each point the lock-in amplifier reads the intensity of the photoluminescence signal from the germanium detector. The detector is liquid nitrogen cooled to improve the noise performance[25], and thus optimise the system performance. The setup is completely automated and the computer can control the scan wavelengths, read the lock-in, step the monochromater, display and record the results. Figure 3.10. shows a typical photoluminescence measurement from an AlGaAs sample (A776 appendix A.).

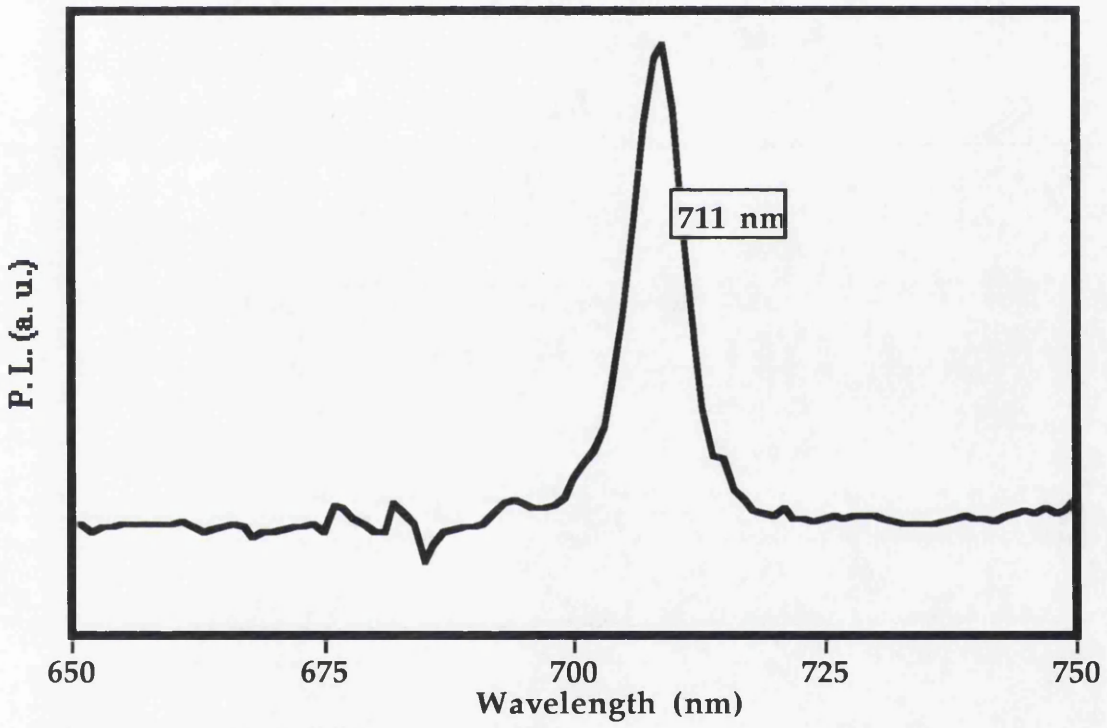


*Figure 3.10. Typical photoluminescence signal.*

### 3.4. Nonlinear AlGaAs Waveguides.

To design waveguides to exploite the nonresonant nonlinearities in AlGaAs, three main design criteria must be met:

- **Waveguides must have a fundamental bandgap below 750 nm.**
- **Disordered waveguides must posses a reasonable shift (≈ 5 %) from the fundamental bandgap.**

- **Waveguides must be low loss and provide strong light confinement, to ensure observation of nonlinear effects.**

Ensuring the waveguides have fundamental bandgaps below 750 nm will minimise the TPA in the waveguides. The second reason is extremely important, as it is only through achieving a large relative difference between the fundamental and disordered bandgaps, that a change in the nonlinearity will be observed.

### 3.4.1. MQW Waveguide Bandgap Design.

To obtain a shift of a bandgap large enough to observe a change in the Kerr type nonlinearity, a MQW structure must be designed so that the difference between the MQW material, and the disordered material bandgaps is of the order of a few percent. The half bandgap of the MQW material will also have to be below 1.50 μm to minimise TPA[26], and maximisation of the effectiveness of the nonlinearity. Initially a quantum well using two aluminium fractions was designed (A 776), this structure gave a fundamental bandgap of 748 nm and an averaged band gap of 681 nm. However, this design proved to be somewhat difficult to grow, since it required two independent aluminium fractions for both the quantum well and the barrier. Therefore, it required three independent aluminium cells in the MBE reactor, which was not readily available.

The next design used a GaAs quantum well sandwiched between $Al_{0.40}Ga_{0.60}As$ barriers (B 415). The 40 % aluminium ensured that the material was still direct gap, but since GaAs was used in the wells it was necessary to make the well thickness relatively thin (< 3 nm), to ensure the bandgap was below 750 nm. This structure met the design criteria quite well, however, the fundamental bandgap proved to be slightly high (744 nm) and thus was compensated for in the final design (B 579) which had the quantum well reduced to 4 monolayers of GaAs (733 nm). B 579 also had a thicker GaAs cap on top of the epilayer (100 nm as opposed to the normal 10 nm), this was to ensure that further oxide studies were based on reactions

confined to GaAs, and that AlGaAs would not complicate matters. All wafers used in this study are shown in appendix A.

### 3.4.2. Slab MQW Waveguide Design.

When designing waveguides for nonlinear optics there are two main points to consider, they are:

- **Optimisation of the waveguide cross section.**
- **Reduction of optical loss mechanisms.**

Both of these factors influence both the type and level of nonlinear phenomena that can be observed. It should be obvious that to prevent ambiguity in experiments, single mode guides should be used since they reduce variables, and thus increase clarity. Conventional single mode guides can typically provide tight confinement which can enhance nonlinear effects. This tight confinement can also increase the influence of epitaxial roughness on the optical losses of waveguides. Hence, some form of compromise between light confinement, and the core width has to be reached in order to gain the optimum performance from the waveguides.

If wafer A 776 is considered the design of the slab waveguide was as follows. If the guide is designed for operation in the low loss telecommunications window (1.55 μm) from equations 2.41. and 2.42. the refractive index for the MQW is:

- **TE mode:** → **3.263**
- **TM mode:** → **3.261**

A P. C. program called Fourlayer[27] written by B. Buhambra, for calculating the effective index of a four layer dielectric waveguide, was converted into a stand alone application for Macintosh computers. It was used to calculated both effective indices and modal thicknesses of the waveguide. The thickness of the guide was initially chosen to be equal to the wavelength of the light to be used. The influence of the cladding index on the propagating mode was investigated using Fourlayer. The

cladding on both sides of the waveguide core was assumed to be infinite, and figure 3.11. shows the influence of the cladding index on the mode thickness.

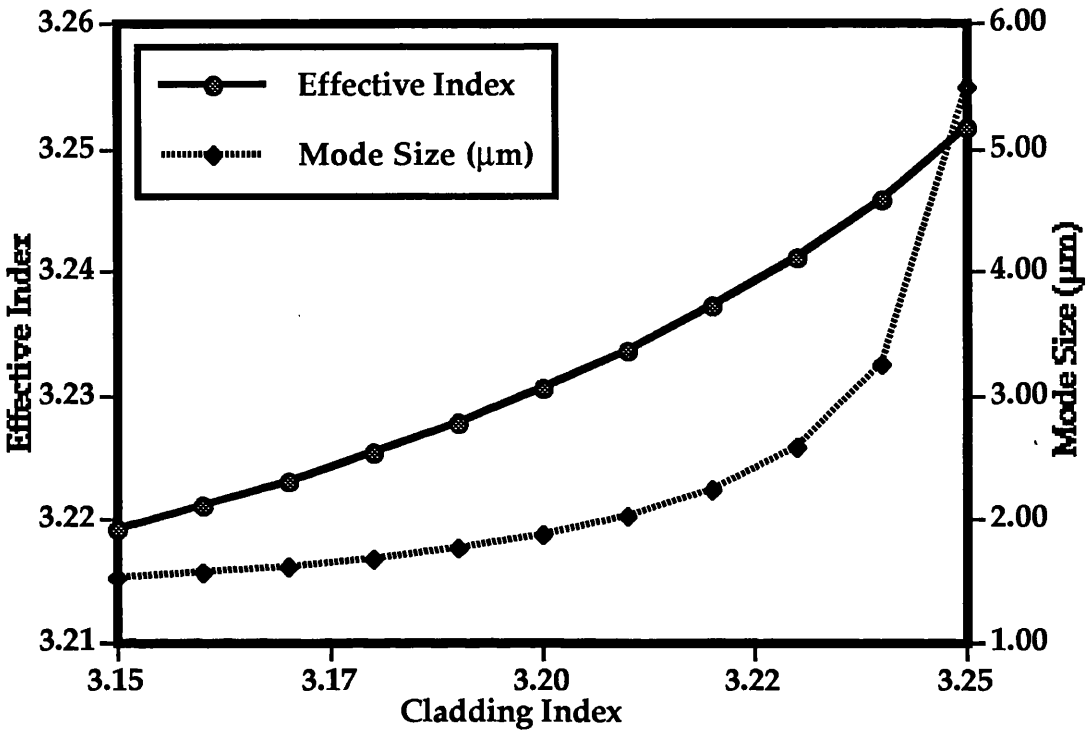


*Figure 3.11. Influence of the cladding index on both the guide's effective index and modal thickness.*

It is apparent that the guide starts to approach cut off at $n_{clad} \approx 3.245$, and therefore by selecting $n_{clad}$ to be close to this the guide should provide relatively weak confinement, but single mode propagation should be ensured. This also provides the advantage that since the interfaces possess a relatively low $\Delta n$ the scattering losses will be lower. The aluminium content of the cladding was therefore set at 37 %, as this corresponded to an index of 3.234.

The thickness of the upper and lower cladding also had to be selected, to ensure that both leakage into the substrate from the lower surface, and scattering from the upper surface is minimised. Since this waveguide was to be used in disordering experiments, it was concluded that the upper cladding layer must be kept relatively thin, so as to promote intermixing and also increase the selectivity the intermixing could achieve. Figure 3.12. shows the effect of altering the cladding thickness.

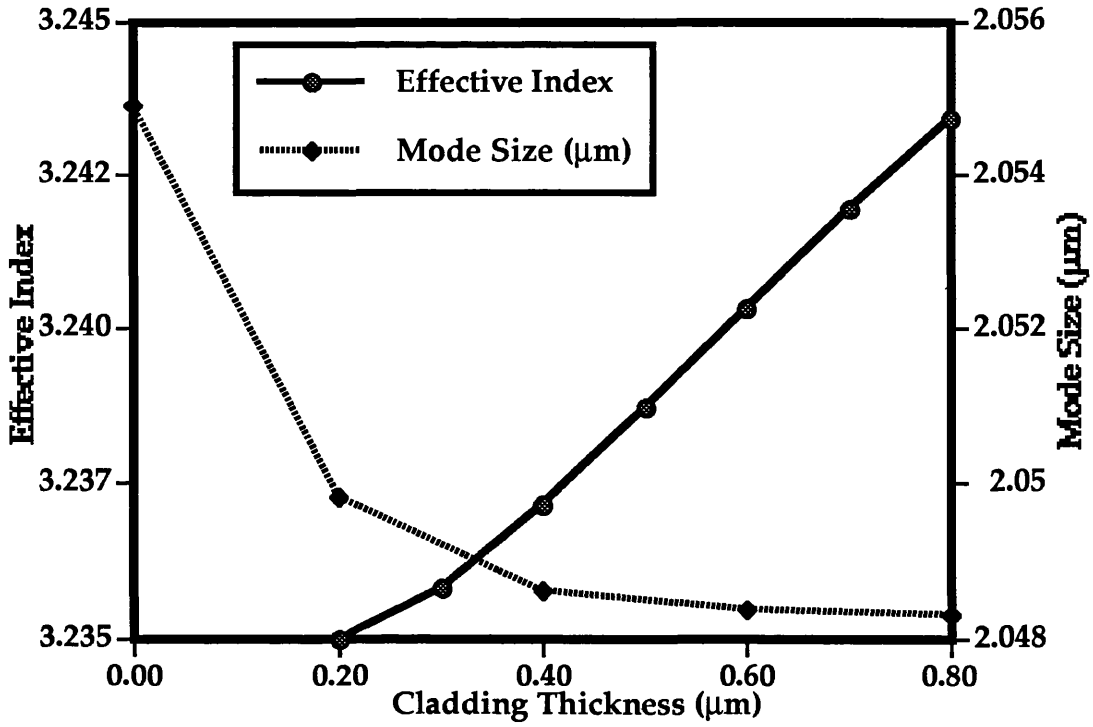


*Figure 3.12. Influence of the cladding thickness on both the guide's effective index and modal thickness.*

### 3.4.3. Lateral Confinement.

The effect of changing the cladding thickness on the effective index is seen from figure 3.12. to be rather weak. The etch depth must then be relatively deep ($\approx 0.7\mu m$), to provide a reasonable degree of confinement in the lateral direction. Figure 3.13. shows the effects of changing the width of the waveguide rib on both the mode size and effective index.

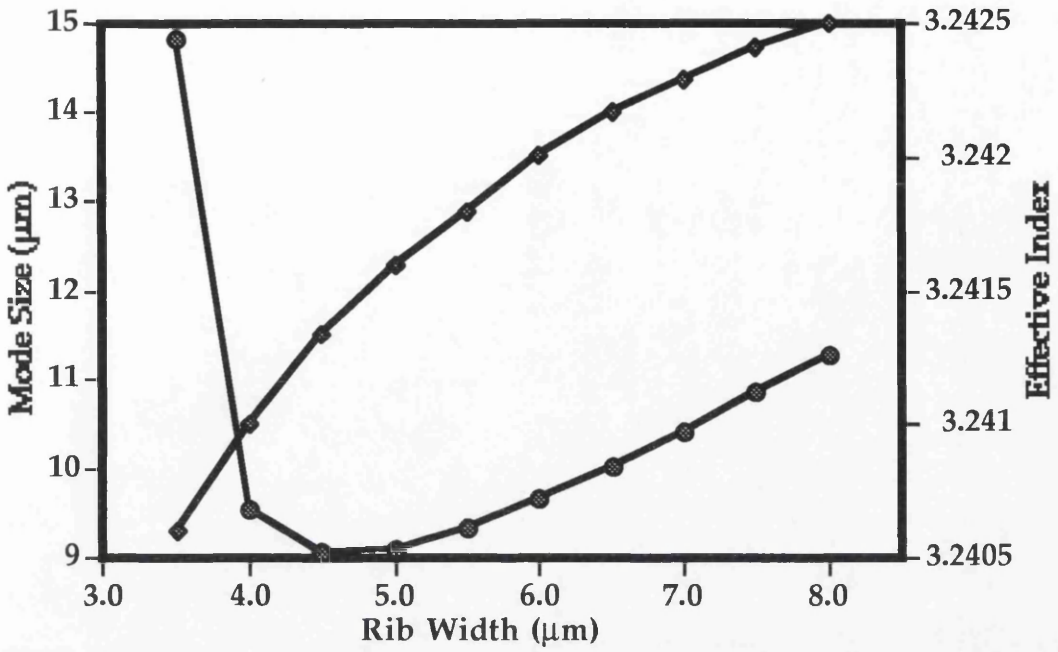


*Figure 3.13. Influence of the rib width on both the guide's total effective index and modal thickness.*

It is clear that the optimum guide width is around 5 μm as this provides the best confinement. After these initial calculations with Fourlayer the guide design was verified using FWave to ensure that the guide was both single moded and possessed reasonable optical confinement, the mode is shown in figure 3.14.

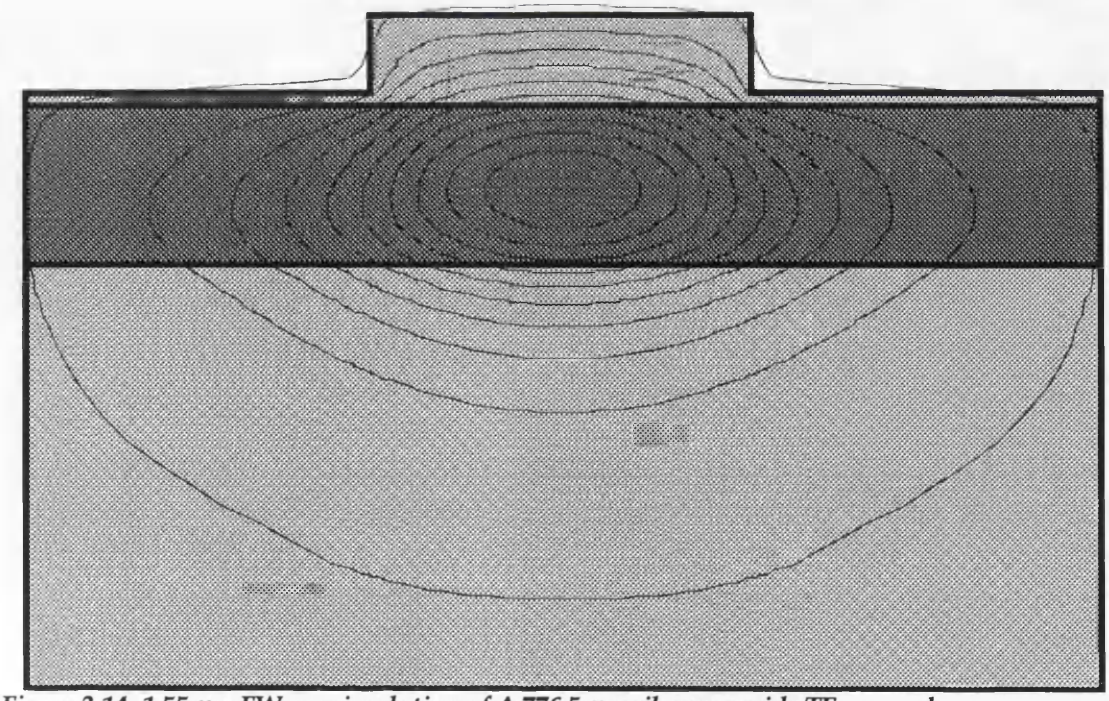

*Figure 3.14. 1.55 μm FWave simulation of A 776 5 μm rib waveguide TE $_{00}$ mode.*

## 3.5. Nonlinear Optical Characterisation.

When studying nonlinear optical materials the nonlinear absorption and refractive index coefficients are of the most interest. There are two major methods used for the characterisation of the nonlinear refractive index. These are the Z-scan and Self Phase Modulation (SPM) spectral broadening measurements[28]. Both methods are well documented and are relatively easy to perform. However because waveguides are used in these studies the nonlinear coefficient was determined using SPM techniques, and therefore this technique is outlined in the following section.

### 3.5.1. Nonlinear Coefficient Measurement Using SPM.

In section 1.2.3. SPM was introduced and an extremely basic outline of the effect was presented, however, to accurately determine the nonlinear coefficient a closer inspection of the technique is required. Considering the case of a Gaussian pulse, which is travelling in a medium with a positive Kerr type nonlinear coefficient. Assuming the dispersion length is greater than the waveguide length and the pulses possess a relatively large peak power. From the basic $\chi^{(3)}$ nonlinear equation (equation 1.4.), it is apparent that at the front of the pulse the refractive index of the medium is increasing, and the opposite is true for the pulse's trailing edge. Consequently light at the front of the pulse begins to travel slower, and at the same time light at the end of the pulse speeds up. The ultimate effect of this is to generate a phase shift across the pulse, which is dependent upon the intensity in the pulse. Also since frequency is the rate of change of phase, it is obvious that this change of phase will lead to a frequency chirp across the pulse. Figure 3.15. shows an example of the phase and frequency chirp generated across a Gaussian pulse.

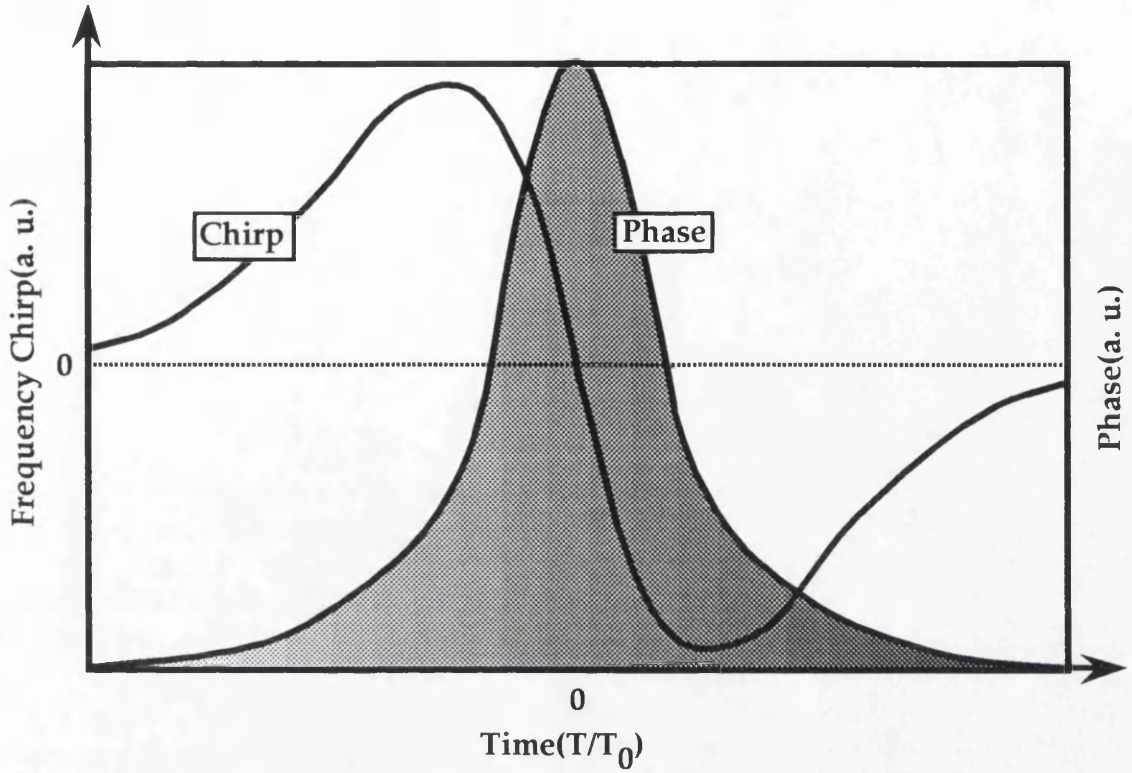


*Figure 3.15. Phase and frequency chirp generated across a high power gaussian pulse by SPM.*

By considering the phase generated by the pulse it is quite apparent from figure 3.15. that two separate frequencies can possess the same phase. This will lead to an interference condition across the pulse, and at certain phases the spectral pulse shapes have been calculated by Stolen et al in reference 28. (figure 3.16 ).

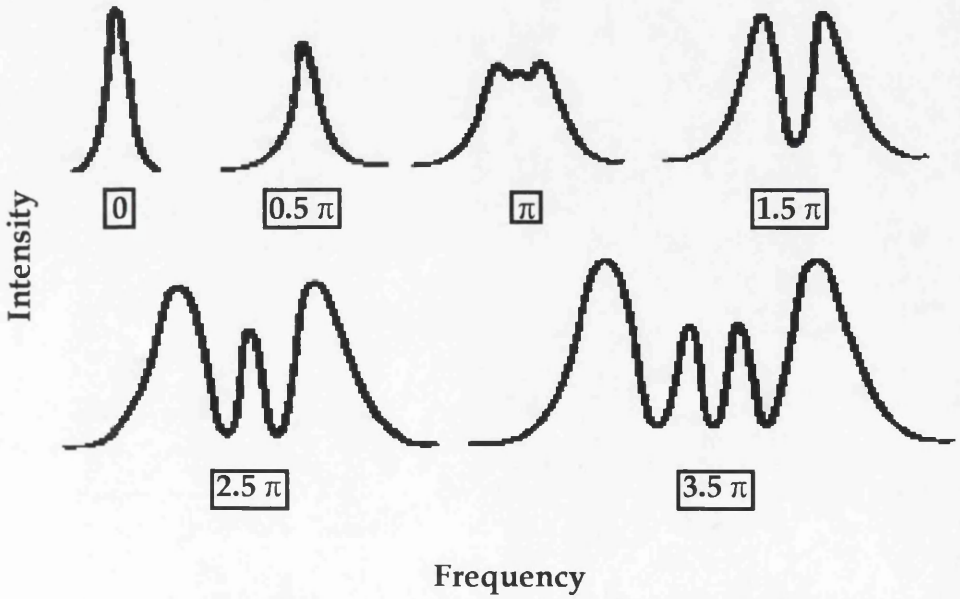


*Figure 3.16. Spectral pulse shapes for different phase shift generated across the pulse. (ref. Stolen et al).*

It is clear that a number of peaks and troughs are generated across the spectrum, the phase shift can be approximately related to the number of peaks by:

$$\phi_{max} \approx \left(M - \tfrac{1}{2}\right)\pi \qquad 3.19.$$

Where M is the number of peaks, and $\phi_{max}$ is the phase shift at the maximum dip in the spectrum. This phase shift can then be inserted into equation 1.6., and the nonlinearity can then be determined. However, this equation does not account for losses within the sample, and therefore an equivalent length has to be defined for the waveguide:

$$z_{eff} = \frac{1 - e^{(-\alpha z)}}{\alpha} \qquad 3.20.$$

$z_{eff}$ is the effective length of the waveguide, $\alpha$ is the optical loss in $cm^{-1}$, and z is the waveguide length. This means that the nonlinearity can be defined as:

$$n_2 = \frac{\phi_{nl}\lambda A_{eff}}{2\pi P_p z_{eff}} \qquad 3.21.$$

Where $P_p$ is the peak power in the guide, $A_{eff}$ is the effective area of the mode and $\lambda$ is the operating wavelength.

### 3.6. Further Work.

Further work in this area will concentrate on optimisation of the wafer parameters. This will include attempts to increase the modal overlap of the laser and waveguide, so as to maximise the power input to the guides, as it will increase the effectiveness of the experiments. This will be run in conjunction with optimisation of the effective nonlinearity of the waveguides, as this is will increase the efficiency of any nonlinear devices.

### 3.7. Conclusions.

Rules and methods for the design of low loss semiconductor waveguides have been presented. The effects of various parameters of the guides, on the modal confinement and effective index have been explored. Fabrication methods commonly used for the

production of AlGaAs optical waveguides have been outlined, and the measurement procedure for the optical losses of the guides has also been presented and investigated. Details of how self phase modulation can be used to measure the Kerr type nonlinearity was also detailed.

# References.


1 D. K. Cheng., "Field and wave electromagnetics.", AddisonWesley Publishing Company, Second edition, 1991.

2 G. B. Hocker and W. K. Burns., "Mode dispersion in diffused channel waveguides by the effective index method.", Appl. Opt. **16**, 1, 113, 1977.

3 M. Kogelink., "Integrated optics.", Topics in applied physics Vol. 7, 1979.

4 M. Nelkon and P. Parker., "Advanced level physics.", Sixth edition. Heinemann Educational Books. 1987.

5 J. Stewart Aitchison., "Optical bistability in semiconductor waveguides.", Ph. D Thesis, HeriotWatt University. Edinburgh, 1987.

6 P. K. Tien., "Light waves in thin films and integrated optics.", Applied Optics., **10**, 11, 2395, 1971.

7 D. L. Lee "Electromagnetic principles of Integrated optics.", John Wiley & Sons, New York, 1986.

8 D. Marcuse., "Theory of dielectric optical waveguides.", Academic Press, New York, 1972.

9 R. Baets, P. Kaczmarski and P. Vankwikelberge., "Design and modelling of passive and active optical waveguides.", Waveguide Optoelectronics, NATO ASI Series E, Applied Science, **226**, 1992.

10 Kadhair A. Al-Hemyari, "Resonant and nonresonant all-optical switching devices in GaAs/AlGaAs" Thesis University of Glasgow, 1992.

11 M. R. S. Taylor., "FWave III, A vector E-M wave solver.", User manual, © MRS Taylor 1989-92.

12 R. P. Espindola, M. K. Udo, D. Y. Chu, S. L. Wu, S. T. Ho, R. C. Tibero, P. F. Chapman and D. Cohen., "All-optical switching with low-peak power in microfabricated AlGaAs waveguides.", IEEE Phot. Technol. Lett. **7**, 6, 641, 1995.

13 R. Cheung, S. Thoms, M. Watt, M. A. Ford, C. M. Sotomayer-Torres, C. D. W. Wilkinson, U. J. Cox, R. A. Cowley, C. Dunscombe and R. H. Williams., "Reactive ion etching induced damage in GaAs and $Al_{0.3}Ga_{0.7}As$ using $SiCl_4$.", Semicon. Sci. Technol. **7**, 1189, 1992.

14 R. J. Deri and E. Kapon., "Low-loss III-V semiconductor optical waveguides.", J. Quant. Electron. **27**, 3. 626, 1991.

15 G. H. Ames and D. G. Hall., "Attenuation in planar optical waveguides: Comparison of theory and experiment.", IEEE J. Quantum Electron. **19**, 845, 1983.

[16] K. H. Park, Y. T. Byun, Y. Kim, S. H. Kim, S. S. Choi and Y. Chong., "Dependence of propagation loss on etching depth in $Al_{0.3}Ga_{0.7}As/GaAs/Al_{0.3}Ga_{0.7}As$ strip-loaded type waveguides.", Opt. Quant. Electron., **27**, 363, 1995.

[17] E. Kapon and R. Baht., "Low-loss single-moded GaAs/GaAsAl optical waveguides grown by organometallic vapour phase epitaxy.", Appl. Phys. Lett., **50**, 1628, 1987.

[18] A. J. N. Houghton, D. A. Andrews, G. J. Davies and S. Ritchie., "Low-loss optical waveguides in MBE-grown GaAs/GaAlAs hetrostructures.", Opt. Comm. **46**, 164, 1983.

[19] M. Haruna, Y. Segawa and H. Nishihara., "Nondestructive and simple method of optical-waveguide loss measurement with optimisation of end-fire coupling.", Electron. Lett. **28**, 17, 1992.

[20] R. G. Walker. "Simple and accurate loss measurement technique for semiconductor optical waveguides.", Electron. Lett. **21**, 13, 583, 1985.

[21] L. S. Yu, Q. Z. Liu, S. A. Pappert, P. K. L. Yu and S. S. Lau., "Laser spectral linewidth dependence on waveguide loss measurements using the Fabry-Pérot method.", Appl. Phys. Lett. **65**, 5, 536, 1994.

[22] D. F. Clark and M. S. Iqbal., "Simple extension to the Fabry-Pérot technique for accurate measurement of losses in semiconductor waveguide.", Opt. Lett. **15**, 22, 1291, 1990.

[23] E. Hecht., "Optics.", Second Edition., Addison Wesley Publishing, 1989.

[24] J. I. Pankove., "Optical processes in semiconductors.", Prentice Hall, Electrical Engineering Series, 1971.

[25] A. Yariv., "Optical electronics.", Fourth Edition, Saunders College Publishing, 1991.

[26] J. H. Betchel and W. L. Smith., "Two-photon adsorption in semiconductors with picosecond laser pulses.", Phys. Rev. B. **13**, 8, 3515, 1976.

[27] B. Buhambra., "Nonlinear optical waveguide devices in GaAs/GaAlAs.", Ph. D. thesis, University of Glasgow, 1991.

[28] R. H. Stolen and C. Lin., "Self phase modulation in silica fibres.", Phys. Rev. A., **17**, 1448, 1978.

# Chapter 4.

# Nonlinear Laser System.

AlGaAs is known to be a good material system for the study of optical nonlinearities (section 2.4.3.), and it has been shown that it is most effective when it is excited at energies below half bandgap[1]. This means that to study all-optical nonlinear phenomena in AlGaAs, it is essential to have access to a high power light source in this wavelength range ($\approx 1.50\ \mu m$). Working in this wavelength region will also ensure that resonant nonlinearities[2] such as the quantum confined Stark effect and band-filling effects can be discounted. F-Centre lasers based around either KCl:Tl or NaCl:$OH^-$ colour centre crystals, posses both tunability and the ability to generate extremely short pulses. Therefore, part of this thesis was concerned with constructing an efficient, low noise, laser system, that was tunable around the AlGaAs half band gap and possed high peak powers.

## 4.1. F-Centre Lasers.

Laser action in colour centres was first observed in 1965[3]. A KCl:$Li^+$ rod was flashlamp pumped and produced pulses at a wavelength of 2.7 μm. Subsequently using techniques developed for dye laser systems tunable CW operation was achieved in this same system[4]. Now there are approximately a dozen colour centre systems that cover the 0.8 → 4.0 μm spectral range. At 1.50 μm colour centre crystal lasers offer many advantages over their main rivals namely, InP based semiconductor lasers[5], and erbium doped fibre lasers[6]. These advantages include:

- **Broad continuous tunability[7] (over 200 nm).**
- **Easy single mode operation[8] (linewidth <1 MHz).**
- **High average output powers[9] (up to 1 W).**
- **Extremely short pulse widths[10] (< 300 fs).**

From the the points indicated it is apparent that the main advantage of F-centre lasers is that they are extremely versatile. One laser can offer all the above benefits and more, where as the two rival systems would need to be specifically configured to provide any one of the above characteristics.

However, there is one drawback associated with colour centre lasers, and that is the fact that the crystals need to be kept at cryogenic temperatures for CW operation[11]. This is due to the centres either thermally disassociating, or becoming mobile and combining with other defects and becoming nonlasing centres.

### 4.1.1. Physics of F-Centres.

Colour centre crystals are so called because microscopic defects in normally transparent crystals tend to absorb visible light and thus the crystal appears coloured. The symbol "F" is sometimes used instead of "colour" due to the fact the German for colour is Fabre. Fundamentally, colour centres are basically point defects in crystal lattices and if alkali-halide crystals are considered, figure 4.1.a shows a basic F-centre which consists of

an electron bound to an anion (halogen ion vacancy). This type of colour centre is not of any use in lasers, since the emission cross section is very small ($< 10^{-17}$ cm$^2$), but it does provide the building block of lasing colour centres.

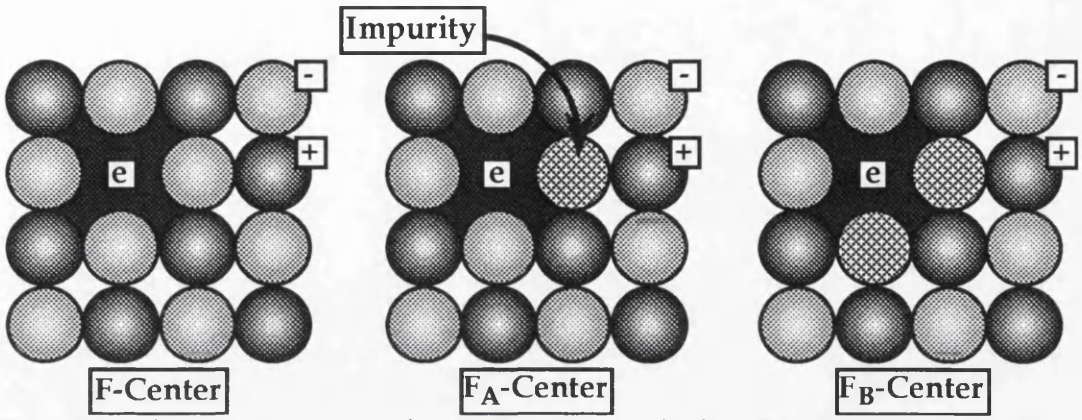


*Figure 4.1. Schematic structures of some F centres in alkali-halide crystals, (a) F-centre, (b) $F_A$-centre and (c) $F_B$-centre.*

The electron/hole associated with the defect essentially sees a 3 D square well potential, which is easily described using a simplified energy level diagram (figure 4.2., normal configuration). As the F-centre absorbs a photon it is excited to a higher state and the energy density of the centre is reduced, this means that the neighbouring centres can relax outwards through Coulomb effects. This results in an increase of the well's lower potential and the excited state's energy levels are effectively raised toward the conduction band. This process goes on and progresses until it is balanced by the crystal restoring forces and an equilibrium state is reached, this is shown in figure 4.2. and termed the Relaxed Excited State (RES).

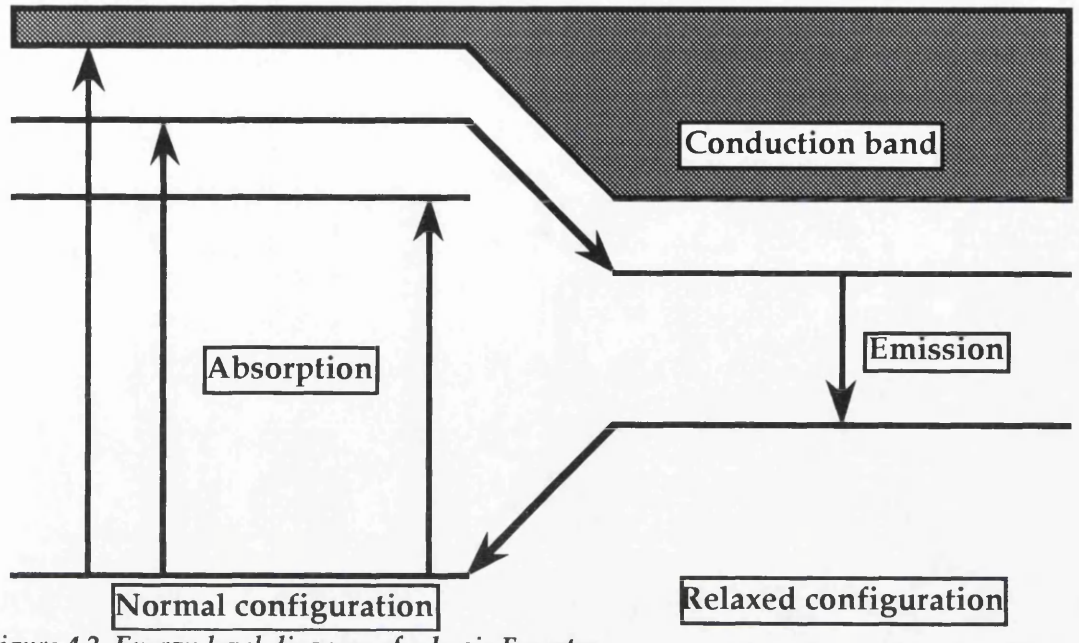


*Figure 4.2. Energy level diagram of a basic F-centre.*

If the alkali-halide crystal is doped with impurity atoms it is possible to obtain lasing colour centres. The simplest type of lasing colour centre is the $F_A$ centre, which is essentially the same as the F-centre except that the vacancy is adjacent to a substitutional impurity (figure 4.1.b).

One of the most important advantages of the colour centre laser are the large homogeneously broadened energy levels, which are due to the influence of phonons and vibrations in the surrounding lattice. Considering figure 4.3. it is possible to understand how these bands are broadened.

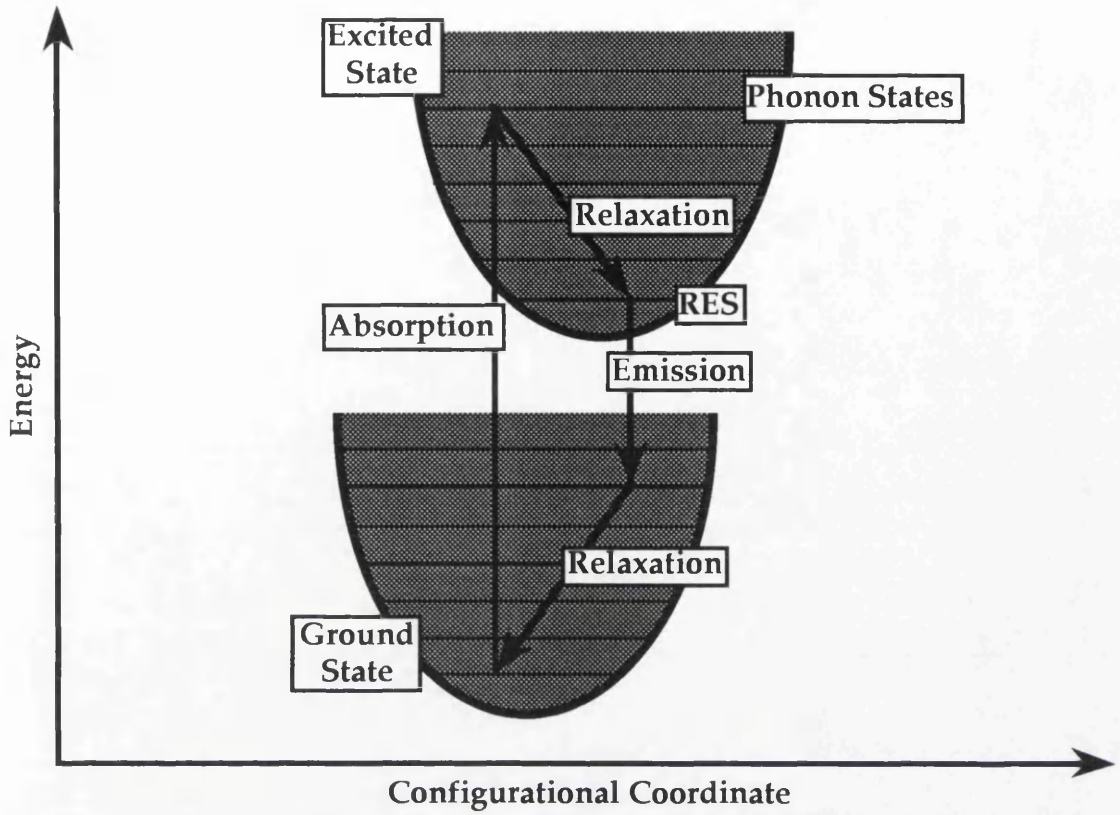


*Figure 4.3. Configurational co-ordinate diagram for two vibronically broadened electronic levels, shown the absorption and emission cycles.*

The electronic ground and excited states of each centre are represented by a parabolic potential well, and the configurational co-ordinate[12] refers to the distance from the lattice vacancy to the first shell of the nearest ions. In these potential wells phonon states are represented by horizontal lines, and if the harmonic oscillator approximation is applied they become equally spaced. The probability of the ion being lifted to an excited state depends on the overlap between the two wavefunctions. When optical excitation occurs there is a vertical transition at a fixed configurational co-ordinate, however, this excited state is not in equilibrium with the lattice and the ion relaxes to a Relaxed Excited State (RES) by emitting phonons. At the bottom of the well the atom can now spontaneously emit a photon and decay to the ground state, where it will continue to emit phonons until it reaches the bottom of the ground state. This interaction between the colour centre and the lattice creates a Stokes shift in the energy levels, and effectively results in a four level system. Also because the time taken to decay down to the RES is much less than the

lifetime in the excited state, quantum efficiencies of approximately unity can be achieved[13].

### 4.1.2. The $Tl^0(1)$ Centre in KCl:Tl.

The colour centre used in this work was the $Tl^0(1)$ centre[14] in a KCl crystal. This system has an absorption band centred at 1.04 μm which makes it suitable for optical pumping by neodymium based solid state lasers. The output wavelength is tunable from 1.40 to 1.63 μm which encompasses the low loss silica communications window. The broad emission band has also made it suitable for short pulse generation and it was an essential part of the soliton laser[15]. Spectroscopy also benefits from these homogeneously broadened energy bands, as intrinsically narrow linewidths can be continuously tuned in single mode operation.

This colour centre consists of a neutral thallium that is perturbed by an adjacent anion vacancy. Unlike the basic F-centre the electron does not exist at the vacancy but is mainly localised at the impurity atom. This means that the energy level diagram is similar to that of the basic thallium atom (figure 4.4.), and changing the crystal host results in only small changes to the laser characteristics.

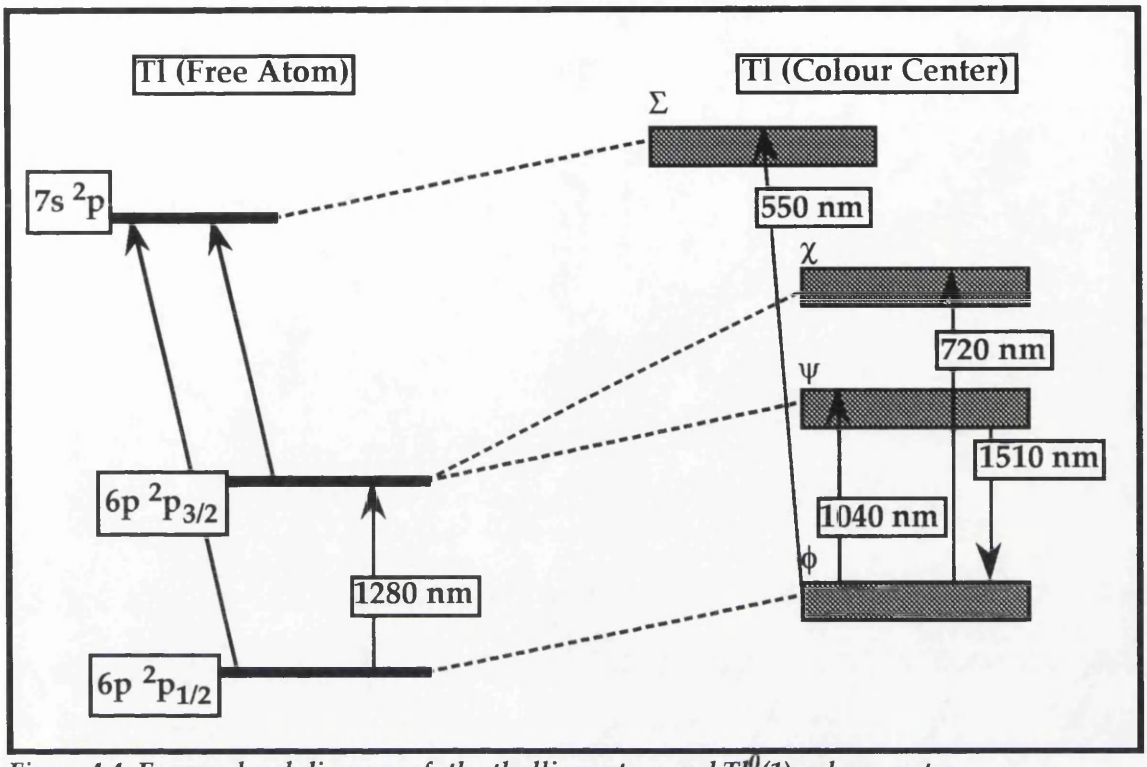


*Figure 4.4. Energy level diagram of the thallium atom and $Tl^0(1)$ colour centre.*

KCl:Tl F-centre laser crystals are formed from KCl crystal doped during growth with typically < 1 % mol $Tl^+$ ions[16]. The F-centres are then created by exposing the crystal to an electron beam at low temperature (≈ -130 °C), these crystals are then subjected to a white light source to ionise the F-centres. The $Tl^+$ ions capture these free electrons and become $Tl^0(0)$. If this process occurs at a temperature slightly above room temperature (≈ 30 °C) the anion vacancies can migrate through the lattice and attach themselves to these $Tl^0(0)$ and become $Tl^0(1)$ centres. These centres are stable at room temperature providing they are kept in darkness, however, storing them in liquid nitrogen helps improve their shelf life. Table 4.1. shows some typical KCl:Tl crystal parameters.

**Table 4.1.**

| KCl:Tl F-Centre | |
|---|---|
| **Parameter** | **Value** |
| Refractive index | 1.47 |
| Peak absorption wavelength | 1.04 μm |
| Absorption band | 650 $cm^{-1}$ |
| Peak emission wavelength | 1.51 μm |
| Tuning range | 230nm |
| Gain cross section | $1.3x10^{-17}$ $cm^2$ |
| Upper level lifetime | 1.60 μs |

*Table 4.1. Typical parameters for KCl:Tl colour centre laser.*

The most significant parameters of the KCl:Tl colour centre are the long decay time, and the relatively large emission cross section.

### 4.2. Diode Pumped Nd:YLF Laser.

As the KCl:Tl F-centre has a strong and wide absorption at around 1.04 μm, the obvious candidate for optical pumping is a neodymium based solid state laser. The usual choice is a mode locked mainframe Nd:YAG laser, which can provide more than enough power with reasonable efficiency and noise levels. However, it was decided that a diode pumped Nd:YLF system would be more appropriate for the application, since both the diode pumping and YLF have characteristics that make them extremely desirable for optically pumping a KCl:Tl F-centre.

Yttrium lithium fluoride (YLF) is the best known alternative to YAG as a neodymium lattice host. YLF possess a lower gain cross section than YAG, therefore for higher average output powers YAG is the preferred choice. However, at the powers needed to pump the KCl:Tl F-centre laser (≈ 2 W) the two lattice hosts produce approximately the same output power, and neither hold a significant output power advantage. Although for this application YLF does possess some very desirable advantages[17] which are:

- **YLF exhibits less thermal lensing than YAG.**
- **YLF has a longer lifetime than YAG.**

- **YLF has a broader gain bandwidth.**
- **YLF possess better amplitude stability.**

All these advantages add up to a pump source that can produce relatively short pulses ($\approx 1.5$ ps)[18] which also possess very good amplitude stability and beam pointing.

At the moderate powers required to optically pump a KCl:Tl F-centre laser, diode pumping is also applicable for the Nd:YLF pump laser and can lead to an extremely efficient laser source. The main advantages associated with diode pumping are[19]:

- **End pumping can produce ultra high quality beams[20].**
- **AlGaAs diodes match the Nd:YLF 800 nm absorption line[21].**
- **Less waste heat production.**
- **Mechanical stability due to size.**
- **Extremely low amplitude noise.**
- **Long life times (typically > 10000 hours).**

These advantages mean that it is possible to achieve a highly efficient mode locked pumped source, since the high quality output beam will lead to a good mode match between the F-centre laser cavity mode and the focused Nd:YLF pump beam.

#### 4.2.1. CW Nd:YLF Laser.

The Nd:YLF laser (figure 4.5.) was pumped by two 4 W AlGaAs diodes, one of which had the polarisation flipped by a half wave plate, since this allowed the pump beams to be combined by a polarising beam splitter. Beam shaping and focusing optics allowed the light to be focused into a $\approx 200$ μm spot in the YLF rod. The YLF rod was 4 mm in diameter and one end was flat polished and had an AR coating at the 0.80 μm pump wavelength, and an HR coating at the 1.047 μm lasing wavelength. The other end was Brewster angle polished and the 1.93 m long cavity was folded to compensate for this.

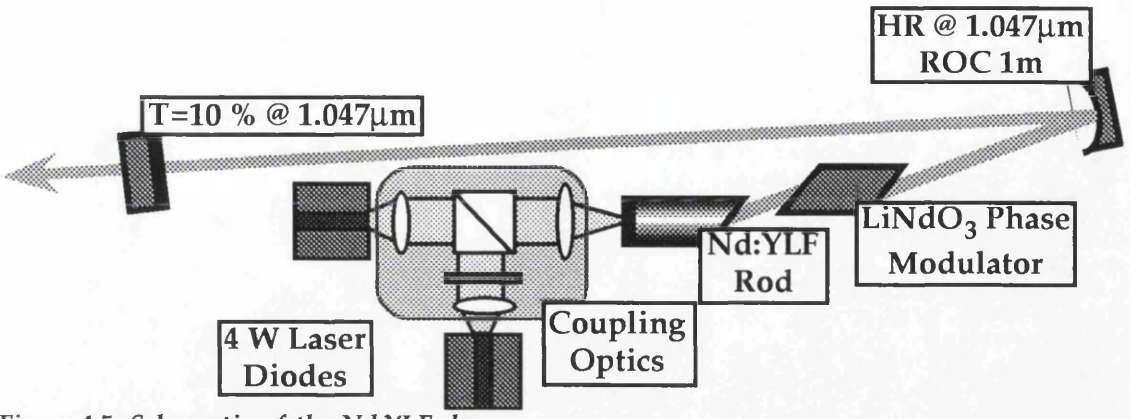


*Figure 4.5. Schematic of the Nd:YLF laser.*

Since the Nd:YLF crystal absorbs the light from the semiconductor pump very effectively the efficiency of the laser is extremely high. In a crude but effective approximation, the efficiency (η) of the laser can be defined as:

$$\text{Total } \eta \text{ (\%)} = \frac{\text{Output Light Power (W)}}{\text{Electrical Input Power (W)}} \qquad 4.1.$$

Each pump diode supplies 4 W of 0.81 μm light and the actual power supplied to each of the diodes is 15.5 W, this results in an electrical to light conversion of 26 % for the diodes. When the Nd:YLF laser is returning an optimum performance of 2.20 W output power at 1.047 μm the overall efficiency is 7.15 %. This compares very favourably with flashlamp pumped lasers in this output power range where the typical efficiency is much less than 1 %.

End pumping the Nd:YLF rod also results in a high quality output beam which does not display any astigmatism, since the folding angle of the cavity is designed to compensate for the Brewster angled rod. This high quality beam is seen in figure 4.6. and is essential for good power transfer characteristics between the modes of the Nd:YLF pump and the F-centre lasers.

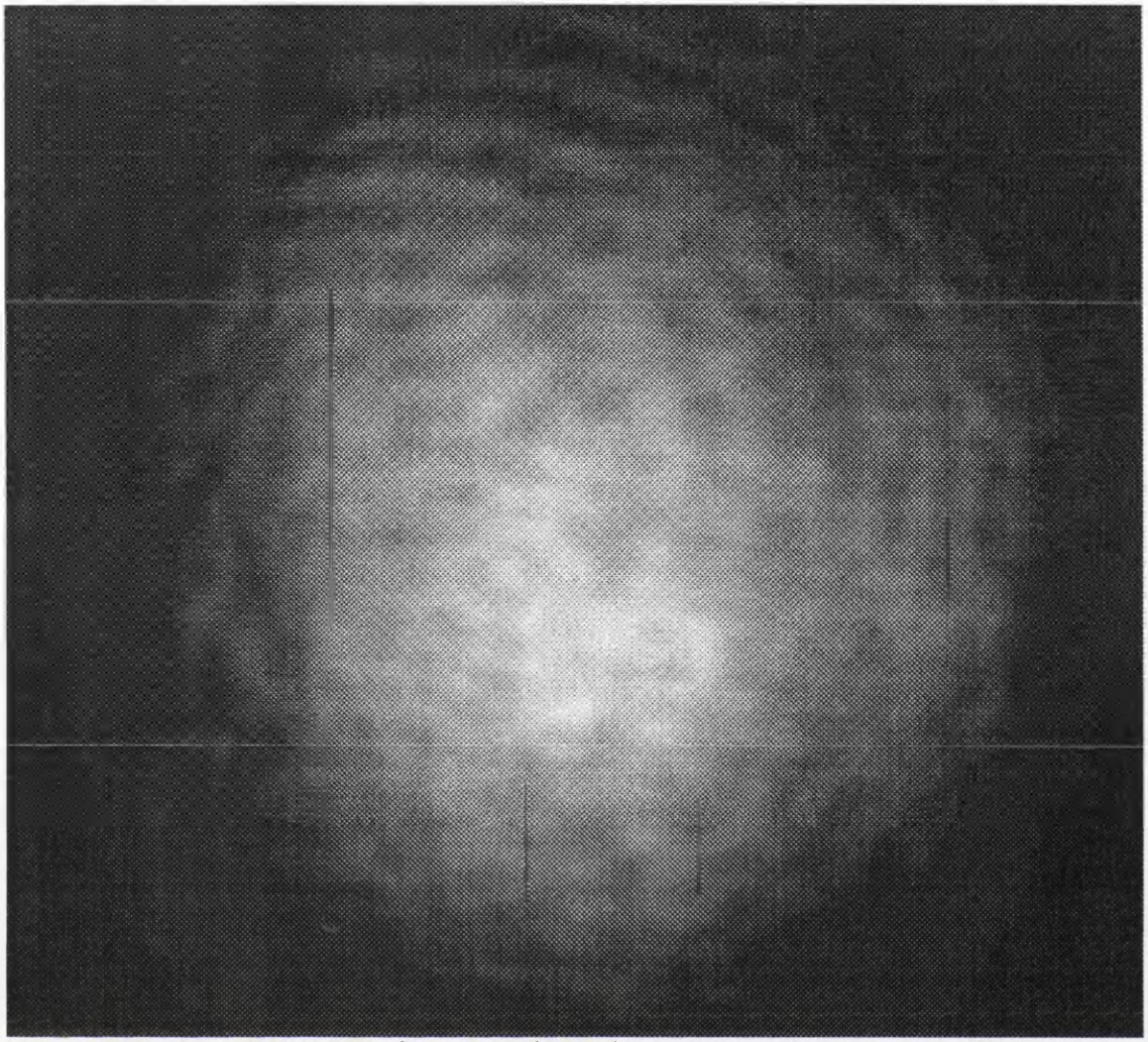

*Figure 4.6. Output $TM_{00}$ profile from the Nd:YLF laser (1 cm ≈ 200 μm).*

### 4.2.2. FM Mode locked.

To passively mode lock the F-centre by synchronous pumping, the Nd:YLF pump laser must produce suitable pulses to ensure reasonable mode locking. One way in which this was achieved was by using a lithium niobate phase modulator, which was driven by a 400 mW r. f. signal at 77.74 MHz. An electro-optic frequency modulator was chosen as the active element due to the advantages[22] it offers over acousto-optic modulators, such as:

- **Operation far above 100 MHz.**
- **The operating frequency is easily set.**
- **Relatively insensitive to angular adjustment.**

- **Require relatively low drive power.**

The modulator was a Brewster angled $LiNbO_3$ crystal that was 25 mm long and has an aperture of 5 x 4 mm, the field was applied transversely to the modulator and thus used the $r_{33}$ electro-optic coefficient. The laser tended to operate "hopping" between two trains of pulses[23], which corresponded to either of the nulls in the sinusoidal drive signal. One of these pulse trains, was seen to be consistently shorter than the other, and could be selected by slightly altering the cavity length and tuning off the cavity resonance. The total average power when the laser was mode locked was found to be very similar to that of the CW laser ($\approx$ 2 W), and in fact dropped by less than 10 %. The actual length of the shorter pulses was measured by autocorrelation, giving a length of 20 ps.

### 4.2.3. Kerr Lensed Mode locked.

During optimisation of the phase modulator it was found that under certain conditions, the pulses from the laser would undergo unprecedented shortening, and the width would compress to around 4 ps. It was found to occur with most probability when the power to the lithium niobate crystal was increased. It was concluded that this shortening of the pulses was due to Kerr lens[24] mode locking in the laser cavity. The width of these pulses was also measured by an autocorrelator and is shown in figure 4.7..

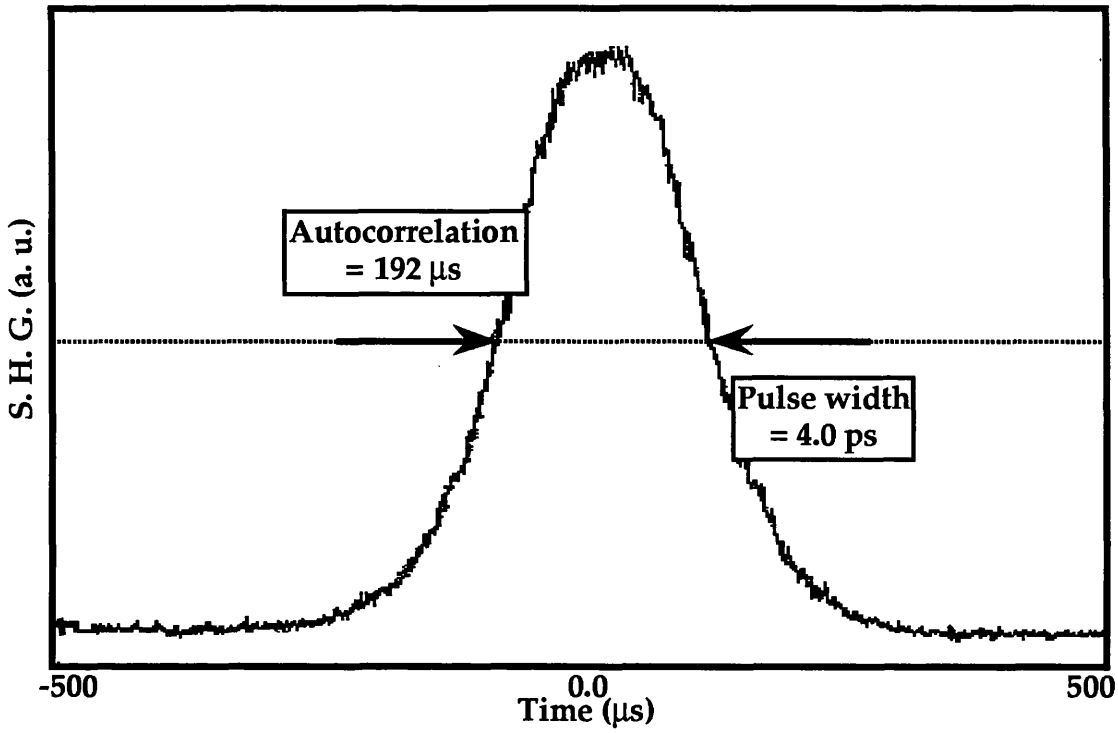


*Figure 4.7. Autocorrelation from the Kerr lens mode locked Nd:YLF laser.*

When the cavity was forced into this type of mode locking the pulses were observed to be very stable for periods of around 10 → 15 minutes. This however, is not stable enough to be a reasonable pump pulse source, for synchronously mode locking the F-centre laser. Therefore, an attempt at producing hard aperture mode locking was made, by placing a slit in the cavity. This mode locked the laser for periods of approximately 30 minutes, and could be restarted by simply blocking and unblocking the cavity. Unfortunately the power also dropped to ≈ 1.50 W when this approach was taken. It was thought that the thermal loading due to the increased power supplied to the modulator, was the cause of the Kerr lensing, and could perhaps be investigated in the future.

### 4.3. KCl:Tl Laser.

The F-centre laser used for these studies was built by St. Andrews University. It consists of a crystal holder mounted on a cold finger which is directly connected to a liquid nitrogen Dewer. Optical access to the crystal was through two fused silica Brewster angled windows. The crystal holder clamps the F-centre crystal at Brewsters angle and good thermal contact is ensured by using a thin piece of indium foil

between the crystal and holder. The crystal mount is slotted into the cold finger and Crycon compound is used between the contacts to ensure thermal continuity. The crystal can be moved relative to the access windows by means of a micrometer, and threaded feet provide height adjustment. Liquid nitrogen from the Dewer is supplied directly to the cold finger by a nearly concentric tube arrangement and this can cool the holder to 77 K within 10 minutes. The Dewer also possess an absorption pump that helps maintain the high vacuum after it is pumped down, and indeed initially the Dewer hold time was approximately 48 hours. One of the practical advantages of the cryostat design is that it allows for the crystal chamber and the liquid nitrogen Dewer to be isolated through use of a three way valve. Therefore, by placing a heater element around the cold finger it is possible to close the liquid nitrogen supply to the cold finger and bring the crystal chamber to room temperature within 30 minutes and replace the crystal within minutes.

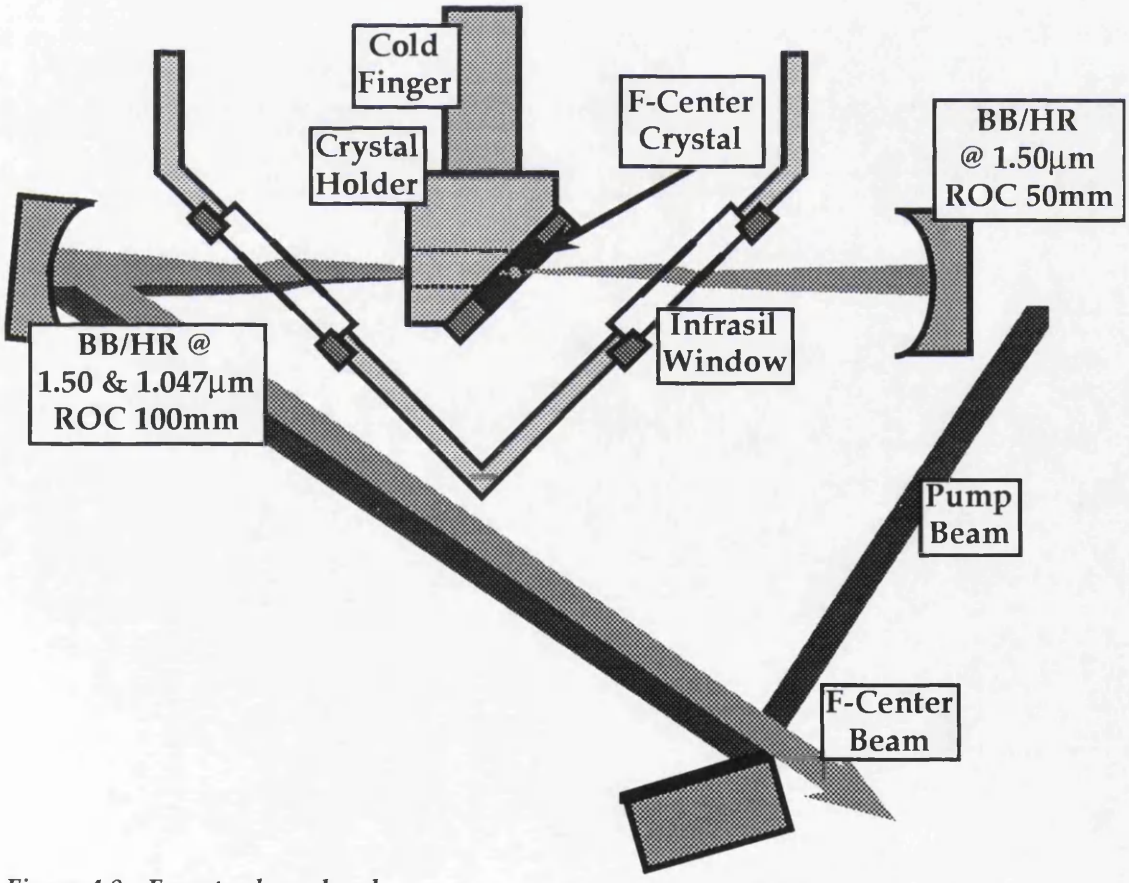


*Figure 4.8. F-centre laser head.*

The laser is fundamentally different from the commercially available Burleigh Instruments model, in that it is only the crystal

that is located within the cooled chamber. This means that the laser is free from stiction problems that are associated with flexible bellows and moreover the cavity configuration may be changed without the crystal being disturbed. However, these advantages are slightly offset by the fact that the distance between the curved mirrors is increased and subsequently the spot size within the gain medium is larger and this results in a slightly higher threshold power. One other advantage of using this type of crystal mounting is that a nearly collinear pumping scheme can be used, rather than the intracavity beam splitter of the Burleigh Instruments model. Hence feedback from the F-centre to the pump laser is totally eliminated, and the subsequent degradation of performance is eradicated.

### 4.3.1. CW KCl:Tl Laser.

The F-centre laser was constructed in an extended five mirror cavity (figure 4.9.) used for matching the cavity to the Nd:YLF for synchronous mode locking[25].

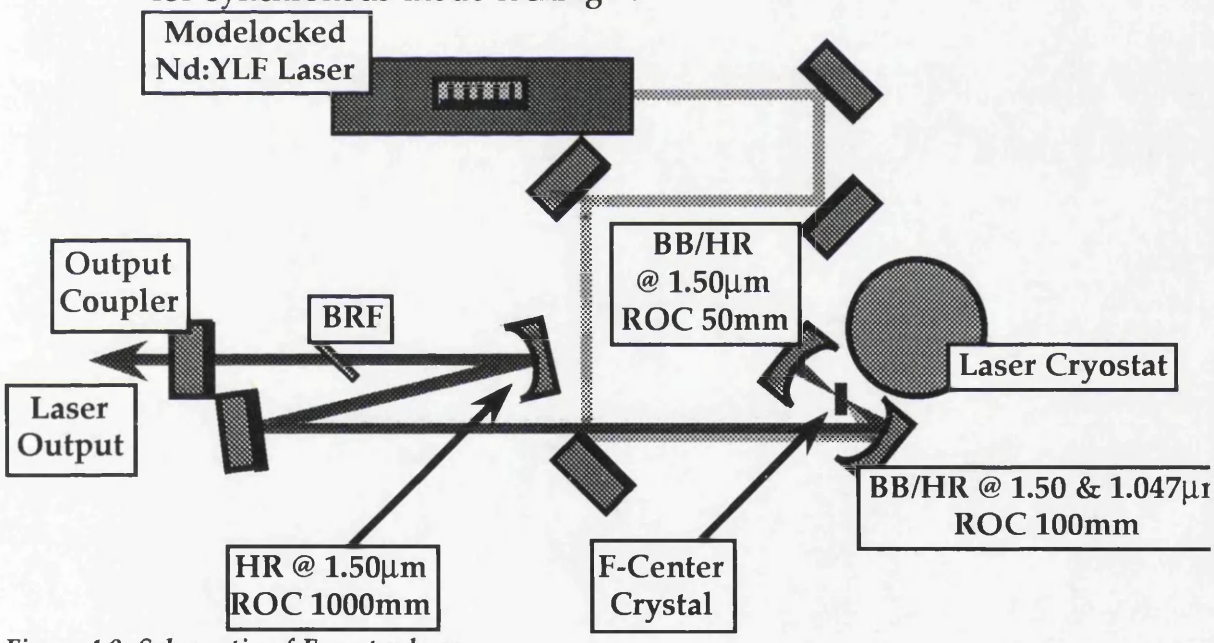


*Figure 4.9. Schematic of F-centre laser.*

Since the available infra-red viewer could not detect the low intensity of the 1.51 μm fluorescence, all alignment procedures used a germanium photodetector, and a long wavelength pass filter to block any residual 1.047 μm light. Initially the threshold characteristics were examined for both 10 and 20 % output couplers, figure 4.10. shows the power transfer characteristics.

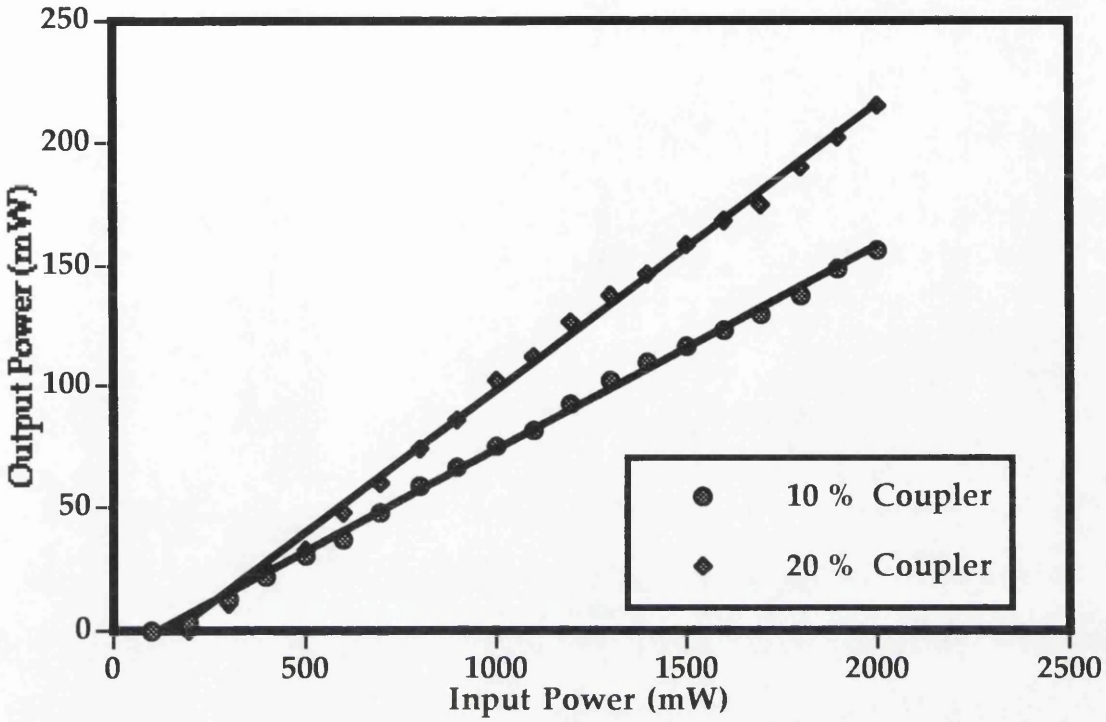


*Figure 4.10. Power transfer characteristic of F-centre laser with 10 and 20 % output couplers.*

As expected the threshold power was lowest with the 10 % output where it could be as low as 175 mW. To investigate the tuning characteristics of the laser, a birefringent filter was placed within the cavity. As this data was taken approximately 3 months after the threshold data it is apparent that the output power has decreased as the centres were bleached out within the crystal.

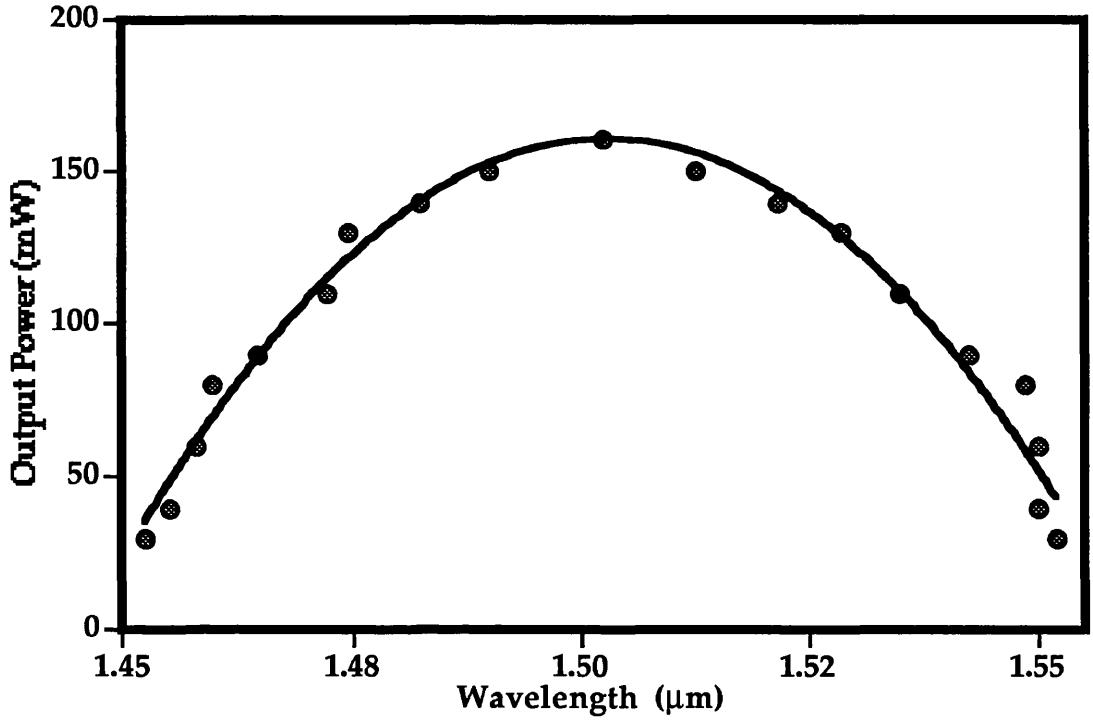


*Figure 4.11. Wavelength tuning characteristics of the F-centre laser.*

Figure 4.11. shows that even after 3 months of continual use, the laser could still produce useful output powers at 1.45 to 1.55 μm.

### 4.3.2. Synchronously Pumped KCl:Tl Laser.

Due to the long life time (section 4.1.2.), synchronously mode locking KCl:Tl colour centre lasers is not particularly effective. This is because the repetition rate of the pulses is approximately 12 ns, and thus the gain modulation appears only as a small ripple. However, the gain will saturate through the average power contained within the cavity, and due to this long gain storage time the mode locked laser output is little different to that of the CW laser. The long gain storage time also has the benefit that the laser will oscillate for any length of cavity.

Typically when using flashlamp pumped neodymium lasers to synchronously mode lock KCl:Tl colour centre lasers, pulses produced are in the region of 60 ps[26]. Since the pulses from the diode pumped Nd:YLF laser were almost an order of magnitude shorter than flashlamp based lasers, it was thought

that this would have some influence on the length of the output pulses. In figure 4.12. an autocorrelation for the output pulses, when the laser was pumped by the FM mode locked Nd:YLF laser is shown.

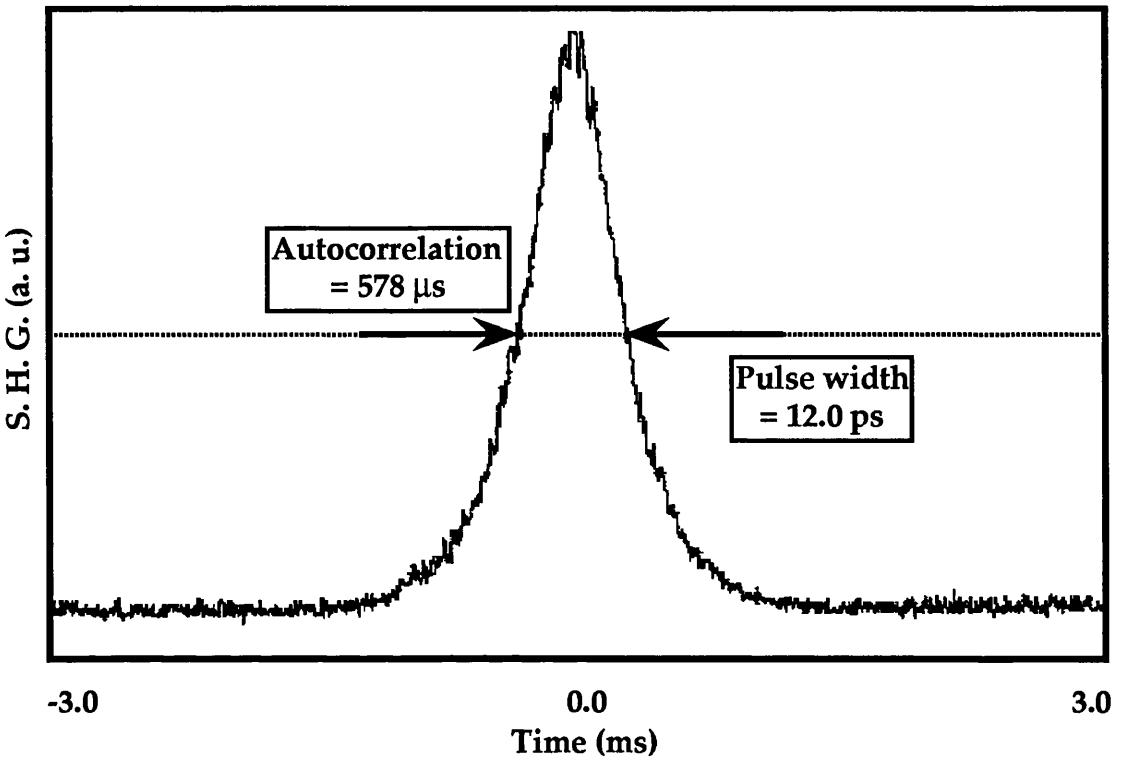


*Figure 4.12. Autocorrelations from the F-centre when pumped by both the FM mode locked Nd:YLF laser.*

When the Nd:YLF operated FM mode locked the pulses are indeed slightly shorter (≈ 12 ps) than the pump pulses (≈ 20 ps), however, when Kerr lens mode locked, the F-centre pulses were measured to be approximately the same length as the pump pulses (≈ 4 ps). This shows that the operational effectiveness of synchronous pumping is being approached, but the pulses are still shorter than those obtained from flashlamp based lasers.

### 4.3.3. Mode locked KCl:Tl Laser Peak powers.

To accurately determine nonlinear coefficients and required powers for all-optical switching, the peak powers delivered from the F-centre must be accurately known. If $T_o$ is defined as the pulse width at the $\frac{1}{e}$ points, it can be related to the $T_{FWHM}$ by:

Gaussian Pulse.

$$T_{FWHM} = 1.665T_o \qquad 4.2.$$

Sech$^2$ Pulse.

$$T_{FWHM} = 1.763T_o \qquad 4.3.$$

Therefore, the peak power in the pulses can be derived from:

Gaussian Pulses.

$$P_p = \frac{E}{2T_o} = \frac{P_{ave}}{2T_o f_p} = \frac{P_{ave}}{1.065T_{FWHM} f_p} \qquad 4.4.$$

Sech$^2$ Pulses.

$$P_p = \frac{E}{2T_o} = \frac{P_{ave}}{2T_o f_p} = \frac{P_{ave}}{1.134T_{FWHM} f_p} \qquad 4.5.$$

Where $f_p$ is the repetition rate of the pulses E is the energy in the pulses and $P_{ave}$ is the average laser power. Using these equations the peak powers available from the synchronously mode locked F-centre laser can be calculated:

Nd:YLF FM Mode locked.

- **Peak Power:** → **189 W.**

Nd:YLF Kerr Lensed Mode locked.

- **Peak Power:** → **567 W.**

## 4.4. Further Work.

Further work on the laser system will concentrate on stabilising the pulses from the Nd:YLF laser and also increasing the peak powers available from the F-centre. Where the Nd:YLF is concerned, stabilisation of the shorter FM mode locked pulses will be attempted by optimisation of the power supply to the PM modulator in an attempt to reduce the influence of the other null point of the drive signal. For the Kerr lensing of the Nd:YLF laser, it is thought that this is predominately due to thermal loading effects from the modulator. It is therefore assumed that this could be increased by

supplying more power to the modulator, and perhaps an active stabilisation scheme employing a feedback loop controlling either the power to the modulator or the length of the laser cavity.

To increase the peak power available from the F-centre, Additive Pulse Mode locking (APM) will be employed in either Michelson or Fabry-Pérot configurations to reduce the pulse width down to the femtosecond regime. Other methods of passive mode locking the laser are also being considered, these include Antiresonant Fabry-Pérot Saturable Absorbers[27] (A-FPSA) and saturable Bragg reflectors[28]. Both of these methods have been applied to solid state laser systems at wavelengths of approximately 1 μm, and by successful application to F-centre lasers they could provide a high peak power laser at 1.50 μm, that could present both a simpler alternative to APM mode locking, and a somewhat cheaper one than erbium doped fiber amplifier based systems.

### 4.5. Conclusions.

For the first time, an all solid state tunable laser, has been shown to operate in both the CW and mode locked regimes at wavelengths of around 1.5 μm. The laser had a tuning range in excess of 100 nm. A diode pumped Nd:YLF laser operating at 1.047 μm was shown to be a suitable source for pumping KCl:Tl F-centre laser crystals, and threshold powers of approximately 175 mW were achieved. From the electrical power supplied to the diodes, to the generated 1.50 μm light the overall system efficiency was shown to be relatively high (0.72 %). The system also produced relatively short pulses of only a few ps, which are among the shortest recorded for KCl:Tl F-centre lasers using synchronous mode locking. The amplitude noise was also monitored, and was less than 1 % for the Nd:YLF laser, and similar for the F-centre laser.

# References.


1 S. T. Ho, C. E. Soccolich, M. N. Islam, W. S. Hobson, A. F. J. Levi and R. E. Slusher., "Large nonlinear phase shifts in-low loss AlxGa1-xAs waveguides near 1/2 gap.", Appl. Phys. Lett. **59** 2558, 1991.

2 R. W. Munn and C. N. Ironside, "Principles and applications of nonlinear optical materials.", Blackie Academic & Professional, 1993.

3 B. Fritz and E. Menke, "Laser effect in KCl with $F_A$(Li) centers.", Solid State Commun., **3**, 61, 1965.

4 L. F. Mollenauer and D. H. Olsen, "A brosdly tunable cw laser using color centers.", Appl. Phys. Lett. **24**, 386, 1974.

5 W. T. Tsang., "Low threshold and high power output 1.5 μm InGaAs/InGaAsP seperate confinement multiple quantum well laser grown by chemical beam epitaxy.", Appl. Phys. Lett., **57**, 20, 2065, 1990.

6 Y. Kimura, K. Suzuki, and M. Nakazawa., "Laser-diode-pumped mirror free Er3+-doped fiber laser.", Opt. Lett. **14**, 18, 999, 1989.

7 W. Gellerman, F. Lüty and C. R. Pollock., "Optical properties and stable, broadly tunable CW laser operation of new FA-type centers in Tl+-doped Alkali halides.", Optic. Comm. **39**, 6, 391, 1981.

8 Burleigh Ltd, "Color center lasers.", Application notes.

9 G. T. Kennedy "Novel mode-locking techniques for colour-center lasers.", St. Andrews University, Ph. D. Thesis, 1993.

10 M. N. Islam, E. R. Sunderman, C. E. Soccolich, I. Bar-Joesph, N. Sauer, T. Y. Chang and B. I. Miller., "Color center lasers passively mode locked by quantum wells.", IEEE. J. Quant. Elec. **25**, 12, 1989.

11 L. F. Mollenauer, N. D. Vieira and L. Szeto., "Mode locking by synchronously pumping using a gain medium with microsecond decay times.", Opt. Lett. **7**, 9, 414, 1982.

12 W. B. Fowler and D. L. Dexter., Chem. Phys. **43**, 768, 1965

13 J.Wiesenfield, L. F. Mollenauer and E. P. Ippen., "Ultrafast configurational relaxation of optically excited color centers.", Phys. Rev. Lett.**47**, 1668, 1981.

14 E. Goovaerts, J. Andriessen, S. V. Nistor and D. Schoemaker., "Electron-spin-resonance study of Tl atom defects in KCl and relativistic many-body analysis of the hyperfine structure.", Phys. Rev. B. **24**, 1, 29, 1981.

15 L. F. Mollenauer and R. H. Stolen, "The soliton laser.", Optic. Lett. **9**, 1, 13, 1984.

16 L. F. Mollenauer, N. D. Vieira and L. Szeto., "Optical properties of the $Tl^0$(1) center in KCl.", Phys. Rev. B. **27**, 9, 5332, 1983.

[17] N. Merilliod, R. Romero, I. Chartier, C. Garapon and R. Moncorgé., "Performance of various diode-pumped Nd:Laser materials: Influence of inhomogeneous broadening.", J. Quant. Electron. **28**, 4, 1179, 1992.

[18] G. P. A. Malcolm, P. F. Curley and A. I. Ferguson., "Additive-pulse mode locking of a diode pumped Nd:YLF laser.", Optic. Lett. **15**, 22, 1990.

[19] J. Hecht, "The laser guidebook.", second edition TAB Books 1992.

[20] J. Berger, D. F. Welch, D. R. Scifres, W. Streifer and P. S. Cross., "High power, high efficient neodymium:yttrium aluminium garnet laser end pumped by a laser diode array.", Appl. Phys. Lett. **51**, 16, 1212, 1987.

[21] T. Y. Fan and R. L. Byer., "Diode laser-pumped soild-state lasers.", J. Quant. Electron. **24**, 6, 895, 1988.

[22] G. T. Maker and A. I. Ferguson., "Frequency modulation mode locking of a diode-pumped Nd:YAG laser.", Opt. Lett. **14**, 15, 788, 1989.

[23] Z. Su "Generation and propagation of ultrashort laser pulses using nonlinear waveguides.", St. Andrews University, Ph. D. Thesis, 1994.

[24] G. P. A. Malcolm and A. I. Ferguson., "Self-mode locking of a diode pumped Nd:YLF laser.", Optic. Lett. **16**, 24, 1991.

[25] S. Kelly, G. H. C. New and D. Wood., "Mode-Locking dynamics of synchronously-pumped colour-center lasers.", App. Phys. B. **47**, 349, 1988.

[26] R. S. Grant "Mode locked colour-center lasers and their applications.", St. Andrews University, Ph. D. Thesis, 1991.

[27] L. R. Brovelli, U. Keller and T. H, Chin., "Design and operation of antiresonant Fabry-Pérot saturable semiconductor absorbers for mode-locked solid-state lasers.", J. Opt. Soc. Am. B. **12**, 2, 311, 1995.

[28] S. Tsdua, W. H. Knox, E. A. de Souza, W. Y. Jan and J. E. Cunningham., "Low-loss intracavity AlAs/AlGaAs saturable Bragg reflector for femtosecond mode locking in solid-state lasers.", Optic. Lett., **20**, 12, 1406, 1995.

# Chapter 5.

# Localised Nonlinearities.

The third-order nonlinearity ($n_2$) in AlGaAs, has become the focus for an increasing amount of research in nonlinear optics, since Aitchison et al used it to demonstrate efficient ultrafast, all-optical switching[1] in an integrated format. This focus exists for several reasons, which include:

- **AlGaAs has an ultrafast nonlinearity that is more than two orders of magnitude larger[2] than that of silica.**
- **AlGaAs possess a mature fabrication base.**
- **The ultrafast nonlinearity is most effective, when operated in the low loss (1.55 μm) telecommunications window.**

Since that first demonstration there have been many further ultrafast nonlinear studies in AlGaAs, these have included switching experiments in different device configurations (e.g. Asymmetric Mach-Zehnders[3] and X-junctions[4]), and planar AlGaAs waveguides have been shown to

support spatial solitons[5]. Theoretical studies have moved from these simple devices and are modelling more exotic structures[6] which have regions with different nonlinear coefficients. To date most of these structures have been impractical, due to the lack of a suitable material system, however, theory presented by D. C. Hutchings et al[7] has suggested that AlGaAs may be a excellent candidate for the realisation of such devices. The main reason for this being that the magnitude of $n_2$ is determined to be inversely proportional to $E_g^4$ (section 2.4.2.), and this relationship implies that if it was possible to exercise some control over a semiconductor's bandgap, it should also be possible to control $n_2$.

Such control over the bandgap can be achieved by using Multiple Quantum Well (MQW) structures and disordering techniques[8]. MQW structures can be disordered to induce a blue shift. Therefore, if it was possible to intermix a MQW structure in predefined areas, it should be possible to produce regions which have different nonlinear coefficients. This chapter therefore presents a new technique for the suppression of quantum well intermixing, which has been used to define areas which have different nonlinear coefficients.

## 5.1. Quantum Well Intermixing.

Disordering of GaAs/AlGaAs MQW structures has become an important method for producing various types of Optoelectronic Integrated Circuits[9](OEICs). A number of different techniques have been used to intermix GaAs based systems[10]. These include Impurity Induced Disordering[11] (IID), Neutral Impurity Induced Disordering[12] (NIID), and Photo-Absorption Induced Disordering[13] (PAID).

Disordering occurs through the interdiffusion of various elements of the semiconductor crystal matrix[14] and is reliant on the existence of native crystal defects, since it is through these that the matrix elements will move. Self-diffusion (intermixing) rates are determined by the defect concentration and their diffusion rate. The defect concentration is in turn controlled by the material temperature, the partial pressure of the matrix elements and the position of the Fermi level.

However, in a high purity semiconductor that is in thermal equilibrium at temperatures far below the melting point, where there are very few native defects, disordering rates are extremely small. Therefore, to achieve useful self-diffusion rates we must use some technique (e.g. varying the over-pressure[15] or increasing the defect count) to take the material out of the equilibrium state and hence, influence the disordering rate.

The band edge shifts produced by disordering can be characterised by various means[16]. However, photoluminescence characterisation provides a non-destructive testing method that also allows a rapid turn around of samples. Therefore, it is this method that is used to quantify the bandgap shifts in the following studies.

## 5.2. Impurity Free Vacancy Diffusion.

Impurity Free Vacancy Diffusion[17] (IFVD) makes use of dielectric caps and Rapid Thermal Annealing[18] (RTA), to induce intermixing through the diffusion of induced surface vacancies. This study is mainly concerned with observing the effects that $SiO_2$, $SrF_2$ or $Ga_2O_3$ dielectric caps have on this process in GaAs/AlGaAs based structures.

The first of these three dielectric caps is used to promote the intermixing of GaAs based quantum well structures through the preferential absorption of gallium atoms into a $SiO_2$ cap[19] at high temperatures (typically 900 °C). However, if any useful devices are to be fabricated through disordering, it must also be possible to suppress the disordering in specific areas. This is so the relative difference of the bandgaps in the disordered and undisordered regions can be used, and it is for this reason the study concentrates on the effects of the other two caps. The effects of the caps were characterised using low temperature photoluminescence (section 3.3.2.), which used the 514.5 nm line of an Argon ion laser to study the fundamental (*e-hh*) exiton transition and hence, infer any bandgap shifts.

### 5.2.1. Silica Cap Disordering.

It is well known that silica is permeable to gallium atoms at high temperatures[20]. This is the key mechanism underlying

IFVD, and by studying figure 5.1. the disordering process can be easily followed. A thin film of $SiO_2$ is deposited on top of the GaAs sample, this is then placed into a RTA reactor chamber face down on a piece of GaAs. This piece of GaAs provides protection for the sample surface and a relatively high As overpressure which reinforces the disordering effects of the group III vacancy. The sample is then quickly raised to high a temperature, whereupon the GaAs bonds begins to break and the gallium is absorbed in to the $SiO_2$ . This removal of gallium from the GaAs matrix produces group III vacancies at the surface of the GaAs. It is these vacancies that diffuse down into the MQW layer and instigate intermixing.

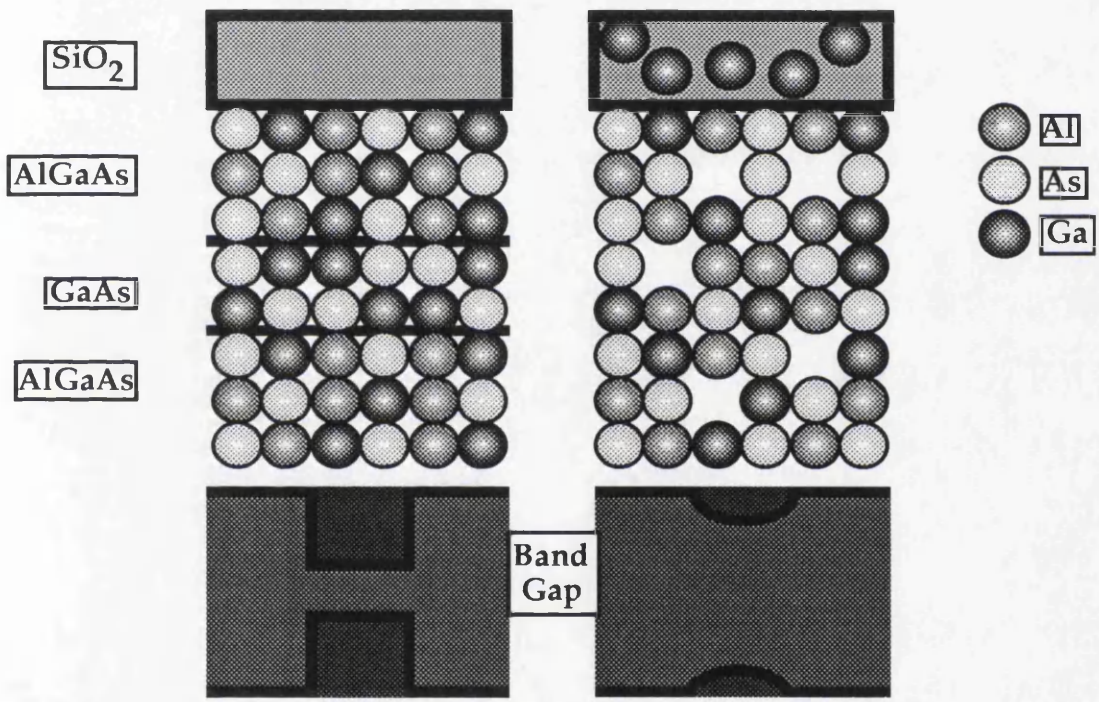


*Figure 5.1. Impurity free vacancy disordering.*

Initial work concentrated on producing shifts in MQW structures that were typically buried 0.8 μm below the surface of waveguide structures. As this technique had not been routinely performed previously on guides buried at these depths, a MQW waveguide wafer (A776, appendix A) was designed to be a single moded waveguide at the half bandgap of 1.55 μm. Thin films of $SiO_2$, typically 200 nm thick were deposited on the samples using Plasma Enhanced Chemical Vapour Deposition (PECVD). Initial studies of the disordering concentrated on

temperatures around 900 °C and time scales of approximately 1 minute.

Although it was initially expected that since the MQW possessed over 70 periods, there would be some degree of irregular disordering, this was not observed. From figure 5.2., we can see that although PL peak from the MQW experiences some broadening, the structure appears to move as a whole. This phenomena has been studied by Guido et al (reference 15), and as yet the effect has not been attributed to a definite mechanism.

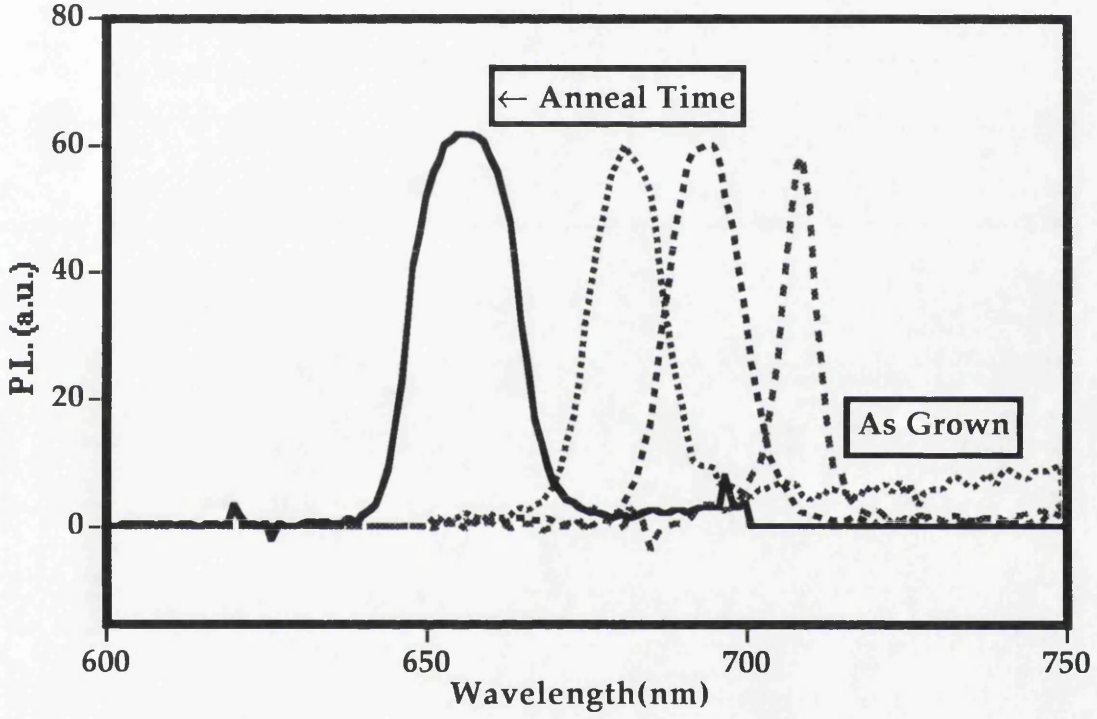


*Figure 5.2. Movement of disordered material photoluminescence spectra with increasing anneal time.*

As mentioned above the IFVD disordering of deeply buried MQW waveguide structures has not been routinely investigated, therefore, a preliminary study was carried out to calibrate the behaviour of these types of structures.

### 5.2.2. Temperature Effects.

The temperature stability of the MQW waveguide sample was investigated to determine the temperature levels at which the structure started to disorder. From previous studies it was expected that this would occur at approximately 900 °C and it

was there that the study was centred. The samples were all taken from a piece of wafer deposited with silica by PECVD and the time in the RTA was held constant at 90 seconds. Figure 5.3. shows the results of varying the annealing temperature.

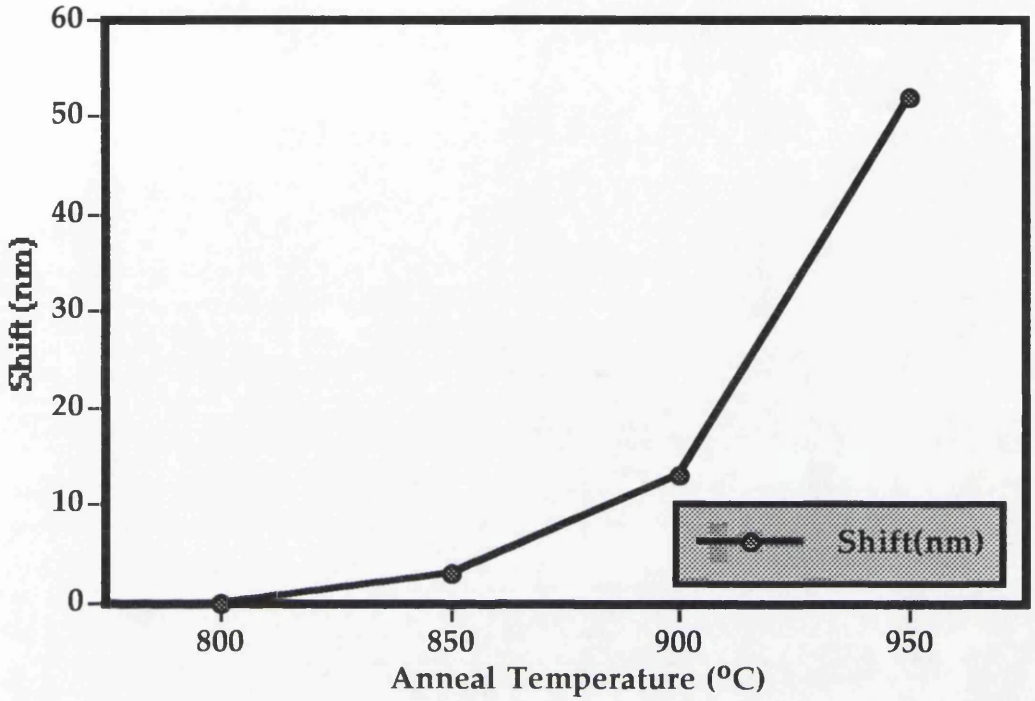


*Figure 5.3. Shift dependence on RTA temperature.*

As expected the sample begins to become thermally unstable around 850 °C and as we increase the temperature the PL shift becomes greater. However, these larger shifts are also accompanied by some amount of irreproducibility. For temperatures above 950 °C a small amount of surface damage was observed.

### 5.2.3. Time Effects.

The structures started to experience bandgap shift at around 850 °C, and although larger shifts could be attained at higher temperatures, these temperatures do not afford the control that operating slightly above the stability temperature does. Therefore 900 °C was chosen as the bench mark, since it gave a reasonable shift with no damage and good reproducibility.

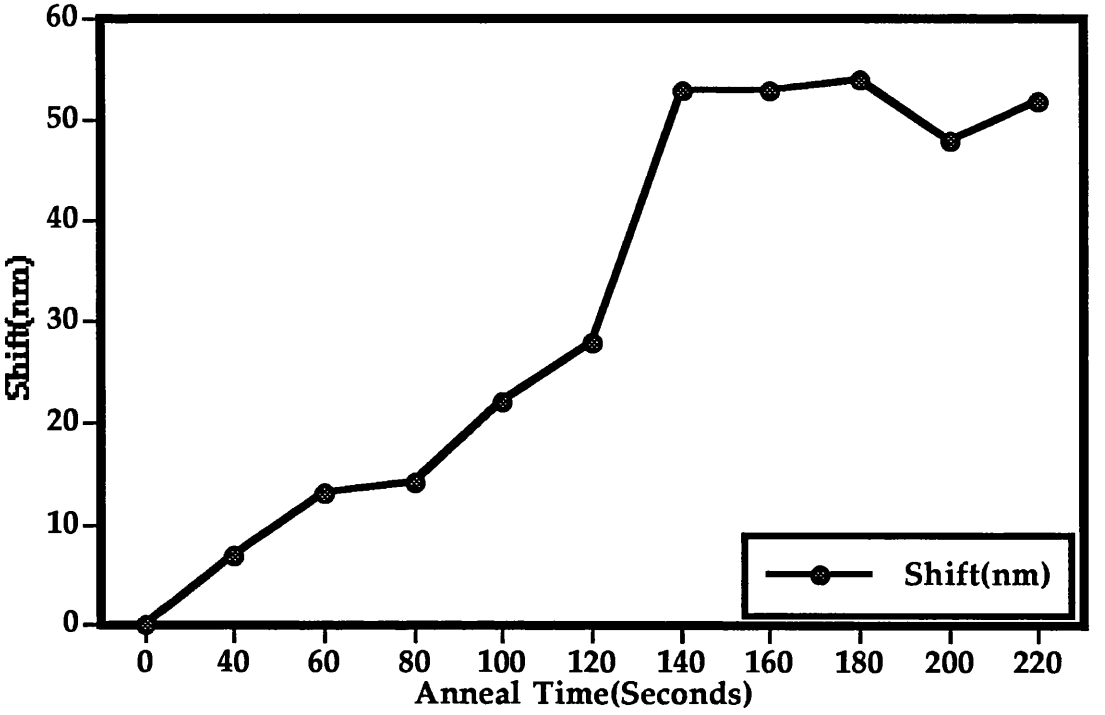


*Figure 5.4. Shift dependence on RTA time.*

What was apparent from this study was that although the structures disordered at the same temperature as typical laser structures[21], they needed longer times in the reactor to achieve the same bandgap shifts. Also there is an effective saturation of the band edge shift which is approximately 50 nm, which is beginning to approach the theoretically calculated band edge of the average composition material (67 nm shift). This anomaly is attributed to growth tolerances, and the fact that some of the crystal components are not very mobile at the annealing temperatures and total intermixing cannot be achieved.

### 5.2.4. Surface Stability.

In the previous section it was indicated that the silica cap disordering was reasonably reproducible, however, this is not strictly true. The surface of a GaAs wafer is not pure GaAs (section 5.4.) but a mixture of various gallium and arsenic containing compounds. Studies have concluded that this surface layer is not static with time[22] but changes, and progresses toward a surface covering of $Ga_2O_3$, which can be seen in equation 5.1.:

$$As_2O_3 + 2GaAs \Rightarrow 4As + Ga_2O_3 \qquad 5.1.$$

However, the surface will not become completely covered with $Ga_2O_3$, but it will reach some gallium rich equilibrium state after an extended period of the order of months. This can be seen in figure 5.5., which shows the atomic percentage composition of $Ga_2O_3$ (ADXPS data) in the first few monolayers (sine 1.0 ≈ 3 nm) of the sample surface, over the time period of 15 weeks.

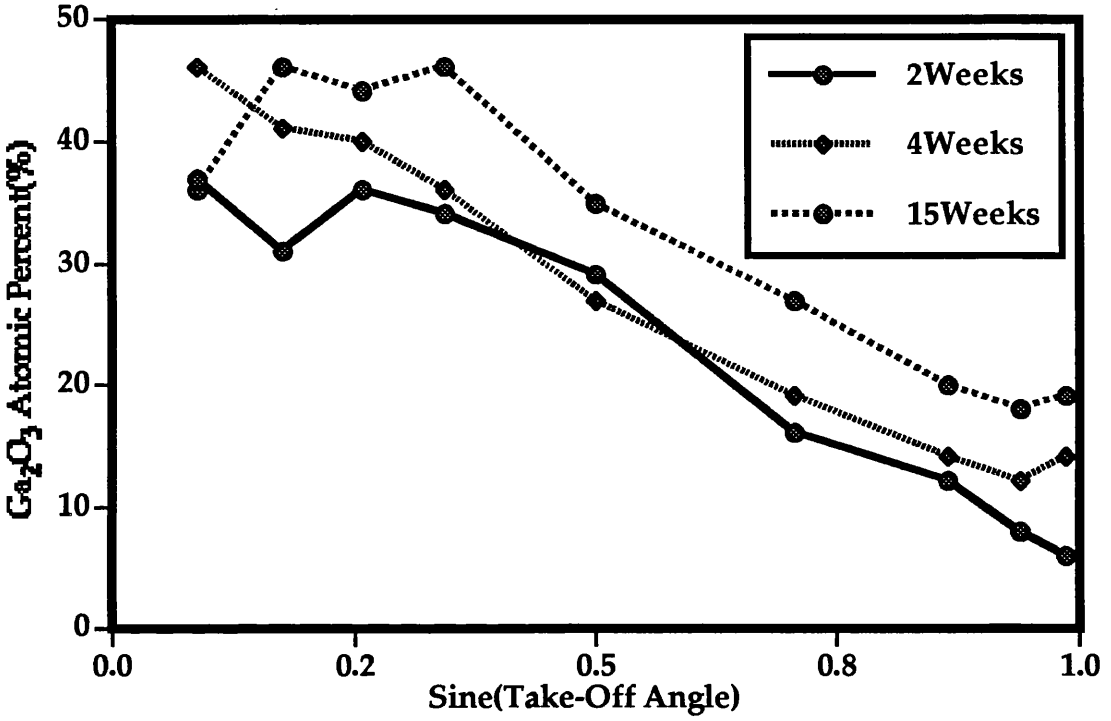


*Figure 5.5. Change of $Ga_2O_3$ atomic percentage composition at a GaAs surface, over an extended period of time. (Data from W.F. Stickel et al).*

In section 5.4., $Ga_2O_3$ will be shown to suppress intermixing, and therefore, it should be determined if this surface stability phenomenon, has any long term effects on the reliability of quantum well disordering. Hence, the shift attained from a sample taken every month from the wafer (A776) was examined, to determine if there was any detrimental intermixing performance. Each sample was cleaned, coated (200 nm PECVD $SiO_2$ ), and annealed (900 °C, 60 seconds) in the same way. The shift over these investigated months are shown in figure 5.6..

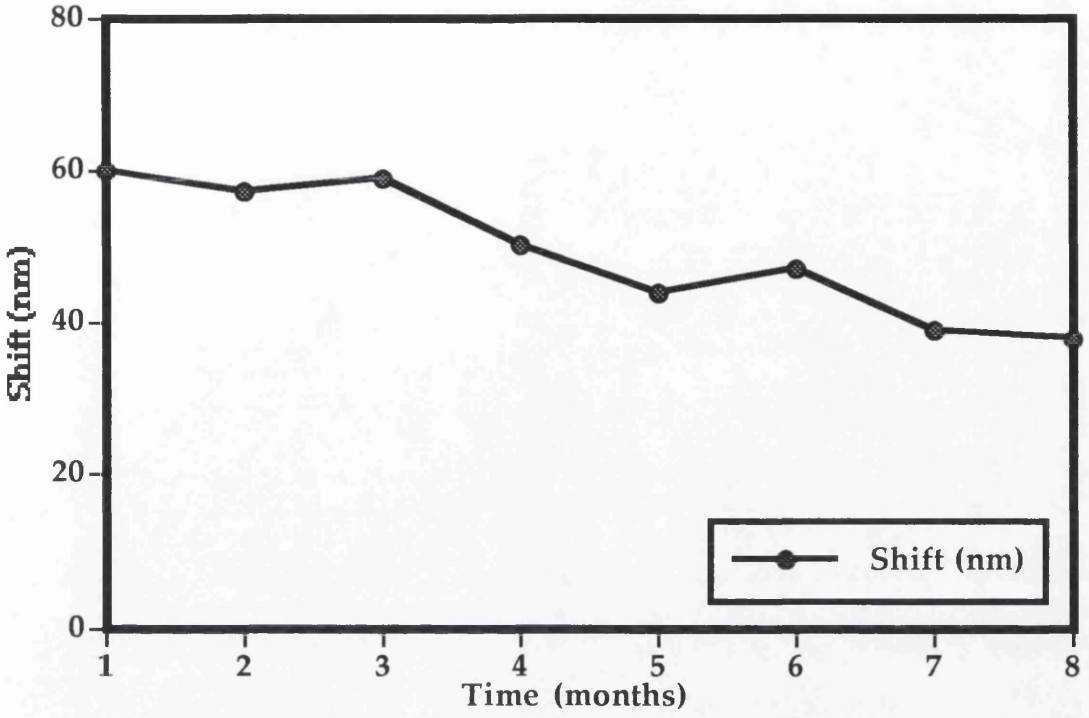


*Figure 5.6. Deterioration of shift over extended period of time.*

It is clear from figure 5.6. that there is a reduction in the PL shift from the wafer as time goes on. To be able to attribute this decrease in PL shift to the build up of $Ga_2O_3$ and not just a coincidence with other process parameters, another wafer (B415) was subsequently monitored, and it too has shown similar characteristics.

### 5.3. Strontium Fluoride Shift Suppression.

In section 5.2. it was mentioned that disordering would only be of use, if it was possible to selectively activate and suppress, the disordering in predefined areas. Using dielectric cap annealing this was first attempted using films of $Si_3N_4$[23] with limited success. This was due to the fact that it is difficult to produce high quality $Si_3N_4$ films, since they are usually $SiO_2$ rich due to the deposition methods available. $Si_3N_4$ also possess undesirable strain characteristics[24], which can be a major problem at high temperature due to the cap cracking and peeling.

Since the limitations of $Si_3N_4$ were realised a number of different caps have been proposed and studied. One which has been used with some success, and has produced devices such as extended

cavity[25] and bandgap tuned lasers is $SrF_2$[26]. Initially $SrF_2$ was found to be a highly successful method for suppressing the disordering of MQWs with differential shifts of over 40 nm (figure 5.7.).

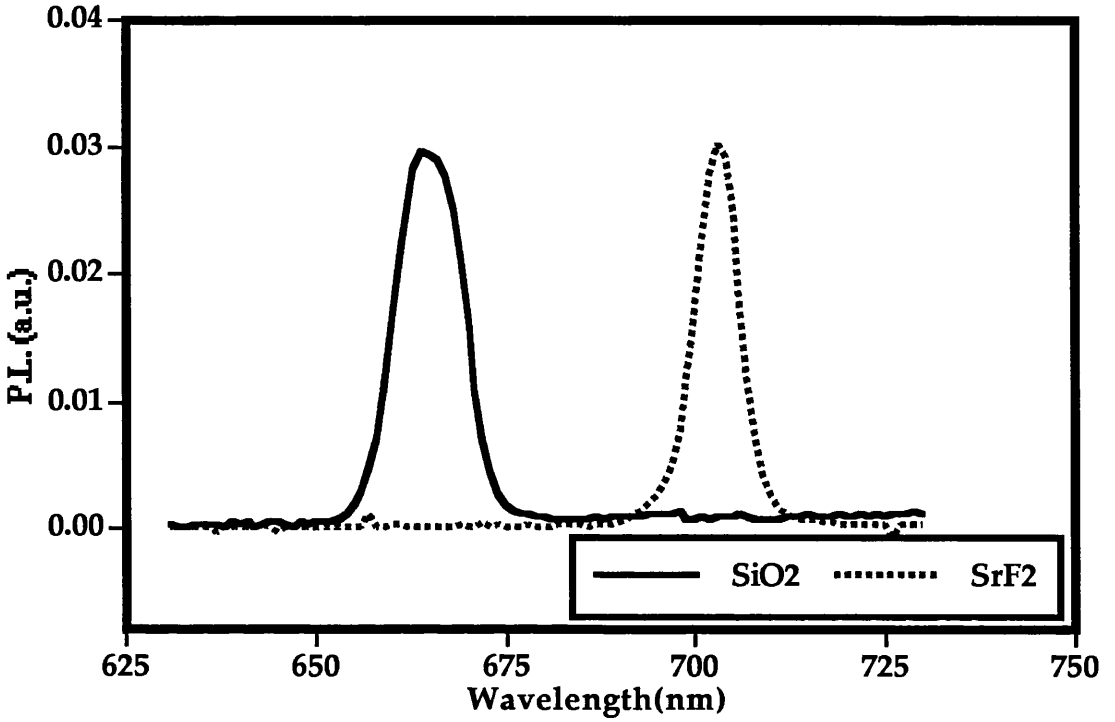


*Figure 5.7. Low temperature (77°K) relative bandgap shifts under $SrF_2$ and $SiO_2$.*

### 5.3.1. Strontium Fluoride Induced Damage.

One problem with the combined $SrF_2/SiO_2$ process is that it is accompanied by a small amount of localised damage (figure 5.8.). This damage can normally be tolerated when fabricating semiconductor lasers, since it leads to nothing more drastic than a reduction in yield. However for the fabrication of nonresonant nonlinear devices, the amount of damage that the process produces cannot be tolerated, since the waveguides are typically 1-2 orders of magnitude longer than semiconductor laser devices.

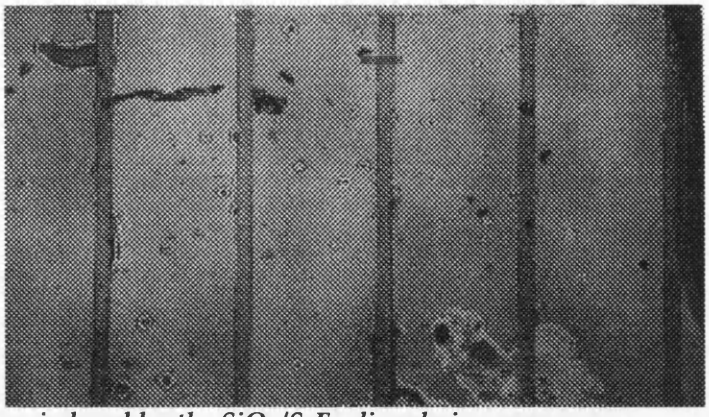

*Figure 5.8. Damage induced by the $SiO_2/SrF_2$ disordering process.*

The damage tends to appear in the form of either cracks along the boundary interfaces between the $SiO_2$ and $SrF_2$, or else "pits" in the sample surface where it has been coated with $SrF_2$. The damage in figure 5.8. is attributed to the mismatch of the linear thermal expansions[27] between GaAs, $SiO_2$ and $SrF_2$, and this mismatch is defined here as:

$$\Delta\alpha(\%) = \frac{\alpha_1 - \alpha_2}{\alpha_2} \times 100 \qquad 5.2.$$

Table 5.1. shows the values of the room temperature linear thermal expansion coefficients, and the effective mismatches

**Table 5.1.**

| Linear Thermal Expansion Constants ($\alpha$) and Percentage MisMatches ($\Delta\alpha$) at 293 °K. | | | |
|---|---|---|---|
| | **GaAs** | **$SiO_2$** | **$SrF_2$** |
| **$\alpha$ ($10^{-6}K^{-1}$)** | 5.7 | 10.3 | 18.4 |
| **GaAs MisMatch** | | 45 % | 70 % |
| **$SiO_2$ MisMatch** | 45 % | | 45 % |
| **$SrF_2$ MisMatch** | 70 % | 45 % | |

*Table 5.1. Linear thermal expansion coefficients, and thermal expansion mismatches of GaAs, $SiO_2$ and $SrF_2$ at room temperature .*

It is clear that the difference between the thermal expansion mismatches of GaAs and $SiO_2$, is the same as that of $SiO_2$ and $SrF_2$, and the biggest mismatch is between the GaAs and $SrF_2$. If

the surface pits are examined closely it is apparent that there is a small dot (figure 5.9.) in the middle of each.

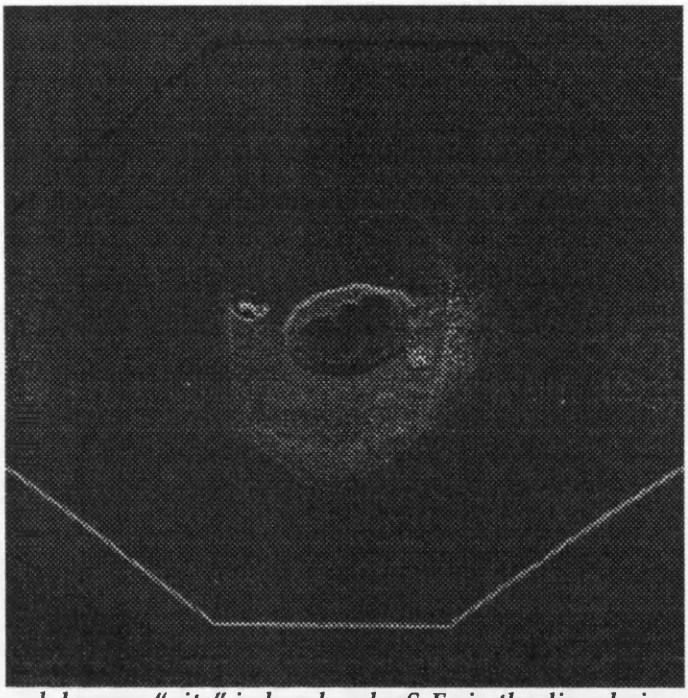

*Figure 5.9. Octagonal damage "pits" induced under $SrF_2$ in the disordering process.*

It is thought that these are extremely small particles (e.g. $SrF_2$ crystals) incorporated into the $SrF_2$ during the evaporation stage. These particles then expand rapidly upon RTA processing, and cause ruptures in the GaAs surface due to the large thermal expansion mismatch.

### 5.4. Hydrogen Plasma Shift Suppression.

For the reasons explained in the previous section, the $SrF_2$ suppression process is inappropriate for the fabrication of low loss waveguides. Therefore, another dielectric cap had to be found, that would provide a low damage alternative to $SrF_2$. It was proposed that this cap could be $Ga_2O_3$, which would be grown from a modification of the surface oxide states of GaAs by a hydrogen plasma.

The poor electronic properties of native-oxide containing GaAs surfaces, has spawned extensive studies on the analysis and modification of these surfaces. The initial surface state of GaAs is known to be a mixture[28] of $Ga_2O_3$, $As_2O_3$, $As_2O_5$, $Ga(OH)_4$, and $H_3AsO_3$. The main problem with the electronic properties is that

$As_2O_3$ is unstable in the presence of GaAs, and reacts to produce As and $Ga_2O_3$ through the solid state reaction of equation 5.1. This elemental As creates surface states that are near the mid bandgap and this effectively pins the Fermi level. From a disordering point of view this free As effectively means that matrix vacancies exist at the sample surface, and this is exactly what we wish to avoid when we want to suppress the disordering.

Many processes have been investigated that can modify the surface state and effectively passivate the surface. However, many of these studies have used wet processes that are hard to control and employ undesirable chemicals[29], they also produce surfaces that are not very stable after passivation[30]. Therefore, it was decided to use dry processing[31] which is able to overcome these problems.

It has been shown that by subjecting GaAs to a hydrogen plasma, the mixture of surface constituents can be forced to form a continuous covering of $Ga_2O_3$[32]. This would reduce the amount of vacancies at the surface and since $Ga_2O_3$ is stable at high temperatures it would be suitable for RTA processing. To visualise how this continuous coverage of $Ga_2O_3$ is achieved we can break the process down into 3 steps.

- **Removal of free As and $As_2O_3$.**
- **Water production.**
- **Formation of $Ga_2O_3$.**

If we first consider the effect that the hydrogen radicals (indicated by $H^\bullet$) have on the As and $As_2O_3$; from the following reaction equations:

$$As + 3H^\bullet \Rightarrow AsH_3 \qquad \textbf{5.3.}$$

$$As_2O_3 + 12H^\bullet \Rightarrow 3H_2O + 2AsH_3 \qquad \textbf{5.4.}$$

From equation 5.3., it is apparent that the As is removed as it reacts with the hydrogen radicals to form $AsH_3$. The As in $As_2O_3$ is also removed as $AsH_3$, and the oxygen also reacts with the hydrogen radicals to form water. Concerning the water production, the

previously mentioned mechanism is not the only source of water in the chamber. The reactor chamber is not ultra-high vacuum and posses a base pressure of around 1 mTorr, therefore, it is reasonable to expect that some residual atmospheric water vapour will exist in the chamber.

Finally if we consider this build up of water within the chamber, and its significance at the sample surface, we can expect the following reactions:

$$2GaAs + 6H_2O \Rightarrow Ga_2O_3 + As_2O_3 + 6H_2 \qquad 5.5.$$

$$2GaAs + 3H_2O \Rightarrow Ga_2O_3 + 2As + 3H_2 \qquad 5.6.$$

It should be quite clear through careful consideration of equations 5.3. through 5.6., that the As and $As_2O_3$ will be removed by the hydrogen radicals, and the resulting water will prompt the surface towards a continuous covering of $Ga_2O_3$. It is possible to combine all of these reactions, and describe the formation of $Ga_2O_3$ in the presence of a hydrogen plasma[33] by one solid state reaction:

$$As_2O_3 + 2GaAs + 12H^{\bullet} \Rightarrow Ga_2O_3 + 4AsH_3 \qquad 5.7.$$

However, as the plasma reactor (parallel plate) used in this thesis was different to those of the references (ECR, Downstream Microwave), the build up of $Ga_2O_3$ in the hydrogen plasma had to be confirmed.

### 5.4.1. XPS Analysis.

To confirm the build up of $Ga_2O_3$ at the surface, a sample from the wafer B415 was subjected to a hydrogen plasma (parameters typical of section 5.4.2.) and then analysed at Loughborough University using X-ray photo-electron spectroscopy (XPS) The results of this analysis can be seen in figure 5.10..

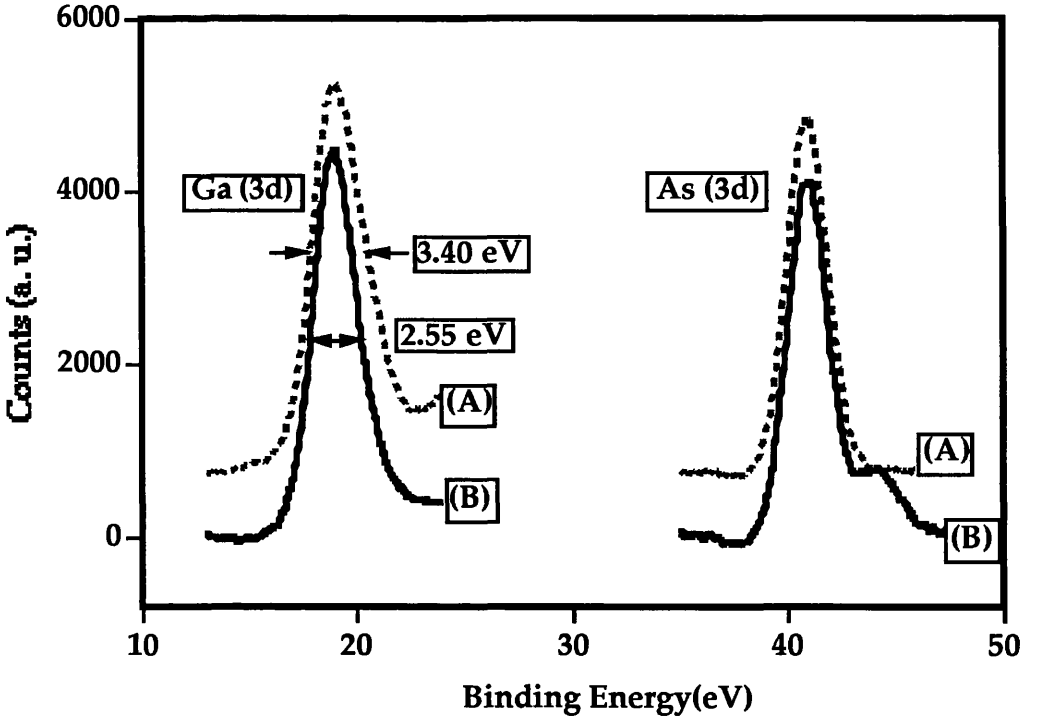


*Figure 5.10. XPS analysis of the Ga(3d) and As(3d) peaks of processed and unprocessed GaAs.*

By examining the Ga(3d) and As(3d) peaks for the plasma processed (A) and the unprocessed (B) samples. The high energy shoulder of the As(3d) peak of sample B is associated with an arsenic oxide and its absence from sample A indicates the removal of the arsenic oxide during the plasma treatment. The gallium associated with the Ga(3d) peak oxidisation state is not as clear, since it is only shifted by $\approx 1$ eV and is only noticeable by an increase in the width of the peak accompanied by a slight asymmetry towards the higher binding energies[34], but, this increase is observed in the FWHM of the Ga(3d) peak. Since we have now confirmed the build up of $Ga_2O_3$ in a parallel plate reactor's hydrogen plasma, we shall use PL data as an indication to how effectively the oxide has formed.

### 5.4.2. Plasma Power Effects.

As the r. f. power to the reactor is raised, there is a subsequent increase in the disassociation efficiency of the plasma, and therefore, the amount of radicals present within the plasma increases. Consequently this should lead to an increase in the rate of which the $Ga_2O_3$ forms. Therefore, to look at how the

rate changes with plasma power, the power applied to the reactor electrodes was varied and the following parameters were held constant:

- **Gas overpressure:** → **900 mTorr.**
- **Gas flow rate:** → **20 sccm.**
- **Table temperature:** → **40 °C.**
- **Plasma exposure time:** → **15 minutes.**

From the PL data of figure 5.11. it could be inferred that the $Ga_2O_3$ formation rate is almost linear as it is exposed to denser plasmas.

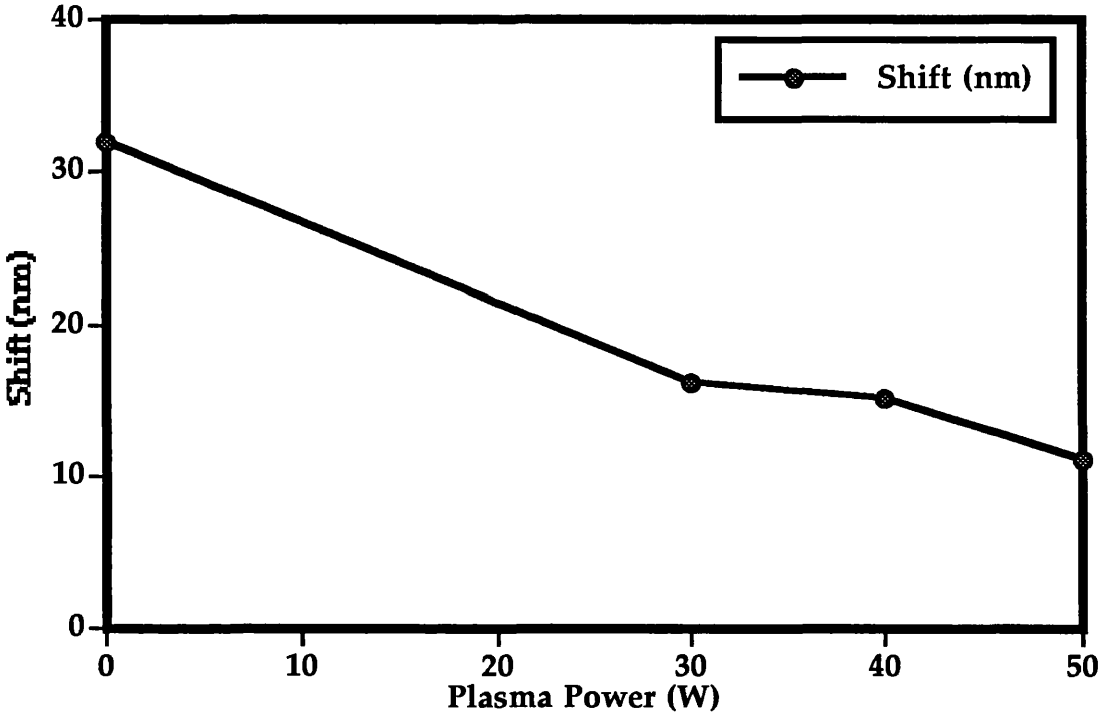


*Figure 5.11. Shift suppression as a function of r. f. power applied to the hydrogen plasma.*

However, this is not the full story since increasing the plasma power also increases the D. C. bias seen by the plasma, and hence, any sputtering effects that may be slowing down the formation of $Ga_2O_3$ will become more pronounced. We cannot consider sputtering effects alone, since, as the surface coverage of $Ga_2O_3$ increases the formation rate should slow down.

### 5.4.3. Plasma Time Effects.

As indicated it is thought that the relationship between the time in the plasma and the growth rate of the $Ga_2O_3$ is not a clear one, but it contains many interdependencies. Therefore, to look at how the rate changes with plasma exposure time, the time the sample was exposed to the plasma was varied and the following parameters were held constant:

- **Gas overpressure:** → **900 mTorr.**
- **Gas flow rate:** → **20 sccm.**
- **Table temperature:** → **40 °C.**
- **Plasma power:** → **50 Watts.**

From the PL data of figure 5.12., it could be inferred that the $Ga_2O_3$ formation rate slows down, as the sample is exposed to the plasma for longer time periods.

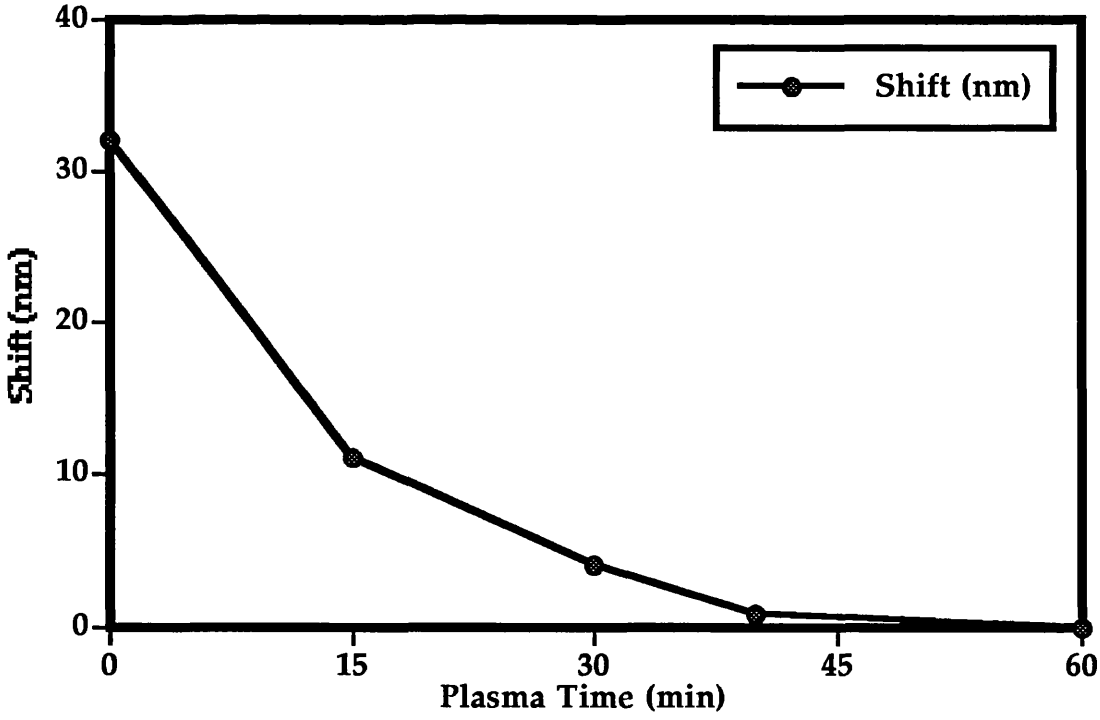


*Figure 5.12. Shift suppression as a function of exposure time to hydrogen plasma.*

From figure 5.12. it is very obvious that the formation of $Ga_2O_3$ is not linear, this is as expected and most probably due to $As_2O_3$ being continually cleaned from the sample and the oxygen

being used in the formation of $Ga_2O_3$. Therefore, as time passes there is less and less oxygen (i.e. less $As_2O_3$) available for the hydrogen radicals to react with and produce water (equation 5.4.), and as the production of water slows so will the rate of $Ga_2O_3$ formation.

### 5.4.4. Combined Samples.

Samples with combined areas of $SiO_2$ and bare GaAs were prepared, to investigate the effect of the plasma on the surface under the $SiO_2$. To fabricate the sample it was required to deposit $SiO_2$ (e-beam evaporated) all over the surface, and then use conventional photolithography techniques to impose the required pattern on to the surface. The removal of $SiO_2$ from areas where it was not required, was performed by buffered hydrofluoric acid (4:1), followed by an RO water rinse. Figure 5.13. shows the PL positions after annealing.

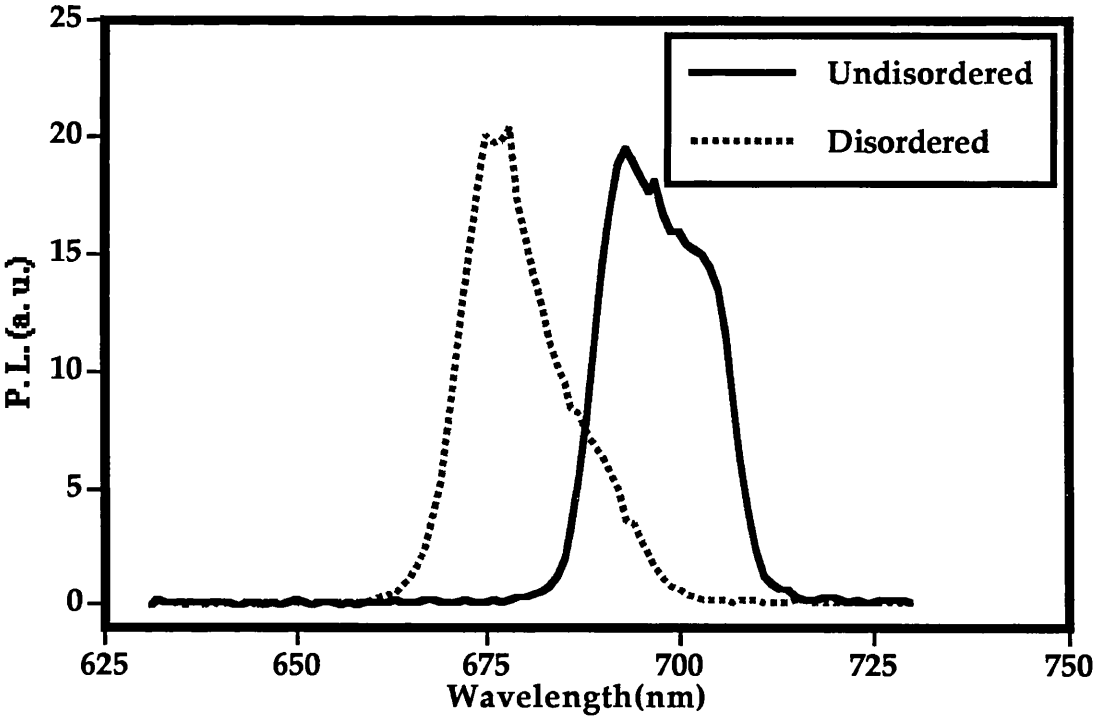


*Figure 5.13. Disordered and undisordered shifts on a combined sample.*

After annealing it was discovered that the bare GaAs surface behaved nearly as expected. The suppression, however, was not as complete as in previous experiments with material that had been subjected to similar plasma parameters, but had not received any pre-processing. This reduction in suppression was

attributed to effects that the extra processing steps would have on the sample surface. Hydrofluoric acid also attacks $Ga_2O_3$ and will therefore generate more vacancies, and these vacancies have indeed been shown to promote disordering[35].

The area under the $SiO_2$ did not behave at all as expected. It was found that even though the $SiO_2$ was covering the area to be disordered, it did not promote the disordering to the degree as was the case with samples not subjected to the plasma. The reasons for this are still not perfectly clear although it is thought that since hydrogen atoms are extremely small, they are being driven through the $SiO_2$ matrix by the plasma D. C. self bias, and passivating the surface to some extent. This is confirmed to some extent in section 5.4.5., in which the experiment reduces the effects of the plasma dark space.

### 5.4.5. Dark Space Effects.

To explore the effect that the plasma dark space has on the formation of $Ga_2O_3$ and subsequently limiting the disordering under the $SiO_2$, some samples were fabricated that were half coated with $SiO_2$ and half bare GaAs. The samples were raised into the plasma on top of a 1 inch glass dish, this effectively raised them out of the dark space and should lower any damage due to ion bombardment. Therefore, to look at how these factors changed plasma density, the power in the plasma was varied and the following parameters were held constant:

- **Gas overpressure:** → **900 mTorr.**
- **Gas flow rate:** → **20 sccm.**
- **Table temperature:** → **40 °C.**
- **Plasma exposure time:** → **20 minutes.**
- **Sample height:** → **25 mm.**

From figure 5.14. we can see that the shift under the silica half of the sample remains reasonably constant, as the plasma power is increased.

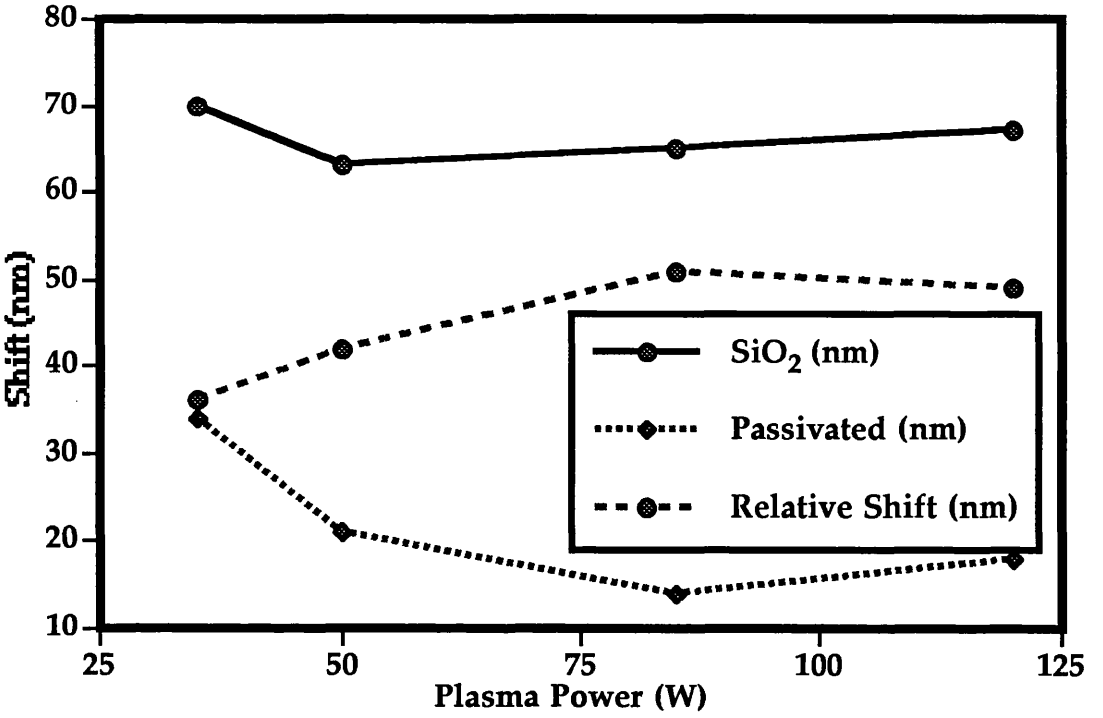


*Figure 5.14. Disordered and undisordered shifts on a combined sample.*

Under the bare GaAs part of the sample there is a definite nonlinear dependence on the plasma density, as was expected from section 5.4.2.. This indicates that there was some ion damage effects from the plasma dark space, which limits the formation rate of $Ga_2O_3$. From figure 5.14. it is also apparent that it is possible to achieve relative shifts of around 50 nm.

### 5.4.6. Insitu Monitoring.

The growth of $Ga_2O_3$ on the surface of GaAs samples has been monitored insitu so that the growth dynamics could be studied in greater detail. These studies have centred around PL. measurements which tend to increase as recombination states at the sample surface are eliminated. During the course of these studies reflectometry was used with some effect to monitor changes at the sample surface. Figure 5.15. shows the typical time dependent reflection from the sample.

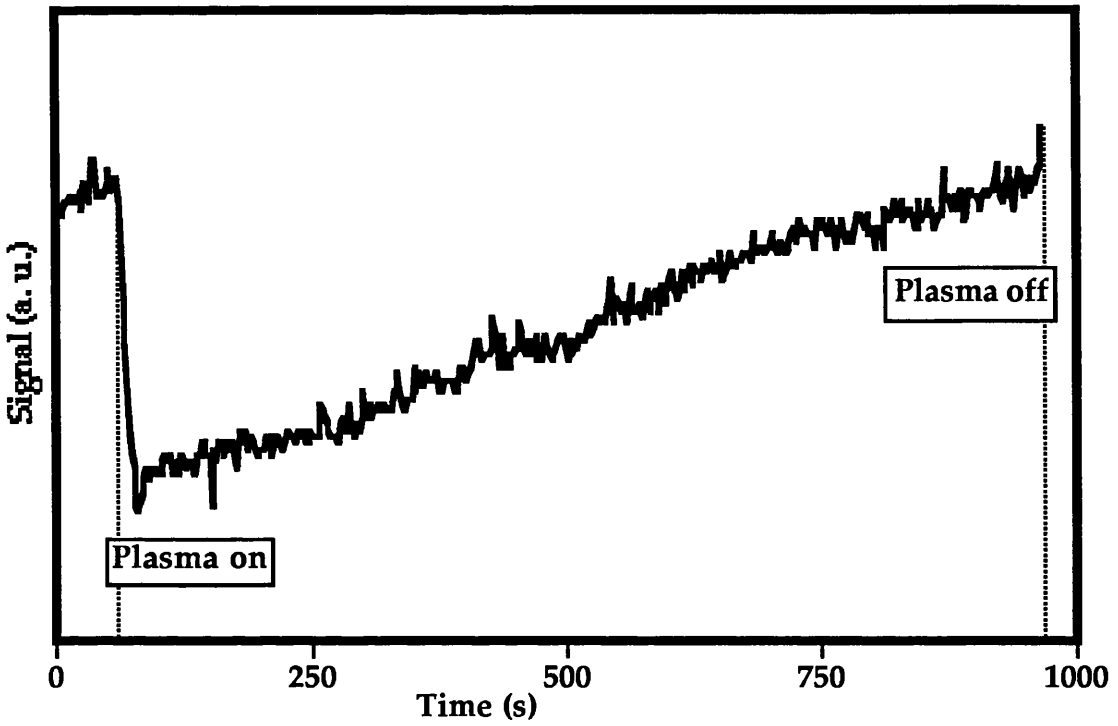


*Figure 5.15. Reflectometry data taken from a GaAs sample subjected to a hydrogen plasma.*

The reason for the shape of the reflectometry data is unclear, however, it is thought that the dip at the start is due to free As being rapidly cleaned from the surface. The slow rise in the signal is then thought to be due to the gradual build up of $Ga_2O_3$.

## 5.5. Fabrication of Waveguides With Selective Nonlinearites.

The main purpose of this investigation is to determine if it is possible to fabricate areas with different Kerr type nonlinearities. It was therefore proposed to make a sample which had two sets of similar waveguides which were formed in either disordered or undisordered regions of the a sample (figure 5.16.). These two sets of waveguides would then possess different bandgaps and hence according to the theory of Hutchings et al (section 2.4.2.) different nonlinear coefficients.

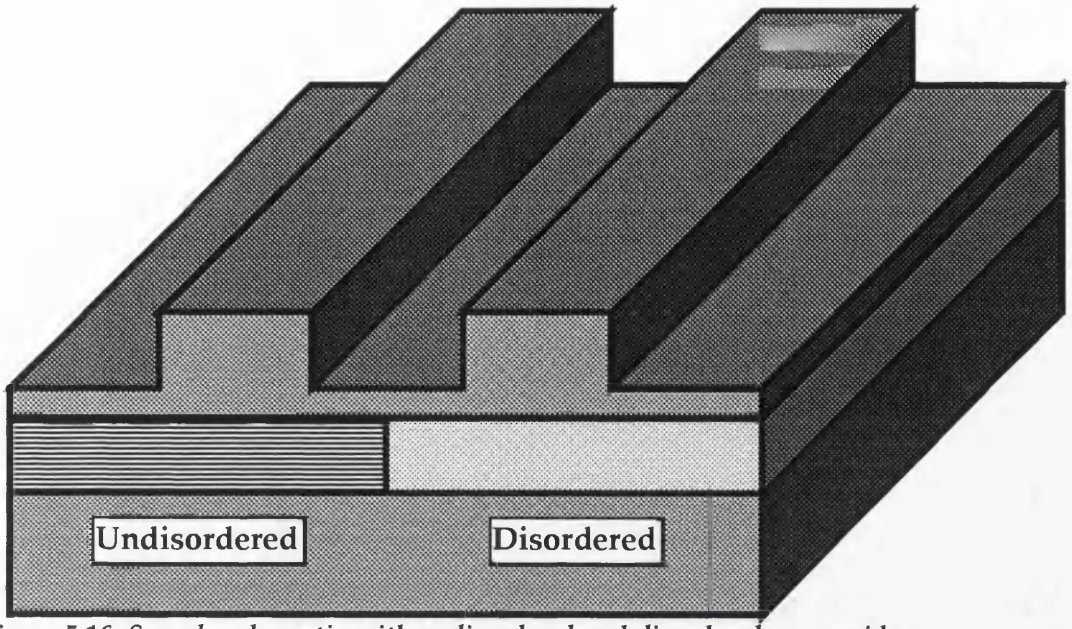


*Figure 5.16. Sample schematic with undisordered and disordered waveguides.*

Initially a 200 nm cap of $SiO_2$ was deposited across the whole sample using E-beam evaporation. Standard photolithography and wet etching with buffered HF was used to remove half of the $SiO_2$.

- **Gas overpressure:** → **400 mTorr.**
- **Gas flow rate:** → **20 sccm.**
- **Table temperature:** → **40 °C.**
- **Plasma power:** → **30 Watts.**

The sample was then thermally processed in a rapid thermal annealer. It was placed face down on a piece of fresh GaAs and was heated within 10 s to a temperature of 900 °C and held there for 60 seconds. During processing the RTA chamber was evacuated and purged with $N_2$ to prevent contamination. The PL from each side of the sample was subsequently examined and is shown in figure 5.17..

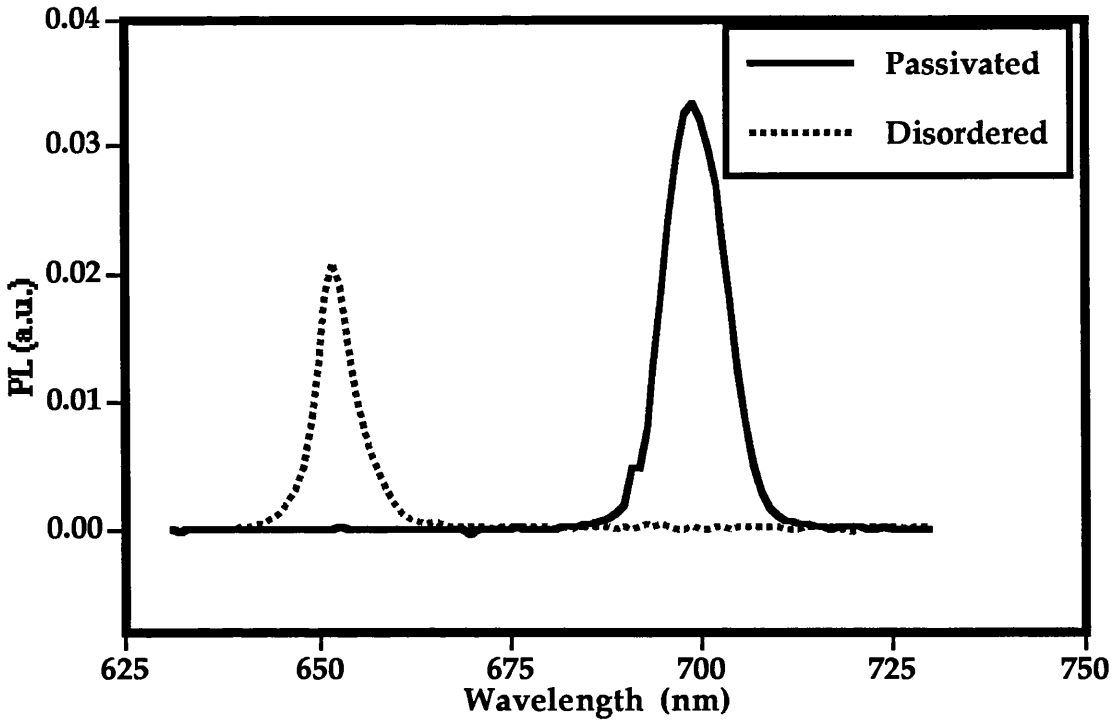


*Figure 5.17. PL from the disordered and undisordered sides of the sample.*

It is apparent that there is a differential shift of over 40 nm and this should provide a reasonable change in the nonlinearity between each side of the sample. After PL characterisation the remaining $SiO_2$ was removed and waveguides fabricated on the sample using conventional photolithography and dry-etching techniques.

### 5.5.1. Linear Loss Characterisation.

To characterise how the optical quality of the semiconductor is affected by intermixing processes the propagation losses of the various optical waveguides were measured by the Fabry-Pérot technique (section 3.3.1) using a 1.556 μm DFB InGaAsP laser (line-width < 10 MHz) end-fire coupled into the waveguides.

Loss measurements were initially conducted in rib loaded guides, that were manufactured in as-grown material (no high temperature annealing or hydrogen plasma processing) by standard fabrication processes (section 3.2.). Even though the MQW material intrinsically contained many scattering interfaces, the optical quality was found to be of an extremely high standard and indeed the total guide losses were found to

be lower than 1 $dBcm^{-1}$ (0.94 $dBcm^{-1}$, sample length 6.96 mm, guide width 4 μm).

The losses of similar waveguides fabricated from high temperature processed material, were then characterised. The thermal processed guides were cleaved to a length of 7.82 mm and the losses characterised in the 4 μm wide guides. It was found that the undisordered material had a loss of 2.9 $dBcm^{-1}$, while those fabricated in the disordered section had a loss of 6 dB $cm^{-1}$.

It is quite apparent that the losses have increased in both sets of waveguides, especially those of the disordered guides. Figure 5.18. clearly shows that both sides of the sample do not possess the usual "mirror" finish to the surface after dry-etching, but there clearly is a significant amount of grass. The increase of loss in the sample is attributed to various mechanisms (section 3.3.), however, increased scattering losses from all the concerned surfaces is thought to be the major reason. For the disordered guides it is quite apparent that they have considerably more grass than the undisordered side (figure 5.18.).

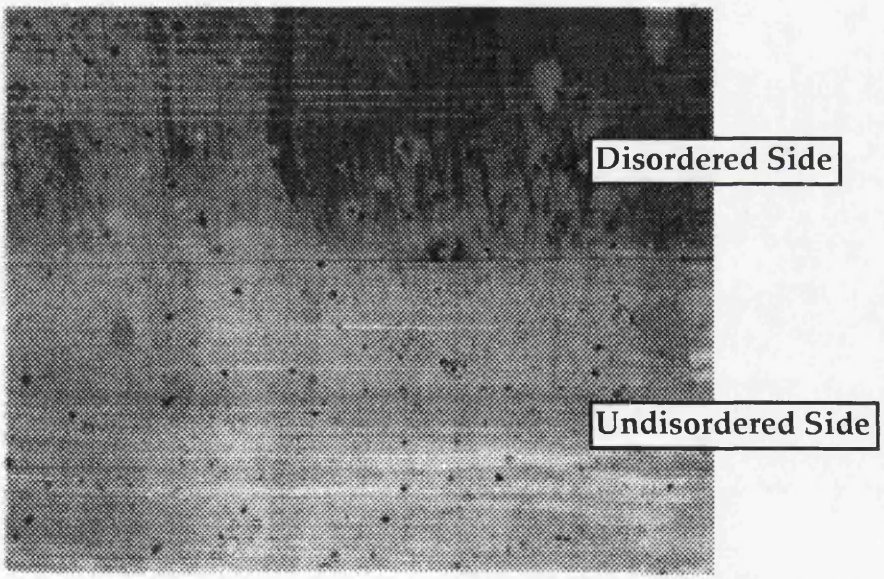


*Figure 5.18. Waveguides fabricated on the disordered and undisordered sides of the sample.*

This could be due to a number of factors which include, the build up of free gallium at the surface in the annealing stage, which is not removed by the buffered HF. Indeed not all of the

$SiO_2$ may not be removed by the HF and it could be causing problems, or it may have reacted with the GaAs, or free gallium to make a hard to etch compound. Also, because the gallium atoms are removed from the surface of the semiconductor, there is most probably some microscopic damage here and it is quite possible that is where the problems occur with the dry etching. Finally, by intermixing we introduce vacancies and defects into the guiding region, and here they will act as scattering centres and add to the guides losses.

### 5.5.2. Measurement of Nonlinearity.

Nonlinear self-phase modulation (SPM) measurements (section 3.5.1.) were performed using a synchronously mode-locked NaCl:$OH^-$ colour centre laser producing ≈ 10 ps pulses at 82.6 MHz. This pulse length was chosen to ensure that the effects of GVD could be neglected, since the dispersion length of the pulse was appreciably longer than the sample. The waveguides were excited by end-fire coupling using a 40 x microscope objective at the input and a 25 x objective at the output, the output spectra were recorded using a scanning Fabry-Pérot interferometer.When the propagation distance is much shorter than the dispersion length the pulse propagation can be described by:

$$\frac{\partial U}{\partial z} = \frac{i}{L_{NL}} e^{-(\alpha z)} |U|^2 U \qquad 5.8.$$

Where $L_{NL}$ is the nonlinear length which is defined as:

$$L_{NL} = \frac{1}{\gamma P_o} \qquad 5.9.$$

Where $\gamma$ is a nonlinearity parameter for the waveguide, and is defined as:

$$\gamma = \frac{n_2 \omega_o}{c A_{eff}} \qquad 5.10.$$

Where $A_{eff}$ is the effective guide area. Equation 5.8. can easily be solved, and yields:

$$U(z,T) = U(0,T)e^{-[i\phi_{NL}(z,T)]} \qquad 5.11.$$

U(0,T) is the initial field amplitude at z=0, and the nonlinear phase shift can be described by:

$$\phi_{NL}(z,T) = |U(0,T)|^2\left(\frac{z_{eff}}{L_{NL}}\right) \qquad 5.12.$$

Where the linear loss can be accounted for through the use of an effective propagation length:

$$z_{eff} = \frac{\left[1-e^{-(\alpha z)}\right]}{\alpha} \qquad 5.13.$$

From equation 5.11 it is obvious that the induced phase shift increases with the propagation length, although the pulse shape remains unchanged. The maximium phase change occurs at the center of the pulse and it can by quantified by:

$$\phi_{max} = \frac{z_{eff}}{L_{NL}} = \gamma P_o z_{eff} \qquad 5.14.$$

It is now evident that by using equations 5.11. and 5.12. it is possible to quantify the nonlinear coefficent, by using a known phase modulation (section 3.5.1.).

The nonlinear coefficients were measured by recording the power levels required to produce a $\frac{3\pi}{2}$ phase shift in the SPM spectra in both the disordered and undisordered regions of the sample. Figure 5.19. shows the input spectrum and output spectrum for the equivalent $Pz_{eff}$ in both the disordered and undisordered guides

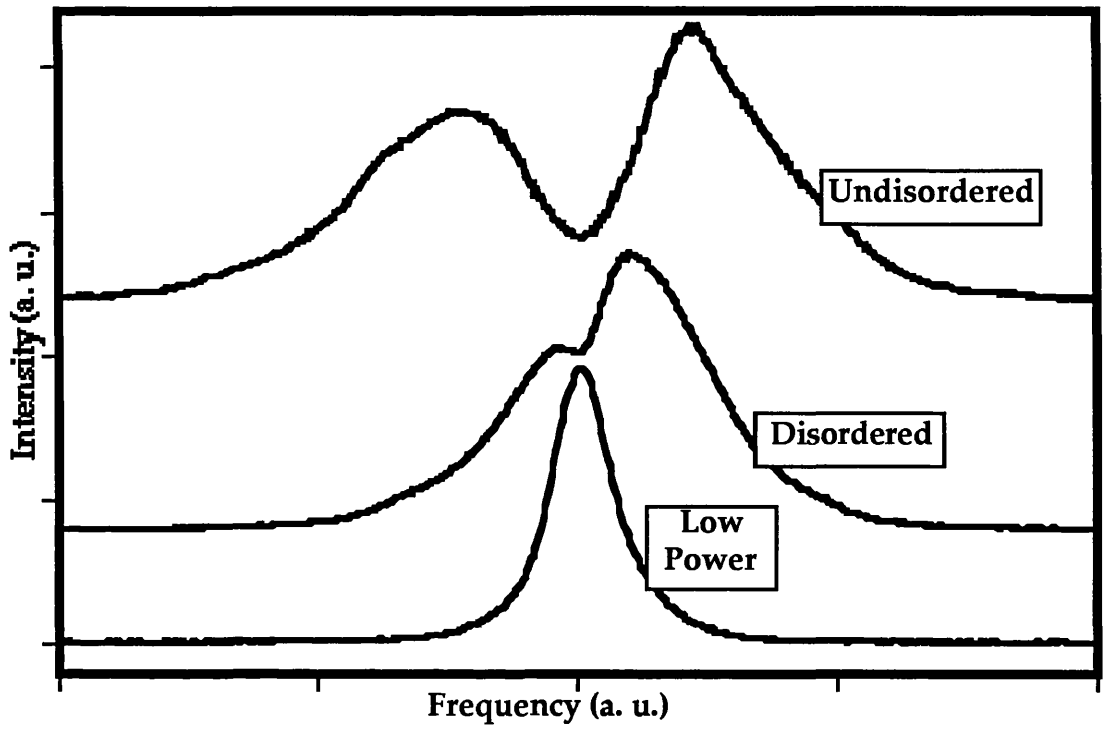


*Figure 5.19. Typical SPM data from the undisordered sample.*

The transmitted power levels were recorded, rather than the input power levels, thereby eliminating any differences in coupling efficiencies and allowing account to be taken of the different linear losses.

The nonlinearity coefficient was measured at a number of wavelengths and Table 5.2. shows the measured $\Delta n_2$ for both the TE and TM polarised modes, where the change in the nonlinearity is defined as:

$$\Delta n_2 = \frac{n_2^{Undis} - n_2^{Dis}}{n_2^{Undis}} \qquad 5.15.$$

The actual values for $n_2$ measured at 1.55 μm in the undisordered material were, $2.6 \times 10^{-13}$ $cm^2W^{-1}$ for the TE and $3.3 \times 10^{-13}$ $cm^2W^{-1}$ for the TM modes, which agree favourably with previous results obtained for GaAs/AlGaAs MQW structures[36]. The change in the nonlinearity coefficient is also observed to be consistent with theory, going from ≈ 30 % to in excess of 60 % as the band edge is approached. It should also be noted that the change in the nonlinearity is not due to either the change in waveguide loss, which has been factored into the

calculations. Or indeed the change in the optical confinement due to any variation in the linear refractive index after disordering. The reason for this being that the waveguides were excited far from the band edge of the semiconductor, and operating in this region it has been reported that the refractive index is just the average composition of the material[37], (section 2.3.2.) which is effectively the same before and after the disordering.

Table 5.2.

| | Nonlinearity Change ($\Delta n_2$) | |
|---|---|---|
| $\lambda(\mu m)$ | TE (%) | TM (%) |
| **1.51** | 64 | 62 |
| **1.53** | 58 | 51 |
| **1.55** | 32 | 33 |

*Table 5.3. The measured change in nonlinearity for both the TE and TM polarised modes, at wavelengths below half bandgap.*

## 5.6. Further Work.

As this IFVD suppression process has only just been shown to be effective it still has many avenues to be investigated and these may lead to a more efficient and effective process. Since it has been shown that it is possible to produce areas of differing nonlinearities on one sample, it may be possible to fabricate novel devices that have at present only been theoretically predicted. Therefore, in the following sections possible areas of process improvement are outlined along with some possible devices.

### 5.6.1. Process Improvement.

The two main areas that can be improved within the process are the reduction of the optical losses, and the enhancement of the relative shift of the bandedge of the sample. The enhancement of the bandedge shift may be obtained in two ways:

- **Increase the amount by which the MQW can be disordered.**
- **Increase the suppression obtained from the plasma.**

The first point may be tackled by either designing a greater degree of disordering into the MQW by increasing the amount of aluminium in the barriers or indeed increasing the barrier thickness. However, it is not thought that this approach will lead to any great enhancement, since it will also lead to a reduction of the number of quantum wells within the MQW. A second and possibly more desirable approach is to increase the initial degree of disordering available by removing any $Ga_2O_3$ at the sample surface. This could be achieved by various techniques such as removal by RO water[38], or ElectroCycoltron Resonance (ECR) hydrogen plasmas operated at elevated temperatures[39].

To increase the amount of suppression from the plasma the number of radicals in the plasma should be raised, while the effects of ion bombardment should be minimised. This could be achieved in a number of ways such as continuing work on the effects of the dark space in the RIE machines. It may also be beneficial to use a machine with different fundamental characteristics. These could include ECR machines which can generate extremely energetic plasmas, and provide a totally independent bias across the sample, and also afford some degree of temperature control. Also some Plasma Enhanced Chemical Vapour Deposition (PECVD) machines possess the facility to generate high pressure plasmas which posses no inherent D. C. bias, and therefore they may also be of use.

These two machines may also help to lower optical losses, since they both should be able to significantly reduce the effect of ion damage at the surface of samples. The effects of reducing this damage should be apparent when samples are dry etched, because the production of grass should be significantly inhibited since there is no initial sample damage.

Another possibility to enhance the suppression due to the plasma, is to expose the sample to air for some period of time after stripping away unwanted silica when patterning the sample. This should increase the quantity of native oxides available for conversion to $Ga_2O_3$ at the sample surface.

### 5.6.2. Devices.

The fabrication of selective nonlinearities opens up the possibility for many new nonlinear devices. Among these devices there is an opportunity to exploit spatial solitons (section 1.3.2.) for the fabrication of nonlinear scanning switches, using nonlinear interfaces. Soliton couplers which make use of the emission of spatial solitons into nonlinear overlayers, to produce switches with high switching ratio threshold switches are also a possibility.

Other types of devices could be based on more conventional Mach-Zehnder interferometer type switches[40]. In this device each arm of the interferometer has a different nonlinearity, and therefore a high power incident pulse will produce a different phase change in each arm. The phase shift will control how light in the two arms recombines, and it is possible to obtain either constructive or destructive interference at the recombination junctions, and thus produce an optical switch. This device could also be used to calculate the relative difference in the $n_2$'s of the device arms.

## 5.7. Conclusions.

In conclusion, a new and novel technique for suppressing the intermixing of GaAs/AlGaAs MQWs has been demonstrated. The technique relies on a hydrogen plasma discharge to produce a $Ga_2O_3$ layer from native oxides on the GaAs surface and suppress vacancy formation. This method for suppressing intermixing has many advantages over similar techniques using Strontium Fluoride, because:

- **It is free from damage.**
- **Highly reproducible.**
- **Can be made area selective using a patterned silica mask.**
- **Does not introduce impurities.**

- **Can be used to fabricate relatively long, low loss GaAs/AlGaAs MQW waveguides.**

This technique was subsequently used to produce samples with approximately 40 nm shift in the band edge, which lead to a corresponding change in the nonresonant optical nonlinearity of in excess of 60 %. This potentially opens the way for the production of many novel nonlinear optics devices which previously had no possible fabrication means.

# References.


1 J. S. Aitchison, A. H Kean, C. N. Ironside, A. Villeneuve and G. I. Stegeman. "Ultrafast all-optical switching in $Al_{0.18}Ga_{0.82}As$ directional coupler in the 1.55 μm spectral region." Electron. Lett. **27**, (1991), pp. 1709.

2 D. C. Hutchings. "Ultra-fast switching in semiconductor waveguides", European summer school on photonics, Copenhagen, Sept. 1994.

3 K. Al-Hemyari, J. S. Aitchison, C. N. Ironside, G. T. Kennedy, R. S. Grant and W. Sibbett. "Ultrafast all-optical switching in GaAlAs integrated interferometer in 1.55μm spectral region." Electron. Lett. **28** (12) June 1992.

4 S. Aitchison, A. Villeneuve, and G. I. Stegeman, "Ultrafast all-optical switching in an AlGaAs X-junction.", Post-deadline paper PD09, Technical Digest of Integrated Photonics Research, New Orleans, April, (1992), pp. 29.

5 J. S. Aitchison, K. Al-Hemyari, R. S. Grant and W. Sibbett. "Observation of spatial solitons in AlGaAs waveguides.", Electron. Lett. **28** (20) 1992, pp. 1879.

6 D. R. Heatly, E. M. Wright and G. I. Stegeman, "Soliton coupler.", Appl. Phys. Lett. **53** (3), 18 July 1988.

7 D. C. Hutchings and B. S. Wherrett, "Theory of the dispersion of ultrafast nonlinear refraction in zinc-blende semiconductors below the band edge.", Phys. Rev. **B.**, 50, 4622, 1994.

8 P. Li Kam Wa. "Intermixing of multiple quantum wells for all-optical integrated circuits.", Optical and Quantum Electronics. **23.** (1991) S925-S939.

9 J. H. Marsh, S. I. Hansen, A. C. Bryce and R. M. De La Rue. "Applications of neutral impurity disordering in fabricating low-loss optical waveguides and integrated waveguide devices.", Opt. Quan. & Elec. **23** (1991) S941-957.

10 J. H. Marsh. "Quantum well intermixing.", Semiconductor Sci. Technol. **8** (1993) pp. 1136-1155.

11 W. D. Laidig, N. Holonyak, Jr., M. D. Camras, K. Hess, J. J. Coleman and P. D. Dapkus, Appl. Phys. Lett. **38** , 1988, pp. 776.

12 M. O'Neill, A. C. Bryce, J. H. Marsh, R. M. De La Rue, J. S. Roberts and C. Jeynes. Appl. Phys. Lett. **55** , 1989, pp. 1373.

13 C. J. M$^{c}$Lean, J. H. Marsh, R. M. De La Rue, A. C. Bryce, B. Garrett and G. W. Glew. Electron. Lett. **28** 1992, pp. 1117.

14 D. G. Deppe and N. Holonyak, Jr., "Atom diffusion and impurity-induced layer disordering in quantum well III-V semiconductor hetrostructures.", J. Appl. Phys. **64** (12), 15 Dec. 1988. R93.

[15] L. J. Guido, N. Holonyak, Jr., K. C. Hsieh, R. W. Kaliski, W. E. Plano, R. D. Burnham, R. L. Thornton, J. E. Elper and T. L. Paoli., "Effects of dielectric encapsulation and As overpressure on Al-Ga interdiffusion in AlGaAs-GaAs quantum well hetrostructures." J. Appl. Phys. **61** (4), 15 Feb. 1987. pp. 72.

[16] B. S. Ooi, "Fabrication of optoelectronic integrated circuits using quantum well intermixing.", Glasgow University Ph.D. Thesis November 1994.

[17] Y. Suzki, H. Iwamura and O. Mikami, "TE/TM selective channel waveguides in GaAs/AlAs superlattice fabricated by $SiO_2$ cap disordering.", J. Appl. Phys. **56** (1), 1 Jan. 1990. pp. 19.

[18] E. S. Koteles, B. Elman, P. Melman, J. Y. Chi and C. A. Arimento. "Quantum well shape modification using vacancy generation and rapid thermal annealing.", Optical and Quantum Electronics. **23**. (1991) S779-S787.

[19] T. Haga, N. Tachino, Y. Abe, J. Kasahara, A. Okubora and H. Hasegawa, "Out-diffusion of Ga and As atoms into dielectric films in $SiO_x$/GaAs and $SiN_y$/GaAs systems.", J. Appl. Phys. **66** (12), 15 Dec. 1989. pp. 5809.

[20] J. Gyulai, J. W. Mayer, I. V. Mitchell and V. Rodrigues, Appl. Phys. Lett. **17** , 1970, pp. 332.

[21] B. S. Ooi, S. G. Ayling, A. C. Bryce and J. H. Marsh, "Fabrication of multiple wavelength lasers in GaAs-AlGaAs structures using a one-step spatially controlled quantum-well intermixing technique", IEEE Photonics Technol. Lett., 7, 944, 1995.

[22] W. F. Stickle and K. D. Bomben, "Angle-dependent X-ray photoelectron spectroscopy investigation of GaAs surfaces.", Thin Solid Films, **154** (1987), pp. 301.

[23] H. Ribot, K. W. Lee, R. J. Simes, R. H. Yan and L. A. Coldren, "Disordering of GaAs/AlGaAs multiple quantum well structures by thermal annealing for monolithic integration of laser and phase modulator.", Appl. Phys. Lett. **55** (7), 1989, 14 Aug. pp. 672.

[24] D. L. Smith, A. S. Almonda, C. C. Chen, S. E. Ready and B. Wacker, "Mechanism of $SiN_xH_y$ deposition from $NH_3$-$SiH_4$ plasma,", J. Electrochem. soc., **137**, (1990), pp. 614.

[25] I. Gontijo, T. Krauss, R. M. De La Rue, J. S. Roberts and J. H. Marsh, "Very low loss extended cavity GaAs/AlGaAs lasers made by impurity free vacancy diffusion.", Electron. Lett. **30**, 145 (1994).

[26] J. Beauvais, J. H. Marsh, A. H. Kean, A. C. Bryce C. Button, "Suppression of bandgap shifts in GaAs/AlGaAs quantum wells using strontium fluoride caps.", Electron. Lett. **28** (17) 1992, pp. 1670.

[27] "Thermophysical properties of matter.", TPRC Data Series Vol. **13**.

[28] C. W. Wilmsen, R. W. Kee and K. M. Geib, "Initial oxidation and oxide/semiconductor interface formation on GaAs.", J. Vac. Sci. Technol., **16**(5), Sept. 1979, pp. 1434.

[29] B. A. Cowans, Z. Dardas, W. N. Delgass, M. S. Carpenter and M. R. Melloch, "X-ray photoelectron spectroscopy of ammonium sulfide treated GaAs (100) surfaces.", Appl. Phys. Lett. **54**(4), Jan, 1989. pp. 365.

[30] C. J. Sandroff, R. N. Nottenberg, J. C. Bischoff and R. Bhat, "Dramatic enhancement in the gain of a GaAs/AlGaAs heterostructure bipolar transistor by surface chemical passivation." Appl. Phys. Lett. **51**(1), July, 1987. pp. 33.

[31] E. S. Aydil, K. P. Giapis, R. A. Gottscho, V. M. Donnelly and E. Yoon, "Ammonia plasma passivation of GaAs in downstream microwave and radio-frequency parallel plate reactors.", J. Vac. Sci. Technol. B. **11**(2), Mar/Apr 1993 pp 195-205.

[32] E. S. Aydil, Z. H. Zhou, R. A. Gottscho and Y. J. Chabal, "Real time *in situ* monitoring of surfaces during glow discharge processing: $NH_3$ and $H_2$ plasma passivation of GaAs.", J. Vac. Sci. Technol., B. **13**(2), Mar. 1995, pp. 258.

[33] G. M. Mikhailov, P. V. Bulkin, S. A. Khudobin, A. A. Chumakov and S. Y. Shapoval, "XPS investigation of the interaction between ECR-excited hydrogen and the native oxide of GaAs(100).", Vacuum, **43**(3), 1992, pp 199-201.

[34] P. W. Li, Q. Wang and E. S. Yang, "Chemical and electrical characterisation of AlGaAs/GaAs heterojunction bipolar transistors treated by electro-cyclotron resonance plasmas.", Appl. Phys. Lett. Vol. **60**(16), 20th April 1992, pp 1996-1998.

[35] S. Shi, P. Li Kam Wa, A. Miller, J. Pamulapati, P. Cooke and M. Dutta, "The controlled disordering of quantum wells using surface oxidation.", Semicond. Sci. Technol. **9** (1994) 1564.

[36] C. C. Yang, A. Villeneuve, G. I. Stegeman, C. -H. Lin and H. -H. Lin. "Measurements of the two-photon absorption coefficient and induced nonlinear refractive index in GaAs/AlGaAs Multiquantum well waveguides." Electronic Letters, Vol. 29(1), p. 37. (1993).

[37] G. K. Hubler, C. N. Waddle, E. P. Donovan and J. M. Zavada. "Below-bandgap refractive index of AlAs/GaAs multiple quantum wells." Optical and Quantum Electronics, Vol. 23, S883-S893. (1991)

[38] J. Massies and J. P. Contour., "X-ray photoelectron spectroscopy study of the effects of ultrapure water on GaAs.", Appl. Phys. Lett. **46**. 12, 1150, 1985.

[39] S. Sugata, A. Takamori, N. Takado, K. Asakawa, E. Miyauchi and H. Hashimoto., "GaAs cleaning with a hydrogen radical beam gun in an ultrahigh-vacuum system.", J. Vac. Sci. Technol. B. **6**, 4, 1087, 1988.

[40] H. Kawaguchi, "Proposal for a new all optical waveguide functional device.", Opt. Lett., **10**, 8, 1985.

# Chapter 6.

# Optical Solitons.

In nonlinear optics essentially two types of solitons are researched, namely; temporal and spatial solitons. Temporal optical solitons[1] have received a great deal of attention, due to their possible application in communication systems. In optical fibres they arise from the balancing of dispersion and nonlinear self phase modulation. Spatial solitons[2] occur in two dimensional optical waveguides when self-focusing and diffraction balance. Within these research areas two families of solitons exist, which are termed bright and dark solitons. Bright solitons are spatial or temporal bundles of light, and dark solitons[3] are localised depressions in a CW background.

As previously indicated, in optical fibres bright temporal solitons arise from the balancing of the anomalous group velocity dispersion, and the positive Kerr nonlinearity[4]. Unfortunately, this condition cannot be met in many attractive nonlinear materials, or at desired wavelengths. In fact, direct bandgap semiconductors, such as AlGaAs which exhibit a much

stronger ultrafast and focusing Kerr nonlinearity below half the bandgap than fused silica, also exhibit a huge normal GVD. Hence, the question arises can bright temporal solitons, or at least solitary pulses exist in this environment.

It is possible to observe solitons in AlGaAs by selecting an operating wavelength where the nonlinearity is defocusing, and the dispersion is positive[5]. This has been recently experimentally verified in an AlGaAs waveguide[6], but unfortunately strong two photon absorption led to considerable pulse broadening. Recently it has been proposed that the GVD of a waveguide can be tailored to give a resulting anomolous dispersion[7]. This would allow bright soliton propagation in semiconductor rib waveguides, and for light bullet formation in planar waveguides.

This chapter is concerned with using Anti-Resonant Reflecting Optical Waveguides (ARROWs), to tailor the magnitude and sign of the GVD. This device could then be used to show bright temporal solitons can exist in a regime where the material dispersion and the Kerr nonlinearity are both positive. The possibility of bright spatial solitons as a mechanism for all optical switching will also be investigated.

### 6.1. ARROW Structure.

Since the ARROW was first demonstrated by Duguay et al[8], it was quickly realised that they possessed many interesting properties, which include.

- **Low propagation losses.**
- **High polarisation selectivity.**
- **Good mode matching with optical fibres.**
- **Wavelength selectivity.**
- **Large design tolerances.**

These properties have lead to the proposal of some novel optical devices, such as all-optical switches[9], and polarisation splitters[10]. Also devices have been fabricated such as semiconductor lasers[11], and wavelength selective photodetectors[12].

A typical ARROW structure is shown in figure 6.1.. The device basically consists of a low index core region, which sits on an interference reflector. The reflector consists of two cladding layers of relatively high then low index, and these are located upon a high index substrate.

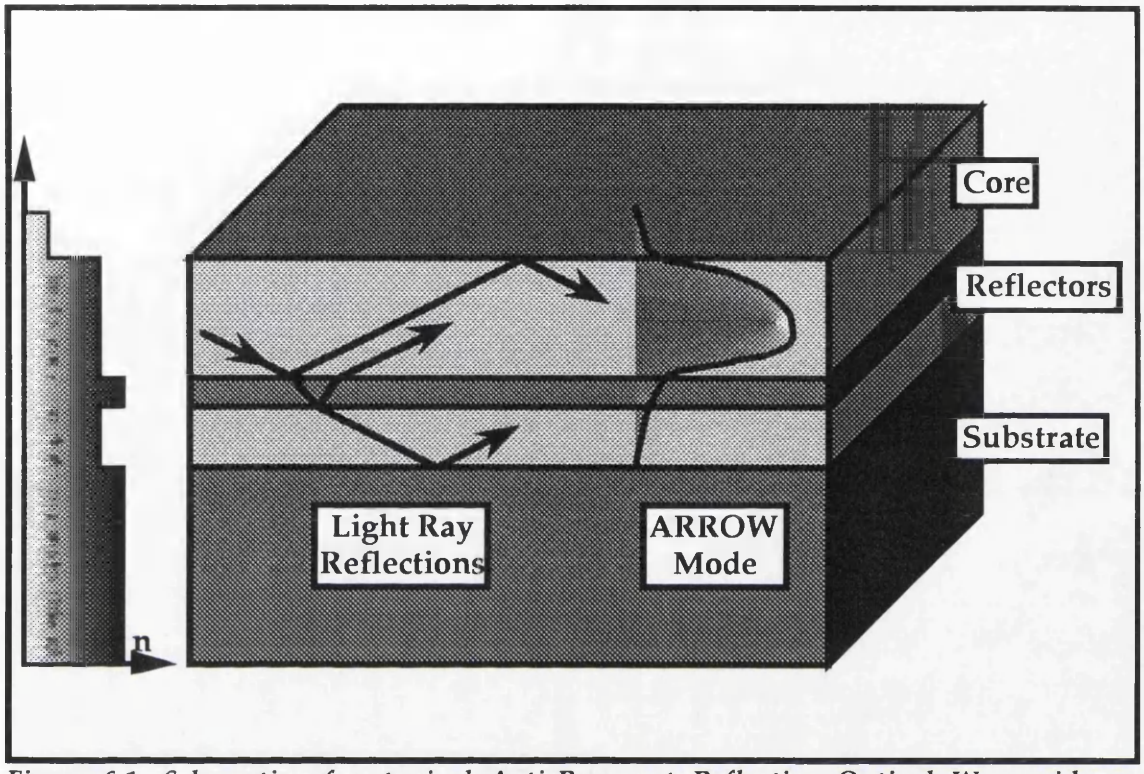


*Figure 6.1. Schematic of a typical Anti-Resonant Reflecting Optical Waveguide (ARROW).*

The refractive index of the bottom interference layer is typically the same as that used for the waveguide core and the thickness is half of the effective core thickness. The effective core thickness is the depth of the core layer, plus the effective field penetration outside the core layer.

The mode which propagates within the ARROW does so through a combination of total internal reflection at the upper air/core boundary and from a high reflection at the lower reflector. A small fraction of the light passes through the lower reflector cladding and is known as the mode radiation loss this can be less than 0.1 %. It should also be noted that since this is a type of Fresnel reflection it will depend on the polarisation of the light, this property has been used for some novel polarisation dependent devices[13]. For the basic ARROW structure higher order modes are effectively prevented

from propagating, due to the low reflectivity at the reflector cladding. Therefore, effective single mode operation can be readily obtained. Through subtle manipulation of the reflector parameters, it is possible to obtain multi-mode operation, which in turn can lead to some very interesting phenomena.

## 6.2. Theoretical Modelling of ARROWs.

To analyse the modal properties of ARROW waveguides, the transfer matrix[14] approach offers a route to a simple algebraic equation, which defines the modal propagation constant. Considering figure 6.2., it is clear that the fields within a relatively simple thin film, can be complicated due to the superposition of the reflected and transmitted waves. The transfer matrix simplifies this by applying a systematic approach, to an arbitrary dielectric stack.

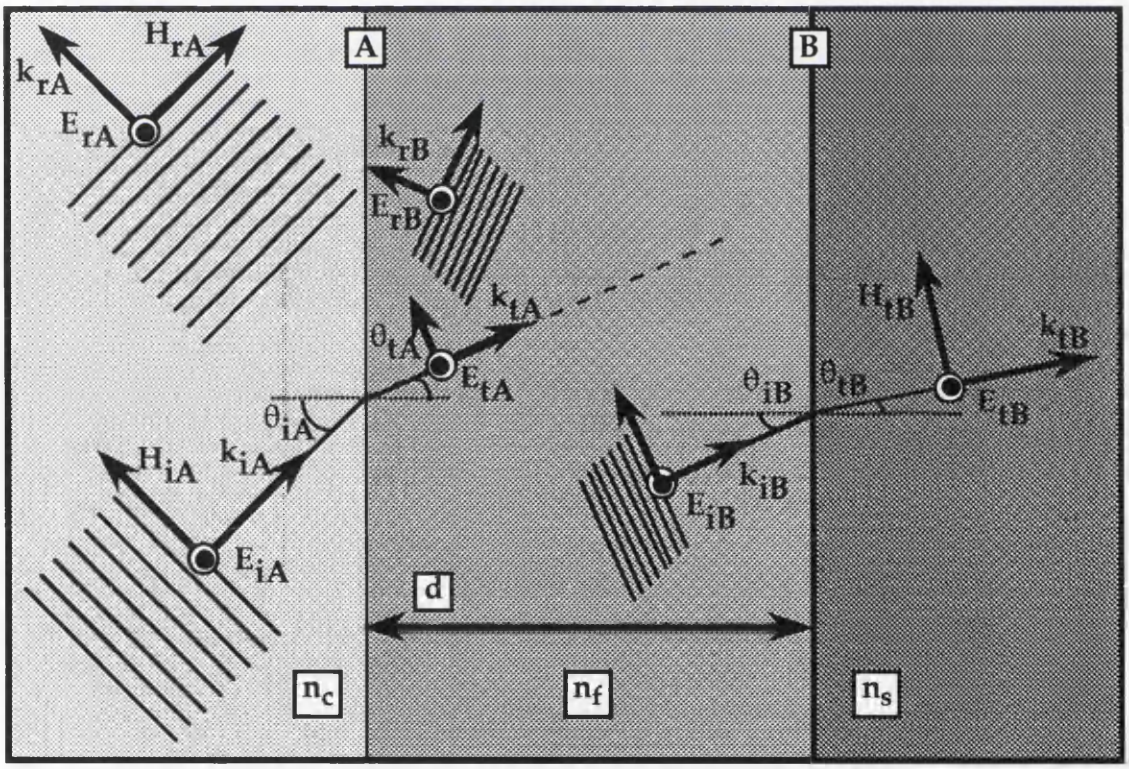


*Figure 6.2. Transmitted and reflected field components within a simple thin film dielectric stack.*

## 6.3. Transfer Matrix.

By considering the structure of figure 6.2. it is possible to visualise how the matrix method is formalised. The cover (typically air) is designated $n_c$, $n_f$ is the film and $n_s$ is the substrate. Initially the case where the electric field of the incident wave is parallel to the plane

of incidence (i. e. TE polarised) is considered. The boundary condition, that the tangential component of the E field is continuous across the interface[15] is applied. If each wave (i. e. $E_{rA}$, $E_{tB}$, etc.) in figure 6.2., represents the resultant of all waves travelling in that specified direction within the medium, by summing the total fields on either side of the interface A:

$$E_A = E_{iA} + E_{rA} = E_{tA} + E_{rB} \qquad 6.1.$$

There are no incident angle dependent cosine terms present in the equation because, the electric field has been chosen parallel to the plane of the layers. The three electric field components at A (i. e. $E_{iA}$, $E_{rA}$, and $E_{tA}$) are in the same direction and therefore, sum algebraically. Similarly at boundary B:

$$E_B = E_{iB} + E_{rB} = E_{tB} \qquad 6.2.$$

The magnetic fields can be similarly expressed, by using the fact that the magnitudes of the $E$ and $H$ fields, in a dielectric medium of refractive index n are related by (reference 14.):

$$H = \frac{nE}{z_o} \qquad 6.3.$$

Where $z_o$ is the impedance of free space[16] $\left( z_o = \sqrt{\frac{\mu_o}{\varepsilon_o}} = 377\Omega m^{-1} \right)$, Also since the $E$ and $H$ fields make a right handed system with the unit propagation vector $k$, it is possible to define the magnetic field at boundary A:

$$H_A = z_o^{-1}(E_{iA} - E_{rA})n_c \cos\theta_{iA} = z_o^{-1}(E_{tA} - E_{rB})n_f \cos\theta_{iB} \qquad 6.4.$$

And for boundary B:

$$H_B = z_o^{-1}(E_{iB} - E_{rB})n_f \cos\theta_{iB} = z_o^{-1}E_{tB}n_s \cos\theta_{tB} \qquad 6.5.$$

As the wave travels through the film (i. e. $n_f$), it incurs a phase shift $\varphi$ which is calculated as:

$$\varphi = k_o n_f d \cos\theta_{tA} \qquad 6.6.$$

Where $\theta_{tA}$ is the angle of incidence, d is the layer thickness, and $k_o$ is the free space wave number. The field equations at interface B can now be related to those at interface A:

$$E_B = E_{tA}e^{-j\varphi} + E_{rB}e^{+j\varphi} \qquad 6.7.$$

Also, for the magnetic field:

$$H_B = z_o^{-1}\left(E_{tA}e^{-j\varphi} - E_{rB}e^{+j\varphi}\right)n_f \cos\theta_{iB} \qquad 6.8.$$

If these equations are solved at the boundaries and then substituted into equations 6.1. and 6.4., at boundary A:

$$E_A = E_B \cos\varphi + \frac{H_B j(\sin\varphi)}{\gamma_1} \qquad 6.9.$$

Again the magnetic field:

$$H_A = E_B \gamma_1 j \sin\varphi + H_B \cos\varphi \qquad 6.10.$$

Where $\gamma_1$ is:

$$\gamma_1 = \frac{n_f \cos\theta_{tA}}{Z_o} \qquad 6.11.$$

It should be noted that if the electric field is in the plane of incidence (i. e. TM polarised), the above arguments are still valid except that $\gamma_i$ is replaced with $\gamma_1 = z_o \cos\theta_{tA}/n_f$. Now if equations 6.9. and 6.10. are converted into matrix notation they can be expressed as:

$$\begin{bmatrix} E_A \\ H_A \end{bmatrix} = \begin{vmatrix} \cos\varphi_1 & -\left(\frac{j}{\gamma_i}\right)\sin\varphi_1 \\ -j\gamma_1 \sin\varphi_1 & \cos\varphi_1 \end{vmatrix} \begin{bmatrix} E_B \\ H_B \end{bmatrix} \qquad 6.12.$$

Or simply:

$$\begin{bmatrix} E_A \\ H_A \end{bmatrix} = M_A \begin{bmatrix} E_B \\ H_B \end{bmatrix} \qquad 6.13.$$

Where $M_A$ is the characteristic matrix that relates the field at the two adjacent boundaries. It readily follows that if we were to add another dielectric film to the stack and thus, introduce another

boundary C, it would have a characteristic matrix $M_B$ associated with it, and the fields would be related:

$$\begin{bmatrix} E_B \\ H_B \end{bmatrix} = M_B \begin{bmatrix} E_C \\ H_C \end{bmatrix} \qquad 6.14.$$

To obtain the total effects of the dielectric stack, and hence relate the field at A to that at C we simply multiply the characteristic matrices:

$$\begin{bmatrix} E_A \\ H_A \end{bmatrix} = M_A M_B \begin{bmatrix} E_C \\ H_C \end{bmatrix} \qquad 6.15.$$

This then leads to a general conclusion that in a dielectric stack of i layers, each possessing particular values of n and d, it is possible to relate the fields at the first and last boundaries by :

$$\begin{bmatrix} E_A \\ H_A \end{bmatrix} = M_A M_B \ldots M_{i-1} M_i \begin{bmatrix} E_{i+1} \\ H_{i+1} \end{bmatrix} \qquad 6.16.$$

It is then possible to define a characteristic matrix $M$ for the entire dielectric stack, by the multiplying all of the individual characteristic matrices together:

$$M = M_A M_B \ldots M_{i-1} M_i = \prod_{i=1}^{I} M_i = \begin{bmatrix} m_{11} & m_{12} \\ m_{21} & m_{22} \end{bmatrix} \qquad 6.17.$$

### 6.3.1. Reflection and Transmission.

One of the main applications of the transfer matrix approach is to theoretically determine the reflectance and transmission coefficents. Also by following the formulation for these quantities, it is possible to gain an important insight to the modal properties of dielectric stacks. If the boundary equations 6.1. and 6.4. are combined with the matrix equation 6.14.:

$$\begin{bmatrix} (E_{iA} + E_{rA}) \\ (E_{iA} - E_{rA})\gamma_A \end{bmatrix} = M \begin{bmatrix} E_{tB} \\ E_{tB}\gamma_B \end{bmatrix} \qquad 6.18.$$

If the reflection ($r = E_{iA}/E_{rA}$) and transmission ($t = E_{tB}/E_{iA}$) coefficients are now defined. By expanding the matrices in equation 6.18., the following relations are obtained:

$$1 + r = m_{11}t + m_{12}\gamma_B t \qquad 6.19.$$

and,

$$(1 - r)\gamma_A = m_{21}t + m_{22}\gamma_B t \qquad 6.20.$$

These can now be solved in terms of r and t, to give:

$$r = \frac{\gamma_A m_{11} + \gamma_A \gamma_I m_{12} - m_{21} - \gamma_I m_{22}}{\gamma_A m_{11} + \gamma_A \gamma_I m_{12} + m_{21} + \gamma_I m_{22}} \qquad 6.21.$$

and,

$$t = \frac{2\gamma_A}{\gamma_A m_{11} + \gamma_A \gamma_I m_{12} + m_{21} + \gamma_I m_{22}} \qquad 6.22.$$

It is now possible to find either the reflection or transmission characteristics of an arbitrary dielectric stack, by working out the characteristic matrix for each layer, and then multiplying them together to find the total characteristic matrix. The components of this matrix can then be substituted into 6.21. and 6.22., which will then yield the reflection and transmission coefficients. However, it is the guided modes of these films that we are interested in, and therefore it is the denominator of these two expressions that is of interest.

### 6.3.2. Transfer Matrix Waveguide Modes.

To calculate the guided modes of the ARROW using the matrix method, the starting point is the general matrix equation defining the field relations at the interfaces:

$$\begin{bmatrix} E_A \\ H_A \end{bmatrix} = M \begin{bmatrix} E_I \\ H_I \end{bmatrix} \qquad 6.23.$$

For modes propagating in the stack, the fields must decay exponentially away from the stack. This means that by following the same conventions as before, equation 6.23. can be put into the form:

$$\begin{bmatrix} 1 \\ -\gamma_A \end{bmatrix} E_A = M \begin{bmatrix} 1 \\ \gamma_I \end{bmatrix} E_I \qquad 6.24.$$

The general characteristic matrix is then written in full form:

$$E_A\begin{bmatrix} 1 \\ -\gamma_A \end{bmatrix} = E_I\begin{bmatrix} 1 \\ \gamma_I \end{bmatrix}\begin{bmatrix} m_{11} & m_{12} \\ m_{21} & m_{22} \end{bmatrix} \qquad 6.25.$$

These relations are then expanded, which gives:

$$E_A = E_I(m_{11} + \gamma_I m_{12}) \qquad 6.26.$$

and,

$$-\gamma_A E_A = E_I(m_{21} + \gamma_I m_{22}) \qquad 6.27.$$

If these transfer equations are now solved, the modal transfer function ($\chi_m(\beta)$) of the waveguide is obtained:

$$\chi_m(\beta) = \gamma_I m_1 + \gamma_C \gamma_I m_{12} + m_{21} + \gamma_I m_{22} = 0 \qquad 6.28.$$

Where $\beta$ is the effective index of the structure. It should be noted that this is in fact the poles of both the reflection and transmission characteristics, and this has been used to calculate the modal dispersion function for multilayer dielectric films[17].

Assuming that losses dielectric films are used, for bound modes $\beta$ is real and can be determined from the roots of equation 6.28.. Figure 6.3. shows the imaginary part of $\chi_m(\beta)$ for the AlGaAs ARROW used in the temporal soliton experiments.

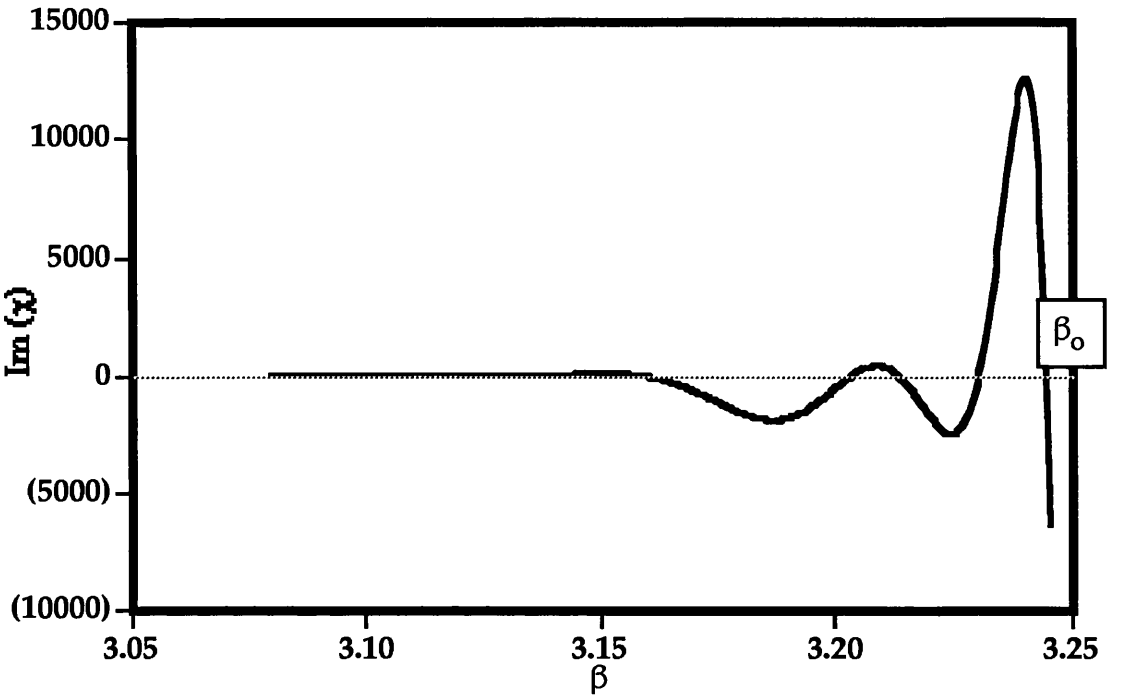


*Figure 6.3. Imaginary part of $\chi_m(\beta)$ calculated at 1.50 μm for the AlGaAs ARROW used for the temporal soliton experiments.*

Bound modes occur when the imaginary part of $\chi$ is zero. The fundamental propagation constant of the ARROW structure is $\beta_o$, and it is found to be approximately 3.24.

### 6.3.3. Mode Structure.

To determine the form of the modal structure within the waveguide is a relatively simple affair. Once the effective indices are found, an arbitrary value for field amplitude can be chosen at a certain point within the dielectric stack. It is then a simple matter to work from this point using equation 6.16., and find the form of the field amplitude distribution within each dielectric layer, as a function of this chosen amplitude.

## 6.4. AlGaAs ARROWs.

It has been possible to exploit some of their unusual characteristics of the ARROW structure to design novel devices[18]. One of the characteristics of ARROWs that is of great interest in the nonlinear optics field, is that it should be possible to manipulate the waveguide dispersion and invert the sign. This would then enable the formation of temporal solitons, in sub half bandgap AlGaAs optical waveguides.

## 6.5. Solitons in AlGaAs.

In conventional AlGaAs based waveguides the dispersion is strongly positive[19] (typically 1000 $ps^2\,km^{-1}$, or conversely 1000 $fs^2\,mm^{-1}$). This means that conventional half bandgap AlGaAs semiconductor waveguides are not suitable for the study of temporal soliton effects, because both the material dispersion and the nonlinearity (section 2.3.1.) are positive. They therefore, reinforce each other's temporal broadening effects, rather than the pulse narrowing associated with soliton formation. To obtain negatively dispersive waveguides, the actual guide geometry must be carefully examined. In normal step index guides (section 3.1.) the amount of dispersion compensation that can be achieved is minimal[20], since the dispersion of a step index waveguide is normal and thus only adds to the material dispersion. However, it is possible to produce guides with significant anomalous dispersion by using ARROWs.

It was predicted that by using an ARROW, it would be possible to tailor the dispersion of AlGaAs to have a similar magnitude to that of the basic material, but to reverse the sign. It would then be possible to observe solitonic effects in waveguides that were several millimetres long, using femtosecond pulses with peak powers of around 100 W (reference 7.).

### 6.5.1. Dispersion Tailoring.

If ARROWs are operated in a region that is detuned from the optimum guidance conditions, the modal dispersion contribution from the guide begins to deviate from its typically flat characteristics[21] and it can start to show strong curvature[22]. This curvature can be physically understood if a typical ARROW is considered far from the resonance condition. It is obvious that a low loss ARROW mode cannot be set up, since there is only a weak reflection from the bottom of the core. This leads to the situation where modes that are mainly contained within the reflectors will propagate. This region will obviously possess a higher effective index than elsewhere in the structure. Now at the point were the ARROW mode has begun to propagate, there are two modes with similar effective

indices within the structure. Since the ARROW modal dispersion characteristics depend not only on the material, as in the step index case, but also on the waveguide geometry and more especially the reflector region, the rate of change in the propagation constants is radically different. The ARROW superstrate mode is a "fast" mode and the mode within the reflectors is a "slow" mode. This means that the ARROW mode and the normal mode will experience a level crossing at some point (figure 6.5.).

## 6.6. Anomolously Dispersive AlGaAs ARROW.

The ARROW structure used in the experiment was fabricated from MBE grown intrinsic AlGaAs, and consisted of a 1.70 μm thick $Al_{0.40}Ga_{0.60}As$ core region bounded by 3 Bragg reflectors, and isolated from the GaAs substrate by a 1.50 μm thick $Al_{0.60}Ga_{0.40}$ As buffer layer (figure 6.4.) .

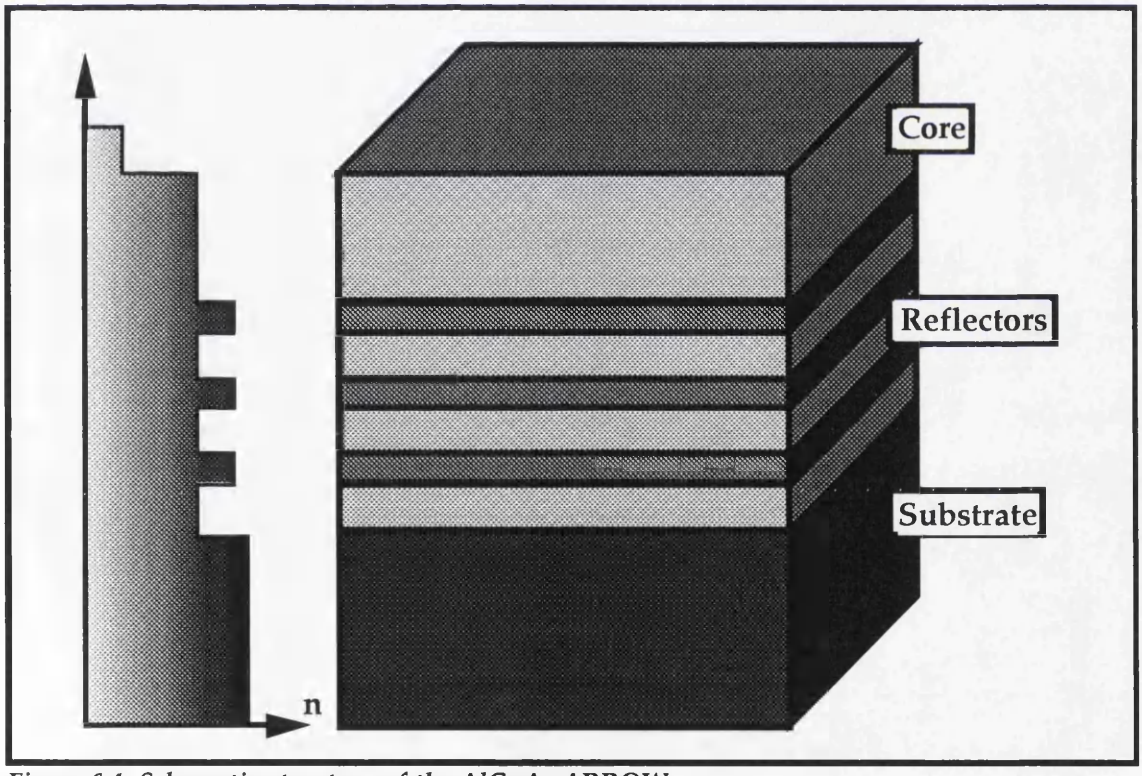


*Figure 6.4. Schematic structure of the AlGaAs ARROW.*

Each of the Bragg reflectors consisted of a 1.19 μm thick $Al_{0.18}Ga_{0.82}As$ layer, on top of a 0.50 μm thick $Al_{0.40}Ga_{0.60}As$ layer, this lead to an overall epilayer thickness of 8.27 μm. Rib loaded guides which were formed in the structure (0.4 μm deep) by

conventional photolithography and $SiCl_4$ dry etching techniques. The sample was finally cleaved to approximately 12 mm in length. The optical loss of these ARROW waveguides was measured using the conventional Fabry-Perot technique, which indicated a figure of approximately 2.5 dB $cm^{-1}$ for the total losses of the fundamental waveguide mode.

### 6.6.1. Modal Effective Index.

In section 2.3.1. the below bandgap refractive index of AlGaAs was shown to possess a normal dispersion, which could be inferred from the curvature of the refractive index verses wavelength graphs. Figure 6.5. shows the effective modal indices of the AlGaAs ARROW structure. The dotted lines are a guide to where the "fast" and "slow" superstrate modes associated with the resonant coupling would exist.

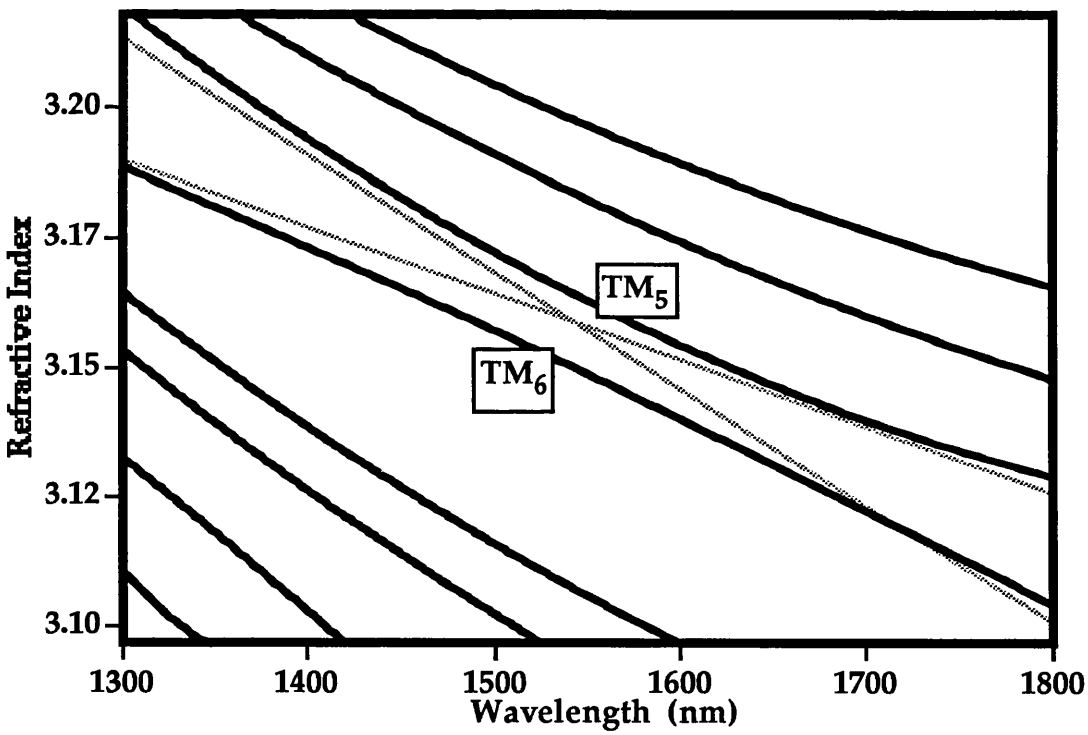


*Figure 6.5. Dispersion of the effective index of some of the ARROW modes.*

The main point of these dispersion relations is to show that the curvature of the modal dispersion can be changed and that it is possible to reverse the material dispersion of AlGaAs by using an ARROW geometry.

### 6.6.2. Modal Structure.

As it is the propagation of the anomalously dispersive $TM_6$ mode that is interesting, it would be extremely desirable to excite only this mode. However, using the typical end-fire coupling technique employed for exciting AlGaAs waveguides, it is found that both the $TM_6$ and the $TM_5$ modes have a good modal match within the ARROW core (figure 6.6.). This means that both modes will have to be considered in the theoretical and experimental pulse propagation. If we assume a Gaussian beam as the input, the efficiency by which the guided modes are excited are estimated to be 28 % for $TM_6$ and 22 % for $TM_5$.

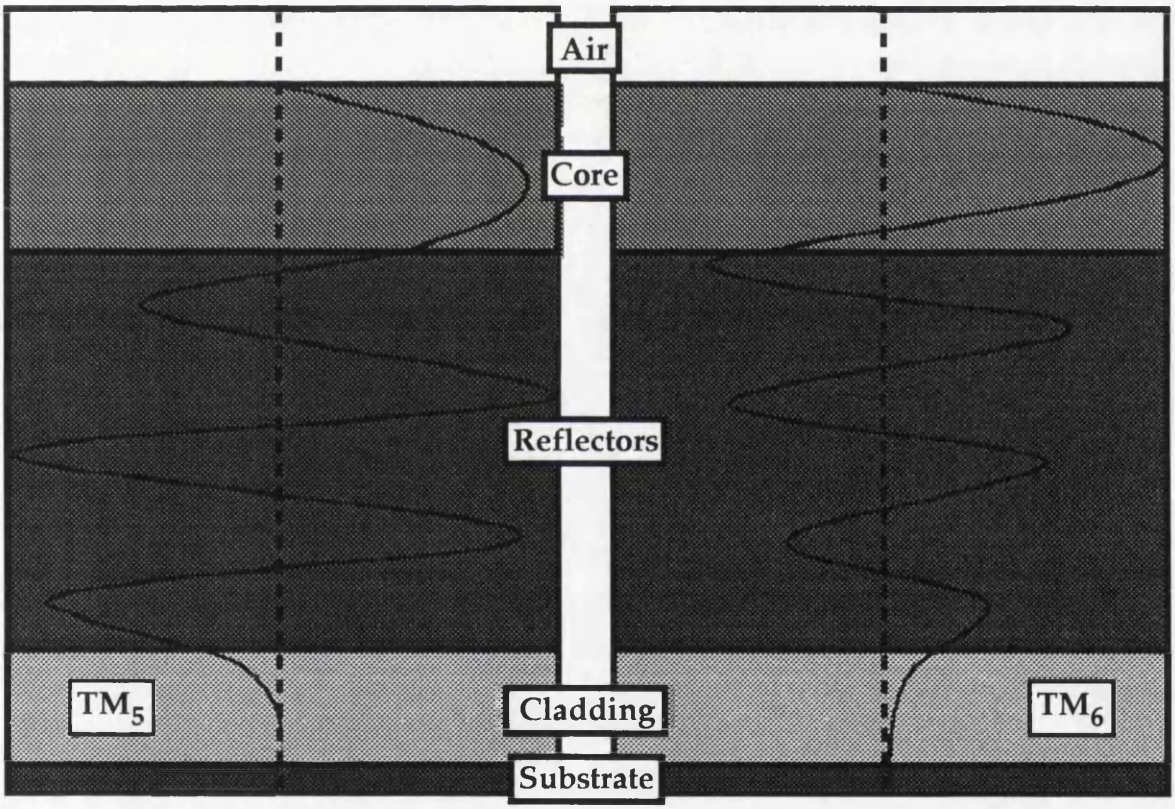


*Figure 6.6. Field distribution for both the $TM_5$ and $TM_6$ modes for the AlGaAs ARROW structure.*

From the field distribution of these modes it is evident that the $TM_6$ is a true ARROW mode, since the peak of the power is contained within the core and not as in the reflectors as in $TM_5$.

### 6.6.3. Modal Dispersion.

The operating wavelength was chosen to be 1510 nm to achieve a compromise between high gain of the laser, maximum nonlinearity, maximum GVD and small third order dispersion. At 1510 nm the calculated dispersion for the excited ARROW modes are $\beta_2 = -1050\ fs^2\,mm^{-1}$ for $TM_6$, and $\beta_2 = 2765\ fs^2\,mm^{-1}$ for $TM_5$. Figure 6.7. shows the dispersion of the two modes.

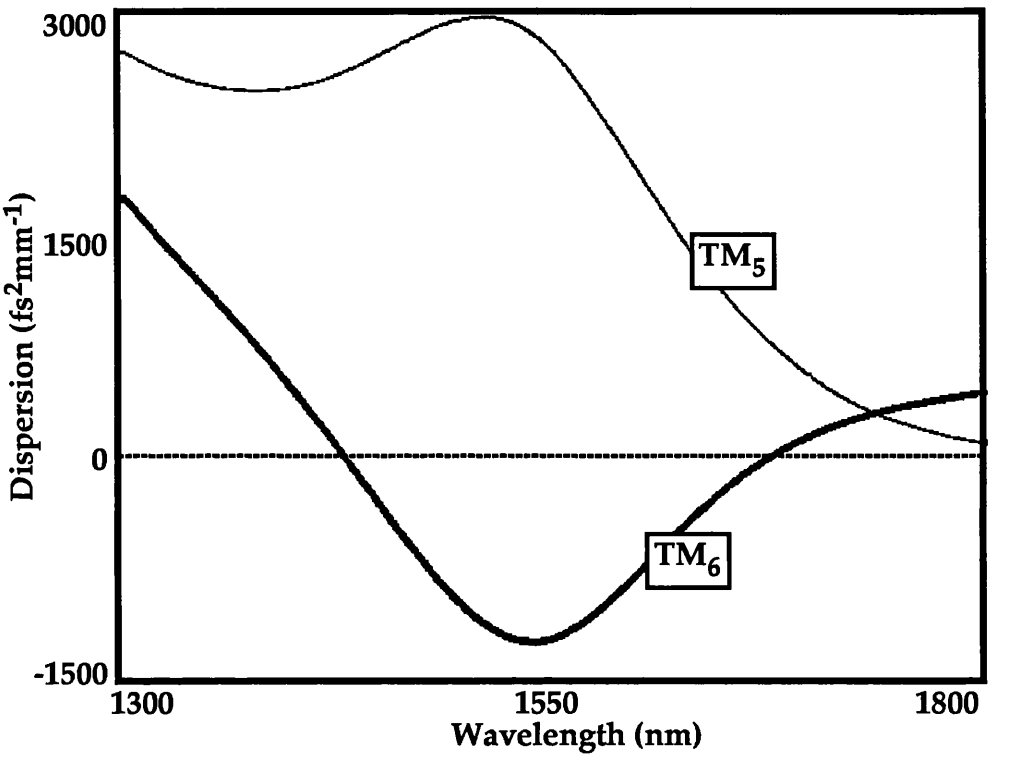


*Figure 6.7. Calculated dispersion of the ARROW modes.*

The dispersion length for a $sech^2$ pulse can be calculated from equation 1.37. For a 125 fs pulse the equivalent dispersion lengths are 4.76 mm for $TM_6$ and 1.79 mm for $TM_5$. Therefore, over the sample length, a low power pulse would spread by a factor of 2.6 and 6.7 for the respective modes. Also, from figure 6.7. it should be noted that because the wavelength does not fit the maximum/minimum of the GVD, a small third order dispersion of $-11040\ fs^3mm^{-1}$ for the anomalously dispersive mode and $11290\ fs^3mm^{-1}$ for the normally dispersive mode has to be taken into account.

## 6.7. Theoretical Pulse Propagation.

Unlike solitons in optical fibers where only dispersion and self-phase modulation make a major contribution to the soliton dynamics, extra effects such as TPA (section 2.4.1.), third order dispersion and linear absorption (section 3.3.), must be considered in order to model the experiment. The next two sections explain the expected pulse output, in both the temporal and frequency domains, when all the major contributing factors are considered.

### 6.7.1. Temporal Model.

To properly model the pulse evolution within the ARROW structure, all the optical effects that have an influence over the propagation within the waveguide must be included. Therefore using the NLSE of section 1.3.1. as the starting point:

$$i\frac{\partial u}{\partial \xi}+\frac{1}{2}\frac{\partial^2 u}{\partial \tau^2}+|u|^2 u=0 \qquad 6.29.$$

All practical waveguides have a linear loss associated with them and the ARROW structure is no different, therefore a linear loss term must be included. Mathematically this is realised by inserting a loss term, related to the normalised amplitude u in the RHS of equation 6.29.:

$$i\frac{\partial u}{\partial \xi}+\frac{1}{2}\frac{\partial^2 u}{\partial \tau^2}+|u|^2 u=\frac{-i\Gamma u}{2} \qquad 6.30.$$

Where $\Gamma$ is related to the loss coefficient by:

$$\Gamma=\alpha L_D \qquad 6.31.$$

A third order dispersion term is now introduced:

$$i\frac{\partial u}{\partial \xi}+\frac{1}{2}\frac{\partial^2 u}{\partial \tau^2}+|u|^2 u+\frac{i\Gamma u}{2}-i\beta_3\frac{\partial^3 u}{\partial \tau^3}=0 \qquad 6.32.$$

Since there are two modes propagating simultaneously within the ARROW structure, both of which contain relatively high power levels, some nonlinear coupling will exist between the modes. Therefore, a set of nonlinearly coupled Schrödinger

equations must be constructed, so that both modes can be accurately modelled. The subscripts a and b will be used for the $TM_6$ and $TM_5$ modes respectively. Initially considering the $TM_6$ mode, and introducing a wave vector mismatch term $\Delta = (\beta_a - \beta_b)L_a$:

$$i\frac{\partial u_a}{\partial \xi} + \frac{1}{2}\frac{\partial^2 u_a}{\partial \tau^2} + |u_a|^2 u_a + \frac{\Delta + i\Gamma}{2}u_a - i\beta_3^a \frac{\partial^3 u_a}{\partial \tau^3} = 0 \qquad 6.33.$$

Now considering the influence of cross phase modulation from the $TM_5$ mode:

$$i\frac{\partial u_a}{\partial \xi} + \frac{1}{2}\frac{\partial^2 u_a}{\partial \tau^2} + |u_a|^2 u_a + \frac{\Delta + i\Gamma}{2}u_a - i\beta_3^a \frac{\partial^3 u_a}{\partial \tau^3} + (\psi_c u_a + \psi_b u_b)\left(u_a^* u_b + u_a u_b^*\right) = 0 \qquad 6.34.$$

Where $\psi$ is the cross phase modulation coefficient. Finally a term is introduced, which describes the nonlinear energy exchange between the two modes as they propagate:

$$i\frac{\partial u_a}{\partial \xi} + \frac{1}{2}\frac{\partial^2 u_a}{\partial \tau^2} + |u_a|^2 u_a + \frac{\Delta + i\Gamma}{2}u_a - i\beta_3^a \frac{\partial^3 u_a}{\partial \tau^3} + (\psi_c u_a + \psi_b u_b)\left(u_a^* u_b + u_a u_b^*\right) + \psi_b |u_b|^2 u_b = 0 \qquad 6.35.$$

It is now possible to present the propagation equation for the $TM_5$ mode and study the two coupled NLSEs.

$$i\frac{\partial u_b}{\partial \xi} - \frac{1}{2}\left|\frac{\beta_2^a}{\beta_2^b}\right|\frac{\partial^2 u_b}{\partial \tau^2} + |u_b|^2 u_b - \frac{\Delta - i\Gamma}{2}u_b - i\beta_3^a \frac{\partial^3 u_b}{\partial \tau^3} + (\psi_c u_b + \psi_a u_a)\left(u_b^* u_a + u_b u_a^*\right) + \psi_a |u_a|^2 u_a = 0 \qquad 6.36.$$

The $\left|\frac{\beta_2^a}{\beta_2^b}\right|$ term arises due to normalisation factors. It is now possible to use this set of equations, to follow the pulse propagation through the ARROW structure.

The power required to form a fundamental temporal soliton can be expressed as:

$$P_s = \frac{3.11|\beta_2|}{\gamma T_{FWHM}^2} \qquad 6.37.$$

Where $\gamma$ is a nonlinearity coefficient, defined as:

$$\gamma = \frac{n_2 \omega_o}{c A_{eff}} \qquad 6.38.$$

Where $A_{eff}$ is the effective area of the waveguide, $\omega_o$ is the operating frequency and c is the speed of light.

### 6.7.2. Temporal Results.

Using typical AlGaAs ARROW parameters the fundamental soliton power was calculated to be 72 W. Figure 6.8. shows calculated autocorrelations for power levels similar to those used in the experiments of section 6.8.. The dashed line shows the autocorrelation of a 125 fs pulse with a $sech^2$ shape and is assumed as the input to the ARROW.

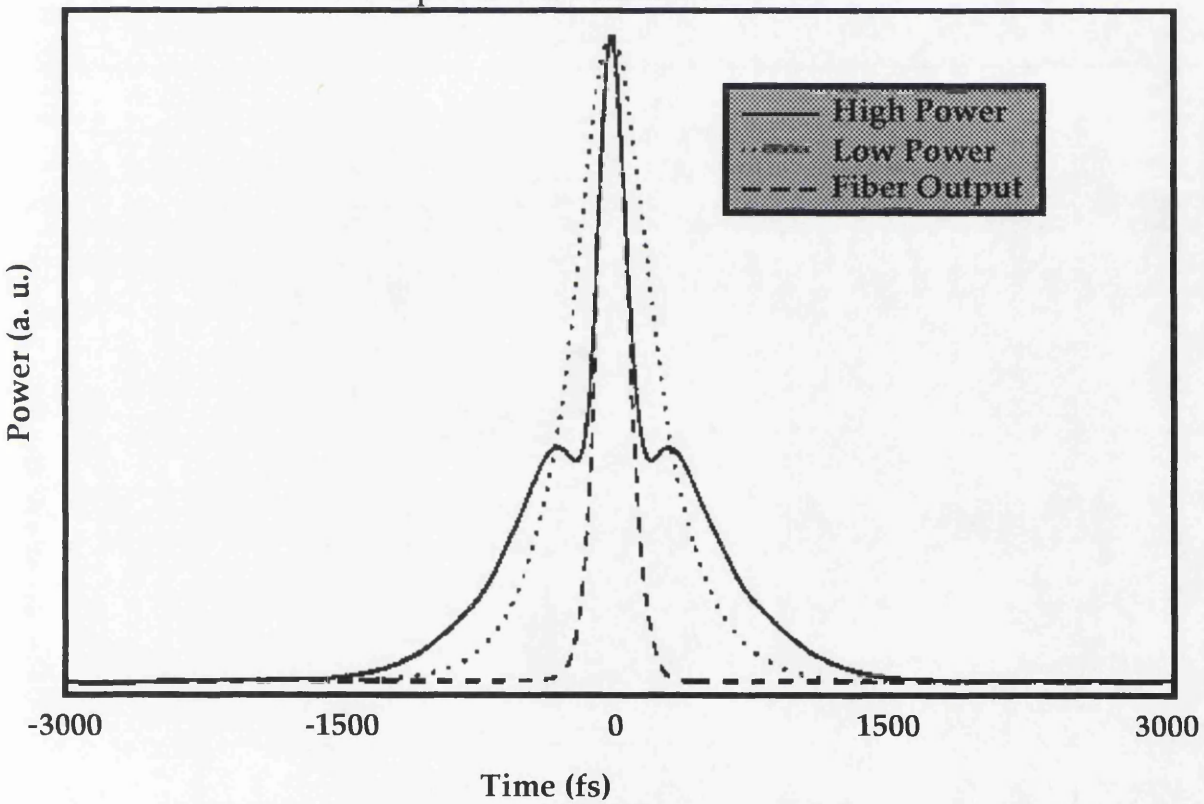


*Figure 6.8. Calculated autocorrelations for a 125 fs pulse propagating in the AlGaAs ARROW.*

At the end of the propagation through the guide, the dotted line shows the guide output at low power, with a peak power of 17 W ($0.24 \times P_s$) in the $TM_6$ mode. Quite clearly the pulse has broadened as expected, and is approximately 3 times wider than the input pulse. If the propagation of both modes is now

considered with a high power pulse; 125 W in the anomalously dispersive mode ($1.75 \times P_s$), the pulse output shape is seen to have drastically changed.

Clearly there is a component which has narrowed as the pulse power was incresed. However, the autocorrelation possess a wide pedestal, which is due to the dispersive mode. The normally dispersive mode broadens considerably, since the SPM serves to broaden the spectrum and not compensate for the dispersion. Eventually the simultaneous excitation of both the $TM_6$ and $TM_5$ leads to a nonlinear coupling between these modes and there is a small exchange of energy. This can be seen in the shoulders of the dispersive wave in the high power case, (figure 6.8.) where energy appears to be "missing" from the dispersive pulse.

It is possible to observe the effects of the third order dispersion term by studying figure 6.9.. This shows the calculated temporal intensities of the pulses rather than the autocorrelations.

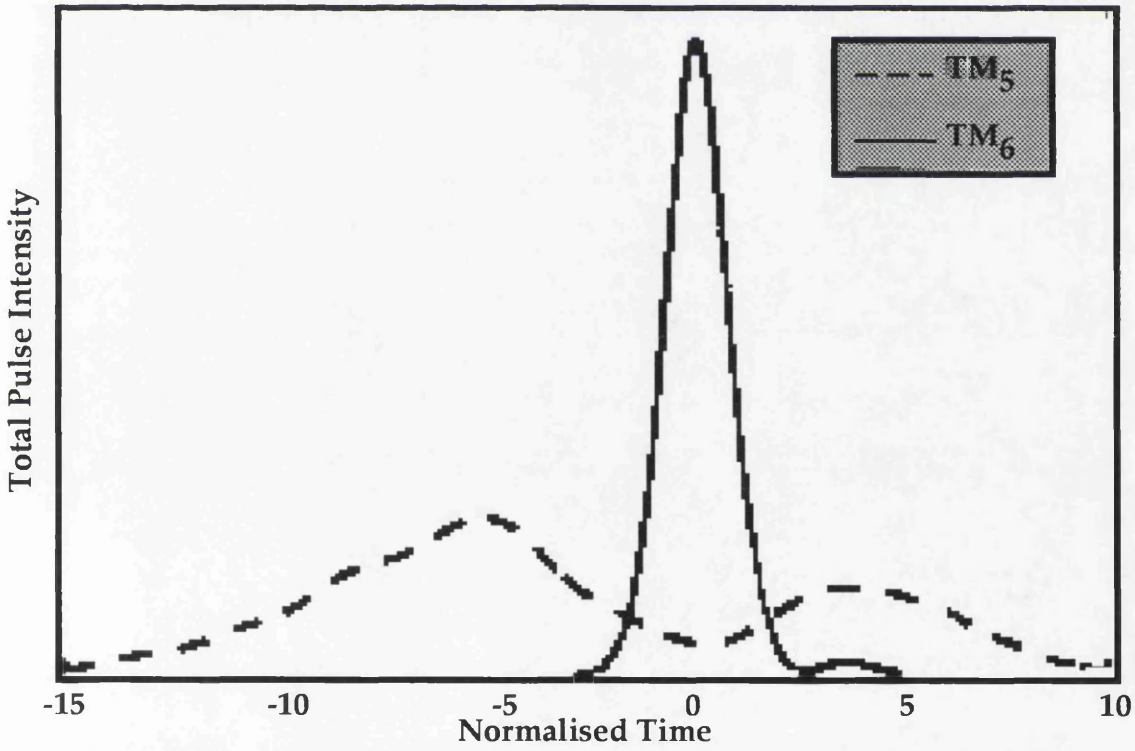


*Figure 6.9. Calculated temporal intensities for a 125 fs pulse propagating in the AlGaAs ARROW.*

Considering the $TM_5$ output (dotted line) and the $TM_6$ (solid line), it is obvious that there is a minor decrease of the pulse

velocity which is due to third-order dispersion. Obviously it can be anticipated that the nonlinear coupling between the modes decreases, as the pulse continues to propagate due to the decrease in the small overlap shown in figure 6.9.. Hence, the pulse in the anomalously dispersive mode will move away from the normally dispersive mode, and evolve as a true soliton where only third order dispersion and linear loss act as small perturbations.

From figure 6.9. it is also possible to see the effect of TPA on the pulse propagation. As the solitonic mode does not experience any spectral broadening the corresponding pulse shape is not affected, since it does not appreciably overlap with the TPA bandedge. However, this is not true for the normally dispersive mode, since as the spectrum begins to broaden it experiences some TPA at shorter wavelengths. This is reflected in the temporal pulse shape, since the symmetry of the pedestal is now lost, and the leading part of the pulse (pedestal on the left-hand side) has a shock-like shape.

### 6.7.3. Spectral Model.

Because TPA has a highly dispersive character it cannot be included into equation 6.29. in a simple manner. However, it is extremely easy to account for TPA in the spectral domain in the form of spectral damping. Assuming the TPA begins at the half bandgap frequency we can approximate the nonlinear loss by:

$$\Gamma_{a,b}^{TPA}(Z,\Omega) = \Gamma_2\Theta(\Omega-\Omega_o)(\Omega-\Omega_o)^{3/2}\left|u_{a,b}(Z,\Omega)\right|^2 \qquad 6.39.$$

Where $\Gamma_2$ is the averaged TPA coefficient, $\Omega$ is the frequency normalised to the pulse length, $\Omega_0$ is the normalised half-band gap frequency and $\Theta$ the Heavyside step function. Equation 6.39 is a fairly crude approximation for the TPA, however, it serves to illustrate the effect on the pulse.

### 6.7.4. Spectral Results.

For obvious reasons it is more convenient to discuss the effect of TPA in the spectral domain. Figure 6.10. shows that TPA causes relatively strong asymmetry in the spectrum.

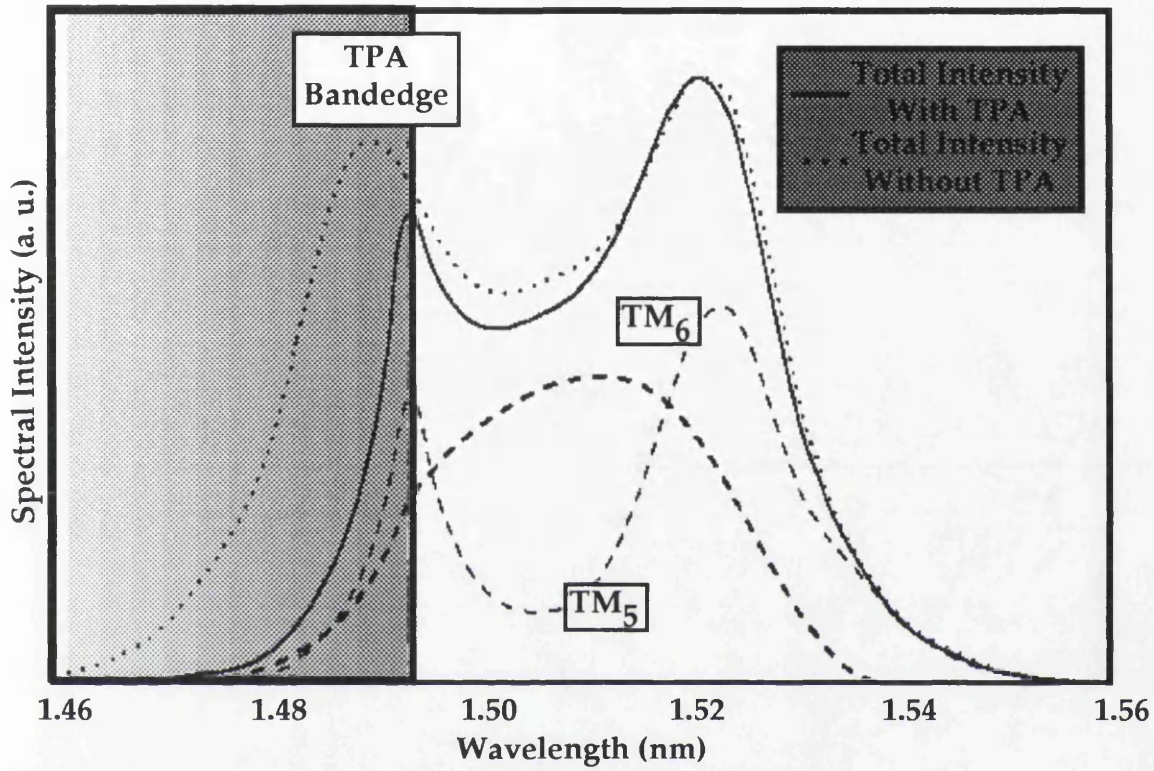


*Figure 6.10. Calculated output spectrum for both the $TM_5$ and $TM_6$ modes.*

It is clear that the NDM suffers from this nonlinear absorption appearing for wavelengths below 1.49 μm. This mode is spectrally broadened because the chirp, acquired by linear dispersion and nonlinear phase modulation, does not balance. The ADM forms a soliton like pulse and thus retains an almost a soliton like spectrum. Moreover, the unbalanced nonlinear phase modulation in the NDM causes the central dip to appear, and from the spectral shape it is possible to infer a phase shift of approximately 1.5 π (section 3.5.1.).

## 6.8. Experimental Pulse Propagation.

In the experiment a 3.5 μm wide waveguide on the sample was excited by TM polarised light, from a coupled cavity KCl:Tl colour centre laser producing 125 fs $sech^2$ pulses at 1510 nm. Due to the

small size of the ARROW core, the required ARROW modes proved extremely difficult to excite. The an input guide was therefore, excited using a large aperture, 30 cm long optical fibre lens, since this produced a input spot which approached the diffraction limit, and was exceedingly well localised. The output pulses from the fibre were checked by interferometric autocorrelation, to ensure that no significant spectral broadening, or chirp, had been incurred along the fiber. However, even using the fibre lens several ARROW modes were excited in the structure, but only two of these modes have low radiation losses ($\approx 0.5$ dB cm$^{-1}$). The rest are therefore assumed not to propagate, since they will radiate away after a few millimetres.

Considering the $TM_6$ mode it is possible to calculate the power for a fundamental soliton using equation 6.37.. For a pulse width of 125 fs, an effective area of 24 $\mu m^2$, and a nonlinearity coefficient of $2.40 \times 10^{-13}$ cm$^2$ W$^{-1}$, the fundamental soliton power is found to be 72 W ($P_s$), and the soliton period for $TM_6$ is calculated as 7.48 mm. However, since the linear absorption over the total sample length was measured to be 3 dB cm$^{-1}$, using the averaged soliton model[23], the linear losses would require an input power of $1.3 \times P_s$ for the formation of the fundamental soliton. The linear loss will also impose a broadening effect on the pulse during propagation, and will lead to an output pulse width a factor of $e^{(\alpha z)}$ longer than expected. Therefore, substituting in the ARROW parameters the output pulse is expected to be a factor of 2 broader, than the predicted soliton width due loss to the waveguide losses.

To investigate the nonlinear response of the ARROW various input pulse powers are investigated. Initially to enable investigation of the low power dispersive characteristics, a low power pulse of 7 mW average power is input to the ARROW, the power was then increased until a maximum of 48 mW average power. Table 6.1. shows the average input and output powers, as well as the peak powers in the respective modes.

Table 6.1.

| Average Input Power (mW) | Average Output Power (mW) | Peak Power Inside $TM_5$ (W) | Peak Power Inside $TM_6$ (W) |
|---|---|---|---|
| 7 | 0.27 | 26.40 | 33.60 |
| 10 | 0.40 | 39.16 | 49.84 |
| 20 | 0.75 | 73.48 | 93.52 |
| 30 | 1.20 | 117.48 | 149.52 |
| 40 | 1.60 | 156.20 | 198.80 |
| 48 | 2.00 | 195.36 | 248.64 |

*Table 6.1. Average input and output powers to the ARROW modes.*

From table 6.1. it is possible to deduce we have launched a minimum and maximum of 0.47 and $3.45 \times P_s$, the results are discussed in the following section.

### 6.8.1. Temporal Results.

If the temporal data is considered first, it can be seen from figure 6.11 that the low power (36 W total input peak power) autocorrelation FWHM points for $TM_6$ and $TM_5$ indicate pulse spreading factors of around 4.50 and 9.00 respectively. These figures are in relatively good agreement with the theoretically predicted values, however, both values are higher than expected. This is thought to be due to both an under estimation of the dispersion values, and low power input to the autocorrelator.

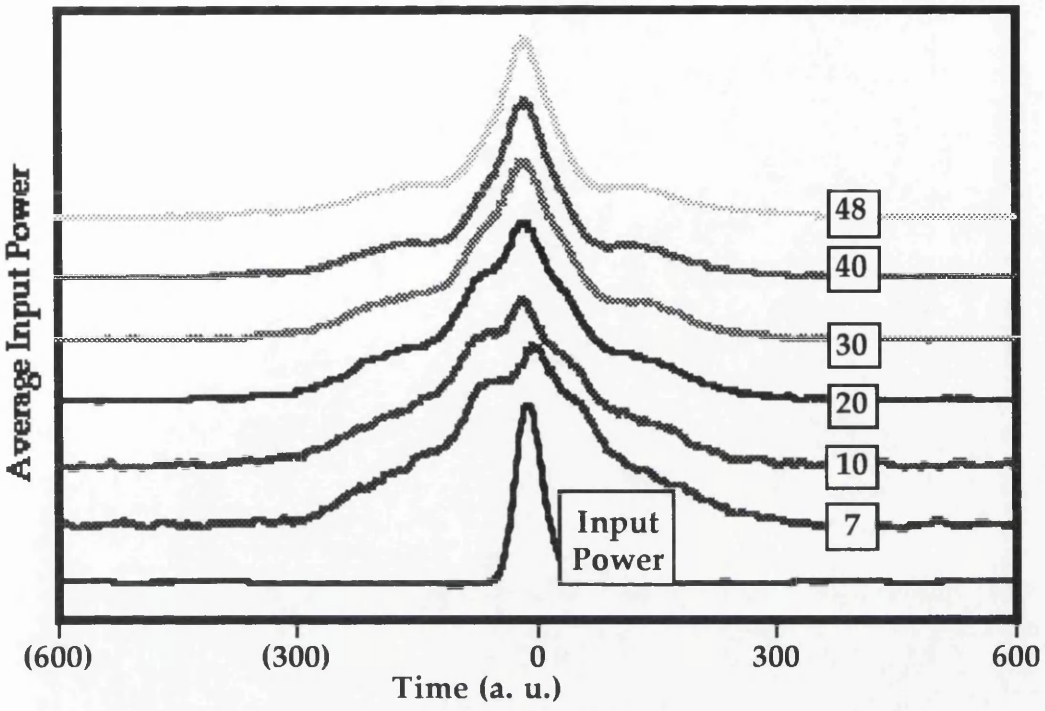


*Figure 6.11. Experimental autocorrelations from the output of the AlGaAs ARROW at various power levels.*

As the input peak power to the ARROW is increased, it is obvious that a solitonic pulse is emerging in the anomalously dispersive mode. When the total input power to $TM_6$ was 2.75 times the soliton peak power ($\approx$ 200 W), it is clear that the autocorrelation indicates the formation of a solitonic pulse, which is approaching the width of the laser input pulse. This indicates that the soliton power lies in the region of 150-200 W, which is higher than predicted. This can be explained by the under estimation of the dispersion value, used in calculating the soliton power. This is corroborated by the fact that the pulse spreading factor is also larger than expected. If the dispersion value used is altered to reflect this difference, the power needed to produce the fundamental soliton increases to 160 W which is closer to the value seen in the experiment. Increasing the power in the mode to $\approx$ 250 W did not result in any significant reduction of the pulse width. This indicated that this was indeed a solitonic pulse, as extra input energy was being shed so the pulse could retain its shape. The width of this output pulse is measured to be 265 fs, which is approximately twice the width of the input laser pulse, and is what was expected due to the waveguide losses. The solitonic pulse is also superimposed

on a pedestal, which indicates the presence of the dispersive mode $TM_5$.

### 6.8.2. Spectral Results.

From the experimental spectral data taken at high powers (figure 6.12.), it is clearly seen that the experimental spectrum is in very good qualitative agreement with the theoretically predicted one (figure 6.10.). It is observed that the shape is also very complicated, however this can again be quite easily explained due to the interaction of the two modes within the waveguide.

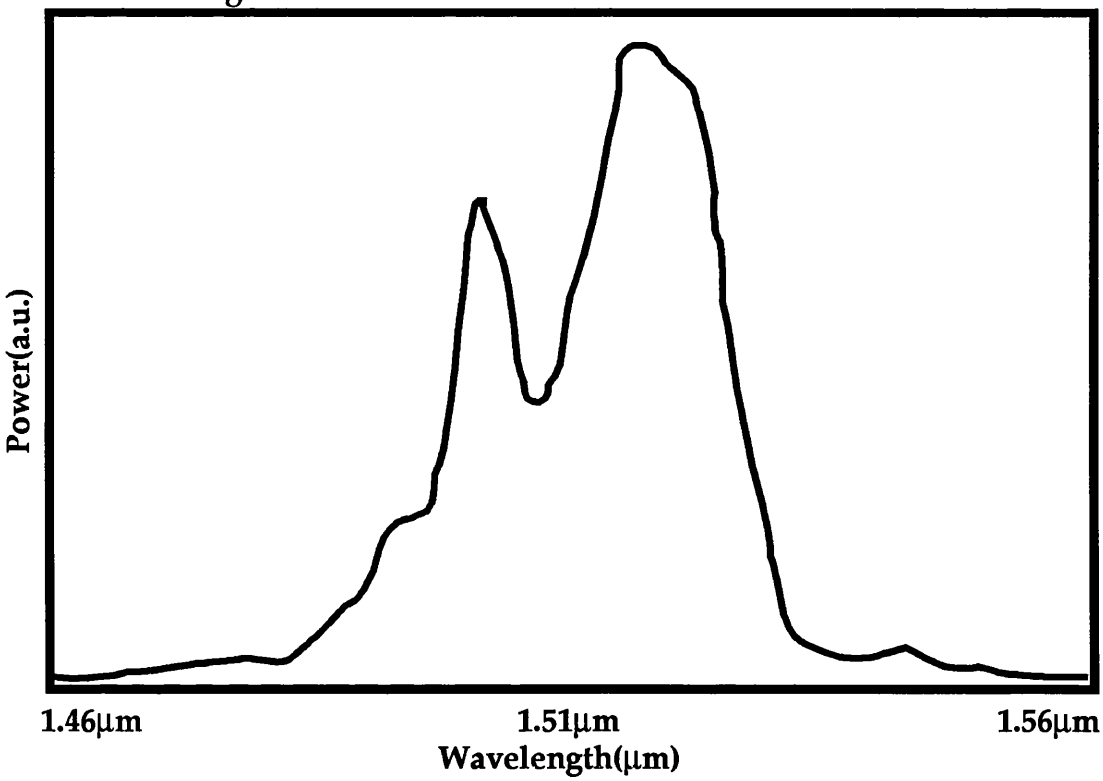


*Figure 6.12. Experimental spectrum from the output of the AlGaAs ARROW.*

The spectrum consists of two main peaks with a considerable dip approximately in the middle of the spectrum. This dip in the middle of the spectrum is due to self-phase modulation (SPM) of the dispersive mode (figure 6.11.), and it is this that also makes the spectra extremely broad. The spectrum is also seen to be very asymmetric, which is due to the TPA losses associated with the shorter wavelengths.

## 6.9. Spatial Solitons.

Spatial solitons are essentially self guided light channels, and it has been proposed that they may provide a mechanism, by which all optical switching may be realised. It has been previously shown that spatial solitons in AlGaAs waveguides may be "steered", by placing a phase shift across the transverse wavefront[24]. This was achieved by placing a silica wedge with a $2^{o}$ angle across the input beam, and then propagating the soliton across the waveguide. This obviously is impractical for communication systems, and the steering control must be either electronic, or optical. The first step however, is to recreate the steering experiment in an integrated format.

### 6.9.1. Soliton Formation.

Spatial optical solitons were introduced in chapter 1 and it was indicated that the power required for their formation is[25]:

$$P_s = \frac{n_o 2w}{n_2 a_o k^2} \qquad 6.40.$$

For the formation of spatial solitons in AlGaAs waveguides the following parameters were used:

- **Kerr coefficient ($n_2$)** $\rightarrow$ $1.6 \times 10^{-13}$ **cm$^2$ W$^{-1}$.**
- **Transverse mode size (w)** $\rightarrow$ **1.7 μm.**
- **Effective guide index ($n_o$)** $\rightarrow$ **3.308.**
- **Input $\frac{1}{e^2}$ half beamwidth ($a_o$)** $\rightarrow$ **23 μm.**
- **Wave vector in material (k)** $\rightarrow$ $1.39 \times 10^{7}$ **m$^{-1}$.**

These parameters give a fundamental soliton power of $P_S \approx 160$ W. A beam was launched into a 15 mm long AlGaAs and was found to diffract by a factor of $\approx 6$ over the sample length. The input power was then increased and self focusing of the output beam was observed. Figure 6.13. shows the input beam and output beam profiles at low and high power.

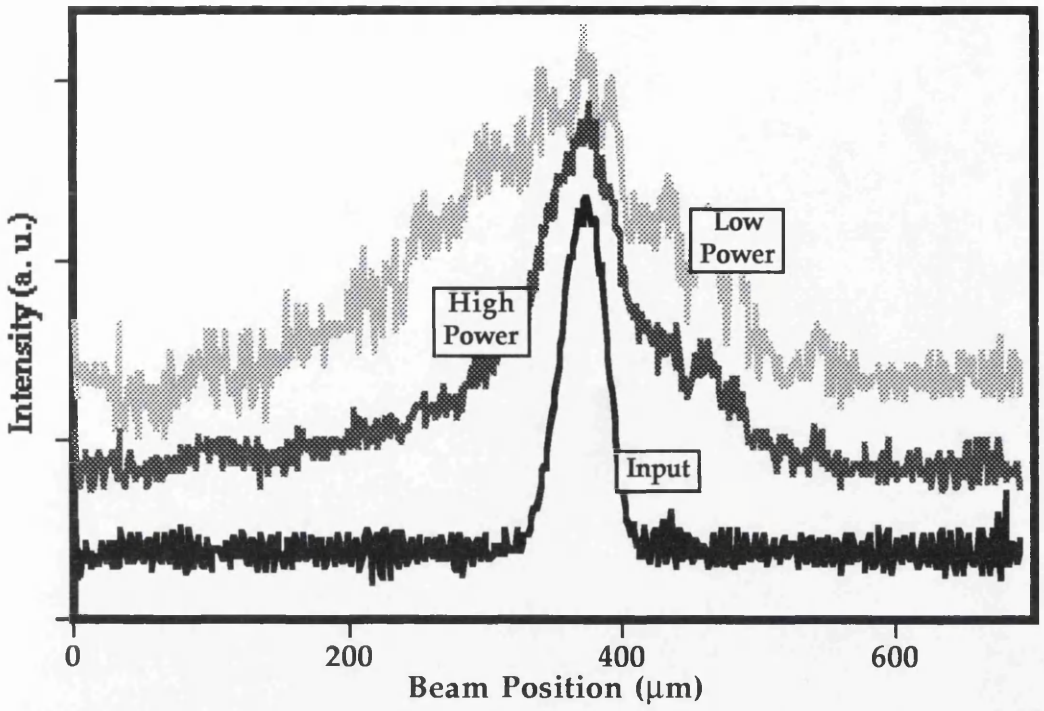


*Figure 6.13. Input beam and output beam profiles for an AlGaAs waveguide at low and high powers.*

The output beam is seen not to narrow down to the input beam width, which can be attributed to the peak power not being large enough. Indeed the average output power was 3 mW and the sample had a loss of $\approx 1.3\ dB\ cm^{-1}$, which indicated a peak input power of $\approx 95$ W, which is approximately $0.6 \times P_s$. However, as previously explained (section 1.3.2.) a soliton which has a different width will be formed for values between $0.25. \times P_s$ and $2.25 \times P_s$. From fitting the high power solitonic beam in figure 6.13., the soliton width was measured to be approximately 40 μm at the $\frac{1}{e^2}$ point. If this value is now inserted into equation 6.40., the predicted power level for fundamental soliton formation is $\approx 90$ W, which is in very good agreement with the input power level.

In calculating the soliton width the wings at the side of the beam were ignored, as these are due to the time averaging effects, which occur when the response time of the nonlinearity is faster than that of the temporal pulse duration.

### 6.9.2. Soliton Steering.

From the discussions in chapter 1 it was concluded that solitons have a sech like distribution, which can be described by:

$$A_o(x,z) = A_o \operatorname{sech}\left(\frac{x}{a}\right) e^{\left(i\frac{z}{2ka^2}\right)} \qquad 6.41.$$

Where the amplitude of the soliton is:

$$A_o = \frac{\sqrt{\frac{n_o}{n_2}}}{ka} \qquad 6.42.$$

If a linear phase ramp is imposed across the transverse profile of the soliton at the start of the waveguide, it can now be represented by:

$$A_o(x,z) = A_o \operatorname{sech}\left(\frac{x}{a}\right) e^{(ik\theta x)} \qquad 6.43.$$

It is quite obvious that if equation 6.43. is used as the initial condition, the soliton will propagate at an angle to the z axis:

$$A_o(x,z) = A_o \operatorname{sech}\left(\frac{x-\theta z}{a}\right) e^{\left(iz\frac{1-k^2a^2\theta^2}{2ka^2}+ikx\theta\right)} \qquad 6.44.$$

As mentioned previously it has been demonstrated that solitons can be steered, by placing a phase shift on the soliton profile before entering the waveguide. However, to unreservedly prove that a soliton can be steered by phase shifts it must receive the phase shift after it has also formed. Placing a phase shift upon the soliton after it has formed, also provides a method for actually proving that the self focused channel is indeed a soliton, as if it is it will show particle like behaviour and move as a whole entity.

To place this phase shift on the soliton a sample was prepared that had a "wedge" of higher refractive index on top of a planar waveguide, and is shown in figure 6.14..

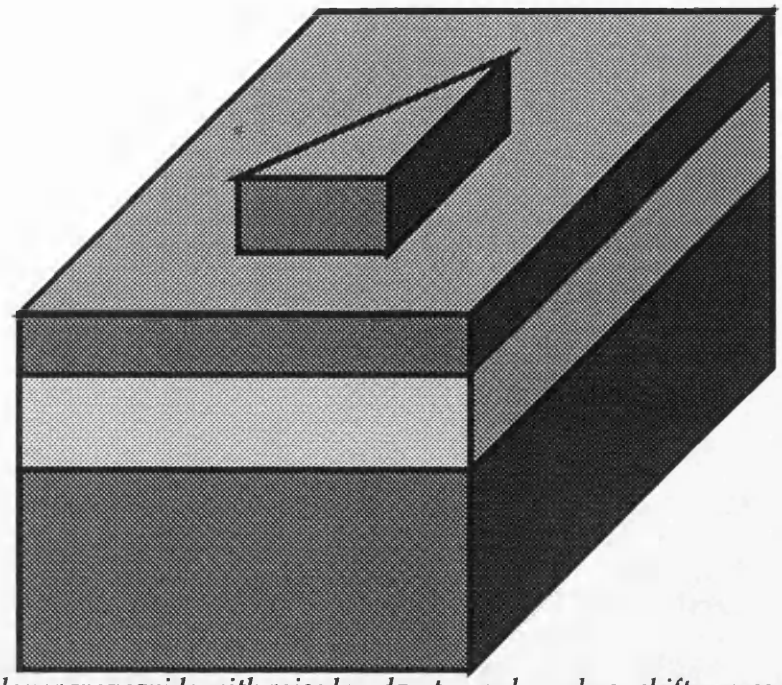

***Figure 6.14. Planar waveguide with raised wedge, to produce phase shift across soliton.***

The wedge is a 50 μm wide triangle which is 100 μm long, the length to the front of the wedge is 1.5 mm and the whole sample is 15 mm long. Using the effective index method the effective indices under the wedge and elsewhere in the guide are $n_{wedge} = 3.317$ and $n_{guide} = 3.308$. Using these indices and Snell's law it is possible to calculate the expected steering angle, which should be $\approx 0.31\ ^{o}$. The experimental shift is shown in figure 6.15..

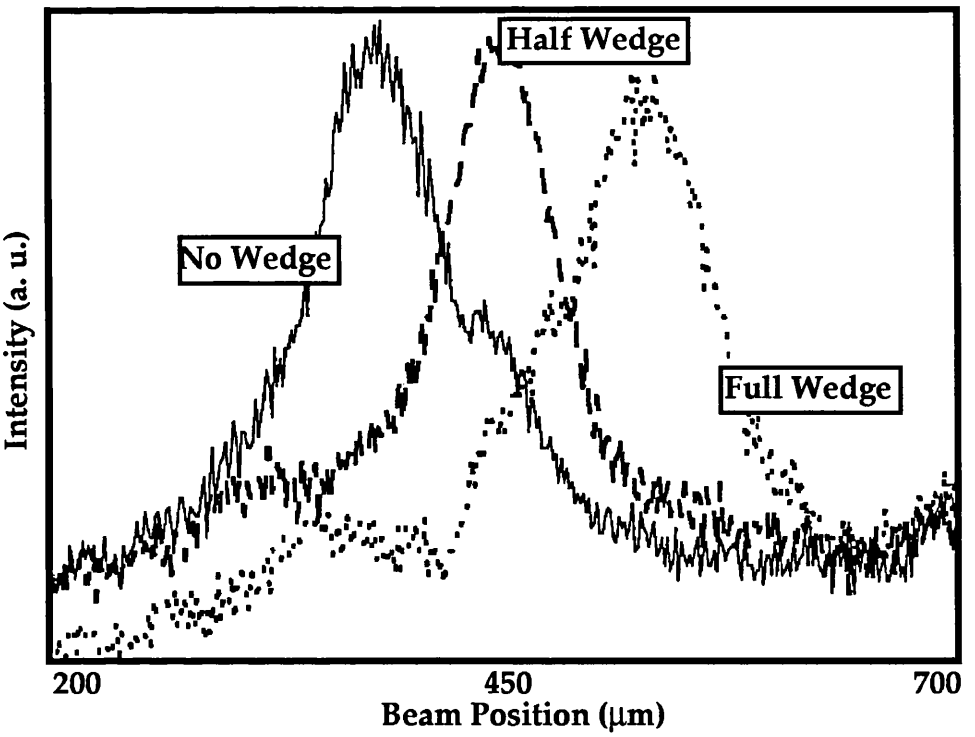


*Figure 6.15. Steering a soliton using a phase shift generated by a raised wedge.*

Using a waveguide feature it was possible to determine the lateral shift in the soliton. The maximum movement in the soliton was ≈ 120 μm, which corresponded to a steering angle of 0.51°. Which is in relatively good agreement with the predicted shift. The soliton in the middle is the case when the soliton is half on the wedge and half off (i. e. a nonuniform phase shift across the beam profile). It is clear that this does not lead to beam break up as with a low power beam, but the phase chirp must have been redistributed across the beam, and the soliton has shown particle like qualities and behaved as a single entity.

## 6.10. Further Work.

Further work on the temporal solitons aspect of this chapter, will concentrate on the selective excitation of the anomolously dispersive mode of the ARROW structure. Initially attempts will be concerned with the production of mode converters, however, selective excitation using directional coupler to match propagation constants.

There may also be a possibility to combine both aspects of this chapter in an attempt to create light bullets. These are essential

localised spatial/temporal packets of light that are contained in the spatial domain by self focusing, and by self phase modulation in the temporal domain (figure 6.16.).

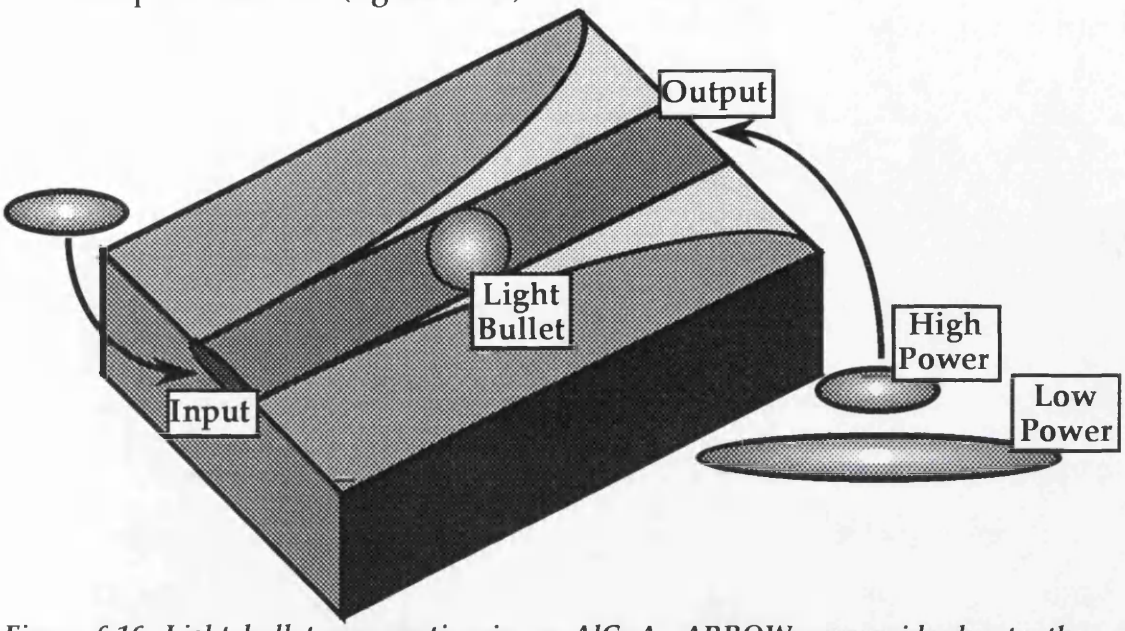


*Figure 6.16. Light bullet propagating in an AlGaAs ARROW waveguide due to the interaction of Anomalous dispersion, diffraction, and the positive Kerr type nonlinearity.*

Other work using spatial solitons will combine the localised nonlinearities realised in chapter 5, to produce novel all optical switching devices.

### 6.11. Conclusions.

In conclusion we have experimentally shown that by using properly designed AlGaAs ARROW waveguides, the natural positive dispersion of the semiconductor can be overcome and waveguide modes can be made anomalous. This fact has been used to demonstrate solitonic compression of 1.51 μm femtosecond pulses propagating in the guide. The results are seen to correlate well with the theoretically predicted values.

The numerical investigations show that primarily linear losses, TPA, and nonlinear mode coupling result in the deviation of the pulse spectrum and temporal shape from the ideal soliton. The spectrally broadened NDM suffers mainly from TPA, but can transform these distortions to the ADM due to nonlinear mode coupling.

Spatial solitons have also been shown to propagate at angles which depend upon the phase imparted upon their profile, and they have been shown to posses a particle-like behaviour.

# References.


1 J. Gowar, "Optical communication systems." Prentice Hall, 1993.

2 J. S. Aitchison, Y. Silberberg, A. M. Weiner, D. E. Leaird, M. K. Oliver, J. L. Jackel, E. M. Vogel and P. W. E. Smith, "Spatial optical solitons in planar glass waveguides.", Opt. Soc. Am. B., 8, 1291, 1991.

3 A. W. Synder, D. J. Mitchell and B. Luther-Davis, "Dark spatial solitons constructed from modes of linear waveguides.", J. Opt. Soc. Am. B., 10, 2341, 1993.

4 G. P. Agrawal, Nonlinear Fiber Optics, Academic Press, San Diego, Boston, New York, 1995.

5 M. Sheik-Bahae, D. C. Hutchings, D. J. Hagan, and E. W. Van Stryland, "Dispersion of bound electronic nonlinear refraction in solids.", IEEE J. Quantum Electron., 27, 1296, 1991.

6 A. Villeneuve, P. Dumais, A. Morel, and J. S. Aitchison, "Bright temporal solitons in AlGaAs waveguides at 810nm." PD2-1 Nonlinear Guided Waves And Their Applications, Dana Point, 1995.

7 F. Lederer and W. Biehlig, "Bright solitons and light bullets in semiconductor waveguides.", Electron. Lett., 30, 1871, 1994.

8 M. A. Duguay, T. Kokubun, T. L. Koch and L. Pfeiffer, "Antiresonant reflecting optical waveguides in SiO2-Si multilayers structures.", Appl. Phys. Lett., 49, 13, 1986.

9 U. Truschel, M. Mann, F. Lederer, C. Wächter and A. D. Boardman, "Nonlinear switching in coupled antiresonant reflecting optical waveguides.", Appl. Phys. Lett., 59, 1940, 1991.

10 K. Thyagarajan and S. Pilver, "Resonant tunneling three-waveguide polarisation splitter.", IEEE, J. Lightw. Tech., 10, 1334, 1992.

11 L. J. Mawst, D. Botez, C. Zmudzinski and C. Tu, "Antiresonant reflecting optical waveguide-type, single-mode diode lasers.", Appl. Phys. Lett. 61, 503, 1992.

12 T. L. Koch, P. J. Corvini, W. T. Tsang, U. Koren and B. I. Miller, "Wavelength selective interlayer directionally grating-coupled InP/InGaAsP waveguide Photodetection.", Appl. Phys. Lett. 51, 1060, 1987.

13 T. Baba, Y. Kokubun, T. Sakaki and K. Iga, "Loss reduction of an ARROW waveguide in shorter wavelength and it's stack configuration.", IEEE J. Lightw. Techn. 6, 1440, 1988.

14 J. Chilwell and I. Hodgkinson, "Thin-films field-transfer matrix theory of planar waveguides and reflection from prism-loaded waveguides.", J. Opt. Am. A, 1, 742, 1984.

15 E. Hecht and A. Zajac, "Optics." Addison-Wesley Publishing Company, 1980.

[16] J. D. Kraus and K. R. Carver, "Electromagnetics.", M$^{C}$Graw-Hill International Book Company, 1981.

[17] R. Ulrich, "Theory of prisim-film coupling by plane-wave analysis.", J. Opt. Soc. Am., 60, 1337, 1970.

[18] M. Cantin, C. Carignan, R. Côté, M. A. Duguay, R. Larose, P. LeBel and F. Ouellette, "Remotely switched hollow-core antiresonant reflecting optical waveguide.", Opt. Lett. 16, 1738, 1991.

[19] Z. Su, "Generation and propagation of ultrashort laser pulses using nonlinear waveguides.", Ph. D. Thesis, University of St. Andrews, 1994.

[20] F. Lederer, W. Biehlig, R. Muschall, and L. Leine, "Soliton switching in propely tailored nonlinear directional couplers.", International Synopsis on integrated optics, April 1994.

[21] M. Mann,U. Truschel, C. Wächter, L. Leine and F. Lederer, "Directional coupler based on an antiresonant optical waveguide.", Opt. Lett. 16, 805, 1991.

[22] J. M. Kubica, J. Gazecki, and G. K. Reeves. "Multimode operation of ARROW waveguides.", Optics Comm., 102, **(3,4)**. October 1993.

[23] A. Hasegawa and Y. Kodama, "Solitons in Optical Communications", Clarendon Press, Oxford, 1995.

[24] P. V. Mamyshev, A. Villeneuve, G. I. Stegeman and J. S. Aitchison, "Steerable opticle waveguides formed by bright spatial solitons in AlGaAs.", Electron. Lett., 30, 726, 1994.

[25] J. S. Aitchison, K. Al-Hemyari, C. N. Ironside, R. S. Grant and W. Sibbett, "Observation of spatial solitons in AlGaAs waveguides.", Electron. Lett., 28, 1879, 1992.

# Appendix A.

## Wafers.

# A 776

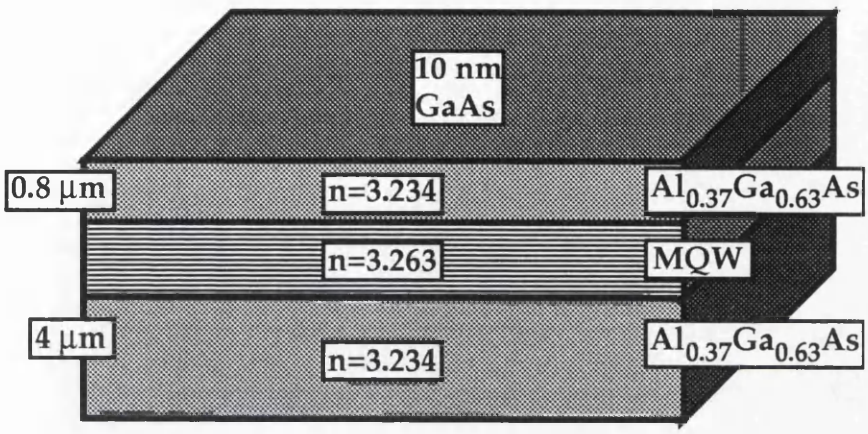


## MQW

| | |
|---|---|
| Number of Periods: | 71 |
| Aluminium Concentration in Barriers: | 40 % |
| Aluminium Concentration in Wells: | 14 % |
| Width of Barriers: | 14 nm |
| Width of Wells: | 7 nm |
| Wave Function at Half Barrier: | 0.91 % |
| Heavy Hole Exciton (290 °K): | 748 nm |
| Average Band Gap (290 °K): | 681 nm |
| Disordered Band Edge Shift: | 67 nm |

# B 415

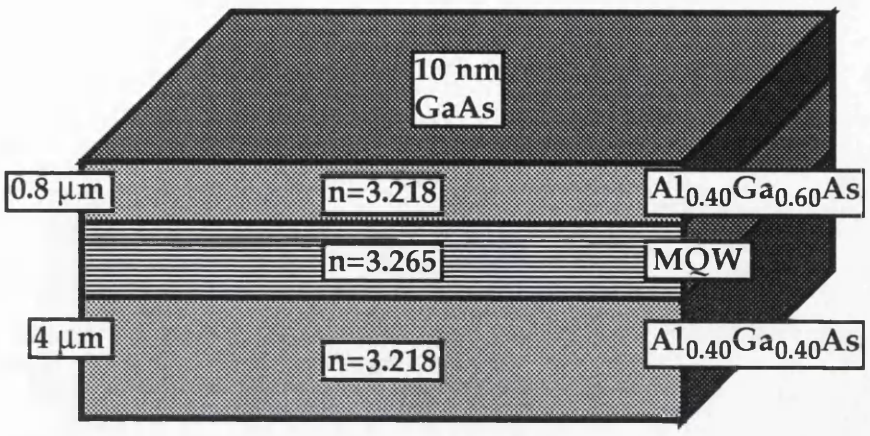


## MQW

| | |
|---|---|
| Number of Periods: | 78 |
| Aluminium Concentration in Barriers: | 40 % |
| Aluminium Concentration in Wells: | 0 % |
| Width of Barriers: | 10 nm |
| Width of Wells: | 2.8 nm |
| Wave Function at Half Barrier: | 3.72 % |
| Heavy Hole Exciton (290 $^{o}$K): | 744 nm |
| Average Band Gap (290 $^{o}$K): | 682 nm |
| Disordered Band Edge Shift: | 62 nm |

# B 579

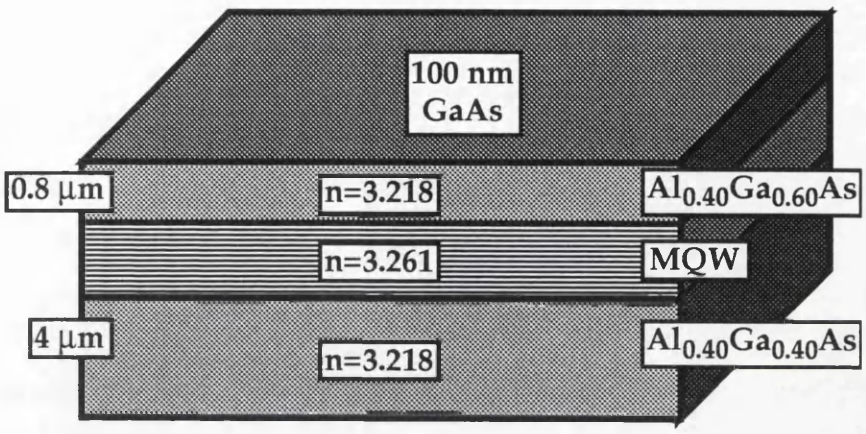


## MQW

| | |
|---|---|
| Number of Periods: | 78 |
| Aluminium Concentration in Barriers: | 40 % |
| Aluminium Concentration in Wells: | 0 % |
| Width of Barriers: | 10 nm |
| Width of Wells: | 2.8 nm |
| Wave Function at Half Barrier: | 3.72 % |
| Heavy Hole Exciton (290 $^{o}$K): | 733nm |
| Average Band Gap (290 $^{o}$K): | 678 nm |
| Disordered Band Edge Shift: | 55 nm |

# B 589

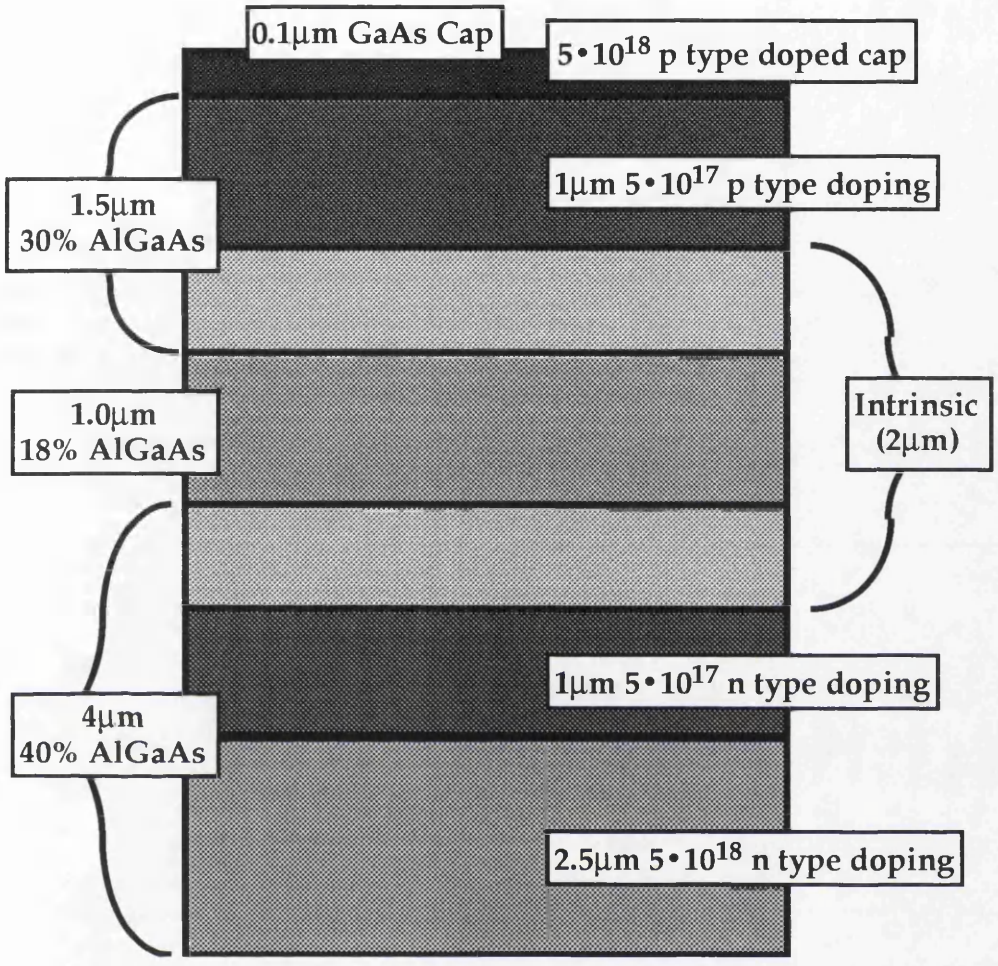
0.1μm GaAs Cap
5•10^18 p type doped cap
1μm 5•10^17 p type doping
1.5μm
30% AlGaAs
Intrinsic
(2μm)
1.0μm
18% AlGaAs
1μm 5•10^17 n type doping
4μm
40% AlGaAs
2.5μm 5•10^18 n type doping

# B 490

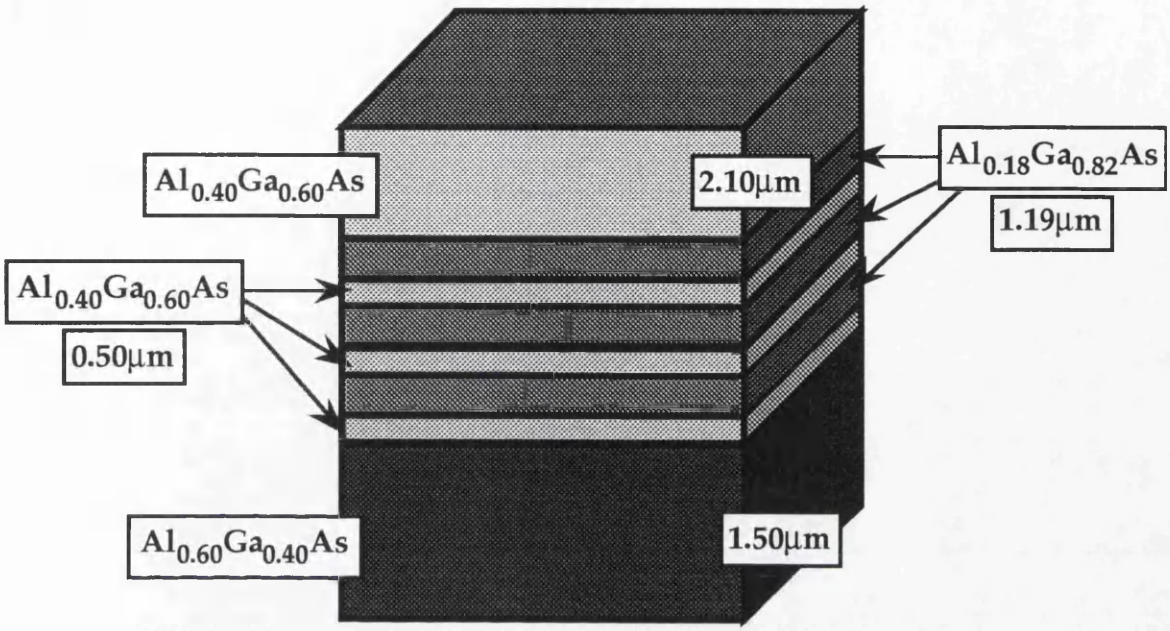
$Al_{0.40}Ga_{0.60}As$
2.10μm
$Al_{0.18}Ga_{0.82}As$
1.19μm
$Al_{0.40}Ga_{0.60}As$
0.50μm
$Al_{0.60}Ga_{0.40}As$
1.50μm

# Appendix B.

# Programs.

## AlGaAs Refractive Index.

A Mathematica program that will calculate the Refractive index of $Al_xGa_{(1-x)}As$ at wavelengths below the bandedge. It has also been converted to generate tables and plots combining the two variables.

## Matrix Method.

A Mathematica program elegantly written by F. Clark that will calculate the effective index of the various modes of an arbitrary defined slab waveguide.

## QW.

Initially written by B. Bumhra, it has been updated and converted using Think Pascal, and now operates as a stand alone application for Macintosh computers. It calculates the energy levels of AlGaAs quantum wells, determines the wave functions in the barriers and the equivalent refractive index of the well.

# AlGaAs Refractive Index.

# (Mathematica)

```
ClearAll[x, n, e, fc, Ao, Bo, Eo, fcso, l, c, cso]
x := 0.18
l := 1.55
hbar := (6.63*10^-34) / (2 * Pi)
PE := 1.24 / l
Ao :=6.3 + (19.0 * x)
Bo :=9.4 - (10.2 * x)
Eo := 1.425 + (1.115 * x) + (0.37 * x^2)
Δo := 0.37 + (0.1 x) - (0.1 * x^2)
c := PE / Eo
cso := PE / (Eo+Δo)
fc :=(c^-2)*(2-Sqrt[1+c]-Sqrt[1-c])
fcso :=(cso^-2)*(2-Sqrt[1+cso]-Sqrt[1-cso])
e :=Ao * (fc+ 0.5 * (Eo/(Eo+Δo))^1.5 * fcso)+Bo
n := Sqrt[e]
N[n]
```

# Matrix Method. (Mathematica)

```
Clear[l]
n={1.,1.44825,2.1,1.40,3.5};
d={0.,3.9,0.145,2.3,0};
l=0.633;
ko:=2*Pi/l;
zo=376;
matrix[x_]:=
        Module[{a11,a12,a21,a22,xx=x,nels},
        Clear[a11,a12,a21,a22,t];
        nels=Length[d];
        t=Map[Sqrt[#^2.-xx^2.]&,n];
        a11=a22=Cos[ko*t*d];
        a12=-I*Sin[ko*t*d]/(t/zo);
        a21=a12*(t/zo)^2.;
        gc=t[[1]];
        If[Re[xx]<Re[n[[nels]]],gs=-t[[nels]],gs=t[[nels]]];
m={{1.,0.},{0.,1.}};
Do[m=m.N[{{a11[[i]],a12[[i]]},{a21[[i]],a22[[i]]}}],{i,2,nels-1}];
Chop[gc*m[[1,1]]+(gc*gs*m[[1,2]]/zo)+zo*m[[2,1]]+gs*m[[2,2]]]];
Plot[Im[matrix[x]], {x, 1.41, 1.45}];
Print[FindRoot[matrix[x]==0,{x,1.439}]];
```

# QW. (Pascal)

```
Program Wafer;

{* Program to design MQW wafer for minimal*}
{* band edge shift on disordering *}

 Const
  eV = 1.602193e-19;
  hbar = 1.054925e-34;
  restmass = 9.10956e-31;
  EnergyRes = 1e-5;

 Var
   WW, BW, VCBD, VVBD, HHMB, HHMW, HHBE, LHBE, HHE, LHE,
EEL, EGW, EGB, EMW, EMB, EX, HHEX, LHEX, WF, AAX, AEG, RITM,
RITE, AlWell, AlBarr, EnergyGap, ElectronLevel, Temperature,
HeaveyHoleMass, TempEnergy: Real;
  Exit, F, FE, FHH, FLH: Boolean;
  QN, Complete: Integer;
   TextWindow: Rect;

 Function Einfunc (ElecEnergy, VcBand, mWell, mBarrier, WellWidth:
Real; Quantnum: Integer): Real;
{* Returns the vaue of the solution of a finite potential well *}

  Var
   Alpha, Beta, Massratio: Real;

 Begin {* Einfunc *}
  WellWidth := WellWidth * 1e-10;
  Massratio := mWell / mBarrier;
  VcBand := VcBand * eV;
  ElecEnergy := ElecEnergy * eV;
   mWell := mWell * restmass;
   mBarrier := mBarrier * restmass;
   Alpha := Sqrt((2 * mBarrier * (VcBand - ElecEnergy)) / (hbar * hbar));
   Beta := Sqrt((2 * mWell * ElecEnergy) / (hbar * hbar));
    Einfunc := WellWidth * Beta - 2 * ArcTan(Massratio * Alpha / Beta) -
Quantnum * Pi;
 End; {* Einfunc *}

 Function Hholemass (AlConc: Real): Real;
{* Returns relative heavy hole mass at zero energy *}

 Begin {* Hholemass *}
  Hholemass := 0.34 + 0.45 * AlConc; {* From Duggan et al *}
 End; {* Hholemass *}
```

```
 Function RefractiveIndex (AlConc: Real): Real;
{* Returns refractive Index at room temperature *}
 Begin {* RefractiveIndex *}
  RefractiveIndex := 3.43289 - (0.537154 * AlConc);
 End; {* RefrativeIndex *}

 Function lhEmass (ElecEnergy, VcBand, AlConc: Real): Real;
{* Returns energy dependent relative light hole mass *}

  Const
   Gamma = 7.35e-19;

  Var
   mx, Sub1: Real;

 Begin {* lhEmass *}
  mx := 0.087 + 0.063 * AlConc;
  Sub1 := (hbar / restmass * hbar / eV) / (2 * mx * Gamma);
  lhEmass := mx * (1 + (ElecEnergy - VcBand) / Sub1);
 End; {* lhEmass *}

 Function eEmass (ElecEnergy, VcBand, AlConc: Real): Real;
{* Returns energy dependent relative mass *}

  Const
   Gamma = 4.9e-19;

  Var
   mx, Sub1: Real;

 Begin {* eEmass *}
  mx := 0.0665 + 0.0835 * AlConc;
  Sub1 := (hbar / restmass * hbar / ev) / (2 * mx * Gamma);
  eEmass := mx * (1 + (ElecEnergy - VcBand) / Sub1);
 End; {* eEmass *}

 Function Gap (AlConc: Real): Real;
{* Returns bandgap in eV as function of Al Concentration *}

 Begin {* Gap *}
  Gap := 1.425 + 1.155 * AlConc + 0.37 * AlConc * AlConc;
 End; {* Gap *}

 Function EgTemp (Temperature: Real): Real;
{* Returns Temperature dependent bandgap of GaAs in eV *}

 Begin {* EgTemp *}
   EgTemp := 1.519 - ((5.405e-4 * Temperature * Temperature) / (204 +
Temperature)); {* From Kawai *}
 End; {* EgTemp *}
```

```
 Procedure MQWSetup (xBarrier, xWell, Temp, WellWidth: Real; Var
Hhmassbarr, Hhmasswell, VcBand, VvBand, HhBinEn, LhBinEn, EgBarr,
EgWell: Real);

{* Establishes the Energy parameters of the MQW *}

 Begin {* MQWSetup *}
  EgBarr := Gap(xBarrier) + EgTemp(Temp) - 1.425;
  EgWell := Gap(xWell) + EgTemp(Temp) - 1.425;
  VcBand := (1 - 0.55 * xBarrier) * (EgBarr - EgWell);
  VvBand := (EgBarr - EgWell - VcBand); {** 0.55 * xBarrier*}
    HhBinEn := (14.47 - 0.0645 * WellWidth - 1.41e-4 * WellWidth *
WellWidth) * 1e-3; {* From Koteles *}
    LhBinEn := (15.74 - 0.0611 * WellWidth - 1.19e-4 * WellWidth *
WellWidth) * 1e-3; {* From Koteles *}
 End; {* MQWSetup *}

 Procedure ElecLevel (xWell, xBarrier, WellWidth: Real; Quantnum:
Integer; Var VcBand, ElecEnergy, emasswell, emassbarr: Real; Var
FoundElec: Boolean);

{* Establishes the lowest electron energy within the well *}

  Var
   Emin, Emax, Emid, Fmin, Fmax, Fmid: Real;

 Begin {* ElecLevel *}
  Emin := EnergyRes;
  Emax := Vcband;
  emasswell := eEmass(Emin, 0, xWell);
  emassbarr := eEmass(Emin, Vcband, xBarrier);
    Fmin := Einfunc(Emin, Vcband, emasswell, emassbarr, WellWidth,
Quantnum);
  emasswell := eEmass(Emax, 0, xWell);
  emassbarr := eEmass(Emax, Vcband, xBarrier);
    Fmax := Einfunc(Emax, Vcband, emasswell, emassbarr, WellWidth,
Quantnum);
  If (Fmin < 0) And (Fmax < 0) Then
   Foundelec := False
  Else
   Begin
    Foundelec := False;
    Repeat
     Emid := (Emin + Emax) / 2;
     emasswell := eEmass(Emid, 0, xWell);
     emassbarr := eEmass(Emid, Vcband, xBarrier);
       Fmid := Einfunc(Emid, Vcband, emasswell, emassbarr, WellWidth,
Quantnum);
     If (Fmid > 0) Then
      Emax := Emid
     Else
```

```
    Emin := Emid;
    If Abs(Emax - Emin) < Energyres Then
     Foundelec := True;
    Until Foundelec;
   ElecEnergy := Emid;
    emasswell := eEmass(Emin, 0, xWell);
    emassbarr := eEmass(Emin, Vcband, xBarrier);
  End;
 End; {* ElecLevel*}

  Procedure LholeLevel (xWell, xBarrier, WellWidth, Vvband: Real;
Quantnum: Integer; Var LholeEnergy: Real; Var FoundLhole: Boolean);
{* Establishes the lowest light hole energy within the well *}

  Var
   Emin, Emax, Emid, lhmasswell, lhmassbarr, Fmin, Fmax, Fmid: Real;

 Begin (* Lholelevel *)
  Emin := Energyres;
  Emax := Vvband;
  lhmasswell := lhEmass(Emin, 0, xWell);
  lhmassbarr := lhEmass(Emin, Vvband, xBarrier);
   Fmin := Einfunc(Emin, VvBand, lhmasswell, lhmassbarr, Wellwidth,
Quantnum);
  lhmasswell := lhEmass(Emax, 0, xWell);
  lhmassbarr := lhEmass(Emax, Vvband, xBarrier);
   Fmax := Einfunc(Emax, VvBand, lhmasswell, lhmassbarr, Wellwidth,
Quantnum);
  If (Fmin < 0) And (Fmax < 0) Then
   FoundLhole := False
  Else
   Begin
    FoundLhole := False;
    Repeat
     Emid := (Emin + Emax) / 2;
     lhmasswell := lhEmass(Emid, 0, xWell);
     lhmassbarr := lhEmass(Emid, Vvband, xBarrier);
      Fmid := Einfunc(Emid, VvBand, lhmasswell, lhmassbarr, Wellwidth,
Quantnum);
     If (Fmid > 0) Then
      Emax := Emid
     Else
      Emin := Emid;
     If Abs(Emax - Emin) < Energyres Then
      FoundLhole := True;
     Until FoundLhole;
    LholeEnergy := Emid;
   End;
 End; {* LholeLevel *}
```

```
 Procedure HholeLevel (xWell, xBarrier, WellWidth, Vvband: Real;
Quantnum: Integer; Var HholeEnergy: Real; Var FoundHhole: Boolean);

{* Establishes the lowest Heavey hole energy within the well *}

 Var
  Emin, Emax, Emid, Hhmasswell, Hhmassbarr, Fmin, Fmax, Fmid: Real;

 Begin {* HholeLevel *}
 Emin := Energyres;
 Emax := Vvband;
  Hhmasswell := Hholemass(xWell);
  Hhmassbarr := Hholemass(xBarrier);
  Fmin := Einfunc(Emin, VvBand, Hhmasswell, Hhmassbarr, Wellwidth,
Quantnum);
  Fmax := Einfunc(Emax, VvBand, Hhmasswell, Hhmassbarr, Wellwidth,
Quantnum);
  If (Fmin < 0) And (Fmax < 0) Then
   FoundHhole := False
  Else
   Begin
    FoundHhole := False;
    Repeat
     Emid := (Emin + Emax) / 2;
          Fmid  :=  Einfunc(Emid,  VvBand,  Hhmasswell,  Hhmassbarr,
Wellwidth, Quantnum);
     If (Fmid > 0) Then
      Emax := Emid
     Else
      Emin := Emid;
     If Abs(Emax - Emin) < Energyres Then
      FoundHhole := True;
    Until FoundHhole;
    HholeEnergy := Emid;
   End;
 End; {* HholeLevel *}

  Procedure Exciton (FoundElec, FoundHeavyHole, FoundLightHole:
Boolean; HholeEnergy, LholeEnergy, HhBinEn, LhBinEn, ElecEnergy,
EgWell: Real; Var HHExcEnergy, LHExcEnergy: Real);
 Begin
  If FoundElec And FoundHeavyHole Then
   HHExcEnergy := ElecEnergy + HholeEnergy + EgWell - HhBinEn;
  If FoundElec And FoundLightHole Then
   LHExcEnergy := ElecEnergy + LholeEnergy + EgWell - LhBinEn;
 End;{* Exciton *}

  Procedure WaveFunction (FoundElec: Boolean; VcBand, ElecEnergy,
EffMassWell, EffMassBarr, Barrier: Real; Var WaveFunc: Real);

  Var
```

```
  Kappa, BindEnergy, EffMass, MidBarr: Real;

 Begin
  If FoundElec Then
   Begin
    Barrier := Barrier * 1e-10;
    MidBarr := Barrier / 2;
    BindEnergy := (VcBand - ElecEnergy) * eV;
    EffMass := (EffMassWell + EffMassBarr) * RestMass / 2;
    Kappa := sqrt((2 * EffMass * BindEnergy) / (hBar * hBar));
    WaveFunc := 100 * Exp(-1 * MidBarr * Kappa);
   End {* If *}
  Else
   WaveFunc := 0;
 End; {* WaveFunction *}

 Procedure Control (Var Finish: Boolean);

  Var
   Answer: Char;
   Leave: Boolean;

 Begin
  Leave := False;
  WriteLn('Re-Run Program ? (Y/N):');
  Repeat
   ReadLn;
   ReadLn(Answer);
   Answer := Answer;
   If (Answer = 'n') Or (Answer = 'y') Or (Answer = 'N') Or (Answer = 'Y')
Then
    Begin
     Leave := True;
     If (Answer = 'y') Or (Answer = 'Y') Then
      Finish := False
     Else
      Finish := True
    End;{* If *}
  Until leave;
 End;{* Control *}

 Procedure Average (Temp, xBarrier, xWell, Wellwidth, BarrWidth: Real;
Var AveAlConc, AveEg, RefractiveTM, RefractiveTE: Real);

  Var

   RefractiveBarr, RefractiveWell: Real;

 Begin
  RefractiveBarr := RefractiveIndex(xBarrier);
  RefractiveWell := RefractiveIndex(xWell);
```

```
  AveAlConc := ((xWell * WellWidth) + (xBarrier * BarrWidth)) /
(WellWidth + BarrWidth);
 AveEg := Gap(AveAlConc) + EgTemp(Temp) - 1.425;
 RefractiveTE := RefractiveIndex(AveAlConc);
 RefractiveTM := RefractiveIndex(AveAlConc);

End;{* Average *}

Procedure Header;
Begin
  WriteLn('Program to Determine the Exciton Energies within a
Quantum Well');
 WriteLn;
 WriteLn;
End; {* Header *}

 Procedure EnterData (Var xBarrier, xWell, WellWidth, BarrWidth,
Temp: Real);

Begin
 xBarrier := 10;
 xWell := 10;
 If (xBarrier > 1) Or (xWell > 1) Then
  Begin
   Write(' Please enter the aluminum concentration in the barrier (%): ');
   Read(xBarrier);
   WriteLn;
   xBarrier := xBarrier / 100; {* Convert to fraction *}
   Write(' Please enter the aluminum concentration in the well (%): ');
   Read(xWell);
   WriteLn;
   xWell := xWell / 100; {* Convert to fraction *}
   Write(' Please enter the width of the barrier (Å): ');
   Read(BarrWidth);
   WriteLn;
   Write(' Please enter the width of the well (Å): ');
   Read(WellWidth);
   WriteLn;
   Write(' Please enter the temperature of the structure (K): ');
   Read(Temp);
   WriteLn;
  End {* If *}
End; {* EnterData *}

 Procedure DisplayDataHeader (xbarrier, xWell, WellWidth, BarrWidth,
EgBarr, EgWell, VcBand, VvBand, AveAlConc, AveEg, RefractiveTM,
RefractiveTE: Real);

Begin
```

```
  WriteLn('
       Al Concentration                    Width
       BandGap');
  WriteLn('                                                    (
% )
                          ( Å )          ( eV )');
  WriteLn;
  WriteLn('Well', '                          ', xWell * 100 : 5 : 2, '

            ', WW : 5 : 0, '                                    ',
EgWell : 5 : 4);
  WriteLn;
  WriteLn('Barrier', '          ', xBarrier * 100 : 5 : 2, '
                                              ', BW : 5 : 0, '
                          ', EgBarr : 5 : 4);
  WriteLn;
  WriteLn('The well depth in the conduction band is ', VcBand : 5 : 4,
'eV');
  WriteLn;
  WriteLn('The well depth in the valence band is ', VvBand : 5 : 4, 'eV');
  WriteLn;
  WriteLn('The average composition is ', AveAlConc * 100 : 5 : 1, '%');
  WriteLn;
  WriteLn('The average band gap is ', 1.24e3 / AveEg : 4 : 1, 'nm', ' (',
AveEg : 5 : 4, 'eV)');
  WriteLn;
  WriteLn('The linear refractive index (TM) is ', RefractiveTM : 5 : 4);
  WriteLn;
  WriteLn('The linear refractive index (TE) is ', RefractiveTE : 5 : 4);
  WriteLn;
  WriteLn('
                          Heavy                              Light
                                Heavy
                    Light');
  WriteLn('                     Electron          Hole
                    Hole                                    Exciton
                                      Exciton
              Half Barrier');
  WriteLn('n                    Energy                     Energy
                          Energy
       Transition               Transition
       WaveFunction');
  WriteLn('                     ( eV )                ( eV )
             ( eV )                        ( nm )
                          ( nm )
       ( % )');
 End; {* DisplayDataHeader *}
```

Procedure DisplayData (Quantnum: Integer; FoundElec, FoundHeavyHole, FoundLightHole: Boolean; ElecEnergy, HHoleEnergy, LHoleEnergy, HHoleExciton, LHoleExciton: Real);

```
Begin
 If FoundElec Then
  Begin
   Write(Quantnum : 1);
   If FoundElec Then
   Write(ElecEnergy : 9 : 4)
  Else
     Write('    ______');
   If FoundHeavyHole Then
   Write(HHoleEnergy : 10 : 4)
  Else
     Write('    ______');
   If FoundLightHole Then
   Write(LHoleEnergy : 10 : 4)
  Else
     Write('    ______');
   If FoundHeavyHole Then
   Write(1.24e3 / HHoleExciton : 11 : 1)
  Else
     Write('    ______');
   If FoundLightHole Then
   Write(1.24e3 / LHoleExciton : 13 : 1)
  Else
     Write('    ______');
   If WF = 0 Then
     Write('    ______')
  Else
   Write(WF : 13 : 2);
   WriteLn;
 End
 Else
  Begin
   WriteLn;
   WriteLn;
   WriteLn('There are no more bound states. ');
   WriteLn;
  End;{* If *}
End; {* DisplayData *}

Begin {* Main program *}
 F := False;
 Repeat
  GetTextRect(TextWindow);
  With TextWindow Do
   Begin
    Top := 50;
    Bottom := 450;
    Left := 50;
    Right := 600;
   End;
   SetTextRect(TextWindow);
```

```
 ShowText;
 Header;
  EnterData(AlBarr, AlWell, WW, BW, Temperature);
   Average(Temperature, AlBarr, AlWell, WW, BW, AAX, AEG, RITM,
RITE);
   MQWSetup(AlBarr, AlWell, Temperature, WW, HHMB, HHMW,
VCBD, VVBD, HHBE, LHBE, EGB, EGW);
   DisplayDataHeader(AlBarr, AlWell, WW, BW, EGB, EGW, VCBD,
VVBD, AAX, AEG, RITM, RITE);
 QN := 0;
 Exit := False;
 Repeat
  ElecLevel(AlWell, AlBarr, WW, QN, VCBD, EEL, EMW, EMB, FE);
   HholeLevel(AlWell, AlBarr, WW, VVBD, QN, HHE, FHH);
   LholeLevel(AlWell, AlBarr, WW, VVBD, QN, LHE, FLH);
   Exciton(FE, FHH, FLH, HHE, LHE, HHBE, LHBE, EEL, EGW, HHEX,
LHEX);
   WaveFunction(FE, VCBD, EEL, EMW, EMB, BW, WF);
  DisplayData(QN, FE, FHH, FLH, EEL, HHE, LHE, HHEX, LHEX);
  QN := QN + 1;
  If FE = False Then
   Exit := True
 Until Exit;
 Control(F);
Until F;
End.
```

GLASGOW UNIVERSITY LIBRARY